Methods of Improving the Surface Flatness of Thin Glass Sheets and Silicon Wafers

by

Mireille Akilian

B.E., Mechanical Engineering, American University of Beirut (2002)

S.M., Mechanical Engineering, Massachusetts Institute of Technology (2004)

Submitted to the Department of Mechanical Engineering
in partial fulfillment of the requirements for the degree of

Doctor of Philosophy in Mechanical Engineering

at the

MASSACHUSETTS INSTITUTE OF TECHNOLOGY

September 2008

Author .....
Department of Mechanical Engineering
August 21, 2008

Certified by .....
Mark L. Schattenburg
Senior Research Scientist
Kavli Institute for Astrophysics and Space Research
Thesis Supervisor

Accepted by .....
Lallit Anand
Chairman, Department Committee on Graduate Students

Methods of Improving the Surface Flatness of Thin Glass Sheets and Silicon Wafers

by

Mireille Akilian

Submitted to the Department of Mechanical Engineering
on August 26, 2008, in partial fulfillment of the
requirements for the degree of
Doctor of Philosophy in Mechanical Engineering

Abstract

The manufacturing of high quality sheet glass has allowed for many technologies to advance to astonishing frontiers. With dimensions reaching $\sim 3 \times 3$ m^2, sheet glass is pushing the envelope for producing massive size flat panel displays that can be hung on walls like paintings. Many other applications utilize sheet glass, such as the hard disk drive industry for making platters, the x-ray telescope industry for making high precision optics, and the semiconductor industry for making masks and substrates.

The exceptional optical qualities of sheet glass give them a leading advantage in many technologies; however, one main impediment that remains with manufacturing larger sheets is their surface waviness. The sheets have large warps, on the order of hundreds of microns, that present many challenges in all the industries utilizing such sheets, especially in the liquid crystal display and precision optics industries. The thinner the sheets, the larger their waviness, thus placing a limit on the minimum thickness that can be used in such applications before surface distortions become unacceptable.

A novel method of shaping sheet glass is presented. This method reduces the surface waviness of a glass sheet and changes its shape while it is in its hot state and without contacting its surface. A sheet of glass is inserted between two parallel porous mandrels such that it is at a predefined distance from the two. A thin layer of pressurized gas flows through each mandrel and out against the glass surfaces. The resulting viscous flow against the heated soft glass sheet changes its surface topography. By using flat mandrels and controlled pressurized gas at temperatures close to 600°C, the outcome is a flat sheet of glass with its original immaculate optical qualities.

The flow in porous mandrels and the resulting pressure distribution along the surfaces of a glass sheet inserted between two porous mandrels is modeled. The design and manufacturing of an apparatus used to reduce the surface waviness of glass sheets at elevated temperatures is described. The apparatus designed addresses individual sheets; however, guidelines on how to incorporate this method of shaping glass in a continuous glass sheet manufacturing facility are provided. A method of

rigidly assembling stacks of glass and silicon sheets with precision for x-ray telescope mirrors and gratings is also presented.

Thesis Supervisor: Mark L. Schattenburg
Title: Senior Research Scientist
Kavli Institute for Astrophysics and Space Research

Acknowledgments

I have been extremely fortunate to be surrounded by a group of diverse individuals who supported me throughout my years. The richness of the MIT experience is truly unparalleled.

My advisor, Dr. Mark L. Schattenburg, has provided me with the guidance and freedom I needed to find my way through my research. Mark, thank you for constantly believing. Your motivation and patience kept me going especially during the most difficult times. I owe many thanks to the members of my lab: Dr. Ralf Heilmann, Robert Fleming, Minseung Ahn, Sara Slater and Dr. Yong Zhao, for being more than just colleagues. Thank you for all your support. My office-mate and one of my closest friends, Dr. Chih-Hao Chang, you are truly irreplaceable.

My committee members, Dr. Anette Hosoi and Dr. Martin Culpepper, have been crucial in the progress of my work. Thank you for helping me prepare for potential obstacles in advance and for helping me overcome the ones I encountered during experimentation. I would also like to thank Dr. Shoumen Datta, Prof. Alex Slocum, Dean Steve Lerman and Dean Steve Immerman for their insights and advice on the different aspects of life as a graduate student.

I am very grateful to the administration of the MIT Kavli Institute for Astrophysics and Space Research, particularly Raymond Scuzzarella, Teresa Santiago, Danielle Noonan, Joan Boughan, Jimmy Marolda, Jean Papagianopoulos and Kenton Phillips, for helping me locate my equipment, purchasing it, keeping track of accounts, helping me with computing matters and mostly for being such great friends. I would also like to thank the staff of the MIT Central Machine Shop, particularly Peter Morley, for helping me with my designs, drawings and machining.

Tae Kwon Do has been a part of my graduate education, and I owe it to the MIT Tae Kwon Do Club, especially my coaches, Jephte and Gabe, for teaching me all I know in this art. I would also like to thank all my colleagues in the club for making it such a unique experience. I am very grateful to my friends from the Club Sports Council and the Graduate Student Council for helping me discover different talents

as I pursued my degree. Barbara and Jen, I am very thankful to have had you as my roommates to share my ups and downs with on a daily basis. Paola and Balu', thank you for all the excitement you have added to my life.

On a personal note, I have been blessed to have a very supportive family that shared my successes and failures every step of the way. My parents Edith and Krikor and my sisters Nathalie and Kathia have been my source of inspiration and strength. David, I am forever indebted to your unconditional kindness and support.

Contents

List of Figures

List of Tables

Chapter 1

Glass, Art and Technology

For centuries the mystery surrounding glass has made it a valuable possession. First discovered by the Phoenicians in the region of Syria around 5000 BC, glass has been a jewel that captures light and glows; yet, it is made from the basic elements: sand formed by fire.

Glass was first used as glazes on pots and vases, jewelry, and eventually as glassware until the discovery of glass-blowing sometime between 27 BC and AD 14 by the Syrians, a process which has changed very little since then. The Romans successfully introduced glass into architecture as windows made of both clear and stained glass. Both Venice in Italy and France became competitors in the art of glassmaking, producing some of the finest glass art seen in the Middle Ages.

It was not until the German scientist Otto Schott (1851-1935) that scientific methods were pursued to study the effect of composition on the thermal, mechanical and optical properties of glass. Schott, with the help of Ernst Abbe (1840-1905), started the Carl Zeiss company and pushed for the technological advancement of glass in the field of optics.

1.1 Sheet Glass Manufacturing

One of the first attempts to make sheet glass consisted of pouring molten glass on a table and rolling it out flat, followed by grinding and polishing steps to enhance the

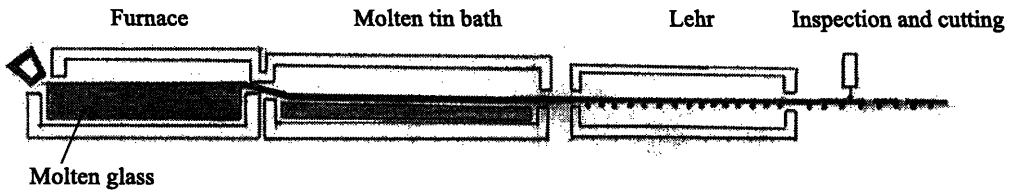

Figure 1-1: In the float process, glass mixed at high temperatures inside a furnace is delivered onto a tin bath, where the glass spreads and cools and is then pulled into a lehr for annealing and further cooling. The glass sheet is then rolled out of the lehr to be inspected and cut [1].

shape of the surface. This time consuming and rather costly process was soon to be replaced by the continuous float process, developed in the late 1950's by Pilkington and fully implemented in the 1970's. Today there are a few other ways of making continuous glass sheets, some of which are explained in this chapter.

1.1.1 The Float Process

Pilkington Bros., Ltd. was the first to develop this process [5], shown in Figure 1-1. A continuous ribbon of molten glass is delivered from a tank held at ~1,100°C onto a bath of molten tin. The ribbon of glass, which has a lower density than tin, floats on the flat layer of tin and obtains an equilibrium thickness of ~6.25 mm. This thickness can be varied by modifying the rate of pulling the glass off the bath to achieve a thickness range of 0.55 - 25 mm [6], [7]. The ribbon cools along the tin bath to have a temperature close to 650°C at the end of the bath. The glass ribbon is then removed from the tin bath and conveyed into a lehr, where it is annealed and cooled to room temperature over a length of 350 ft. The glass is then cut, inspected and packaged. The overall length of the process is 600 ft over a width of ~ 15 ft [1]. The throughput of a float plant is anywhere between 50 and 500 tons of glass sheets per day [8].

Glass produced following this method typically has millimeter-sized warp, despite

the fact that it is referred to as flat glass. These surface irregularities, not necessarily apparent to the naked eye, are the result of air entrapment between the tin bath and the glass sheet, tin residues remaining on the surface in contact with the bath, the errors in the diameters or vertical locations of the rolling wheels pulling the glass in its hot state and poor temperature control of the glass as it cools into a solid state [1].

The presence of tin residue on the glass sheets renders it unsuitable for use in critical optical applications, including flat panel displays [9]. Float glass is typically used in buildings (33%), automotive (30%), mirrors and furniture (16%), commercial construction (15%) and other miscellaneous applications (6%) [1].

1.1.2 The Slot-Draw Process

The slot-draw process is followed by many of the glass manufacturing companies to produce sheet glass. Hot glass is drawn through a slot orifice machined in a platinum bushing [10]. By changing the dimensions of the orifice, the thickness of the glass sheet can be controlled. The glass is allowed to flow vertically downward, as shown in Figure 1-2. The glass cools along its length, and is directed by the use of rollers making contact with the glass after it has solidified. The throughput of the slot-draw process is 1-5 tons per day [8].

Although the glass is solid when rollers make contact, the surface of the sheet is still fragile at high temperatures, and roller stresses can distort the surface. The cooler glass sheet is then cut, inspected and packaged. This glass is used in flat panel display applications. *Schott* produces two main families of flat panel display glass, the D-263 and the AF-45 brands, of which the D-263 is of particular interest in this thesis due to its lower softening temperature.

1.1.3 The Fusion Process

The fusion process developed by Corning utilizes a refractory isopipe or a trough, shown in Figure 1-3, where molten glass is allowed to flow over the outer edges of the isopipe to reunite at its lower tip and flow down with gravity [11]. The advantage

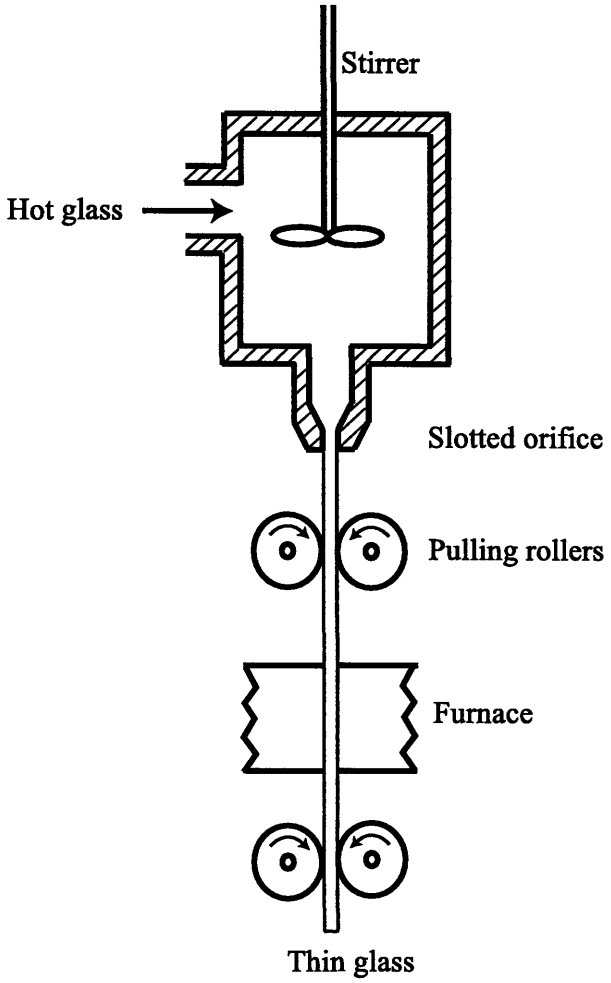

Figure 1-2: In the slot draw process, molten glass is mixed in a furnace and squeezed through a precise orifice to form sheets, which flow with gravity and are eventually rolled down.

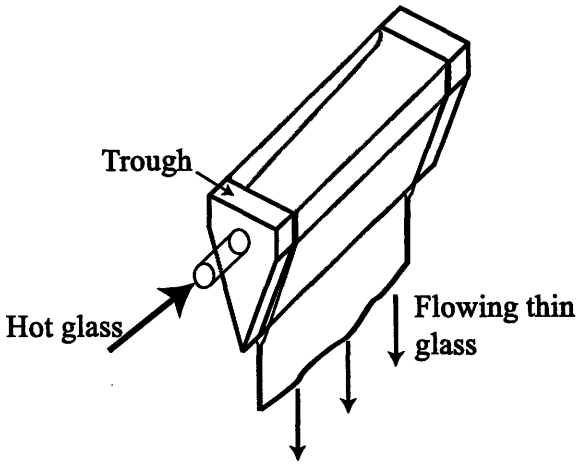

Figure 1-3: In the fusion process, molten glass flows over the edges of an isopipe to reunite at its lower tip and flow down with gravity. Rollers pull the glass down and direct it after it has cooled.

of this process is the fact that the outer surfaces of the glass do not come in contact with the refractory materials while it is being formed, since the glass outer surfaces are exposed to air when flowing over the isopipe and when reuniting to continue flowing downward. The surface that contacts the isopipe fuses and becomes part of the bulk. This results in pristine surfaces. Corning has the Eagle$^{2000^{TM}}$ and Eagle XG substrates manufactured using the fusion process for flat panel displays.

1.2 Sheet Glass Applications

In addition to the applications mentioned above for float glass, high-precision sheet glass is used in various applications, such as filters, touch panels, sensors, masks in the semiconductor industry, hard disk drive platters, cellular phone and computer panels, flat panel displays and precision substrates in optical instruments, such as telescopes.

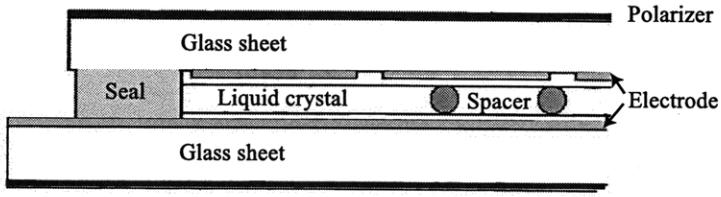

Figure 1-4: An LCD display utilizes two glass sheets separated by a gap of constant thickness. The gap has the electrodes, alignment layers, thickness controlling spacers and the liquid crystal material. The two glass sheets are sealed to keep the material within the gap [2].

1.2.1 Sheet Glass for Flat Panel Display Industry

Perhaps the biggest market for flat glass sheets with precise surfaces is the flat panel display industry. In 2005, about 17.5 million flat panel televisions were sold, generating $25.6 billion in retail revenues. This number is anticipated to grow to 83.5 million units in 2010 with a retail revenue of $45 billion [12]. These numbers do not include other applications in high demand that use flat panels, such as laptops and handheld devices.

Flat panel displays utilize different technologies, most of which require two glass sheets separated by a cavity of uniform thickness. Noble gases for plasma screens or liquid crystal material fills this cavity, as shown in Figure 1-4. Current technology utilizes glass sheets of 0.7 mm thickness [8]. It is desired to decrease this thickness to reduce the overall weight of flat screen displays; however, one of the limiting factors in achieving this goal is the surface warp of sheets as they are currently manufactured. This warp increases with smaller sheet thicknesses.

The liquid crystal display (LCD) industry defines four parameters to determine the quality of glass substrates used in screens [8], [13], [14], [15]. These are:

1. Surface flaws on the order of microns in size, which result in open circuits. The maximum tolerated flaw is <5 μm.

2. Surface roughness over a lengthscale of 3-10 μm, which causes variation in the liquid crystal cell gap. This, in turn, changes the electrical response of the cell

and results in optical irregularities including differences in gray scale. The maximum tolerated roughness is between 5 and 10 nm.

3. Surface waviness, which represents surface errors over a lengthscale of a few millimeters (between 2 and 20 mm). The maximum tolerated waviness is between 0.05 and 0.1 μm.

4. Surface warp, which represents the global surface error. This phenomenon results in misalignment between the deposition layers, since large warps reduce the ability of the stepper lens used during the photolithography process to focus correctly on the substrate. Although at the current stages, a warp of 100-300 μm over the entire surface of a glass substrate is tolerated, having better surface flatness in general would both enhance the performance of the flat panel displays in terms of providing a higher contrast and increase yield, since such substrates are less prone to optical errors during the flat-panel manufacturing process. This, in turn, would reduce the cost of making these panels.

The focus of this thesis is on the third and fourth parameters, the surface waviness and warp of sheet glass. Commercially available sheet glass warp, whether manufactured using the slot-draw process or the fusion process, is on the order of 100 - 600 μm peak-to-valley (P-V). This has been quoted by the manufacturers [8], [16], [17] and measured in the *Space Nanotechnology Laboratory* at MIT.

Stringent requirements also exist on the material composition of the glass substrates; however, this topic is beyond the scope of this thesis, and further information can be found elsewhere [8], [14].

In addition to its importance during the photolithographic steps, surface warp plays a role in the final assembly step. Currently, spacers with controlled thickness are placed along the glass sheets, separating the two sheets and forming a uniform gap. If a glass sheet has a warp much larger or smaller than the nominal thickness of the spacers, this will affect the brightness uniformity of the screen and vary the voltage across the panel, resulting in a shorter panel usable life [18]. The variation in brightness is many times referred to as "mura" in the flat panel industry. Pratt et al. [19] discuss the different types of mura typically seen during the manufacturing

of flat panel screens. Mura is typically detected by visual inspection or automated sensors after the screen has been assembled. Once detected, mura is difficult to correct for. In some elaborate flat panel display units, hundreds of points are measured across the screen to build a 3-D correction matrix and digitally correct each pixel to compensate for differences in color along the screen before it is assembled. Most flat panel display manufacturers inspect glass sheets before manufacturing and only choose the sheets that have the tightest dimensional tolerances, resulting in a low yield and higher flat screen television prices in general. This is particularly important as the size of flat panel displays becomes larger. The yield loss as a result of fatal defects is far greater with the 52-in screens than it is for the 32-in ones, thus driving the cost of the larger displays much higher. Material costs represent a large percentage of the total flat panel display cost as the display sizes increases [20].

1.2.2 Sheet Glass for X-ray Telescopes

X-ray astronomy has revealed an otherwise invisible universe. X-rays emitted from exploding stars and high-temperature gases have high energies of 0.1 - 10 KeV (short wavelengths of 0.1 - 10 nm) and are absorbed in materials, including the atmosphere; thus, x-ray telescopes must be launched into space to capture these images [21].

Typical x-ray telescopes utilize reflective optics rather than refractive ones to avoid x-ray absorption during imaging. Even with reflective optics challenges exist. To obtain total external reflection without loss in efficiency, x-rays must hit the surface of the optics at grazing incidence angles of 1° or less. This represents the critical angle at which total external reflection occurs.

Grazing incidence optics or mirrors require at least two reflecting surfaces to produce an image of an x-ray emitting object [22]. For an object placed at infinity, which is the case of stars and gases in the universe, the first mirrors are parabolic and the second mirrors are hyperbolic. The hyperbolic mirrors reduce the focal length of the telescope, making it easier to package, as shown in Figure 7-7 and cancel aberrations, particularly coma, introduced by the parabolic mirrors. This is known as the Wolter I configuration. Another configuration, designed by Kirkpatrick and Baez and thus

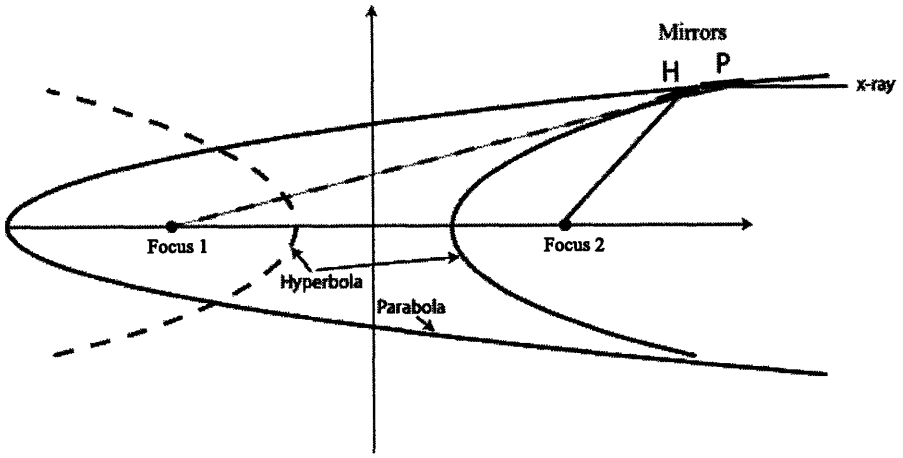

Figure 1-5: Imaging of x-rays using the Wolter configuration. P: parabola, H: hyperbola. X-rays hit the parabola first and are focused at Focus 1. The hyperbola intercepts the reflected rays and focuses them at Focus 2, reducing the focal length of the system.

named after them, uses successive reflection from cylindrical mirrors rotated 90° with respect to each other, as shown in Figure 1-6 [23].

Modern x-ray telescopes follow the Wolter I configuration shown in Figure 1-7. Even though the mirrors are parabolic and hyperbolic, the surfaces of the mirrors have to be extremely smooth in order for the telescope to have a high resolution. The next generation telescope planned for launch in the near future, the *Constellation-X* mission, requires a resolution of 15 arcsec with a goal of 5 arcsec [24]. This demand is reflected on the optics as well, where the surface of the mirrors has to be formed

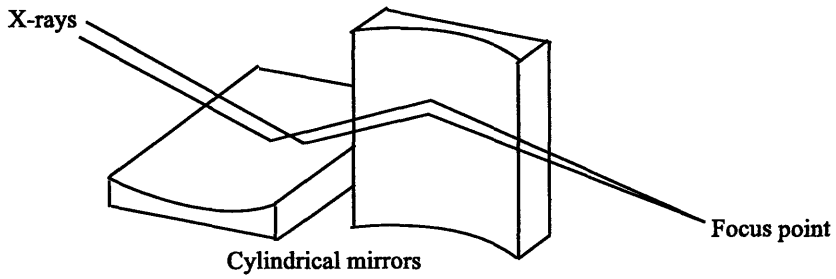

Figure 1-6: Imaging of x-rays using the Kirkpatrick-Baez configuration

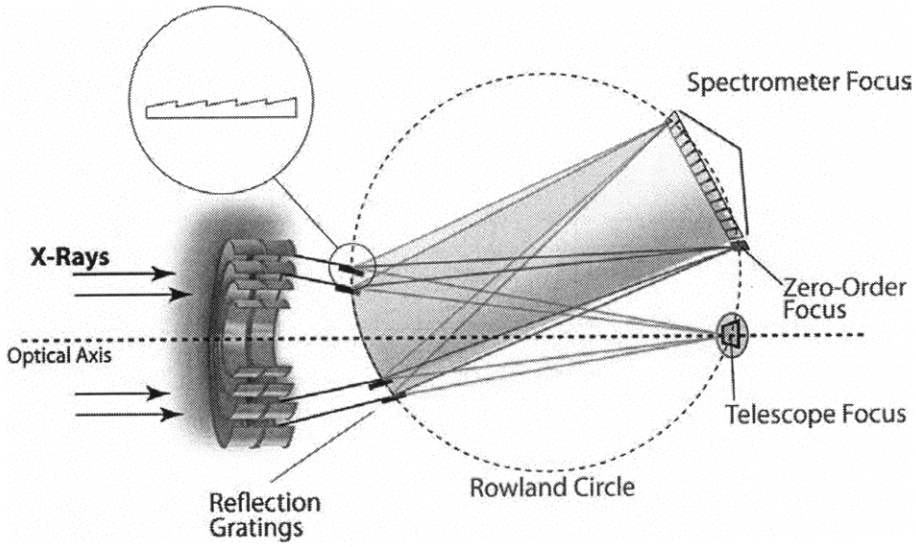

Figure 1-7: Imaging of x-rays using the Wolter I configuration. X-rays hit the surface of the paraboloids (the first set of mirrors on the left) followed by the hyperboloids (the second set of mirrors on the right) to converge to the telescope focus. In some telescopes, gratings are also included in the path of the converging beam. Gratings diffract the incoming light to its different orders. Scientists perform spectroscopy on the diffracted orders to analyze the contents of the beam.

to within 15 arcsec.

Since such a telescope is launched into space, its mass must be kept at a minimum to cut back on costs. *Chandra*, a telescope launched in 1999, utilizes four thick, monolithic mirrors polished to tight tolerances to provide a resolution of 0.5 arcsec; however, due to the limited number of nested mirrors, the collecting area of the telescope is very small, $\sim$ 800 cm^2 at 0.25 keV. To avoid having a similar situation with the *Constellation-X*, a different mirror technology is required [25].

Sheet glass is a strong candidate for the mirrors of *Constellation-X* because of its strength, low density, thermal stability and availability in small thicknesses. If sheets that are 100 mm long are used as mirrors for such a telescope, then the 15 arcsec requirement translates to a surface error of $\sim$ 2 μm P-V for a single bow in the center of the sheet and along its length, as shown in Figure 1-8.

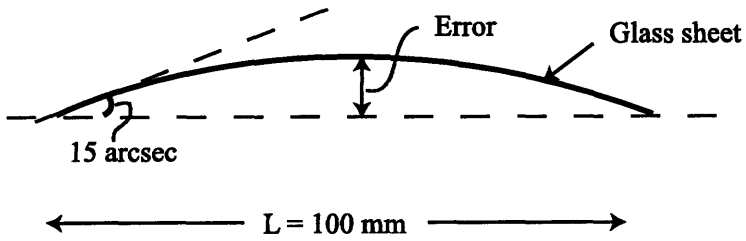

Figure 1-8: Tolerated error on glass sheet surface figure to meet the requirements of *Constellation-X* x-ray telescope

1.3 Proposed Solution for Improving the Surface Figure of Glass Sheets

As glass flows down during the slot-draw and the fusion process, there are no lateral constraints to stop the sheet from warping. Ripples in the glass sheet can result from vibrations in the system that imprint their effect on the soft flowing glass, errors from roller forces at the lower edge of the glass and a temperature gradient across the thickness of the glass. Due to such sources of error, current glass sheets have a warp of 100 - 600 μm P-V.

It is desirable to have glass manufactured with less surface warp (also referred to as better surface flatness) during these processes, without the addition of a secondary step after the glass has cooled. Figure 1-9 shows the surface flatness of a glass sheet as purchased and the surface flatness desired for the applications described above. The use of a hot pressurized gas, such as air, on both sides of a glass sheet to constrain it and improve its flatness is considered in this thesis. The experiments conducted in the thesis are performed on individual glass sheets as opposed to a continuous glass sheet, since these experiments are conducted in relatively smaller facilities; however, the concept can be used on the flowing glass sheets as well with some modifications. Although the main goal of this thesis is to produce flat sheets, future work would involve obtaining sheets with specific curvatures and smooth surfaces by following the same technique. Such glass sheets can then be used as optics in the Wolter-I

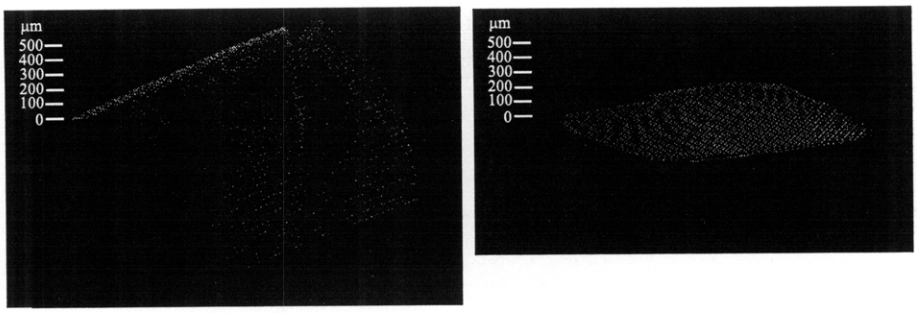

(a) (b)

Figure 1-9: *(a)* Surface flatness of a typical, commercially available glass sheet. *(b)* Desired surface flatness of glass sheet for x-ray astronomy and flat panel screen applications

configuration for x-ray telescopes.

The thesis describes the current methods of improving the surface flatness of glass sheets and silicon wafers in Chapter 2. Chapter 3 covers the theory of blowing pressurized air through different configurations to obtain the most uniform force distribution on the glass sheets and improve their surface flatness. Chapter 4 is dedicated to the experimental procedures involved in obtaining a flat glass sheet. Chapter 5 describes the results obtained. Chapter 6 proposes concepts for future testing with modifications to be able to obtain not only a flat sheet, but also a flat sheet with a desired curvature. Finally, Chapter 7 covers ways of assembling sheet substrates for applications requiring stacks of these substrates, such as the optics of x-ray telescopes.

Chapter 2

Current Glass Flattening Methods

Referred to by manufacturers of glass as flat glass, these sheets are anything but flat. The waviness seen on the sheets varies between tens to hundreds of microns. Since flat glass utilized in buildings and automobiles does not require the same flatness as the flat panel displays and x-ray telescopes, a surface of a few hundred microns peak-to-valley (P-V) is considered flat enough; however, as described in the previous chapter, having glass that is inherently flat to within a few microns would cut back on the production costs and increase yield of the more demanding technologies.

This chapter discusses the various known methods for improving the surface flatness of glass sheets, focusing on the techniques' advantages and disadvantages. The discussion concerns how to make flat glass sheets with and without curvature. The nominal thickness of sheets used in flat panel displays is 0.7 mm [8], and that of sheets used in the next generation x-ray telescope is 0.4 mm [26]. The focus of this thesis is on the thinner of the two, and thus design parameters are determined based on 0.4-0.5 mm-thick sheet requirements.

2.1 Methods for Obtaining Flat Glass without Curvature

Perhaps the first concept that comes to mind when thinking of flat surfaces involves grinding, lapping and polishing. These processes have been thoroughly studied and understood and have provided some of the flattest surfaces ever achieved - on thick substrates. The combination of the normal forces and the shear forces applied on the workpiece result in material removal at the surface to improve its flatness.

2.1.1 Double-Sided Polishing

Double-sided polishing is commonly performed on circular silicon wafers to reduce their thickness variation. In this process, a silicon wafer is squeezed between two rotating polishing pads while the polishing particles remove material from the surfaces. Since the wafer is squeezed, it is forced into a flat configuration during polishing; however, once the normal forces are removed, the wafer springs back to its original shape. The result is an improvement in the wafer's thickness variation, but not its surface flatness. Figure 2-1 shows the difference between what is known as thickness variation and surface flatness (also commonly referred to as warp or bow).

This process can be utilized if the starting wafer is thick and is polished down to the required thickness of 0.4 mm. It is a rather easy process but time consuming and expensive when large quantities are desired.

2.1.2 Slumping on a Flat Mandrel

One of the attrative characteristics of glass is its strength at room temperature; yet, its shape can be varied at higher temperatures due to the rapid change of its viscosity with temperature. Artisans have used this characteristic of glass for many years to make jewelry, art and glassware. This property of glass can help change its shape and improve its flatness if needed.

Slumping glass refers to raising its temperature to a point where its viscosity is

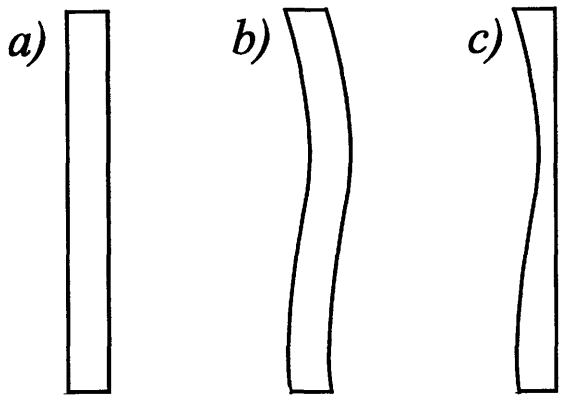

Figure 2-1: *(a)* Glass sheet with flat surfaces and a uniform thickness. *(b)* Glass sheet with uniform thickness but with non-flat surfaces. *(c)* Glass sheet with one flat surface (right surface) but not uniform in thickness.

low enough to allow it to sag under its own weight. This point is typically between the transformation temperature of glass, where glass transforms from its solid to plastic state at a viscosity of 10^{13} poise, and the softening temperature of glass, where it completely sags under its own weight at a viscosity of $10^{7.65}$ poise [27]. Typical temperature ranges are 450-660°C for transformation temperatures and 620-880°C for softening temperatures of glass sheets used in the flat panel industry. Quartz and fused silica have much higher temperatures and are thus avoided due to the high cost associated with them [28].

Several methods of shaping glass rely on slumping. By placing a glass sheet on a thick mandrel that has been accurately lapped and polished to the flatness needed, the glass would ideally replicate the shape of the mandrel surface and obtain its flatness. This method is pursued by various groups to obtain optics for high-resolution x-ray telescopes [26].

A few challenges exist when slumping directly on a mandrel. Particulates such as dust and furnace-insulation particles present between the mandrel and the glass sheet introduce mid-to-high spatial frequency errors on the surface of the sheet. This is shown in Figure 7-15*(a)*. Such particles are very difficult to completely eliminate

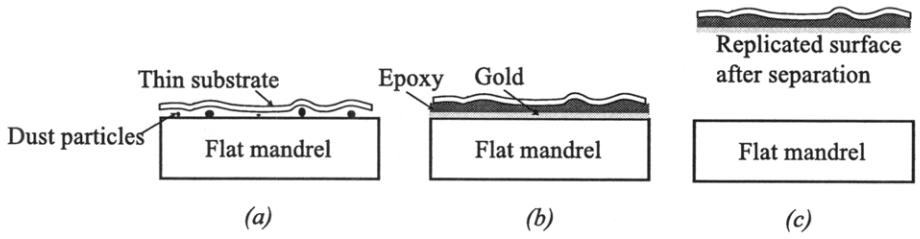

Figure 2-2: Slumping of thin glass sheets on a mandrel with the presence of particulates between the two, followed by an epoxy replication process to fill in the dimples

from between the two surfaces, even in a cleanroom environment. The resulting mid-high spatial frequency errors are also difficult to correct in a subsequent step because it takes much longer periods of slumping time to remove such small dimples.

Particles serve as a barrier between the glass sheet and the mandrel. Since slumping temperatures are typically high, and the process of slumping relies on glass softening, it is very likely that the glass surface would fuse to the mandrel in the absence of a barrier between the two. If the mandrel is made of a thermally different material from the glass sheet, the sheet can crack during cooling as a result of the difference in the coefficient of thermal expansion (CTE) of the two materials, thus damaging both surfaces.

Several attempts have been made to work around the presence of particulates between the mandrel and the glass sheet during slumping. Some [29] utilize a secondary step of shaping to compensate for the presence of particle-induced high-spatial frequency errors. This step involves placing a thin layer of epoxy between the slumped glass sheet and a gold-coated mandrel, as shown in Figure 7-15*(b)*. The epoxy fills the dimples introduced by the particles. The gold layer adheres to the epoxy better than to the mandrel. The glass sheet with the epoxy and gold is then pulled off the mandrel, and the final tri-layer of gold, epoxy and glass has a flat, gold-coated surface, as shown in Figure 7-15*(c)*.

There are various reasons why using epoxy over large areas is not desired. Epoxy shrinks as it cures, applying stresses on the glass sheet and changing its shape with time. Epoxy has a different CTE from glass, resulting in a bi-layer effect whenever

there is a small change in temperature. Finally there is a risk of outgassing after the epoxy has been applied on the glass sheet, protruding bubbles in the gold layer [30]. Epoxy degassing methods can be pursued to minimize this effect. This method does not work for the flat panel display industry due to the presence of gold and epoxy layers on the glass sheet. The glass sheets must be transparent and coating-free during the photolithography process and after screen assembly to allow for light to go through and illuminate the pixels.

Another way of preventing high-spatial frequency errors caused by particles involves cleaning both the mandrel and the glass sheet to eliminate all particles. An anti-stick coating is applied on the mandrel to avoid the glass from fusing to it at the slumping temperatures. In this case, the thickness of the coating is to be well controlled to avoid introducing errors on the glass as a result of coating thickness variation, which is not a trivial task.

2.1.3 Epoxy Replication

The setup described above can be performed at room temperature by eliminating the slumping step [30]. A polished mandrel is coated with gold, and a thin layer of epoxy is applied on the mandrel. The thin, warped glass is then forced against the epoxy. The epoxy fills the gaps caused by the glass sheet's warp and is cured. Afterwards, the sheet with epoxy and gold is pulled off the mandrel, as shown in Figure 2-3. The same challenges associated with epoxy apply to this case, as was described in the section above. This process does not apply to the flat panel industry as well for the reasons mentioned in Section 2.1.2.

2.1.4 Slumping on Discrete Points

To minimize the effects of particulates on the final shape of the glass, slumping on discrete points or pins with minimal cross-sectional areas is considered. This reduces the contact area between the glass and the pins, and thus reduces the probability of a particle becoming trapped between the two.

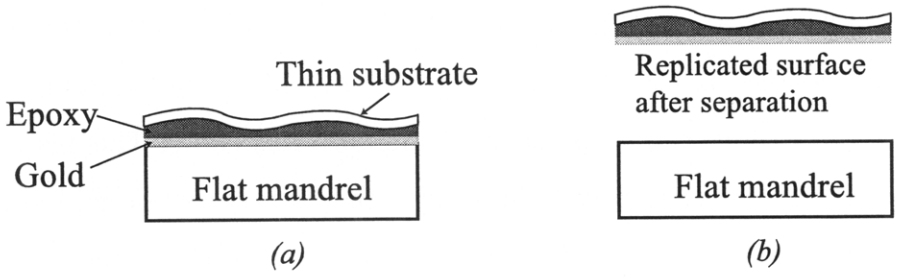

Figure 2-3: Improving the flatness of a sheet by utilizing a layer of epoxy and gold to replicate the shape of a flat mandrel

The first parameter to consider is the distance tolerated between individual pins before the heated glass exceeds the required flatness as it sags. If two pins are placed further apart than this critical distance, the hot glass would sag by more than what is tolerated, deforming the overal final shape. *COMSOL*, a finite element analysis tool, is used to model the elastic behavior of a sheet of glass by constraining discrete points on its surface and analyzing the final shape of the glass as it sags due to its weight. The distance between each two points is varied to study the effect of this distance on the shape of the glass. The glass sheet is a visco-elastic material at the slumping temperature (close to 600°C), which requires a more complicated model than the one presented. Elastic deformations represent the instantaneous response of the glass sheet to the changes in its environment. Once the glass sheet assumes its new shape due to its weight at a lower Young's modulus, it starts to creep with time. When the temperature is lowered again, the glass regains its elastic deformation; however, the visco-elastic deformation resulting from creep remains. The relaxation time for glass, which is a measure of the time it takes for viscous behavior to play a significant role in the overall deformation, can be calculated using the Young's modulus and viscosity of glass at the slumping temperature. The experiments conducted are at a temperature close to the transformation temperature of glass, at which point the viscosity is 10^{13} poise. The Young's modulus at this temperature is ~40 GPa, as described later in Section 4.3.2. By dividing the viscosity by the modulus, the relaxation time for glass is found to be $\sim$ 4 minutes. This is rather short indicating that the glass is mainly

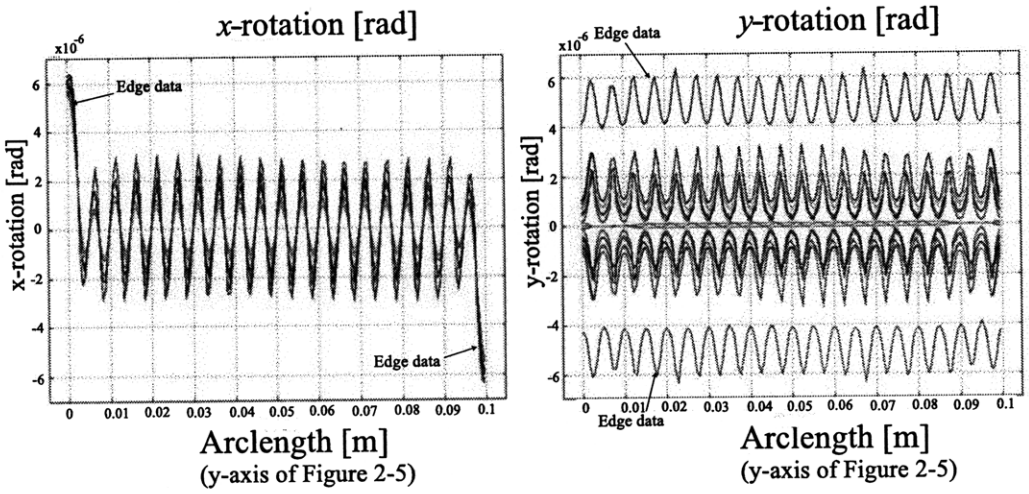

Figure 2-4: Angular errors seen on a sheet of glass slumped on an array of pins separated by 5 mm. Glass modeled is Schott D-263 with 0.4 mm thickness and at 600°C. The data shown is the instantaneous elastic response of the glass.

visco-elastic at the slumping temperatures.

If the requirement of 0.5 arcsec (2.4 μrad) angular error is the goal, then the pins can be separated by as far as 5 mm along the length and width of a 100 mm $\times$ 100 mm sheet of glass before the elastic deformation exceeds the required tolerance. The resulting angular errors around x and y are plotted and shown in Figure 2-4*(a)* and *(b)*, respectively. The different curves shown in these figures correspond to the various lines along which the data is taken, as shown in Figure 2-5. As can be seen from Figure 2-4, the angular errors along the glass sheet, except for at the edges, is equal to or smaller than the 2.4 μrad requirement when the pins are separated by 5 mm.

The next step is the design of such a mandrel that has the required 400 pins, separated by 5 mm and all having an equal height. One way is to have a flat mandrel with high precision ruby balls disbursed along the surface of the mandrel. This might work for flat surfaces but not for conical surfaces, since the ruby balls would roll off the surface. A method of slumping over pin chucks was developed at the *Space Nanotechnology Laboratory* at MIT, where an array of 25 $\times$ 25 $\times$ 2.5 μm^3 fused silica pins separated by a distance of 0.25 mm have been fabricated on a fused silica

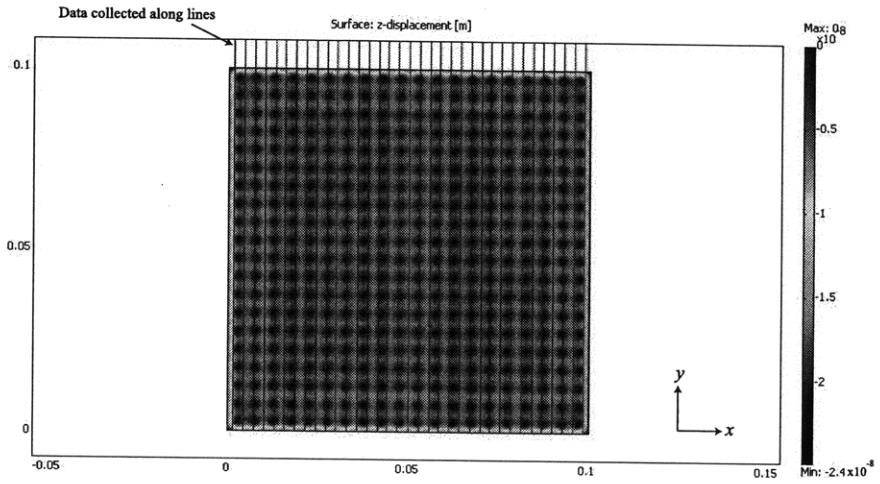

Figure 2-5: Lines drawn to extract data across a 100 mm × 100 mm glass sheet with pins separated by 5 mm (dark regions)

mandrel, as shown in Figure 2-6. The pins are small in dimension to reduce the probability of particles squeezing between the mandrel and the glass, and the gaps between the pins are deep enough for particles to settle in without protruding into the glass sheet. The pins are coated with a thin layer of titanium oxide (TiO_2) to avoid the sheet from sticking to the pins during slumping [31].

The process proves to be successful over small areas; however, at larger areas, glass would stick to the pins and peel them off as it is removed from the mandrel. Also,

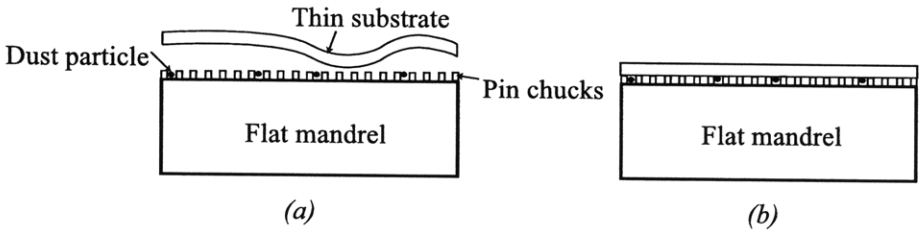

Figure 2-6: Slumping of glass on an array of pins to minimize contact and particle entrapment between glass and mandrel

some particles are found to remain between the glass sheet and the pins. This shows that any contact with the glass sheet at high temperatures, even over small areas, can result in damaging the sheet due to the high possibility of fusion, and particles can still adhere to either of the surfaces and result in dimples in the glass [31].

2.1.5 Shaping using the Magneto-Rheological Finishing Process

Magneto-rheological finishing is a deterministic process developed by *QED Technologies*, typically used to precisely polish complex optical surfaces. The process uses a circulating magneto-rheological fluid, which has a low viscosity until it goes through a magnetic field when in contact with the workpiece, at which point the viscosity of the fluid increases, and the fluid can shear material off from the workpiece. This is shown in Figure 2-7.

The process requires an initial surface map of the workpiece, which is fed into the tool controller. The tool recognizes the peaks on the surface and polishes those peaks away until the required shape is achieved. The resulting surface is frequently measured during the process for iterative polishing. This technique is accurate for thick optics; however, thin optics are not typically polished using this process for one main reason: measuring the surface of thin optics repeatably without optic surface distortion is challenging.

A constraint tool utilizing monolithic flexures developed at the *Space Nanotechnology Laboratory* at MIT holds thin optics without distorting their surface and with a repeatability of 55 nm P-V [4]. This tool was disassembled and taken to *QED's* facilities in Rochester, NY, where it was utilized to measure the surface of thin silicon wafers before, during and after polishing them. Since the tool provides a means to repeatably measure the surface of the wafer, the polishing process could proceed.

Two 100 mm diameter, 0.5 mm thick wafers were polished. The starting surface of the silicon wafers were 3.14 μm P-V for Wafer A and 2.81 μm P-V for Wafer B. It took approximately 4 hours per wafer to repeat the steps of measuring and polishing until the final shapes shown in Figure 2-8 were obtained. The surface of Wafer A has a flatness of 0.18 μm P-V over an aperture of 81 mm, and Wafer B has a surface

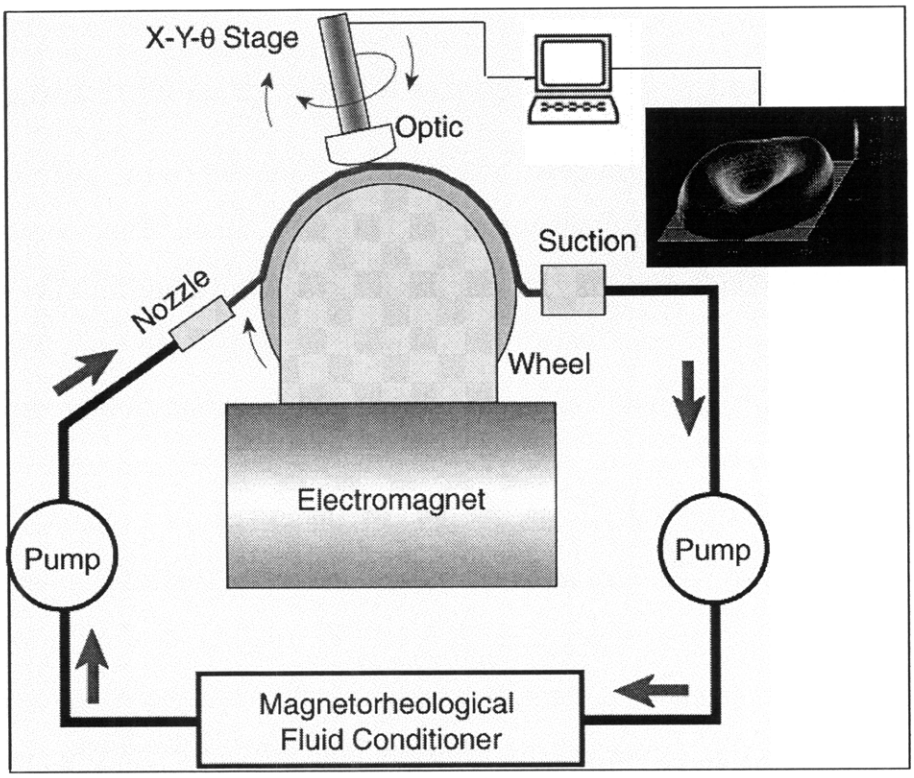

Figure 2-7: Magneto-rheological fluid flows from a nozzle onto a rotating drum. An electromagnet provides a magnetic field across the drum, such that the viscosity of the rotating fluid increases and obtains shearing characteristics. The optic is introduced on a stage with three degrees of motion to control its position as necessary. The original map of the optic is fed into the controller, which moves the optic with respect to the shearing fluid. As the fluid removes material from the optic and leaves the electromagnetic field, its viscosity drops again and the fluid is recirculated in the system.

flatness of 0.07 μm P-V over an aperture of 75 mm. Figure 2-9 shows the before and after 3-D images of the surface of Wafer B. The edges of the wafers were not polished at this time because they have a steep slope that would require additional hours of polishing [32].

This process can produce accurate results; however, the disadvantages include high cost and low rate. The polishing tool itself is quite expensive, and the material removal rate is extremely slow. It is not feasible to use this process on the glass sheets with their original warp of hundreds of microns; however, it can be used as a final step to reduce peaks on the order of a couple of microns as necessary. It should be noted that removing surface material can change the stress distribution across the thickness of a sheet of glass. This can result in an unanticipated warp during the polishing process. Annealing the glass sheets before following this finishing technique would reduce surface stresses and thus the resulting warpage seen when the surfaces are removed. When working with the silicon wafers, a quick run on both surfaces of each wafer was initially performed to remove the stressed surface layer, and accurate polishing is done afterwards.

2.2 Methods for Obtaining Flat Glass with Curvature

If curvature of a flat sheet of glass is needed, it can be obtained by either shaping the glass sheet to the desired curvature, using Magneto-rheological finishing or by forcing the sheet to a specific curvature. The latter is explained in more detail in Chapter 7.

2.2.1 Slumping on a Conical Mandrel

The process described in Section 2.1.2 can be followed to obtain curved sheets. The mandrel in this case is polished to the desired conical shape, and a flat glass sheet is placed on the mandrel and heated. The edges of the glass sheet sag until they make contact with the mandrel. This procedure is currently being followed to make the

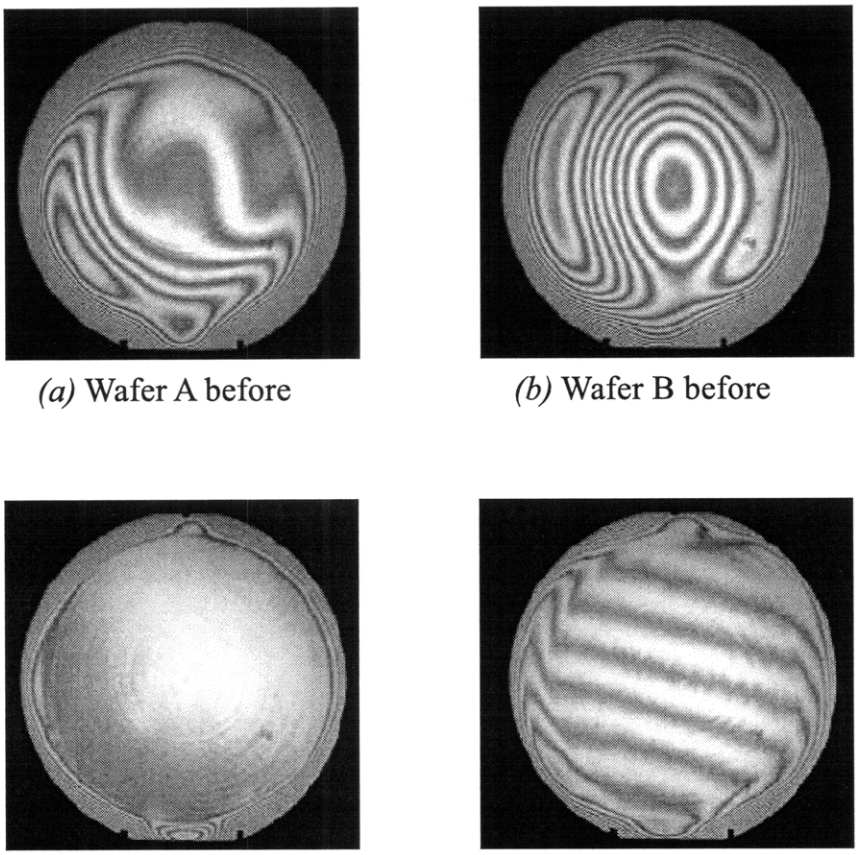

(a) Wafer A before

(b) Wafer B before

(c) Wafer A after

(d) Wafer B after

Figure 2-8: Results obtained from polishing two silicon wafers using the magneto-rheological finishing process. Wafer A has a before surface of 3.18 μm P-V and a final surface of 0.18 P-V over an aperture of 81 mm. Wafer B has a before surface of 2.81 μm P-V and a final surface of 0.07 μm P-V over an aperture of 75 mm.

Wafer B before
P-V: 2.81 μm
RMS: 0.540 μm

Wafer B after
P-V: 0.07 μm
RMS: 0.010 μm

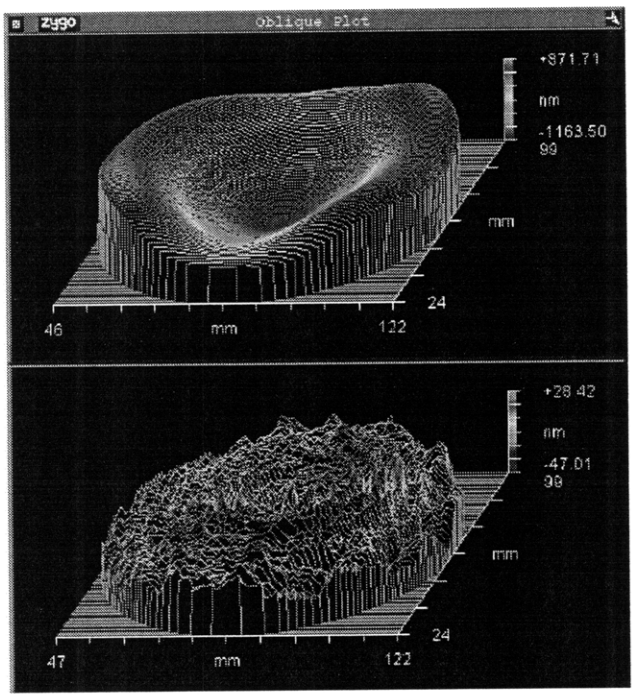

Figure 2-9: Surface of wafer B before and after magneto-rheological finishing

Constellation-X telescope parabolic and hyperbolic mirror substrates [26], [29].

The challenges described in Section 2.1.2 apply in this case as well. The mandrel in this case is typically more expensive than a simpler flat mandrel with no curvature.

2.2.2 Thermal Forming on Cylindrical Mandrels without Contact

A process developed at Columbia University utilizes a semi-cylindrical quartz shell mandrel, where the inner surface of the mandrel is smooth. A thin sheet of glass with a length equal to the diameter of the mandrel is placed on top of the mandrel, as shown in Figure 2-10. The temperature of the set-up is raised for the glass to sag due to its own weight; however, the time of the experiment is controlled such that the glass never makes contact with the actual surface of the mandrel. This eliminates all the problems associated with contact, such as the presence of particles and fusion with the mandrel. The only guidance for the glass sheet during slumping in this case are its edges making contact with the mandrel [30].

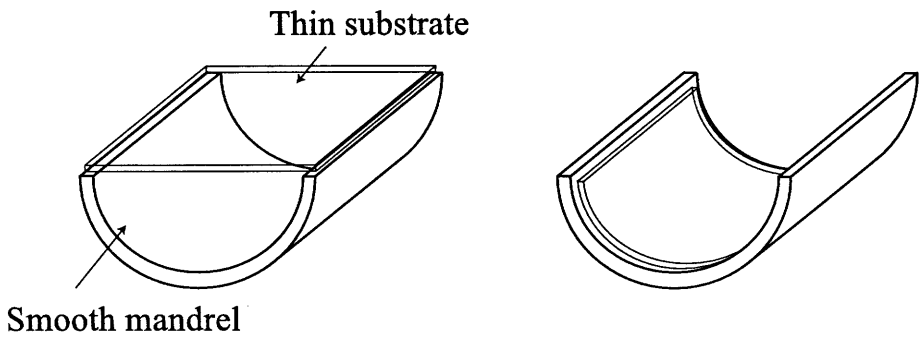

Figure 2-10: A thin glass sheet slumped on a semi-cylindrical shell, replicating the surface of the shell without making contact with it

This process seems to rely heavily on the quality of the glass edges and the mandrel inner surface, the temperature uniformity of the sheet and the time of the experiment. Different sheets with different initial surface flatnesses require different slumping times to ensure that the sheet follows the curvature of the mandrel without making contact with it. This makes it difficult to produce time-temperature profiles that are independent of initial glass warpage, and that can be followed to repeatably slump glass sheets using this method.

Table 2.1 summarizes the strengths and weaknesses of the different approaches discussed above.

2.3 Proposed Method of Shaping

Having seen the pros and cons of different methods of shaping, it is desired to find a way of improving the flatness of glass sheet from its current state of hundreds of microns P-V to a flatness of a few microns P-V, without introducing high-spatial frequency errors associated with particles, and certainly without damaging the surface of the glass sheet due to fusion with mandrels.

A contact-free method is proposed to achieve these goals. This method utilizes a thin layer of air separating the glass sheet from the mandrel during slumping to

Process	Slumping on flat mandrel	Epoxy Replication	Slumping on discrete points	MRF	No-Contact Conical Mandrel
Accuracy	-	+	0	+	-
Repeatability	-	?	-	+	-
No particulate induced dimples	-	+	+	+	+
No fusion with mandrel	-	+	-	+	-
Glass sheet thermal stability	+	-	+	+	+
Cost	+	-	0	-	+
Process rate	+	-	+	-	+

Table 2.1: Advantages and disadvantages of processes currently pursued to shape glass sheets

avoid all the difficulties associated with contact during slumping. Different ways of pursuing such a method are explained in the next chapter.

It should be noted that most experiments run in the laboratory are performed on a sheet-by-sheet basis. In other words, experimental procedures work on one sheet at a time; however, an ideal situation involves establishing a way of improving the surface flatness of sheet glass in its hot state as it is being manufactured in the form of long sheets. This would not only improve the surface quality for the many applications demanding higher quality, but it would cut back on the time and eventually cost of having to improve the flatness of these sheets in a secondary step after they have been formed, cooled, cut and shipped. This is further addressed in Chapter 6.

Chapter 3

Glass Shaping Theory

The previous chapter covered some of the different ways of improving the surface flatness of glass sheets, showing the disadvantages of using methods that result in contact between the heated glass sheets and any other surface. In fact, most flat panel display manufacturers prefer to use glass sheets that have not come in contact with any other surface while the sheets are in the hot phases of manufacturing, since this results in better surface qualities.

By using a thin layer of air to improve the surface flatness of glass sheets, contact is eliminated. Typically used in air bearing applications, viscous forces from pressurized air going through a highly resistive compensation can carry tremendous amounts of load.

Air bearings come in different configurations. The most prominent ones are the porous bearings and the grooved bearings, both known to have a superior pressure distribution in the air gap, thus resulting in more stability and higher stiffness and load carrying capabilities [33]. Air bearings are advantageous because they offer almost zero friction during motion at room temperature, and there are no requirements for recirculating or properly discarding the lubricating fluid after usage. One difficulty with air bearings is the requirement of very small air gaps, ranging between 5 and 10 μm between the bearing and the load. As the gap becomes bigger at room temperatures, the viscous force of air decreases resulting in a loss in stiffness and load capacity.

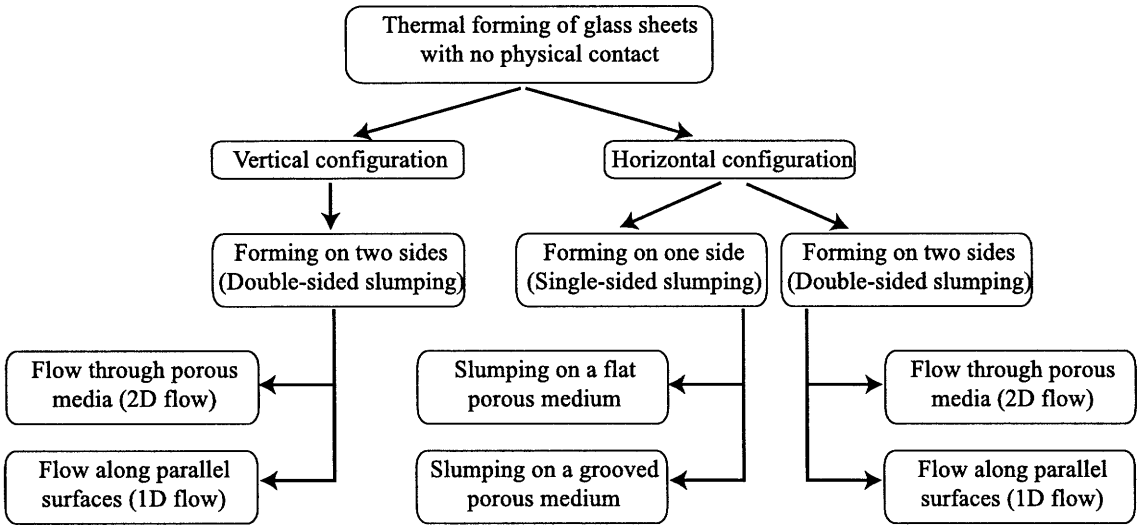

Figure 3-1: Concepts developed for the thermal shaping of thin glass sheets without contacting their surfaces

3.1 Concepts

Figure 3-1 shows the different concepts that have been considered and analyzed for the thermal forming of sheet glass with no physical contact with the critical surface of the sheet. A thorough flow analysis, in addition to a discussion of advantages and disadvantages, is presented in this chapter, starting with the horizontal configurations.

3.2 Material Property Variations

Since all the concepts presented in Figure 3-1 utilize air and are performed at high temperatures close to 600°C, the properties of air and the materials used are studied first.

3.2.1 Air at High Temperatures

All gases are in good agreement with the perfect gas law at high temperatures and low pressures [34]. A perfect gas is one that meets the following requirements:

1. molecules occupy zero volume,

2. molecules are in constant random motion,

3. there are no intermolecular forces between particles,

4. atoms or molecules undergo perfectly elastic collisions.

Gases obeying the perfect gas law are characterized by

$$P = \rho RT, \tag{3.1}$$

where P is the given pressure in Pa, ρ is the gas density, R is the universal constant equal to 284 J/kg.K, and T is the absolute temperature. When the temperature increases from room temperature to 600°C at atmospheric pressure, the density of air varies from 1.2 Kg/m^3 to 0.4 Kg/m^3 from Equation 3.1.

Most solids and liquids undergo a decrease in viscosity as their temperature is raised. Gases on the other hand undergo an increase in viscosity as their temperature is raised. The Sutherland equation given by Equation 3.2 describes the variation in the viscosity of an ideal gas with temperature.

$$\frac{\mu}{\mu_o} = \left(\frac{T}{T_o}\right)^{\frac{1}{2}} \frac{1 + \frac{S}{T_o}}{1 + \frac{S}{T}}, \tag{3.2}$$

where μ is the viscosity at absolute temperature T, μ_o is the viscosity at room temperature T_o and equals 1.83×10^{-5} Pa.s for air, and the ratio $\frac{S}{T_o}$ is empirically taken as 0.505 for air [35]. The viscosity of air thus changes from 18.3 μPa.s at room temperature to 40.65 μPa.s at a temperature of 600°C.

Table 3.1 summarizes the properties of air at both room temperature and at 600°C. The Sutherland equation's error due to pressure is <10% up to 3.45 MPa. It should be noted that the pressure variation in the particular application pursued in this thesis is <1 psi (6,895 Pa), which corresponds to a density change of <7% at room temperature from Equation 3.1. This change is negligible when compared to the effect of temperature on density and thus is ignored [34].

	20°C	600°C	% change
Density (kg/m^3)	1.2	0.4	-66.4
Viscosity (μPa.s)	18.3	40.65	122

Table 3.1: Properties of air at room and slumping temperatures

3.2.2 Material Properties at High Temperatures

As the temperature of most materials is increased, their overall strength and Young's modulus decrease. Ashby and Frost have dedicated a book on the effect of temperature on some commonly used ceramics and metals [36]. The book defines a coefficient $\frac{T_M}{G_o}\frac{dG}{dT}$ relating the shear modulus of materials to temperature through the equation

$$G = G_o\left[1 + \frac{T - 300}{T_M}\left(\frac{T_M dG}{G_o dT}\right)\right], \tag{3.3}$$

where G is the shear modulus at the temperature of interest, G_o is the shear modulus at 300K, T is the absolute temperature of interest and T_M is the melting temperature of the material.

For isotropic materials, the shear modulus G is related to the Young's modulus E by the relationship

$$G = \frac{E}{2(1+\nu)}, \tag{3.4}$$

where ν is the Poisson's ratio of the material. Table 3.2 summarizes the value of the coefficient $\frac{T_M}{G_o}\frac{dG}{dT}$ for various materials of interest in this thesis, the resulting shear modulus at 600°C, the material Poisson's ratio and the corresponding Young's modulus. All these properties assume zero porosity in the material.

3.2.3 Material Properties with Porosity Variation

Introducing pores into a material weakens its properties in general. This is true for the thermal, mechanical and electrical properties. Most ceramics have a small percentage of porosity, anywhere between 1% and 20%, though advanced ceramics

Material	$\frac{T_M}{G_o}\frac{dG}{dT}$	Shear modulus G (GPa)	Poisson's ratio ν	Young's modulus E (GPa)
Alumina	-0.35	136	0.22	330
Silicon Carbide	-0.18	165	0.19	390
Stainless steel	-0.85	64	0.28	168

Table 3.2: Coefficient of shear modulus variation with temperature, shear modulus, Poisson's ratio and Young's modulus for different materials with zero porosity at 600°C

can be manufactured with $< 1\%$ porosity.

There are many models developed to predict the relationship between porosity and Young's modulus. Some provide a basic linear relationship such as

$$E_{eff} = E_1(1 - P_r) + E_2 P_r, \tag{3.5}$$

where E_{eff} is the effective modulus resulting from a composition of two materials having E_1 and E_2 as modulii and P_r as porosity. E_2 is zero when the second material is air.

Other models are more involved and take into consideration factors such as pore size, shape, orientation, disbribution, degree of contiguity, homogeneity and other parameters when developing a relationship between the modulus and porosity. Some of these models are discussed here without detailed derivation, which can be found in the referenced articles.

Weng [37] has proposed a solution to the relationship between the bulk, shear and elastic modulii of a material and porosity in an isotropic medium that has identical spheroidal voids at finite concentrations. In the following resulting equations, K, G and E are the bulk, shear and Young's or elastic modulii of a pore free material, and K_e, G_e and E_e are the corresponding modulii in the presence of voids or pores [38]. Porosity is denoted by P_r and Poisson's ratio by ν.

$$\frac{K_e}{K} = \frac{1 - P_r}{1 + \frac{qP_r}{1-q}}, \tag{3.6}$$

where

$$q = \frac{1 + \nu}{3 - 4\nu}, \tag{3.7}$$

$$\frac{G_e}{G} = 1 - \frac{P_r}{1 - (1 - P_r)q_0}, \tag{3.8}$$

where

$$q_0 = \frac{2}{5}\frac{4 - 5\nu}{2 - \nu}, \tag{3.9}$$

$$\frac{E_e}{E} = \frac{1}{E}\frac{9K_eG_e}{3K_e + G_e}. \tag{3.10}$$

Ju and Chen [39] have come up with a different model to describe the relationship between material modulii and porosity in composites with isotropically distributed identical spherical pores as well, though their results are more complicated than those proposed by Weng.

Fan [40], [41] used both geometrical and topological parameters to come up with a model for a two-phase structure composed of α and β particles with total volume fractions of f_α and $f_\beta = 1 - f_\alpha$, respectively, and any grain size, grain shape and phase distribution, as shown in Figure 3-2.

Fan in his work proves that Figure 3-2 is mechanically equivalent to 3-3 along the aligned direction of the microstructure. This new structure consists of a continuous α-phase with a volume fraction of $f_{\alpha c}$, a continuous β-phase with a volume fraction of $f_{\beta c}$, and a long-range of $\alpha - \beta$ chains with a volume fraction F_s. These are regions EI, EII, and EIII, respectively, where the last region contains only phase boundaries.

The volume fractions of the α- and β- phases ($f_{\alpha III}$ and $f_{\beta III}$, respectively) in region EIII can be calculated by

$$f_{\alpha III} = \frac{f_\alpha - f_{\alpha c}}{F_s} \tag{3.11}$$

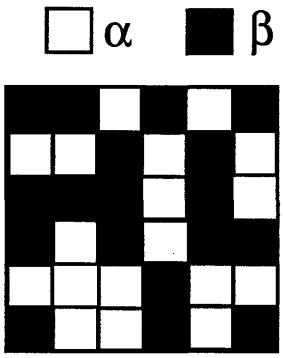

Figure 3-2: A schematic representation of a microstructure composed of randomly distributed α and β phase particles

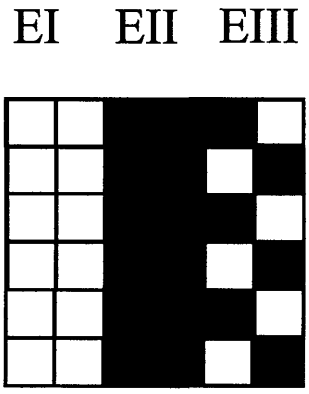

Figure 3-3: Topological transformation of microsturcture shown before to an equivalent model

$$f_{\beta III} = 1 - f_{\alpha III}. \tag{3.12}$$

The microstructure in Figure 3-3 is easier to analyze, yet since it is equivalent to the original microstructure in Figure 3-2, the relationship between Young's modulus and porosity can be determined. Fan uses probability and statistics to derive the topological parameters, which must usually be measured experimentally; however, if random distribution of equiaxed particles is assumed, the following relationships hold

$$f_{\alpha c} = \frac{f_\alpha^2 d_\beta}{f_\beta d_\alpha + f_\alpha d_\beta} = \frac{f_\alpha^2 R}{f_\beta + f_\alpha R}, \tag{3.13}$$

$$f_{\beta c} = \frac{f_\beta^2 d_\alpha}{f_\beta d_\alpha + f_\alpha d_\beta} = \frac{f_\beta^2 R}{f_\beta + f_\alpha R}, \tag{3.14}$$

$$F_s = 1 - f_{\alpha c} - f_{\beta c}, \tag{3.15}$$

where d_α and d_β are the grain sizes of the α- and β-phases, respectively, and R is the ratio of these grain sizes such that $R = \frac{d_\beta}{d_\alpha}$. Boccaccini and Fan show that $R = 1$ overestimates the Young's modulus at low porosity ($P_r \leq 0.25$). However, for intermediate porosity levels ($0.25 \leq P_r \leq 0.5$), $R = 1$ better predicts experimental data than when lower values of R are used. For lower values of porosity, $0.4 \leq R \leq 0.6$ shows a better correlation with experimental results. For accuracy, R should be determined using metallographic measurements, since there is no clear relationship between R and porosity.

The porosity of the material can be calculated if its density is known. The density of the pore-free ceramic ρ_o can be found in literature. The density of the porous ceramic ρ is measured using the Archimedes method. Porosity is defined as

$$P_r = f_\beta = 1 - \frac{\rho}{\rho_o}, \tag{3.16}$$

where f_β is the volume fraction of the β-phase.

Fan and co-workers derived the equation for the effective Young's modulus E_e to be

$$E_e = E_\alpha f_{\alpha c} + E_\beta f_{\beta c} + \frac{E_\alpha E_\beta F_s}{E_\beta f_{\alpha III} + E_\alpha f_{\beta III}}, \tag{3.17}$$

where E_α and E_β are the Young's modulii of the pure $\alpha-$ and $\beta-$phases, respectively. In the case of a porous ceramic, E_β of air is 0, and Equation 3.17 reduces to

$$E_e = E_\alpha f_{\alpha c}. \tag{3.18}$$

It should be noted that Weng [37] takes the Poisson's ratio into consideration, but his model relies on spherical shapes only. The Fan method on the other hand does not take the Poisson's ratio into consideration, yet the model covers any void shape with a degree of contiguity, which describes a degree of particle contact of one phase in a two-phase medium. Figure 3-4 shows the effect of Poisson's ratio on the relationship between Young's modulus and porosity based on Weng's model. It can be seen that for three different materials, silicon carbide, alumina and stainless steel with Poisson's ratio of 0.19, 0.22 and 0.28, respectively, the Young's modulus is slightly affected by the Poisson's ratio at any given porosity. Figure 3-5 shows the difference in the results obtained using both Weng's and Fan's approaches. It can be seen that the two models agree at a porosity of ~45%. Weng's model results in lower Young's modulus at $P_r < 45\%$, whereas Fan's model results in lower Young's modulus at $P_r > 45\%$.

Thus the effective Young's modulus for a 40% porous silicon carbide plate for example at an elevated temperature of 600°C is approximately 0.333×390=130 GPa.

3.3 Concept Analysis

Now that the behavior of air and some common materials at elevated temperatures is better understood, the different concepts described before can be analyzed.

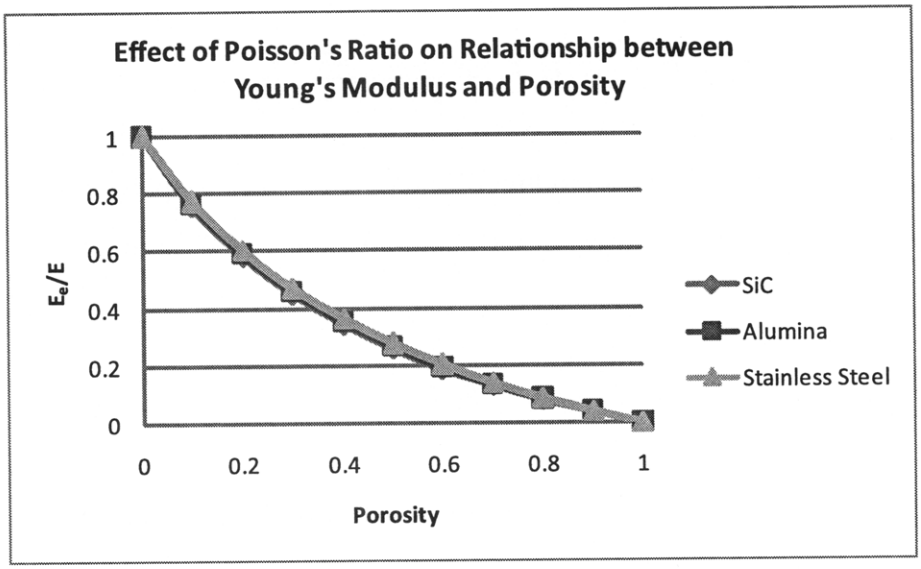

Figure 3-4: The change in Young's modulus with porosity is plotted for three different materials, silicon carbide, alumina and stainless steel having a Poisson's ratio of 0.19, 0.22 and 0.28, respectively. The three resulting curves are almost identical, indicating a very small effect of the Poisson's ratio on the elastic modulus.

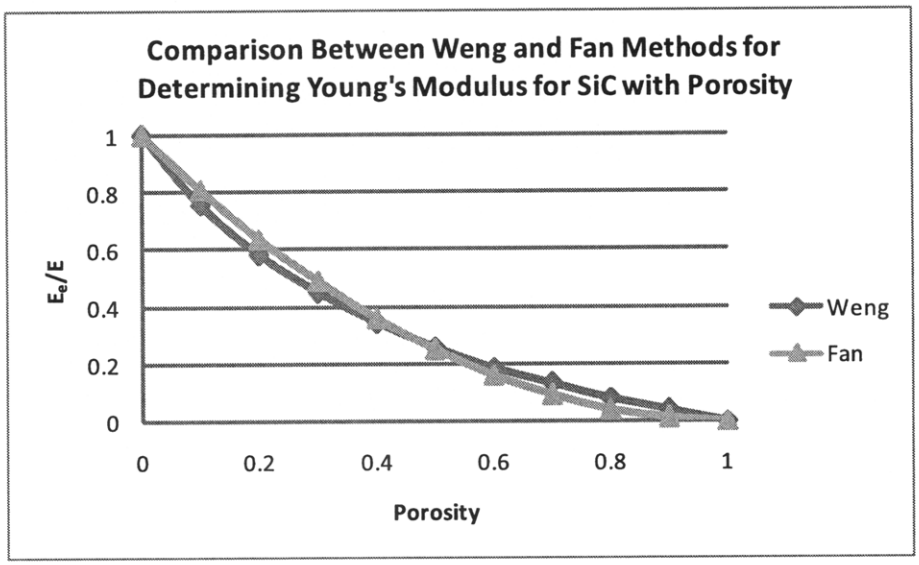

Figure 3-5: The change in Young's modulus with porosity is plotted using both Weng's analysis and Fan's analysis. The models agree at a porosity of ~45%.

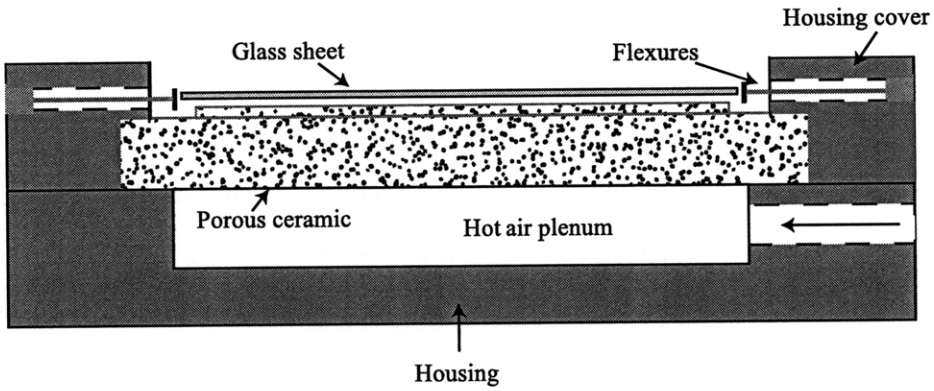

Figure 3-6: A glass sheet resting on a thin layer of air as the temperature of the system is increased. Pressurized air flows through the porous medium and out against the glass to carry its weight, providing a thin layer of air, where particulates smaller than the air gap size are absorbed. The glass sags due to its own weight at high temperatures to replicate the pressure profile in the air gap. The flexures on the edges of the glass constrain it in the lateral direction.

3.3.1 Slumping on a Flat Porous Medium

This is perhaps the easiest approach in terms of apparatus design and building. Figure 3-6 shows a schematic of this concept, where a glass sheet is carried by a thin layer of air going through a porous medium. The air diffuses in this medium, which acts as a high resistance to the flow of the pressurized air. The air emerging from the surface of the porous plate is viscous and at creeping flow rates, giving the thin layer of air its load carrying properties. As the temperature is increased during the experiment, the glass softens and takes the general shape of the object it rests on. In this case, the object is the thin layer of air.

Ceramics are a better candidate for air bearings for various reasons: they do not corrode in any fluid environment that might be used during their machining, they are brittle, which means minimum plastic deformation is generated during grinding and

lapping, leading to a surface with a negative skewness and minimal residual stress, their surface finish is limited by the size of the grain used in sintering, they have a high Young's modulus with a low density and they have high dimensional stability [33]. In an application where the gap between the porous material and the thin optic is on the order of a few microns for viscous flow to develop, the surface integrity of the porous material is critical. If a ductile material is used, such as a metal, any sharp or high points on the surface due to ductility can result in local contact points with the glass, which in turn results in glass surface degradation. This problem is avoided when using ceramics.

This section analyzes the flow of air in the porous medium to determine the pressure profile in the air gap. The heated glass is expected to replicate the shape of this profile during slumping. The following assumptions are made for modeling the flow of air in porous media at elevated temperatures:

1. the flow in the porous medium is at creeping velocities, thus Darcy's relationship shown in Equation 3.19 governs the flow,

2. the material is isotropic; thus, the permeability coefficient of the porous medium is constant in the x, y and z directions,

3. the air follows the perfect gas law, and thus the viscosity and density calculated in Section 3.2.1 can be used,

4. the air is isothermal throughout the porous medium,

5. steady state conditions prevail,

6. the pressure gradient in the thin air gap along the z direction is negligible compared to the pressure gradient along the x and y directions,

7. the flow in the air gap is at a low Reynold's number and thus is laminar (this is proven later in the chapter),

8. there is no fluid accumulation in the porous medium,

9. the velocity of flow is low (creeping flow and low Reynold's number), thus the resulting Mach number is small, and the gas is incompressible.

Flow Equation in Porous Media

Darcy's law for flow in isothermal porous media is given by

$$\vec{U'} = -\frac{k}{\mu}\nabla p', \tag{3.19}$$

where $\vec{U'}$ is the velocity of flow in any given direction in the porous medium, k is the permeability of the porous material and $\nabla p'$ is the pressure gradient. The second equation considered is the continuity equation given by

$$\frac{\partial u'}{\partial x} + \frac{\partial v'}{\partial y} + \frac{\partial w'}{\partial z} = 0, \tag{3.20}$$

where u', v', and w' are the velocity components along the x, y, and z directions, respectively. By substituting the velocity components of $\vec{U'}$ from Equation 3.19 into Equation 3.20, the equation governing flow in the porous ceramic is

$$k_x\frac{\partial^2 p'}{\partial x^2} + k_y\frac{\partial^2 p'}{\partial y^2} + k_z\frac{\partial^2 p'}{\partial z^2} = 0, \tag{3.21}$$

where k_x, k_y and k_z are the permeability of the material in the x, y and z directions, respectively.

To normalize Equation 3.21, the variables are replaced by $\tilde{x} = x/L$, $\tilde{y} = y/W$, $\tilde{z} = z/H$, $\tilde{p'} = p'/p_a$, $K_x = k_x/k_z$ and $K_y = k_y/k_z$, where p_a is the ambient pressure and L, W and H are the length, width and thickness of the ceramic part, respectively, as shown in Figure 3-7. The resulting equation is

$$K_x\frac{\partial^2 \tilde{p'}}{\partial \tilde{x}^2} + K_y\left(\frac{L}{W}\right)^2\frac{\partial^2 \tilde{p'}}{\partial \tilde{y}^2} + \left(\frac{L}{H}\right)^2\frac{\partial^2 \tilde{p'}}{\partial \tilde{z}^2} = 0, \tag{3.22}$$

Boundary Conditions

The boundary conditions, in addition to Equation 3.22, determine the pressure distribution in the air gap. The lower surface of the ceramic is facing a plenum with pressurized air, thus the pressure at this interface is equal to the supply pressure P_s. The edges of the ceramic are sealed. In other words, there is no leakage from the

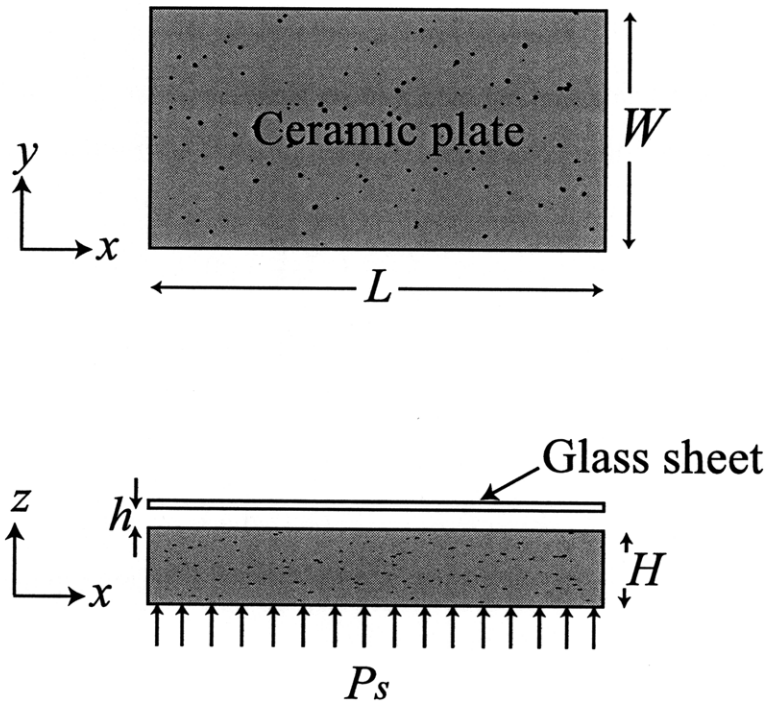

Figure 3-7: Dimensions of a porous ceramic plate used in the flow analysis equations

side walls of the ceramic, and thus the pressure gradient along the edges is zero. The ceramic's top surface perimeter is at atmospheric pressure, since it is exposed. The remaining boundary condition is at the top surface of the ceramic, where air leaves the porous material and enters the thin gap.

To determine the equation governing this final boundary condition, the Navier-Stokes equation is considered for the air flow in the gap between the ceramic and the optic as follows,

$$\rho\left(\frac{\partial \vec{U}}{\partial t} + \vec{U}.\nabla\vec{U}\right) = -\nabla p + \mu\nabla^2\vec{U} + \vec{f}, \tag{3.23}$$

where ρ is the fluid density, $\vec{U}$ is the velocity vector, t is time, p is the fluid pressure, μ is the fluid viscosity and $\vec{f}$ represents other forces, such as body or centrifugal forces. The left side of Equation 3.23 represents inertial forces, whereas the three terms on the right side represent the pressure gradient, viscous forces and other forces, respectively.

The model considers steady state viscous flow conditions, where the gap h shown in Figure 3-7 is much smaller than the length L and width W. The flow between the two surfaces is the result of a pressure gradient in the x and y directions, thus the velocity component w in the z direction is much smaller than the components u and v in the x and y directions, respectively. Since $h << L$ and $h << W$, the order of magnitude of the terms on the left hand side of Equation 3.23 is much smaller than the order of magnitude of the viscous terms on the right hand side of the same equation. Thus the terms on the left hand side are negligible. Also all the second order partial differential terms of the velocity $\vec{U}$ with respect to x and y are negligible compared to those with respect to z. For flow in the x and y directions, the gravity component of $\vec{f}$ is zero.

Thus the Navier-Stokes equation reduces to

$$\frac{\partial^2\vec{U}}{\partial z^2} = \frac{1}{\mu}\nabla p. \tag{3.24}$$

Equation 3.24 can be integrated twice with respect to z such that $\vec{U} = 0$ at $z = h$, which is the air-glass interface and h represents the air gap thickness, and

$\vec{U} = \vec{U'}$ at $z = 0$, which is the air-ceramic interface. In this case, $\vec{U'}$ is the velocity of air in the porous medium at its top surface. This assumes that slip occurs at the porous medium and air interface, where the air flow between the ceramic and the glass follows the average velocity of the air coming out of the porous ceramic at this boundary [42], [43]. The resulting solution is

$$\vec{U} = \frac{1}{2\mu} z \Big(z - h \Big) \nabla p + \frac{h - z}{h} \vec{U'}. \tag{3.25}$$

This provides the velocity distribution of air in the gap; however, the parameter of interest is the pressure in the gap, since the pressure determines the shape of the slumping glass. The variable U' can be replaced by a pressure variable by using Darcy's law from Equation 3.19 to have

$$u = \frac{z - h}{\mu} \left(\frac{z}{2} + \frac{k_x}{h} \right) \frac{\partial p}{\partial x}, \tag{3.26}$$

$$v = \frac{z - h}{\mu} \left(\frac{z}{2} + \frac{k_y}{h} \right) \frac{\partial p}{\partial y}, \tag{3.27}$$

$$w = \frac{z - h}{h} \frac{k_z}{\mu} \frac{\partial p'}{\partial z}, \tag{3.28}$$

where u, v and w are the velocity components of flow in the air gap. The pressure gradient in the gap along the x and y directions is the same as the pressure gradient at the porous plate's top surface ($p = p'$), since the pressure drop across the gap thickness is negligible; however, this is not the case along the z direction. Since the pressure drop in the air gap along the z direction is negligible, Equation 3.28 is left in terms of the pressure p' in the porous medium.

These velocity components are differentiated with respect to x, y and z, respectively and substituted in the continuity equation described before in Equation 3.20, which applies in the air gap as well. Integrating this newly formed equation with respect to z from $z = 0$ to $z = h$ to cover the entire gap height, the equation governing the boundary condition at the ceramic-air interface is given by

$$\frac{\partial}{\partial x}\left[h(h^2+6k_x)\frac{\partial p}{\partial x}\right]+\frac{\partial}{\partial y}\left[h(h^2+6k_y)\frac{\partial p}{\partial y}\right]=12k_z\left(\frac{\partial p'}{\partial z}\right)_{z=H}. \tag{3.29}$$

For the special case of a constant gap height h and equal permeabilities in all directions $k_x = k_y = k_z$, Equation 3.29 becomes

$$\frac{\partial^2 p}{\partial x^2}+\frac{\partial^2 p}{\partial y^2}=\frac{12k_z}{h(h^2+6k_z)}\left(\frac{\partial p'}{\partial z}\right)_{z=H}. \tag{3.30}$$

It should be noted that k_z is on the order of 10^{-15} m^2, whereas h^2 is on the order of 10^{-12} m^2; thus $k_z << h^2$ and if neglected in Equation 3.30, it reduces to

$$\frac{\partial^2 p}{\partial x^2}+\frac{\partial^2 p}{\partial y^2}=\frac{12k_z}{h^3}\left(\frac{\partial p'}{\partial z}\right)_{z=H}, \tag{3.31}$$

which shows that the pressure drop is inversely proportional to the thickness cubed of the air gap.

A normalized form of Equation 3.29 can be obtained similarly to Equation 3.22 to result in

$$a\frac{\partial^2 \tilde{p}}{\partial \tilde{x}^2}+b\left(\frac{L}{W}\right)^2\frac{\partial^2 \tilde{p}}{\partial \tilde{y}^2}=\left(\frac{\partial \tilde{p'}}{\partial \tilde{z}}\right)_{\tilde{z}=1}, \tag{3.32}$$

where $a = 1/\Lambda + 1/2K_x(Hh/L^2)$, $b = 1/\Lambda + 1/2K_y(Hh/L^2)$, and $\Lambda = 12k_zL^2/h^3H$.

Numerical Analysis

To solve the second order partial differential equations that govern the flow of air in the porous plates, the elliptic equations of the finite difference method are utilized [44]. The ceramic plates are composed of a grid of many points or nodes separated by a distance of $\Delta\tilde{x}$, $\Delta\tilde{y}$ and $\Delta\tilde{z}$ along the x, y and z directions, respectively. Thus, the second order partial differential equation at any node is given by

$$\frac{\partial^2 \tilde{p'}}{\partial \tilde{x}^2}=\frac{\tilde{p'}_{i+1,j,k}-2\tilde{p'}_{i,j,k}+\tilde{p'}_{i-1,j,k}}{\Delta\tilde{x}^2} \tag{3.33}$$

$$\frac{\partial^2 \tilde{p'}}{\partial \tilde{y}^2}=\frac{\tilde{p'}_{i,j+1,k}-2\tilde{p'}_{i,j,k}+\tilde{p'}_{i,j-1,k}}{\Delta\tilde{y}^2} \tag{3.34}$$

$$\frac{\partial^2 \tilde{p'}}{\partial \tilde{z}^2} = \frac{\tilde{p'}_{i,j,k+1} - 2\tilde{p'}_{i,j,k} + \tilde{p'}_{i,j,k-1}}{\Delta \tilde{z}^2}, \tag{3.35}$$

For first order partial differential terms, such as the right side of Equation 3.32, the following relationship known as the centered finite-divided-difference formula holds

$$\frac{\partial \tilde{p'}}{\partial \tilde{z}} = \frac{\tilde{p'}_{i,j,k+1} - \tilde{p'}_{i,j,k-1}}{2\Delta \tilde{z}}. \tag{3.36}$$

In this particular case, the mesh sizes $\Delta\tilde{x}$, $\Delta\tilde{y}$ and $\Delta\tilde{z}$ are all set equal to Δ.

Equations 3.33 through 3.36 can now be replaced in Equations 3.22 and 3.32 to obtain a numerical solution in the form of

$$\tilde{p}_{i,j,k} = \frac{K_x(\tilde{p}_{i+1,j,k} + \tilde{p}_{i-1,j,k}) + K_y(L/W)^2(\tilde{p}_{i,j+1,k} + \tilde{p}_{i,j-1,k}) + (L/H)^2(\tilde{p}_{i,j,k+1} + \tilde{p}_{i,j,k-1})}{2\left(K_x + K_y(L/W)^2 + (L/H)^2\right)}, \tag{3.37}$$

$$\tilde{p}_{i,j,k_H} = \frac{a(\tilde{p}_{i+1,j,k_H} + \tilde{p}_{i-1,j,k_H}) + b(L/W)^2(\tilde{p}_{i,j+1,k_H} + \tilde{p}_{i,j-1,k_H}) - \Delta/2(\tilde{p}_{i,j,k_H+1} - \tilde{p}_{i,j,k_H-1})}{2a + 2b(L/W)^2}, \tag{3.38}$$

where Equation 3.37 is the flow in the ceramic plate and Equation 3.38 is the boundary condition at the top of the ceramic plate. By incorporating the remaining boundary conditions discussed above, a Matlab executable code shown in Appendix A runs iterations on these equations and obtain a solution for the pressure profile in the air gap. It should be noted that in Equation 3.38, $\tilde{p}_{i,j,k_H+1}$ is the same as $\tilde{p}_{i,j,k_H}$, where $\tilde{p}_{i,j,k_H}$ is the pressure at the top surface of the ceramic plate, since it has been assumed that the pressure drop in the air gap along the z direction is negligible when compared to the pressure drop along the x and y directions. Thus Equation 3.38 can be rewritten as

$$\tilde{p}_{i,j,k_H} = \frac{a(\tilde{p}_{i+1,j,k_H} + \tilde{p}_{i-1,j,k_H}) + b(L/W)^2(\tilde{p}_{i,j+1,k_H} + \tilde{p}_{i,j-1,k_H}) + \frac{\Delta}{2}\tilde{p}_{i,j,k_H-1}}{2a + 2b(L/W)^2 + \frac{\Delta}{2}}. \tag{3.39}$$

An important parameter that must be known to solve Equation 3.37 is the material permeability K. Unfortunately, this material property is not readily available by the

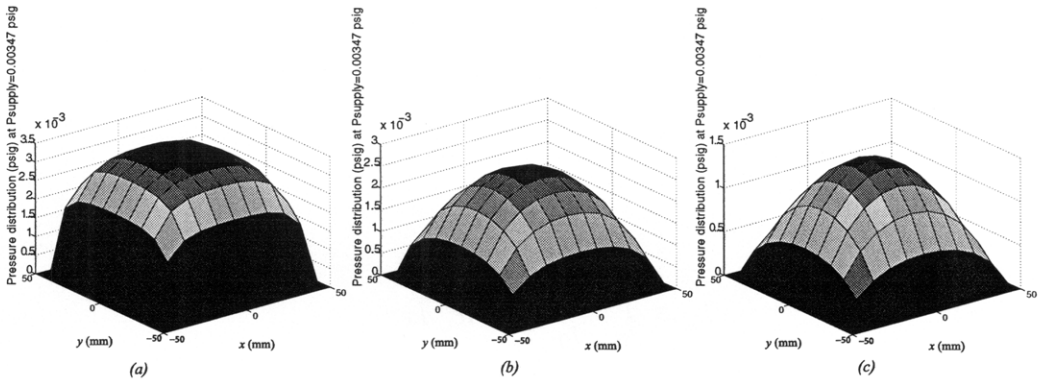

Figure 3-8: The pressure profile at 600°C in the air gap of a 100 mm×100 mm×12.7 mm porous bearing at film thickness of *(a)* 5 μm, *(b)* 10 μm and *(c)* 15 μm. Number of nodes used = 11.

manufacturers of any of the porous materials that have been considered. There are several articles that discuss ceramic permeability and its dependence on temperature, particularly the paper by Innocentini et al. [45], where the permeability coefficients of various materials and their change with temperature is thoroughly discussed and experimented. In general, the higher the permeability, the lower the pressure drop across the thickness of the ceramic plate and thus a higher load carrying capacity.

The ceramics used in these experiments have been sintered at temperatures ranging between 1,200 and 1,500°C. It is assumed that the ceramic is isotropic, and thus the permeabilities in three directions are equal. From Innocentini's article, typical permeability coefficients for such ceramics are on the order of 8×10^{-15} to 10×10^{-15} m^2 at room temperature and 6×10^{-15} and 10×10^{-15} m^2 at around 600°C. Thus a value of 6×10^{-15} m^2 is used in this modeling to determine the pressure profile of air in the gap between the ceramic plate and the slumping glass optic. This profile is shown in Figure 3-8 for the different air gaps of 5, 10 and 15 μm over a cross-sectional area of 100 mm × 100 mm, respectively.

Load Carrying Capacity

Since this horizontal configuration requires that the thin layer of air carry the load of the glass optic, the required air pressure for these experiments can be calculated using

$$G_w = \int_0^W \int_0^L (p - p_a) dx dy, \tag{3.40}$$

where G_w is the weight carried, in this case the weight of the optic. This equation assumes load carrying capacity at zero gap and thus provides the minimal pressure needed to lift the optic; however, as the gap increases, the load carrying capacity at the same supply pressure decreases. The optic used is Schott D-263 glass, which has a density of 2.53 g/c.c. The resulting load per unit area for a 0.4 mm thick glass is 9.93 N/m^2. For an optic that is 140 mm $\times$ 100 mm in area, a supply pressure of 0.0035 psi or 24 Pa provides a pressure distribution in the air gap that satisfies Equation 3.40.

Reynold's Number

Earlier in this section, the flow is assumed to be creeping due to the high resistance to flow resulting from the microporous medium. With the developed model and the predicted pressure profile, the velocity of air in the thin gap and thus the Reynold's number can be calculated.

The Reynold's number Re is given by

$$Re_x = \frac{\rho u_{av} h}{\mu}, \tag{3.41}$$

where u_{av} is the average velocity of flow in the x direction in the air gap. Due to the symmetric nature of flow, the Reynold's number along the y direction is of the same order of magnitude as that along the x direction, and thus only the x direction is analyzed below.

The average velocity in the gap can be calculated from the flow rate relationship

$$u_{av} = \frac{Q}{A} = \frac{1}{A}\int u dA = \frac{2\pi r}{2\pi r h}\int_0^h u dz, \tag{3.42}$$

where Q is the flow rate, A is the cross-sectional area in the gap, r is the radius from the center of the plate and u is the velocity from Equation 3.25. The resulting solution is

$$u_{av} = -\frac{h^2}{12\mu}\nabla p + \frac{u'}{2}. \tag{3.43}$$

The value of h used in the experiments described in Chapter 4 ranges between a critical value of 12.7 μm and a maximum value of 50 μm. ∇p representing $\frac{\partial p}{\partial x}$ in this case, is obtained from the results of the numerical analysis conducted in Matlab over a length Δ, which represents the spacing between two nodes, also described as the mesh size in the numerical analysis solution. The viscosity of air ranges between 18.3 and 40.65 μPa.s, as shown in Table 3.1. The value of u' can be calculated from Darcy's Equation 3.19 for a pressure gradient along a specific length. Table 3.3 summarizes the Reynold's number for the flow in the air gap at both room temperature and slumping temperature and for different air gaps and supply pressures.

As can be seen in Table 3.3, the Reynold's number for the flow of air going through a porous medium and exiting through a very narrow channel is extremely small, thus justifying the initial assumption of creeping flow in the theoretical analysis.

The limitations of this method of slumping glass on one flat porous medium are obvious. The pressure profile shown in Figure 3-8 is not flat but rather curved, with a high pressure at the center and atmospheric pressure at the edges. This pressure profile is replicated on the surface of the glass as it slumps on the ceramic. However, the theoretical analysis described in this section is the cornerstone for the analyses to come for the other concepts considered.

3.3.2 Slumping on a Grooved Porous Ceramic Medium

One way to minimize the effect of the pressure gradient seen when utilizing a pressurized porous ceramic as a slumping mandrel is to have channels machined into the

T	h	**Supply pressure** P_s	u_{av}	Re_x
°C	μm	Pa (psi)	m/s	
20	12.7	24 (0.0035)	2.91×10^{-5}	2.42×10^{-5}
20	12.7	2069 (0.3)	2.52×10^{-3}	2.10×10^{-3}
600	12.7	24 (0.0035)	1.20×10^{-5}	1.50×10^{-6}
600	12.7	2069 (0.3)	1.03×10^{-3}	1.29×10^{-4}
20	50	24 (0.0035)	2.53×10^{-6}	8.28×10^{-6}
20	50	2069 (0.3)	4.32×10^{-4}	1.42×10^{-3}
600	50	24 (0.0035)	6.90×10^{-7}	3.39×10^{-7}
600	50	2069 (0.3)	1.18×10^{-4}	5.82×10^{-5}

Table 3.3: Average air flow velocity in a thin gap and corresponding Reynold's number at various temperatures, gap sizes and supply pressures to be used in the experiments described in Chapter 4. The properties of air are temperature dependent, as shown in Table 3.1

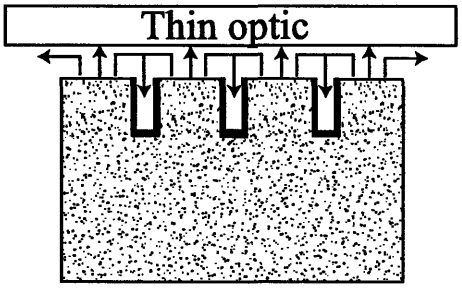

Figure 3-9: Air leaves a porous ceramic through the peak regions to lift the optic and escape through the channels to the atmosphere without building up a large pressure gradient

surface of the ceramic, such that air from the center of the ceramic has a low resistance pathway to the atmosphere through these channels. This results in a smaller pressure build-up in the center of the ceramic, thus reducing the pressure gradient from the center to the edges of the ceramic and providing a flatter pressure profile in the air gap.

It is preferrable to have the side walls and valleys of the channels sealed to avoid air leakage through these areas. Air would leave the porous medium only through the top surface of the ceramic plate, as shown in Figure 3-9, and escape to the atmosphere through the channels.

The theoretical flow analysis presented in the previous section must be modified to take the geometry of these channels into consideration. In the previous analysis, the partial differential equations governing the flow of air in the porous medium and in the air gap are solved using the finite difference method, which divides the ceramic medium into nodes and applies the equations on every node. In the case of the grooved surface of the porous medium, the method is replaced by the control volume approach to solve the partial differential equations. The difference between the two approaches is that the finite difference method assumes that the boundaries of all nodes are identical, whereas the volume control method can take the varying boundary geometries of every node into consideration and is therefore usually used when solving nodes with irregularly shaped boundaries. The similarity between the

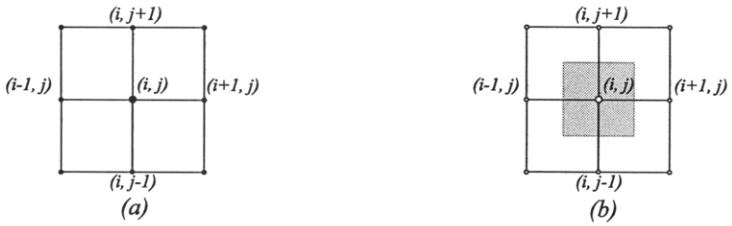

Figure 3-10: 2-D schematic of two different methods for developing approximate solutions for partial differential equations: *(a)* finite-difference and *(b)* control volume

two approaches is that both require that the medium studied be divided into a series of points. Instead of solving the partial differential equations at the nodes, the solution is performed at the volume surrounding the node, as shown in Figure 3-10. This volume is created by drawing a perpendicular line at the midpoint of each line joining adjacent nodes.

Flow Equation in a Porous Medium with Grooves on the Surface

The volume surrounding the nodes in the porous medium is identical for all nodes except for the ones near the surface, where the grooves are surrounding the nodes. The grooves are diamond sawn into the ceramic, as explained in detail in the next chapter. The thinnest blade that could machine such grooves with accuracy is 0.012" or 0.305 mm wide, and it could go as deep as 1 mm. Figure 3-11 shows the control volumes around a single groove along the y direction.

To understand how the presence of the groove affects the flow equations at these surface nodes, the flow rate sum in all directions around the node must be zero, since it has been assumed that fluid does not accumulate in the porous material. The flow rate Q inside the porous medium is given by

$$Q = U'A, \tag{3.44}$$

where U' is the velocity in the porous medium governed by Darcy's law from Equation 3.19, and A is the area of the control volume edge surfaces. In the case of the nodes underneath the groove, such as node M shown in Figure 3-11, there is no flow

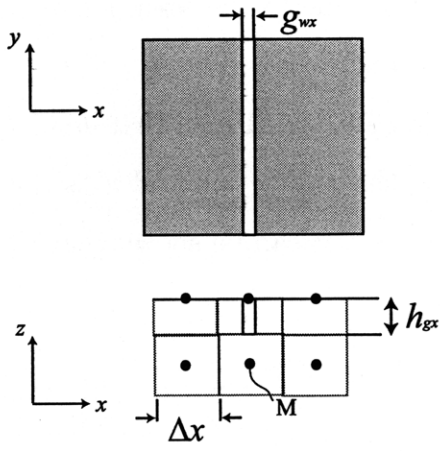

Figure 3-11: Nodes surrounding a groove along the y direction

through the edge where a groove is located, since the valleys of the grooves are sealed. Thus A is the product of $(1-delx)\Delta x\Delta y$, where $delx = n \times g_{wx}/\Delta x$ is the ratio of the channel width to the control volume length Δx, with n being the number of channels found in one Δx ($n = 1$ in Figure 3-11). For control volumes with length, width and height of Δx, Δy and Δz, respectively, the sum of flow rates along the edges of the control volume is

$$\sum Q = u_1'\Delta y\Delta z + u_2'\Delta y\Delta z + v_1'\Delta x\Delta z + v_2'\Delta x\Delta z + w_1'\Delta x\Delta y + w_2'(1-delx)\Delta x\Delta y = 0, \tag{3.45}$$

where the u', v', and w' are the velocity components of air flow along x, y and z, respectively, and the 1 and 2 subscripts represent both sides of a single direction. Replacing velocity with pressure from Darcy's law using Equation 3.19, and writing the pressure using the i, j, and k subscripts the following equation is obtained

$$\tilde{p}_{i,j,k} = \frac{K_x(\tilde{p}_{i+1,j,k} + \tilde{p}_{i-1,j,k}) + K_y(L/W)^2(\tilde{p}_{i,j+1,k} + \tilde{p}_{i,j-1,k}) + (L/H)^2(\frac{\Delta\tilde{x}}{\Delta\tilde{z}})^2(\tilde{p}_{i,j,k+1}(1-delx) + \tilde{p}_{i,j,k}}{2\left(K_x + K_y(L/W)^2 + \frac{(L/H)^2}{2}(\frac{\Delta\tilde{x}}{\Delta\tilde{z}})^2(1+(1-delx))\right)} \tag{3.46}$$

In this case, $\Delta\tilde{x}$ is equal to $\Delta\tilde{y}$; however, both these terms are not set equal to $\Delta\tilde{z}$, and the reason is that the mesh size along the z direction is chosen to be different from

that along the x and y directions due to the presence of the predetermined groove depth at the surface of the ceramic.

If channels in the x direction are added such that $dely = n'g_{wy}/\Delta Y$, where g_{wy} is the width of the channel along the x direction and n' is the number of channels per Δy, then by following similar steps, it can be shown that Equation 3.46 becomes

$$\tilde{p}_{i,j,k} = \frac{K_x(\tilde{p}_{i+1,j,k} + \tilde{p}_{i-1,j,k}) + K_y(L/W)^2(\tilde{p}_{i,j+1,k} + \tilde{p}_{i,j-1,k}) + (L/H)^2(\frac{\Delta\tilde{x}}{\Delta\tilde{z}})^2(\tilde{p}_{i,j,k+1}C + \tilde{p}_{i,j,k-1})}{2\left(K_x + K_y(L/W)^2 + \frac{(L/H)^2}{2}(\frac{\Delta\tilde{x}}{\Delta\tilde{z}})^2(1+C)\right)}, \tag{3.47}$$

where $C = (1 - delx)(1 - dely)$.

Boundary Conditions

The boundary conditions for this case are all the same except at the top surface of the ceramic, where Equation 3.29 governing the boundary condition at the ceramic-air interface is modified to take the variation in the air gap thickness as a result of the channels into consideration. In this analysis, grooves that are g_{wx} wide and h_{gx} deep are machined along the y direction.

The pressure drop across the width of the grooves is much smaller than the drop across their lengths. The Resistance Network Method (RNM) developed by Kogure et al. [46] is utilized to average the resistance along the groove direction in proportion to the land and groove widths. For this case, $1 - delx$ of the land has a height of h, and $delx$ fraction of the land has a height of $h + h_{gx}$, where h_{gx} is the depth of the grooves. This method has been utilized by many to estimate the load capacity of solid grooved air bearings with one inlet hole and a network of grooves distributing air across the area of the bearing [47], [48].

Equation 3.29 governing the flow of air at the top surface of the ceramic is modified to take the grooves into consideration. The resulting equation considers grooves in both x and y directions even though the particular case considered here has grooves in the y direction only. The following equation includes the mesh sizes, since in this case the normalized mesh is not set equal in all directions.

$$\tilde{p}_{i,j,k_H} = \frac{\frac{t}{\Delta\tilde{x}^2}(\tilde{p}_{i+1,j,k_H} + \tilde{p}_{i-1,j,k_H}) + \frac{o}{\Delta\tilde{y}^2}(\tilde{p}_{i,j+1,k_H} + \tilde{p}_{i,j-1,k_H}) - \frac{1}{2\Delta\tilde{z}}(\tilde{p}_{i,j,k_H+1} - \tilde{p}_{i,j,k_H-1})}{\frac{2t}{\Delta\tilde{x}^2} + \frac{2o}{\Delta\tilde{y}^2}}, \tag{3.48}$$

where

$$t = \frac{H}{12k_zL^2}\left((1-dely)h^3+dely(h+h_{gy})^3\right)+\frac{HK_x}{2L^2}\left((1-dely)h+dely(h+h_{gy})\right) \tag{3.49}$$

$$o = \frac{H}{12k_zL^2}\left(\frac{L}{W}\right)^2\left((1-delx)h^3+delx(h+h_{gx})^3\right)+\frac{HK_y}{2L^2}\left(\frac{L}{W}\right)^2\left((1-delx)h+delx(h+h_{gx})\right). \tag{3.50}$$

In this case as well, $\Delta\tilde{x}$ is equal to $\Delta\tilde{y}$; however, both these terms are set not equal to $\Delta\tilde{z}$. Since it has been assumed that there is no pressure drop across the air gap height, $\tilde{p}_{i,j,k_H+1} = \tilde{p}_{i,j,k_H}$, and the resulting equation is

$$\tilde{p}_{i,j,kH} = \frac{t(\tilde{p}_{i+1,j,k_H} + \tilde{p}_{i-1,j,k_H}) + o(\tilde{p}_{i,j+1,k_H} + \tilde{p}_{i,j-1,k_H}) + \frac{\Delta\tilde{x}^2}{2\Delta\tilde{z}}(\tilde{p}_{i,j,k_H-1})}{2t + 2o + \frac{\Delta\tilde{x}^2}{2\Delta\tilde{z}}}. \tag{3.51}$$

The porous ceramic plate is 100 mm $\times$ 100 mm $\times$ 14 mm in dimensions with 0.305 mm wide $\times$ 1 mm deep grooves separated by a distance of 0.457 mm. The reason why these dimensions are chosen is explained in the next chapter. Both Δx and Δy are chosen to be 4 mm, thus $\Delta\tilde{x}$ and $\Delta\tilde{y}$ are equal to $4/100 = 0.04$ mm. Thus every mesh has 3 grooves and 3 land areas, as shown in Figure 3-12. The mesh along the z direction is such that the mesh size is twice the depth of the surface grooves, in this case 2×1 mm $= 2$ mm. Thus $\Delta\tilde{z} = 2/14 = 0.143$.

The results of the flow analysis are shown in Figure 3-13(a). This is for a supply pressure of 0.3 psi (2069 Pa) and an air gap h of 10 μm. Figure 3-13(b) shows the results of flow through a similar porous plate under identical conditions but with no grooves on the surface. As can be seen from this figure, the channels or grooves provide a rather uniform pressure profile along their length in addition to significantly reducing the overall maximum pressure in the air gap from ~ 0.25 psi to $\sim 2.5 \times 10^{-6}$ psi. However, the pressure gradient along the x direction, where no grooves are

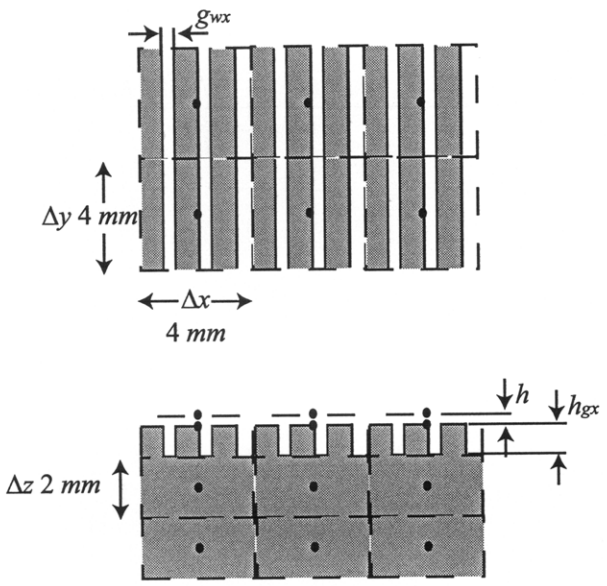

Figure 3-12: Actual node sizes used in the analysis of flow through a grooved porous plate

present, is predominant in this case. It should be noted that the overall mesh size in this analysis is larger than the size of individual grooves, thus the slight pressure drop at the groove due to its depth is not seen in these figures despite the fact that it is included in the analysis, as was described in the sections above. The overall number of nodes on the ceramic is $26 \times 26 \times 8$.

3.3.3 Horizontal Slumping by Flow of Air through Porous Media onto Both Surfaces of Glass Sheets

Another method to minimize the bow of glass slumping on a porous plate due to the pressure gradient in the air gap is to approach the glass sheet on both its surfaces with equal pressure, as shown in Figure 3-14. This can be achieved by squeezing the glass sheet between two porous plates having flat surfaces and forcing air through the porous plate and onto the glass surface. In this scenario, both sides of the glass would see the same pressure gradient as long as the glass is equidistant between the two surfaces.

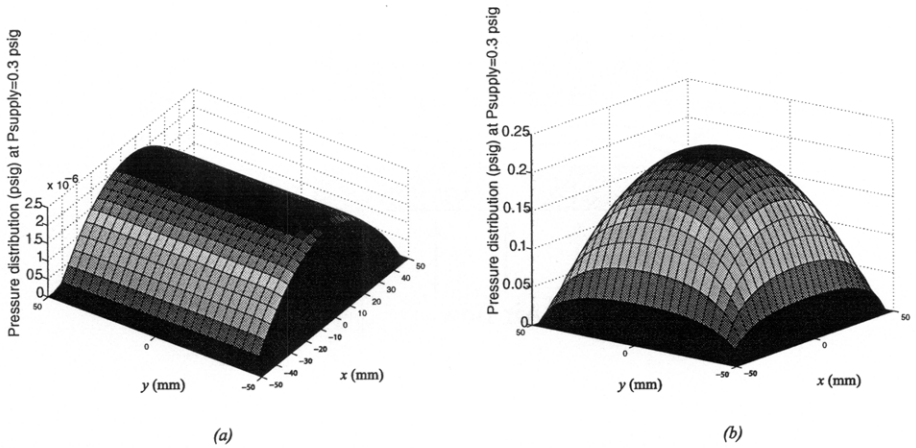

Figure 3-13: Pressure profile in 10 μm air gap and supply pressure of 0.3 psi for *(a)* porous ceramic with 0.305 mm wide and 1 mm deep grooves machined on its surface and *(b)* flat porous ceramic with no grooves

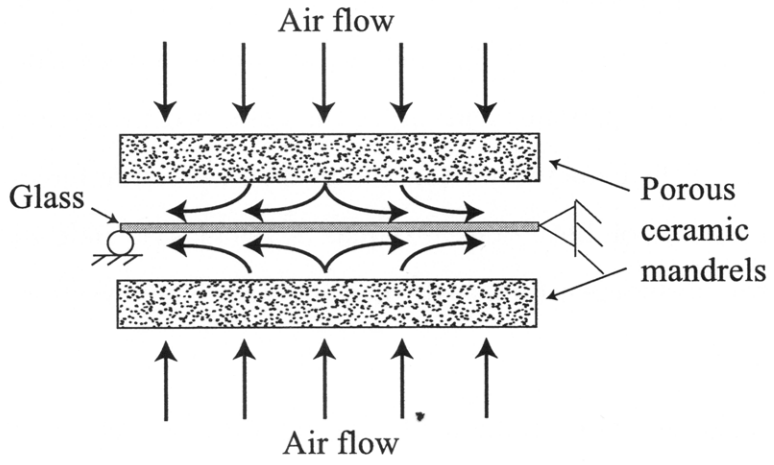

Figure 3-14: Slumping glass between two porous flat ceramic plates while glass is constrained in the horizontal plane

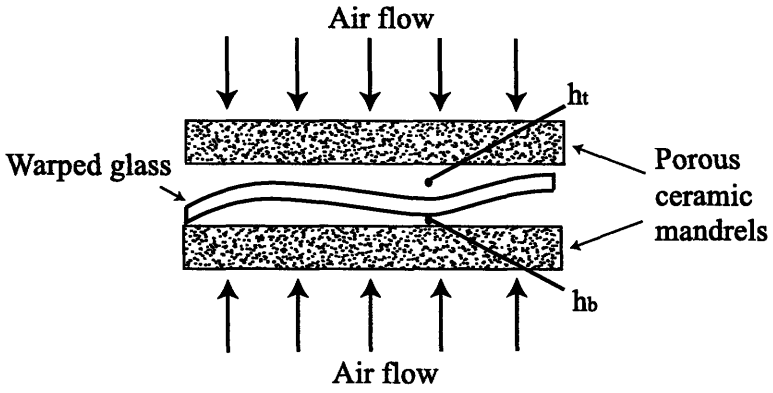

Figure 3-15: Slumping glass between two porous flat ceramic plates while glass is constrained in the horizontal plane

An initially warped glass squeezed between two flat porous plates will be in closer promixity to one of the plates at any given point along the length of the glass. This means that at that specific point, the air gap h_b would be smaller on one side and larger (h_t) on the other side, as shown in Figure 3-15. For equal supply pressures and permeabilities, the pressure at the side of the glass with the smaller gap h_b will be larger than the pressure on the equivalent point h_t on the other side of the glass. This relationship between pressure and air gap is described in Section 3.3.1. Thus as the glass softens with temperature, this difference in pressure forces the glass to flatten until the pressures on both sides are equal. If the glass is uniform in thickness, ideally pressure equilibrium is established when the glass is midway between the two plates.

In addition to the pressure profile in the air gap on both sides of the glass, the weight of the glass affects its final shape in this configuration. When held in the horizontal plane, the glass sags due to its own weight. This can be accounted for by increasing the supply pressure of the lower ceramic or varying the actual shape of the two ceramic plates to make up for the gap variation caused by the optic bow; however, this is not an easy task, since the weight of the glass varies with different glass sheets depending on their thickness uniformity. Sheet glass has a thickness

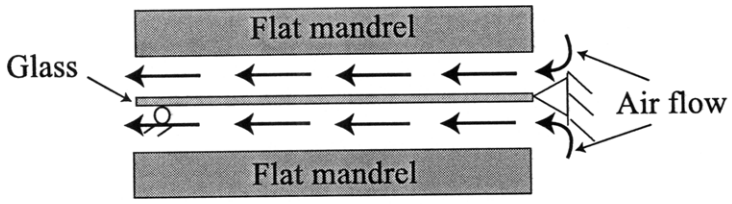

Figure 3-16: Slumping glass between two flat mandrels with air flowing parallel to the glass while it is constrained in the horizontal plane

variation in the range of ± 20 μm, as quoted by the manufacturers [16] [49]. Thus the deformation of a glass sheet with gravity can vary between -9.3% and 10.8% of the nominal deformation value expected. This in turn affects the size of the gap between the glass sheet and the lower mandrel, affecting the pressure forces from this mandrel and thus the final shape of the sheet.

3.3.4 Horizontal slumping by Flow of Air Between Parallel Surfaces and on Both Sides of Glass Sheets

Another way of slumping glass without physical contact is to have air flow from one end of the glass sheet parallel to it, as shown in Figure 3-16. In this case, the flow must be laminar such that the viscous properties of air that provide the shaping force are utilized as well. The flow on each side of the glass sheet is equivalent to Poiseuille's flow case between two quasi-parallel plates.

The mandrel shown in Figure 3-16 can be made of any material that withstands the slumping temperature of glass. In order to improve the flatness of the glass sheets, this mandrel must be machined flat as well, which can be accomplished using fly-cutting, optical polishing, or grinding and lapping techniques, depending on the material selected.

Poiseuille's flow assumes incompressible, steady-state, fully developed flow. For flow along the x direction, the Navier-Stokes equation given by Equation 3.23 reduces to

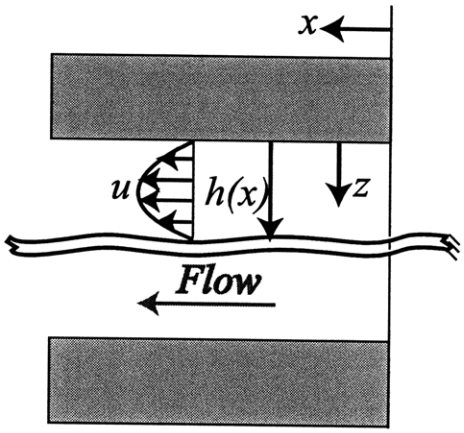

Figure 3-17: Properties of flow between two parallel plates

$$\frac{dp}{dx} = \mu\left(\frac{d^2u}{dz^2}\right), \tag{3.52}$$

where p is the pressure in the gap, x is the direction of flow, u is the velocity of the flow along the x direction and z is the direction of the gap. By integrating this equation twice with respect to z and substituting the boundary conditions of zero velociy at $z = 0$ and $z = h$, where h is the size of the air gap, Equation 3.52 becomes

$$u = -\frac{1}{2\mu}\frac{dp}{dx}\left(h(x)z - z^2\right). \tag{3.53}$$

Since the glass is warped, h is a function of the glass length along the x direction. The velocity vector has a parabolic profile along the z direction, as shown in Figure 3-17.

The velocity u is maximum when $\frac{du}{dz} = 0$, which happens at $z = h/2$. At this point,

$$u_{max} = -\frac{h^2(x)}{8\mu}\frac{dp}{dx}. \tag{3.54}$$

The average velocity U can be calculated using the flow rate equation per unit width

$$Q = Uh = \int_0^h u dz, \tag{3.55}$$

where Q is the flow rate, which results in

$$U = -\frac{h^2}{12\mu}\frac{dp}{dx} = \frac{2}{3}u_{max}. \tag{3.56}$$

By substituting Equations 3.55 and 3.56 in Equation 3.54, the relationship between the pressure profile, the air gap and the flow rate can be obtained as

$$\frac{dp}{dx} = -\frac{12\mu Q}{h^3}. \tag{3.57}$$

As can be seen from Equation 3.57, the pressure drop along the length of the glass is directly proportional to the flow rate of the shaping air. This analysis does not take the weight of the glass into consideration; however, the weight of the glass causes it to sag towards the bottom surface, thus decreasing the air gap size on that side. This will automatically increase the pressure on that side if the flow rate on both sides is equal, a phenomenon similar to the one explained in Section 3.3.3. The shaping of the glass happens through a balance of pressure on both its surfaces. For a glass of uniform thickness, the balance happens midway between the two flat mandrels, without considering the effect of the weight of the glass. Just as was the case in Section 3.3.3, the effect of the glass weight can be reduced by either increasing the pressure along the lower side of the glass or varying the geometry of the lower mandrel.

Another challenge in this case is the introduction of air between the glass and the mandrel at small air gaps, while maintaining the initially warped glass midway between the two mandrels. This is particularly challenging in the case of continuously flowing glass discussed later on in this chapter. The challenge is in controlling leakage and thus controlling the flow rate when air enters the gap; however, an advantage is that the pressure drop along the length of the gap is linear and easier to control once in the gap, as opposed to the second-order pressure drop seen in the case of flow through porous ceramics.

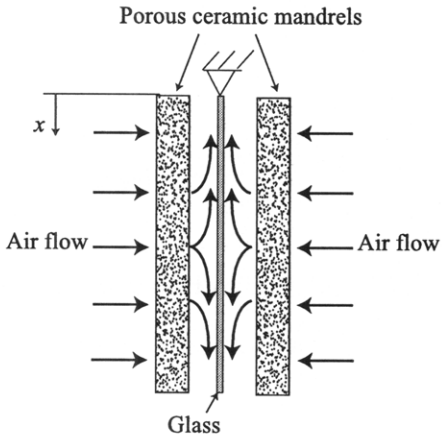

Figure 3-18: Slumping of glass squeezed between two porous ceramic plates

3.3.5 Vertical Slumping by Flow of Air through Porous Media onto Both Surfaces of a Glass Sheet

To eliminate the effect of the glass weight on its final shape, slumping can be performed in the vertical direction, as shown in Figure 3-18. Two cases are considered in this section: the case of one glass sheet and the case of a continuously flowing glass sheet.

Vertical Slumping of One Glass Sheet by Flow of Air through Porous Media

This case is similar to the case discussed in Section 3.3.1. The main difference is the fact that the air flow is along the gravity plane, which means that gravity would need to be taken into consideration in the modeling.

The flow in the porous medium itself is not affected, since viscosity is the dominent parameter in this case. The velocity in the air gap must be rederived from the Navier-Stokes equation to take the gravity vector g and thus body forces into consideration.

$$\frac{\partial p}{\partial x} = \mu \frac{\partial^2 u}{\partial z^2} + \rho g, \tag{3.58}$$

$$\frac{\partial p}{\partial y} = \mu \frac{\partial^2 v}{\partial z^2}, \tag{3.59}$$

and

$$\frac{\partial p}{\partial z} = \mu \frac{\partial^2 w}{\partial z^2} = 0, \tag{3.60}$$

for the x, y and z directions, respectively.

Equations 3.59 and 3.60 are similar in form to Equation 3.24 with identical boundary conditions, thus their solution is the same as Equations 3.27 and 3.28. By solving Equation 3.58 with boundary conditions of $u = u' = -\frac{k_x}{\mu}\frac{\partial p}{\partial x}$ at $z = 0$ and $u = 0$ at $z = h$, the result is

$$u = \frac{z-h}{\mu}\left(\frac{z}{2} + \frac{k_x}{h}\right)\frac{\partial p}{\partial x} - \frac{z(z-h)}{2\mu}\rho g. \tag{3.61}$$

Although the u component of velocity depends on density, as is expected, the density of air is assumed to be constant along the length of 100 mm of the glass sheet. Thus the change in u with respect to x is independent of density or gravity, since both these terms are constant with x. When differentiating Equations 3.61, 3.27 and 3.28 with respect to x, y and z, respectively to substitute them in the continuity equation given by Equation 3.20 and integrating with respect to z from 0 to h, the same boundary condition is obtained for flow in the vertical direction as is given by Equation 3.29.

Thus the pressure profile in the gap on each side of the glass sheet is the same as what was shown in Section 3.3.1 for flow on a horizontal porous plate with identical parameters. The additional advantage in this case is the fact that the glass is held in equilibrium with respect to the two opposing ceramic plates. If one area of the glass is closer to one of the plates, that reduces the size of the air gap in that area, increasing the pressure the soft glass feels and pushing the glass away from the surface. This continues until the pressure forces decrease with increased gap size, and a balance of forces from the air coming out of both ceramic plates is achieved.

Vertical slumping of a Continuously Flowing Glass Sheet by Flow of Air through Porous Media

In the case when glass is manufactured in a continuous process, it is possible to shape the glass while it is being manufactured in its molten state. Once the glass sheet is formed and is flowing vertically downwards, either due to gravity or due to the pulling forces the sheet sees in the lower cooler sections, a porous ceramic plate with pressurized air flow can be placed on each side of the sheet with the air flowing against the hot sheet to shape it.

The flow in the porous ceramic is identical to what has been described earlier; however, the difference in this case is the velocity of the flowing glass U_G in the x direction. This difference affects the boundary condition when solving the Navier-Stokes relationships given by Equation 3.58 through 3.60. The v and w components are not affected in this case, since the glass velocity is only in the x direction. Equation 3.58 is revisited to incorporate the glass sheet velocity U_G. The boundary conditions are $u = u' = -\frac{k_x}{\mu}\frac{\partial p}{\partial x}$ at $z = 0$ and $u = U_G$ at $z = h$. The resulting equation is

$$u = \frac{z-h}{\mu}\left(\frac{z}{2} + \frac{k_x}{h}\right)\frac{\partial p}{\partial x} - \frac{z(z-h)}{2\mu}\rho g + \frac{U_G z}{h}. \tag{3.62}$$

By differentiating this equation along with Equations 3.59 and 3.60, replacing them in the continuity equation and integrating with respect to z from 0 to h, the resulting boundary equation becomes

$$\frac{\partial}{\partial x}\left(h(h^2+6k_x)\frac{\partial p}{\partial x}\right) + \frac{\partial}{\partial y}\left(h(h^2+6k_y)\frac{\partial p}{\partial y}\right) = 12k_z\left(\frac{\partial p'}{\partial z}\right)_{z=H} - 6\mu h\frac{\partial U_G}{\partial x} + h^3\frac{\partial(\rho g)}{\partial x}. \tag{3.63}$$

Thus depending on U_G and the change of density of air along the length of the continuous glass sheet, both Equations 3.21 and 3.63 can be non-dimentionalized and solved using the finite difference method described above to obtain the pressure profile in the air gap.

3.3.6 Vertical Slumping by Flow of Air Between Parallel Surfaces onto Both Surfaces of a Glass Sheet

This concept is similar to the one described in Section 3.3.4 except that slumping is performed with the glass in the vertical plane. This eliminates any surface errors induced by the weight of the glass during the process. The main difference to include in the equation governing the pressure gradient along the length of the optic is to incorporate the density and gravity terms into the equation.

The Navier-Stokes governing the flow in each gap is the same as Equation 3.58, which is integrated twice to solve for velocity with boundary conditions of $u = 0$ at both $z = 0$ and $z = h$. The resulting equation is

$$u = -\frac{\rho g}{2\mu}\frac{d}{dx}\left(\frac{p}{\rho g} + e_x\right)\left(h(x)z - z^2\right), \tag{3.64}$$

where e_x is the unit vector (1,0,0) along the x direction. The term de_x/dx equals -1 since flow is downward. By finding the maximum velocity and using that to substitute the flow rate Q in the above equation, as was performed in Section 3.3.4, the pressure drop with x for this one dimensional flow on each side of the glass is

$$\frac{dp}{dx} = \rho g\left(1 - \frac{12\mu}{\rho g}\frac{Q}{h^3(x)}\right). \tag{3.65}$$

As can be seen, the pressure drop is linear along the length of the sheet in this case. The challenges in this design are the same as those presented Section 3.3.4.

3.4 Pressure Differential across Glass Thickness

When slumping glass between two mandrels, the supply pressure in both mandrels is assumed to be equal in order to obtain flat glass. However, it is important to understand how much of a pressure difference can be tolerated before the glass shape exceeds the required flatness. This helps determine the type of sensors and flow control valves needed during the experiment.

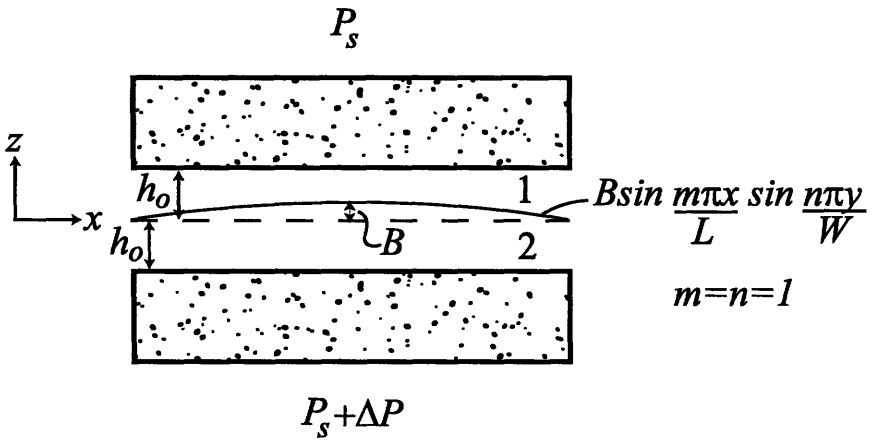

Figure 3-19: Glass sheet bow as a result of the pressure difference applied between the upper and lower mandrels. Figure not to scale.

The final shape of the glass sheet depends on its boundary conditions. However, in the model presented next, the edges of the glass sheet are simply-supported, and the glass sheet is fully viscous, such that it fully conforms to the forces exerted by the difference in pressure on its two surfaces. Gravity is not taken into consideration in this model. Figure 3-19 shows the setup described. The upper mandrel is at a supply pressure P_s, whereas the lower mandrel is at a supply pressure $P_s + \Delta P$, where ΔP is the difference in the supply pressure of the two mandrels. Since the pressure in the lower gap is higher, it pushes the glass sheet upwards; however, this in turn decreases the gap in the upper area, resulting in a pressure increase in that gap. An equilibrium position is obtained when the pressure in both gaps is equal. The resulting dome-shape on the glass sheet is approximated by the function $B \sin \frac{m\pi x}{L} \sin \frac{n\pi y}{W}$, where x and y are the coordinates along the surface of the glass sheet, m and n are integers, L and W are the dimensions of the porous mandrels and B is the amplitude. For the first order approximation, where the final shape of the glass sheet is a sinusoidal function of x and y of a wavelength equal to twice the length and width of the mandrel, m and n are equal to 1.

The gap thickness in the top area labeled 1 and the lower area labeled 2 is given by

$$h_1 = h_o - B \sin \frac{\pi x}{L} \sin \frac{\pi y}{W}, \tag{3.66}$$

and

$$h_2 = h_o + B \sin \frac{\pi x}{L} \sin \frac{\pi y}{W}, \tag{3.67}$$

where h_o is the nominal gap thickness and is equal on both sides of the glass sheet, and h_1 and h_2 are the gap size in areas 1 and 2. Replacing these values of the gap height for h in Equation 3.29, differentiating with respect to x and y and non-dimensionalizing, the resulting equations governing the flow in the top and lower gaps are

$$M_1 \frac{\partial^2 \tilde{p}}{\partial \tilde{x}^2} + R_1 \frac{\partial \tilde{p}}{\partial \tilde{x}} + S_1 \frac{\partial^2 \tilde{p}}{\partial \tilde{y}^2} + Q_1 \frac{\partial \tilde{p}}{\partial \tilde{y}} = \left(\frac{\partial \tilde{p'}}{\partial \tilde{z}} \right)_{\tilde{z}=1}, \tag{3.68}$$

and

$$M_2 \frac{\partial^2 \tilde{p}}{\partial \tilde{x}^2} + R_2 \frac{\partial \tilde{p}}{\partial \tilde{x}} + S_2 \frac{\partial^2 \tilde{p}}{\partial \tilde{y}^2} + Q_2 \frac{\partial \tilde{p}}{\partial \tilde{y}} = \left(\frac{\partial \tilde{p'}}{\partial \tilde{z}} \right)_{\tilde{z}=1}, \tag{3.69}$$

where

$$M_1 = \frac{H}{12 k_z L^2} (h_o - B \sin \pi \tilde{x} \sin \pi \tilde{y}) \left((h_o - B \sin \pi \tilde{x} \sin \pi \tilde{y})^2 + 6 k_x \right), \tag{3.70}$$

$$R_1 = -\frac{\pi H B}{4 k_z L^2} (\cos \pi \tilde{x} \sin \pi \tilde{y} \left((h_o - B \sin \pi \tilde{x} \sin \pi \tilde{y})^2 + 2 k_x \right), \tag{3.71}$$

$$S_1 = \frac{H}{12 k_z W^2} (h_o - B \sin \pi \tilde{x} \sin \pi \tilde{y}) \left((h_o - B \sin \pi \tilde{x} \sin \pi \tilde{y})^2 + 6 k_y \right), \tag{3.72}$$

$$Q_1 = -\frac{\pi H B}{4 k_z W^2} (\sin \pi \tilde{x} \cos \pi \tilde{y} \left((h_o - B \sin \pi \tilde{x} \sin \pi \tilde{y})^2 + 2 k_y \right), \tag{3.73}$$

$$M_2 = \frac{H}{12 k_z L^2} (h_o + B \sin \pi \tilde{x} \sin \pi \tilde{y}) \left((h_o + B \sin \pi \tilde{x} \sin \pi \tilde{y})^2 + 6 k_x \right), \tag{3.74}$$

$$R_2 = \frac{\pi HB}{4k_z L^2}(\cos\pi\tilde{x}\sin\pi\tilde{y}\left((h_o + B\sin\pi\tilde{x}\sin\pi\tilde{y})^2 + 2k_x\right), \tag{3.75}$$

$$S_2 = \frac{H}{12k_z W^2}(h_o + B\sin\pi\tilde{x}\sin\pi\tilde{y})\left((h_o + B\sin\pi\tilde{x}\sin\pi\tilde{y})^2 + 6k_y\right), \tag{3.76}$$

$$Q_2 = \frac{\pi HB}{4k_z W^2}(\sin\pi\tilde{x}\cos\pi\tilde{y}\left((h_o + B\sin\pi\tilde{x}\sin\pi\tilde{y})^2 + 2k_y\right). \tag{3.77}$$

It should be noted that the flow equations inside the porous mandrels follow the same equations provided in Section 3.3.1. With the new equations for flow in the gap between the mandrel and the glass sheet, the finite difference method can be utilized again to perform a numerical analysis and find an equilibrium position for the glass sheet, such that the difference in pressure between areas 1 and 2 is zero for a given ΔP. The unknown in these equations is the amplitude B, which represents the deformation of the glass sheet. Figure 3-20 shows the relationship between the amplitude of the bow of the glass sheet B versus the pressure difference ΔP for a nominal gap, h_o, of 12.7 μm (Left) and 50 μm (Right). The nominal pressure used for the modeling is 0.3 psi, which is the highest pressure value anticipated during the experiment. B in this case represents the bow of a glass sheet as a result of a pressure difference between the two plenums feeding the two mandrels.

As can be seen from Figure 3-20, the larger gap of 50 μm can tolerate larger errors in the supply pressure than the smaller gap of 12.7 μm. Thus the advantages of using a larger air gap are the smaller forces acting on the glass sheet, the additional space to minimize particulate effects and the ability to accommodate pressure differentials without having the glass touch the ceramic mandrel.

3.5 Effect of Mandrel Surface Errors on Slumped Glass

In order to estimate the effect of the shape of the mandrels on the final result of the slumped glass, the flow analysis inside the gap is modified to incorporate surface

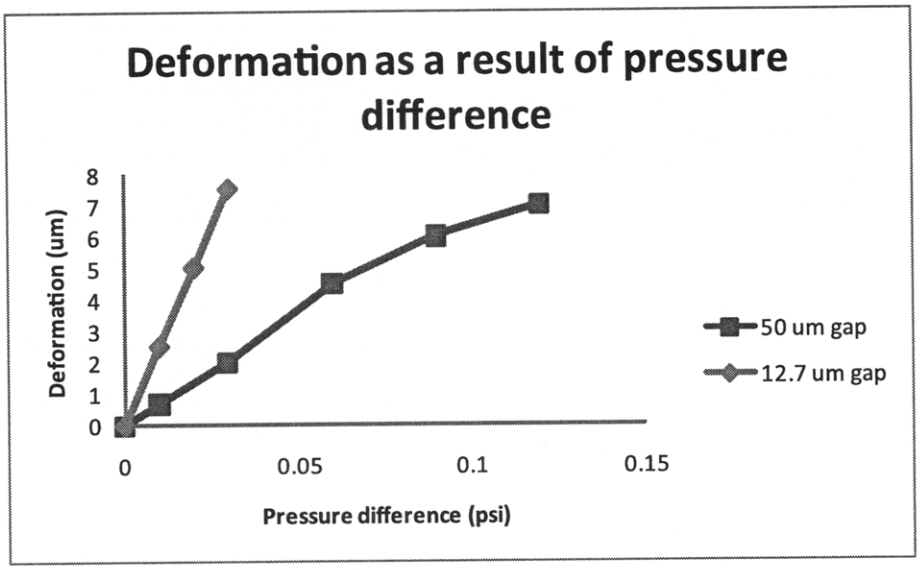

Figure 3-20: Deformation of a fully viscous glass sheet as a result of a pressure difference in the two plenums feeding the porous mandrels. Data shown is for two nominal gaps: 12.7 μm and 50 μm.

irregularities. For the purpose of simplification, only one mandrel is assumed to have a deformed surface compared to the second flat mandrel. This is shown in Figure 3-21 for the two integers $m = 1$ and $m = 2$. To simplify the problem, the deformed mandrel is assumed to have a sinusoidal shape of $A \sin \frac{m\pi x}{L}$ with amplitude A over the mandrel length L along the x direction only. The glass sheet would have a surface of $B \sin \frac{m\pi x}{L}$ with amplitude B. The ratio of B to A needs to be calculated. The gap height in the top area labeled 1 and the lower area labeled 2 is given by

$$h_1 = h_o - B \sin \frac{m\pi x}{L}, \tag{3.78}$$

and

$$h_2 = h_o - (A - B) \sin \frac{m\pi x}{L}, \tag{3.79}$$

where h_o is the nominal gap height and is equal on both sides of the glass sheet, and h_1 and h_2 are the gap size in areas 1 and 2. Replacing these values of the gap height for h in Equation 3.29, differentiating with respect to x and y and non-dimensionalizing,

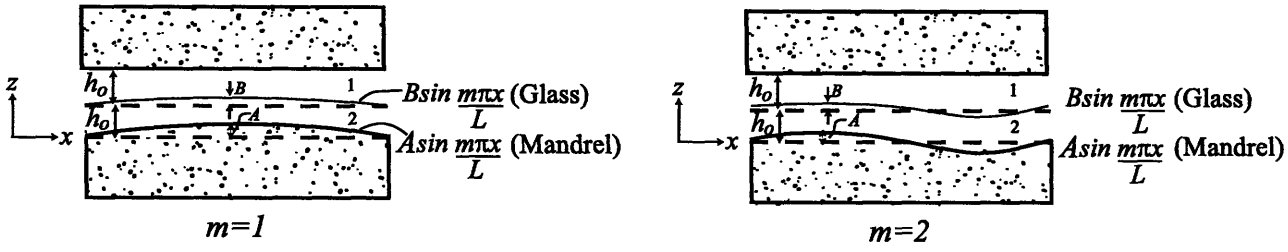

Figure 3-21: Effect of mandrel surface deformations on the shape of a glass sheet. The lower mandrel has a sinusoidal surface of amplitude A resulting in a sinusoidal surface of the glass sheet with amplitude B

the resulting equations governing the flow in the top and lower gaps are

$$M_3\frac{\partial^2\tilde{p}}{\partial\tilde{x}^2}+R_3\frac{\partial\tilde{p}}{\partial\tilde{x}}+S_3\frac{\partial^2\tilde{p}}{\partial\tilde{y}^2}=\left(\frac{\partial\tilde{p'}}{\partial\tilde{z}}\right)_{\tilde{z}=1}, \tag{3.80}$$

and

$$M_4\frac{\partial^2\tilde{p}}{\partial\tilde{x}^2}+R_4\frac{\partial\tilde{p}}{\partial\tilde{x}}+S_4\frac{\partial^2\tilde{p}}{\partial\tilde{y}^2}=\left(\frac{\partial\tilde{p'}}{\partial\tilde{z}}\right)_{\tilde{z}=1}, \tag{3.81}$$

where

$$M_3=\frac{H}{12k_zL^2}(h_o-B\sin m\pi\tilde{x})\left((h_o-B\sin m\pi\tilde{x}L)^2+6k_x\right), \tag{3.82}$$

$$R_3=-\frac{m\pi HB}{4k_zL^2}(\cos m\pi\tilde{x}\left((h_o-B\sin m\pi\tilde{x})^2+2k_x\right), \tag{3.83}$$

$$S_3=\frac{H}{12k_zW^2}(h_o-B\sin m\pi\tilde{x})\left((h_o-B\sin m\pi\tilde{x})^2+6k_y\right), \tag{3.84}$$

$$M_4=\frac{H}{12k_zL^2}(h_o-(A-B)\sin m\pi\tilde{x})\left((h_o-(A-B)\sin m\pi\tilde{x})^2+6k_x\right), \tag{3.85}$$

$$R_4=\frac{m\pi H(A-B)}{4k_zL^2}(\cos m\pi\tilde{x}\left((h_o-(A-B)\sin m\pi\tilde{x})^2+2k_x\right), \tag{3.86}$$

$$S_4 = \frac{H}{12k_z W^2}(h_o - (A-B)\sin m\pi\tilde{x})\left((h_o - (A-B)\sin m\pi\tilde{x})^2 + 6k_y\right), \quad (3.87)$$

With the new equations for flow in the gap between the mandrel and the glass sheet, the finite difference method can be utilized again to perform a numerical analysis and find an equilibrium position for the glass sheet, at which point the pressure on one of its sides is equal to the pressure on the opposite side. For the different values of the integer m representing low-mid spatial frequencies on the surface of the mandrel, the ratio $\frac{B}{A}$ is found to be 0.5, which is anticipated, since the glass sheet finds equilibrium at points that are equidistant from both mandrels.

3.6 Conclusion

Different strategies for shaping hot glass utilizing forces from air are presented and analyzed. There are many advantages for using air at high temperatures. It provides a viscous lubricating layer that shapes glass sheets without distorting their surface and absorbs any particulates that might be trapped between the sheets and the flat mandrel during the shaping process. Such particulates have the tendency to cause indentations in the surface of the glass in its soft state. The layer of air also protects the surface of glass from touching other surfaces while it is formed.

Having considered and analyzed different options for shaping glass sheets with air, experimental testing is followed to better understand the limitations of the concepts. The first concepts tried are the ones approaching the glass sheet on one side only, which are the slumping on a single porous mandrel and slumping on a grooved porous mandrel. This is because it is easier to manufacture one set of parts, where no alignment to one another is necessary, as opposed to manufacturing and aligning two symmetric components and finding ways to assemble them. If the need to slump between two mandrels arises, the vertical configuration is followed to reduce gravity induced errors.

Chapter 4

Experimental Procedures

Porous materials used in air bearing applications have millions of micron sized pores through which pressurized air flows to reach the surface of the bearing and carry a load. These pores ensure a relatively uniform pressure across the bearing area.

As shown in the previous chapter, the pressure distribution in the gap between the bearing surface and the carried load depends on the supply air pressure and the size of the gap between the load and the bearing surface. The pressure at the center of the bearing area is close to the supply pressure, yet the edges of the bearing are at atmospheric pressure. As the gap increases between the load and the bearing, the flow resistance decreases, and thus the uniformity of the pressure profile in the gap decreases.

The search for porous materials able to withstand high temperatures without creeping began with companies that design and manufacture air bearings for load carrying applications. Typical materials used by *NewWay Air Bearings* and *Nelson Air*, two of the leading vendors of air bearings, are graphite, bronze and alumina. Silicon carbide, though not commonly used by these two manufacturers, is also available in porous form for many biological and filtering applications. Table 4.1 summarizes some properties of these materials in their pore-free state.

Bronze creeps at slumping temperatures >500°C, since creep initiates at temperatures between $0.3T_M$ and $0.5T_M$, where T_M is the melting temperature of a material [50]. After discussing options with *NewWay Air Bearings*, alumina plates have

Material	**Young's modulus**	**Thermal conductivity**	**CTE**	**Melting Point**
	GPa	W/mK	10^{-6}/°C	°C
SiC	455	155	4.5	2730
Al_2O_3 (96%)	300	24	7.4	2054
Al_2O_3 (99.7%)	375	28	8.1	2054
Al_2O_3:Si	320	1.26	3.6	1790
Graphite	4.8	24	0.6-4.3	3650
Bronze*	41-125	33-208	17	762-1050

*Bronze material properties vary with percentage composition of constituent metals.

Table 4.1: Properties of different materials that can be used as porous compensation media in air bearing applications

been chosen for the first set of experiments over graphite, since the former is harder than the latter and has better scratch and surface damage resistance. Two plates have been purchased at the price of $1,000 per plate. The vendor claims the plates are made of alumina, which is typically white or ivory, whereas the actual plates are grey. This indicates the presence of silicates in the plates as well. The vendor also claims the plate is made of sub-micron sized pores with a surface flatness of one micron peak-to-valley (P-V). Unfortunately, the actual material properties of the ceramic plates purchased from *Newway Air Bearings* have not been made available by the vendor, and thus the properties of 96% alumina are used in estimating stresses and deformations of the ceramic plates.

4.1 Slumping on Flat Porous Ceramic Plates

The first attempt at understanding how the presence of a thin layer of air can eliminate the effects of dust particles and impurities entrapped between the glass sheet and the mandrel involves slumping on a flat porous ceramic, as shown in Figure 3-6. The glass is constrained in the lateral direction by using flexures. The flexures stop the

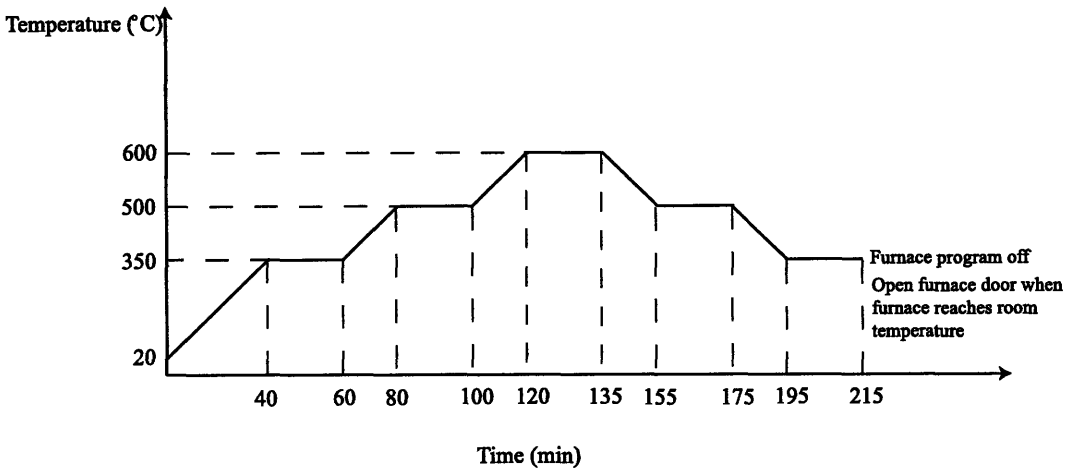

Figure 4-1: The temperature profile for slumping a 0.4 mm thick Schott D-263 glass on a pressurized porous rectangular ceramic.

glass from sliding away from the bearing surface. Only one side of the optic is in contact with the flexures at any given time to avoid overconstraining the glass sheet.

The slumping time-temperature profile followed is shown in Figure 4-1. The temperature is held at both 350°C and 500°C to allow for the furnace environment to reach thermal equilibrium throughout the experiment. The slumping temperature is maintained for about 15 minutes, which is longer than the relaxation time calculated previously in Section 2.1.4. This profile is close to what others in the field of slumping follow [30]; however, the actual slumping profile will be fine tuned as the experimentation continues throughout the chapter.

After this experiment, the glass sheet, which has an initial bow of a few hundred microns, is left with a final bow of approximately a millimeter P-V. This is anticipated, since the pressure profile of the air in the gap between the glass and the ceramic has a dome-shape, as shown in Figure 3-8. Although the resulting surface warp is rather large, no evidence of high-spatial frequency errors or dimples due to dust particles is seen on the surface of the glass. In order to improve the slumping-on-air method to obtain flat glass, the first requirement is to minimize the pressure gradient seen in the air gap to reduce the resulting bow on the glass. Looking back at the concepts that have been considered in Chapter 3, a possible way of achieving this is through

the machining of grooves on the porous ceramic surface.

4.2 Slumping on Ceramic with Grooves

As shown in Section 3.3.2, the presence of grooves or channels on the surface of the ceramic mandrel reduces the pressure gradient in the air gap. This also results in a loss in the load-carrying capacity of pressurized bearings. Since the weight of the glass sheet is very small (0.1-0.14 N), and the area of the sheet is large (100 mm $\times$ 140 mm), the reduced pressure is sufficient to lift the glass.

4.2.1 Design Criteria

Several processes have been considered for the machining of grooves. Laser beam machining ablates material using a laser. Electron beam machining uses a focused stream of electrons to melt and vaporize material. Both these processes have tight tolerances but are slow and very expensive. Ultrasonic machining is another option which is typically used on hard and brittle materials, however, in this case it would be expensive to manufacture the counterpart machining tool needed. Wire-electric-discharge machining, which is ideal when machining slots, can not be used on non-conductive materials. The easiest and most cost-effective method that can be followed on these porous ceramics is diamond die-sawing, where a diamond saw cuts through the material. This process does not have the tight tolerances that the aforementioned processes have, but it is relatively fast and inexpensive.

The thinnest blade that could be used in this case is 0.012" or 0.3 mm thick. *Machined Ceramics Inc.*, a precision ceramic machining company located in Bowling Green, KY, has been selected to machine the parts. A small sample was sent out to them beforehand to study the behavior of porous alumina during the diamond-sawing process. It was noted that the 0.3-mm thick blade could go as deep as 1 mm before the blade starts wobbling and introduces errors in the machined groove cross-section. It was also noted that the closest spacing between the grooves can be 0.018" or 0.457 mm without the ceramic fracturing and chipping off in the areas between

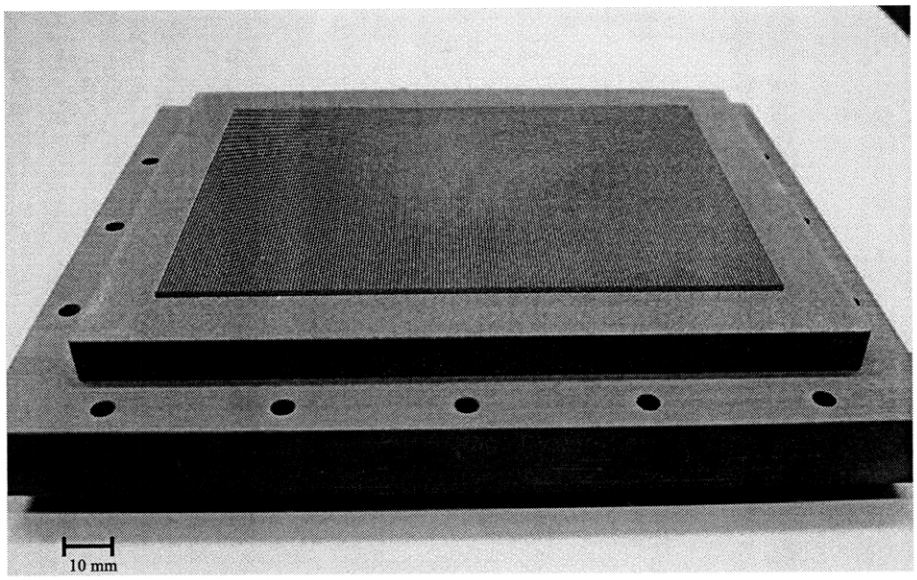

Figure 4-2: A total of 182 grooves, 0.3 mm wide and 1 mm deep, machined on a porous alumina ceramic plate

the grooves. This has been successful when machining grooves in one direction only. When attempting to machine grooves orthogonal to the first set to have a 2D layout, the ceramic surface fractured and the groove pattern was lost. It is hypothesized that the more grooves there are on the ceramic surface, the less of a pressure gradient there would be in the air gap, and thus, the smaller the resulting bow in the slumping glass. Given the brittle nature of the alumina ceramic, it was decided to have grooves in only one direction. The first attempts of slumping glass have been on an area of 140 mm $\times$ 100 mm. A total of 182 grooves has been machined into the porous alumina plate, as shown in Figure 4-2. A closer top view of the ceramic reveals material chipping in some areas after machining, as shown in Figure 4-3.

With the porous plate ready, a housing is required that would form a plenum for the porous plate and constrain the porous plate as air flows through it. The first thing to consider is its material. Aluminum can not be considered for this application, since components will see temperatures as high as 600°C, which is close to the melting temperature of aluminum. Stainless steel has a coefficient of thermal expansion (CTE) twice as large as that of alumina and a thermal diffusivity three

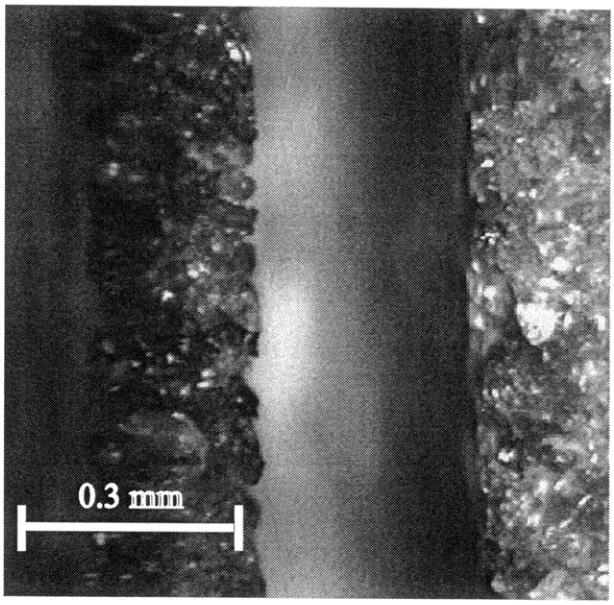

Figure 4-3: Top view of machined grooves on porous ceramic showing chipping in some areas

times that of the ceramic. This introduces thermal stresses both during transient and steady states, which is an undesired phenomenon into the test setup. Most metals have similar characteristics. The candidates for the housing should be materials that have similar thermal properties as the porous ceramic and that can be fabricated within the constraints of the scope of this project. Alumina silicate plates sold by *McMaster-CARR* have a porosity of 1-2% and can be machined using carbide tools. Since *NewWay's* porous alumina plate is grey in color, it is believed to contain silicates as well and be a close match to the pore-free alumina silicate ordered from *McMaster-CARR* for the housing. The machining has been done in the MIT *Central Machine Shop* to form a housing and a top cover, as shown in Figure 4-4.

The porous part is placed on the housing plate, and the cover put on top. The mating surfaces of the cover and the housing are ground. A series of bolts are used to connect the cover with the housing such that the cone of influence of every bolt overlaps with the cone of the adjacent bolt. This ensures that the two surfaces mate well enough to seal the plenum and avoid uncontrolled leakages. The bolts in this design are made of titanium, which has a comparable thermal diffusivity to that

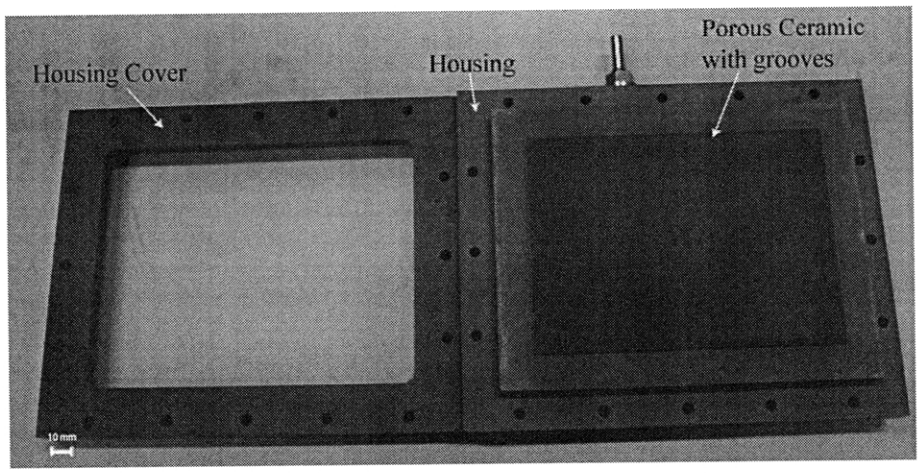

Figure 4-4: A total of 182 grooves, 0.3 mm wide and 1 mm deep, machined on a porous alumina ceramic plate

of stainless steel, but a lower CTE, which is comparable to that of alumina. This minimizes the difference in overall expansion of the bolts and the ceramic housing at steady state. Stainless steel belleville washers are used to reduce joint loosening during the heating cycle.

4.2.2 Performance Assessment

With the hardware ready, a first set of tests was performed to see what the shape of the glass will be. A *Lindberg/Blue* furnace was purchased with an interior chamber size of 15" × 11" × 13" and a maximum temperature of 1,200°C. Approximately 4 m of tubing was bent and put inside the furnace to ensure that the air transferred from the outside of the furnace to the inside of the plenum is at the required temperature.

A glass sheet was placed on the grooved ceramic, and the pressure turned on. The pressure P_1 outside the furnace is at 0.8 psig. The pressure inside the plenum is measured at room temperature, as shown in Figure 4-5, and is P_1'=0.075 psig. This loss in pressure is the result of the many elbows and 180° turns of the bent tubes. At this point in the experiment, no pressure sensors were found to measure the pressure before entering the plenum with accuracy and at high temperatures. It was noticed that as the temperature of the air increases from room temperature to 600°C, the

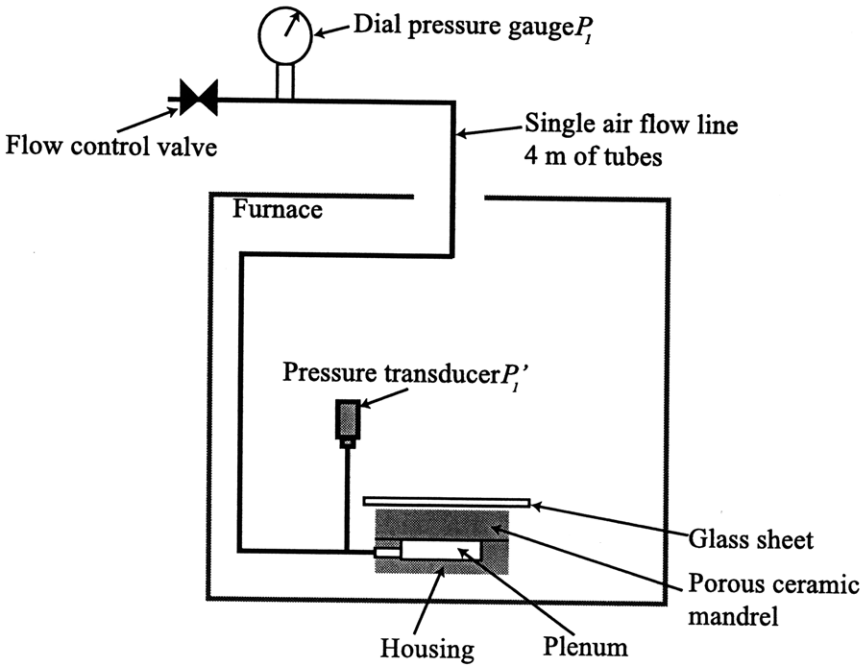

Figure 4-5: Measuring the pressure P_1' inside the plenum at room temperature by connecting a pressure transducer, Baratron 740B21TFE3GA from *MKS Instruments, Inc.*, to the air flow line right before it enters the plenum. Any fluctuations in the plenum pressure are registered on this transducer. The pressure outside the furnace, P_1, is measured with a dial gauge.

outside pressure P_1 increases by a factor of 4. This is due to the fact that the viscosity of air increases, and thus resistance to flow increases. At a constant flow rate, the overall pressure in the system increases. Thus, assuming that the pressure inside the plenum P_1' increases by a factor of 4 as well, P_1' becomes 0.3 psig.

The first set of results showed a glass bowed on the order of magnitude of $\sim$ 1 mm. Unfortunately, this is beyond the measurement range of the metrology tool used for glass sheets, thus at this point, there was no exact value of the peak-to-valley seen on the glass.

To try and understand what might be causing this bow, a few hypotheses were developed. Some of the causes might be:

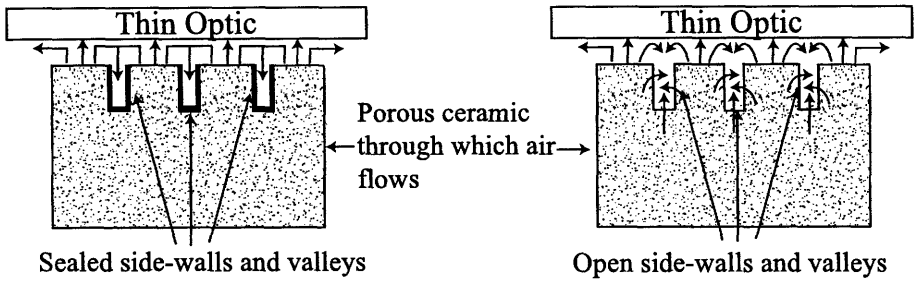

Figure 4-6: *(Left)* Sealed side-walls and valleys of grooves create a channel through which air from the peaks escapes. *(Right)* Open side-walls and valleys result in air escaping through them in addition to the peaks.

1. the fully constrained ceramic is bowing due to the pressure in the plenum and this bow is being imprinted on the glass sheet,

2. there is a temperature gradient across the thickness of the glass, since one surface is exposed to flowing air while the other is exposed to the furnace ambient conditions resulting in thermal stresses,

3. the side walls and valleys of the grooves are not sealed, allowing for air to escape from the porous ceramic out into the grooves, and not allowing the grooves to act as escape channels, as shown in Figure 4-6. This could result in a higher pressure build-up in the air gap than anticipated,

4. the pressure gradient that is anticipated along the length of the porous mandrel is still higher than what can be tolerated,

5. the free edges of the glass sheet are not supported by the viscous forces from the air, causing the edges to slump and touch the mandrel.

To understand these potential sources of error, each point is studied separately.

Bow of Ceramic due to Pressure To start with the bow of the ceramic due to the pressure on one side, the ceramic is modeled as a fully constrained plate with a uniformly distributed load P_L on one face. The weight of the ceramic is acting in the opposite direction as the air pressure load P_L, as shown in Figure 4-7. The maximum deformation of the ceramic plate δ_{max} is

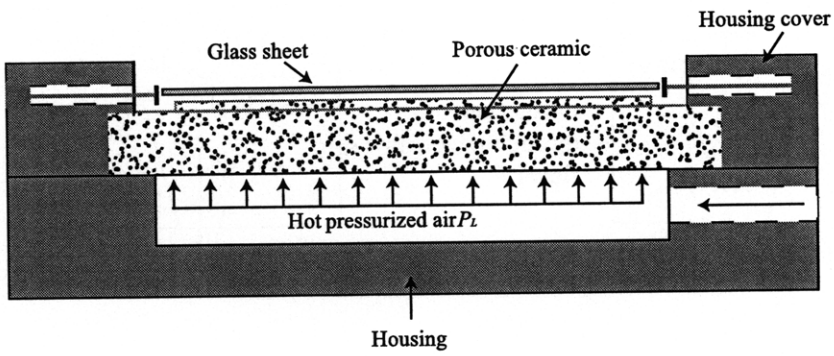

Figure 4-7: Porous ceramic mandrel modeled as a clamped plate with a uniform air pressure force acting on the lower side.

$$\delta_{max} = \frac{0.0226qb^4}{Et^3}, \tag{4.1}$$

where 0.0226 is a coefficient of bending from Roark's formulas for Stress and Strain [51] for a fully constrained plate with edge ratio of 1.4, q is the force per unit area acting on the plate, which equals the air pressure load minus the ceramic weight, b=100 mm is the plate width, E is the Young's modulus and t=0.4 mm is the plate thickness. The effective plate Young's modulus is calculated from Sections 3.2.2 and 3.2.3. The temperature of the experiment is at 600°C. The porosity of the part can be determined from the density, which is calculated using the Archimedes method to be 2.68 g/cm^3. The density of pore-free alumina is 3.7 g/cm^3. The resulting porosity, P_r, is calculated from Equation 3.16 to be 30%. This represents f_β in Equation 3.13, with $f_\alpha = 1 - f_\beta$. The Young's modulus of pore-free alumina is 300 GPa. By using Equations 3.13 through 3.18, the Young's modulus for a 30% porous alumina is found to be 147 GPa.

By taking the effect of temperature into account as well and using Equations 3.3 and 3.4, the effective Young's modulus of a 30% porous alumina at 600°C is 135 GPa.

The resulting maximum deformation of the porous ceramic due to the presence of pressurized air in the plenum at high temperature is ~15 nm, which is much smaller than the bow seen on the glass and thus does not account for it.

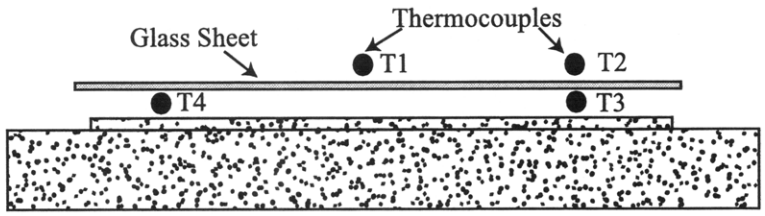

Figure 4-8: Location of four thermocouples placed above and below a glass sheet as it slumps. The diagram only shows the grooved porous ceramic plate and the glass sheet for clarity.

Bow of Glass due to a Temperature Gradient If the temperature on each side of the glass sheet is different as it is cooling and solidifying, the glass would bow. This would happen if the air going through the porous plate and against the glass sheet is at a different temperature from the furnace environment on top of the glass. After the glass reaches the slumping temperature, it is slowly cooled back to room temperature. During the cooling process, the glass sheet goes through a transformation temperature at which point it changes from a fluid to a solid. If one surface reaches this temperature before the other because of the temperature gradient across the sheet thickness, that surface solidifies first, storing the bow that the sheet had as it was cooling. As the temperature further drops, the other surface solidifies and the final shape of the solid glass has the thermal strains that were stored into the sheet during solidification.

To test this hypothesis, two thermocouples were placed above the glass, one at the center of the glass and one near its edge during slumping. Another pair of thermocouples were placed underneath the glass. The configuration is shown in Figure 4-8. Readings were taken throughout the experiment, where the temperature is raised from room temperature to 600°C. The temperature variation across the thickness of the glass was found to be on the order of 2°C, with the top of the glass being at the higher temperature.

A first order calculation is performed to see if this will cause the millimeter size bow seen on the glass. When a plate is at a temperature T on one face and a

temperature of $T + \Delta T$ on the other face, with a linear temperature gradient across its thickness, the resulting radius of curvature, R, of the bowed plate is given by [51]

$$R = \frac{t}{\Delta T \alpha}, \tag{4.2}$$

where t is the plate thickness and α is the material CTE. For a 0.4 mm thick D-263 glass sheet, the resulting radius of curvature is 37.746 m. Figure 4-9 shows a first order geometry of the deformed plate. The maximum deformation δ is at the center. From this figure, the length M is calculated by $M^2 = R^2 - (L/2)^2$, and the deformation δ is calculated by $\delta = R - M$. For a glass length L of 100 mm, the resulting deformation is 40 μm. This is rather significant for a 2°C temperature gradient across the glass thickness. Although alone this does not explain the much larger bow seen on the glass, it tells us that the temperature of the experiment must be monitored closely, and the ramp-up and ramp-down intervals must be long enough to ensure that the temperature of the air lifting the glass and shaping it is the same as the temperature of the surrounding air above the glass. If a maximum deformation of 0.1 μm is desired as a result of a temperature gradient during the experiment, then by following the same analysis, the maximum temperature gradient tolerated across the glass sheet is ~ 0.005°C. This is very difficult to achieve in commercially available furnaces, which typically have a temperature gradient of up to 10°C across their height. Thus, a glass sheet slumped on one porous mandrel and held horizontally inside a furnace will always have a temperature gradient across its thickness; however, if a glass sheet is constrained vertically, the temperature gradient will be along the length of the sheet and not its thickness. If a glass sheet is slumped between two porous mandrels, then the temperature gradient can be significantly reduced due to the symmetric air flow along the two surfaces of the glass.

Bow of Glass due to Leakage of Air through Side-Walls and Valleys of Grooves When the grooves are machined into the part, the overall surface area where air escapes at the top of the ceramic increases due to the presence of the exposed side-walls of the grooves, as shown in Figure 4-6. This might increase the

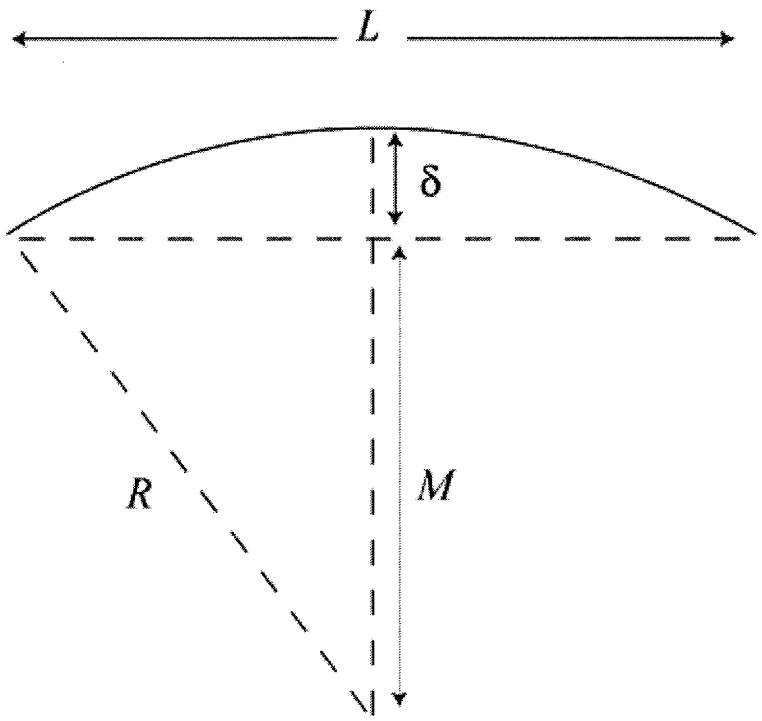

Figure 4-9: Deformation of a glass sheet due to a temperature gradient across its thickness

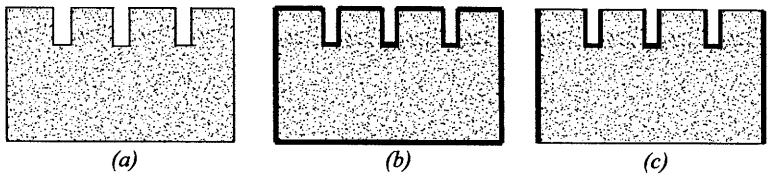

Figure 4-10: *(a)* A grooved porous ceramic plate. *(b)* Grooved ceramic plate coated to seal all edges. *(c)* Top and bottom surfaces of the porous ceramic are ground to remove the coating and expose these surfaces. The side-walls and valleys of grooves are sealed.

resistance to flow of air from the peak areas where the glass is being shaped and thus result in a pressure gradient. To reduce this effect, the pores of the groove side-walls and valleys must be sealed.

Chemical vapor deposition (CVD) is a process used for coating deep and narrow grooves. The coating material is in vapor state and known as the precursor. It is mixed with an inert gas and introduced in the chamber where the workpiece is at hot temperatures. The precursor molucules diffuse and get adsorbed at the surface of the workpiece, releasing molecular biproducts that are carried away from the chamber [52].

Since slumping covers a wide temperature range, it is important to choose a coating material that has similar thermal characteristics as the alumina ceramic plate to avoid cracks and peeling of the coating. The idea is to coat all surfaces of the ceramic, including the side-walls and valleys of the grooves, and then have a final grinding process of the top surface to re-expose the porous structure and have air flow out onto the glass, as shown in Figure 4-10.

A company called *Richter Precision* agreed to perform the coating process at a reasonable price of $500 per plate (whereas other companies willing to try and coat deep trenches such as *Ultramet* have asked for $5,000 a plate). The *Titankote H5* recipe, which is typically used to coat tools, is 1 μm titanium nitride (TiN), 2-3 μm titanium carbonitride (TiCN) and 3-4 μm alumina Al_2O_3 [53]. The CVD process is done at 1,050°C, and the coating has a maximum working temperature of 850°C,

which is above the slumping temperature. To test this process on ceramics, a pore-free sample with a few grooves was sent out to the company to ensure that the coating covers the side-walls and valleys. The process was successful with a black coating covering the entire grooved ceramic plate, and thus the actual porous ceramic with 182 grooves was later sent out for coating. Unfortunately, the result on the porous part was not promising. The returned part had a dark brown color instead of the typical black.

Once coated, the ceramic plate was tested to see if it was actually sealed. The test was performed by blowing air through the ceramic plate while it is in water to see if any air bubbles are formed as air escapes any unsealed pores. No air bubbles were seen coming from the ceramic plate, and this guaranteed that the plate surface was properly sealed.

The next step was to grind the top and bottom surfaces of the ceramic to re-expose the surface pores, as shown in Figure 4-10*(c)*. The bottom surface is where air enters the part, and the top surface is where it exits the part to blow against the glass and shape it. The part was sent out to *NewWay Air Bearings* for grinding. After removing over 100 μm of material and not succeeding in exposing the pores, which have a light grey color, the part was sent back to MIT, still dark brown in color. The ceramic was placed in water again to see if bubbles form as air goes through the part, but no bubbles were seen. This indicated that the pores were still clogged. At this point, a cross-sectional view of the plate was needed to understand how deep the coating had penetrated.

The plate was sent to a ceramic machining facility, *Belanger Industrial Group, Inc.*, located in Poughkeepsie, NY. A cross-sectional cut was made near the edge of the plate, and the part was sent back for assessment. The cross-section revealed a uniform dark brown color through the thickness of the plate. The pores have been clogged throughout the plate. The coating company does not have any experience in coating porous parts and could not give any insight as to what may have gone wrong with the process.

A glazing process was attempted next as an alternative to CVD. Another sample

piece, having one groove was sent to *Elcon, Inc.* to apply a high-temperature glaze coating and seal all ceramic faces, including the groove. The part was returned with the glaze applied everywhere but inside the groove, simply because the viscous glaze material could not go through the groove, leaving the side-walls and valleys exposed. In order for the glaze to coat the walls of the grooves, they must be machined wider.

It is unclear whether leakage from the side-walls and valleys of the grooves is causing the additional bow on the glass after slumping. This work has revealed that sealing the side-walls and valleys of the deep, narrow grooves is going to challenge the state of the art, and be a costly endeavor. For this reason, a smaller, less expensive model is considered for testing.

A smaller model made of pore-free metal was designed. The slumping area on this model is 50 mm $\times$ 50 mm. The metal selected is stainless steel, since it withstands a temperature of 600°C and is relatively inexpensive compared to titanium and copper. The standard grooves that have been machined on the original ceramic plate would need to be machined on this smaller stainless steel model as well; however, the narrowest grooves that can be machined at the MIT facilities are 0.024" (0.61 mm) wide for a total of 20 such grooves with inherently sealed side-walls and valleys. Since the stainless steel plate is pore-free, the effect of porosity is replicated by machining a series of inlet holes and connecting channels to connect the holes on the surface, as shown in Figure 4-11. A total of 21 channels was machined parallel to the 20 grooves, each channel connecting 5 holes along its length on the surface of the plate. More holes per channel would provide a better pressure distribution along the channel; however, machining more holes in every channel raises the overall cost of machining. These channels are not open to the atmosphere; thus, air from the plenum exits the holes, flows through the channels to have a uniform distribution of pressure along the length of the channels and eventually finds its way out through the neighboring grooves that are open to the atmosphere, as shown in Figure 4-11.

A lower stainless steel plate is machined to mate with the part shown in Figure 4-11. The 3D model of the part is shown in Figure 4-12.

The machining was done at the *MIT Central Machine Shop*; however, in the

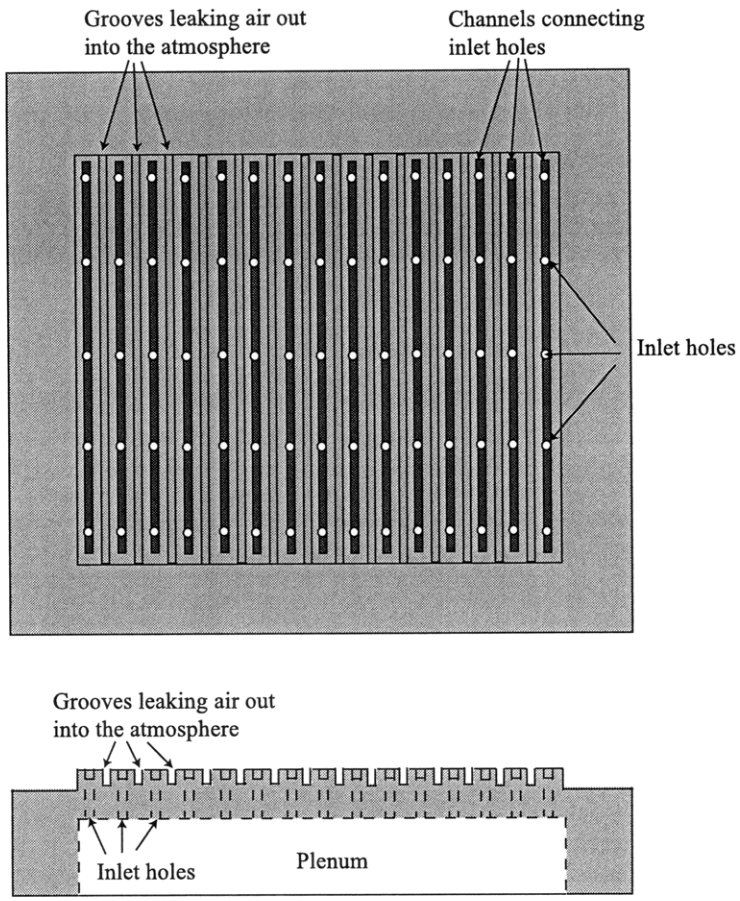

Figure 4-11: Smaller scale stainless steel part with slumping area of 50 mm $\times$ 50 mm with a set of grooves open to the atmosphere and a set of channels connecting the inlet holes together. Figure not to scale.

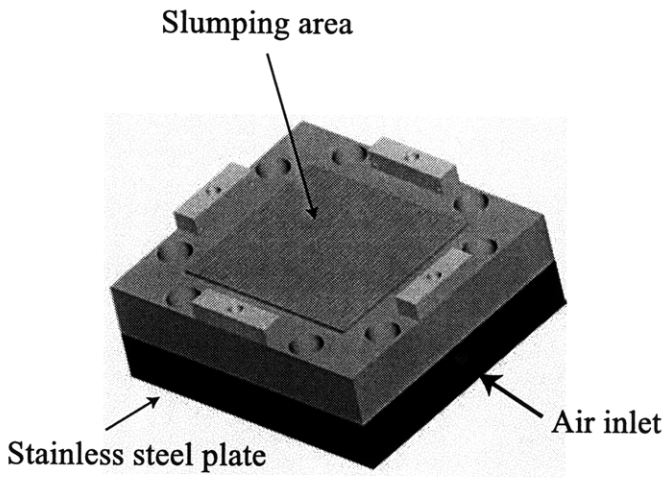

Figure 4-12: 3D model of small scale slumping apparatus with slumping area of 50 mm $\times$ 50 mm

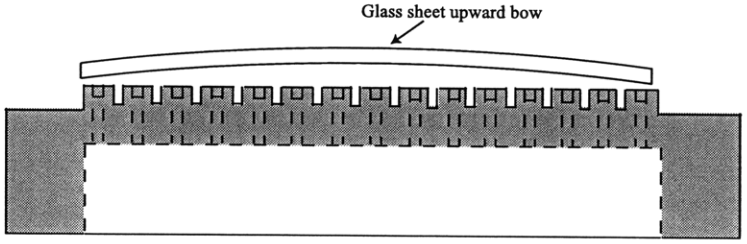

Figure 4-13: Glass sheet bows upwards after slumping on a grooved mandrel.

future, it would be faster and more cost-effective to actually have the grooves open to the atmosphere machined using wire-electric-discharge machining instead. With the smaller apparatus ready, the slumping test was run again on a 50 mm $\times$ 50 mm $\times$ 0.4 mm glass sheet. The glass sheet came out consistently bowed upwards, shown in Figure 4-13, as has been the case before using sealed grooves. Since the overall bow of the glass is beyond the metrology system's capability, only visual inspection could be done on the workpiece.

The conclusion after this work is that sealing the grooves, whose role is to help reduce the pressure build-up in the gap, does not significantly reduce the bow of the glass as it slumps on a thin layer of air.

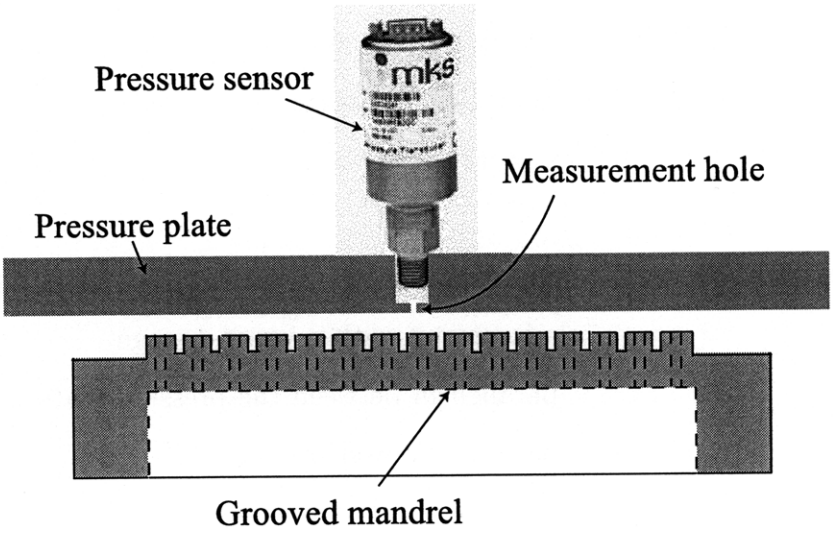

Figure 4-14: Pressure sensor mounted on a plate with a small hole to measure the pressure profile of the air in the gap. Figure not to scale.

Bow of Glass due to the Presence of a Small yet Significant Pressure Gradient The modeling done on a grooved porous ceramic plate anticipates a small pressure gradient, as is shown in Figure 3-13. This gradient could be the main cause for the bow of the glass sheet. To observe the actual gradient in the air gap, a fixture was designed to scan the slumping area of the smaller stainless steel, grooved mandrel with the help of a high precision pressure transducer.

The pressure transducer selected is a custom made 740 Baratron series capacitance manometer from *MKS Instruments, Inc.* with a pressure range of 20 Torr or 0.387 psi (2,666 Pa) and a resolution of 4×10^{-5} psi. In order to measure the pressure in the air gap, a plate was designed to mount the pressure sensor. A small diameter hole in the plate exposes the sensor to the pressure in the air gap, as shown in Figure 4-14. The diameter of the hole must be smaller than the groove width to resolve the pressure readings at the peaks and valleys. A diameter of 0.01" or 0.25 mm was chosen for this application.

The requirements and some parameters for designing the fixture that would measure the pressure profile in the air gap are summarized in Table 4.2.

In order to measure the entire surface of the grooved mandrel, linear stages are

Requirements	**Design Parameters**
2 DOF parallel to grooved surface	manual linear stages
	motorized linear stages
Controlled air gap size	cap gauge
	micrometer with a vertical stage
	parallelism between the pressure plate
	and the grooved surface
No air leakage	large enough plate to cover entire
	mandrel during the measurement process

Table 4.2: Requirements and design parameters for measuring pressure in the air gap between the grooved air bearing mandrel and a flat plate

required to move either the mandrel itself or the plate with the pressure sensor. Since the mandrel is connected to a pressure input line, it is chosen to have the pressure sensor plate move with respect to the mandrel.

Motorized linear stages are much more expensive than linear stages and have a longer range of motion; however *Newport* sells a set of manual linear stages with a range of motion of 50 mm with an angular error of < 150 μrad. The main disadvantages of these stages is their rather large size and heavy weight. Two such stages were purchased from *Newport* for motion in the x and y directions. A vertical linear stage with a range of motion of 5 mm was also used to vary the gap during the measurement whenever necessary. Although the vertical linear stage has a micrometer with a resolution of 2.5 μm, a capacitance gauge was used to yield a more accurate reading of the air gap. A schematic of the measurement set-up is shown in Figure 4-15.

With the configuration shown in Figure 4-15, the vertical stage was placed underneath the grooved mandrel to raise and lower it with respect to the pressure sensor. A capacitance gauge connected to the grooved mandrel and facing a stationary reference surface provided the vertical distance travelled by the vertical stage. The linear

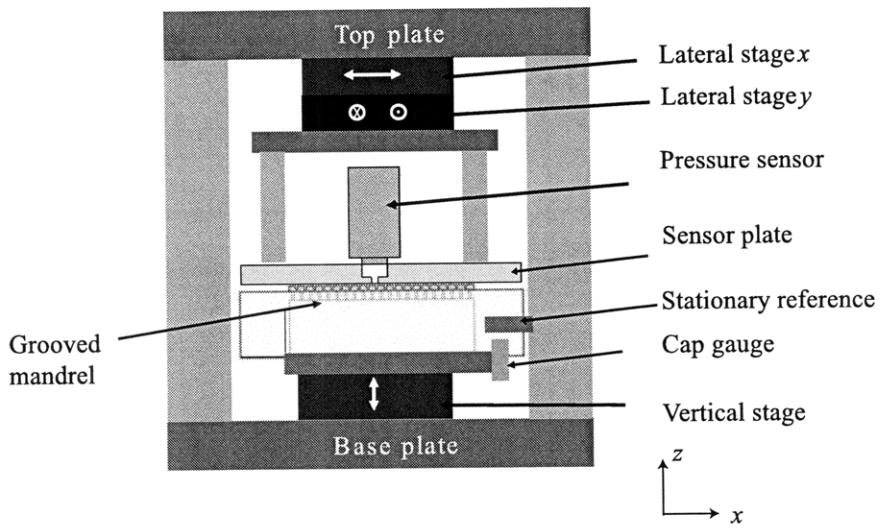

Figure 4-15: Schematic of measurement system with linear stages and pressure sensor to measure the pressure gradient in the air gap

x and y stages were stacked on top of each other from the top of the fixture to move the sensor plate laterally with respect to the grooved mandrel. The sensor plate, to which the pressure sensor is connected, was itself attached to the lateral linear stages by means of rods.

The most critical part in this set up is the parallelism between the sensor plate and the top surface of the grooved mandrel. Tilt between the two surfaces causes errors in the sensor reading due to gap size variation. The two surfaces were ground to a flatness of $\sim$20 μm at the MIT facilities. To ensure alignment between the two critical surfaces, the sensor plate was placed on top of the grooved surface at the start of the experiment, and the capacitance gauge reading was taken. The top of the sensor plate has cones, as shown in Figure 4-16. Parallelism between the sensor plate and the grooved mandrel is achieved by resting the former on the latter. The rods were then attached to the sensor plate by means of balls and retainers, as shown in Figure 4-17. A screw attaching the ball to the rod, as shown in Figure 4-18 was turned to change the elevation of the ball with respect to the sensor plate. This was done until contact was achieved between the ball and the cones on the sensor plate.

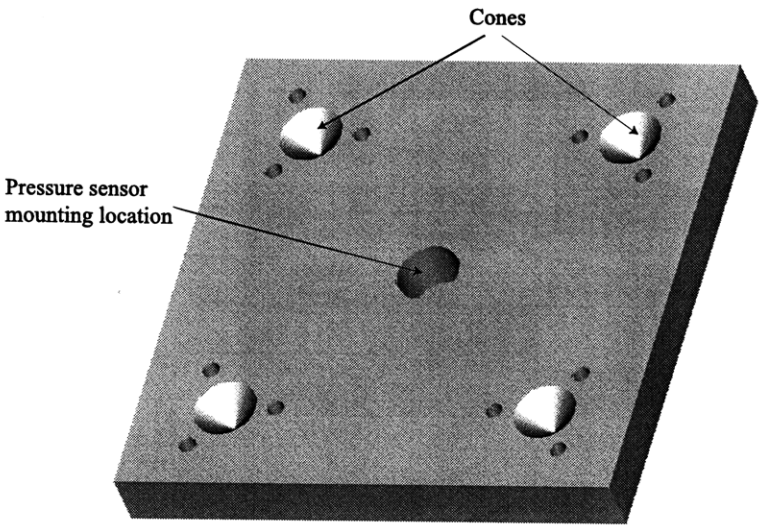

Figure 4-16: Plate on which pressure sensor is mounted to measure the pressure profile of air coming out of the grooved mandrel

Upon contact, the retainer, which itself has a cone cross-section and is loosely sitting on the ball was now connected to the sensor plate by means of screws. Thus, if the rods, and as a result the balls, are slightly slanted, as shown schematically in Figure 4-19, the contact line between the balls and the cones on the sensor plate remains unchanged, minimizing sensor plate angular errors once it is connected to the rods. Four sets of rods, retainers, balls and cones were used to connect the sensor plate to the linear stages at the top. This overconstrains the plate; however, it results in less sag of the plate as it is lifted off the grooved mandrel. The overall set-up is shown in Figure 4-17.

Once the sensor plate was connected to the lateral linear stages through the rods, the vertical stage was lowered moving the grooved mandrel away from the sensor plate and introducing a gap of controlled size between the two. The capacitance gauge also moves away from its reference surface thus registering the distance traveled.

An error budget was performed on the fixture to better understand the effect of

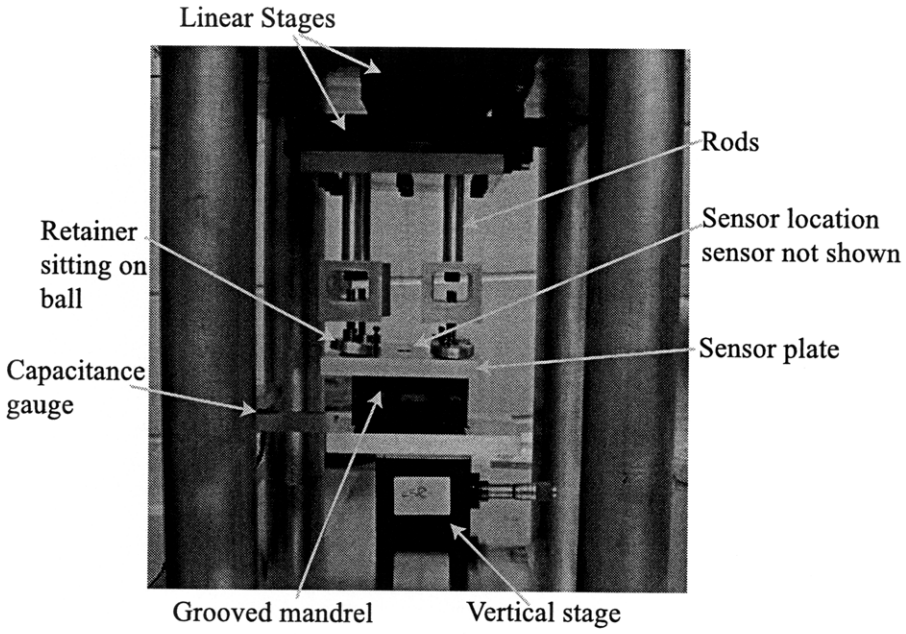

Figure 4-17: Set-up for measuring pressure gradient in air gap for a grooved mandrel

errors on the parallelism between the sensor plate and the grooved mandrel while the sensor plate was scanned across the length of the mandrel. The error budget reveals an angular error of 0.0003 rad between the two critical surfaces. This error is dominated by the wobble in the lateral linear stages across their range of motion.

Due to the symmetry of the small, grooved mandrel, only one-fourth of the area need be measured. This corresponds to a length of 1" or 25.4 mm, and thus the resulting gap variation due to the angular error across this length is approximately 8 μm. This is rather significant for very small gaps (<10 μm); however, the effect of the error decreases as the gap size increases at room temperature.

For a supply pressure of 0.3 psi (2,069 Pa) and a gap of $\sim$ 10 μm, the resulting pressure profile is plotted in Figure 4-20. It should be noted that the actual pressure measured along the area of the small metal mandrel is two orders of magnitude larger than what the model has predicted for a porous mandrel in Section 3.3.2, Figure 3-13. This is because the actual permeability of a stainless steel grooved mandrel with a finite number of holes blowing air at room temperature is much larger than

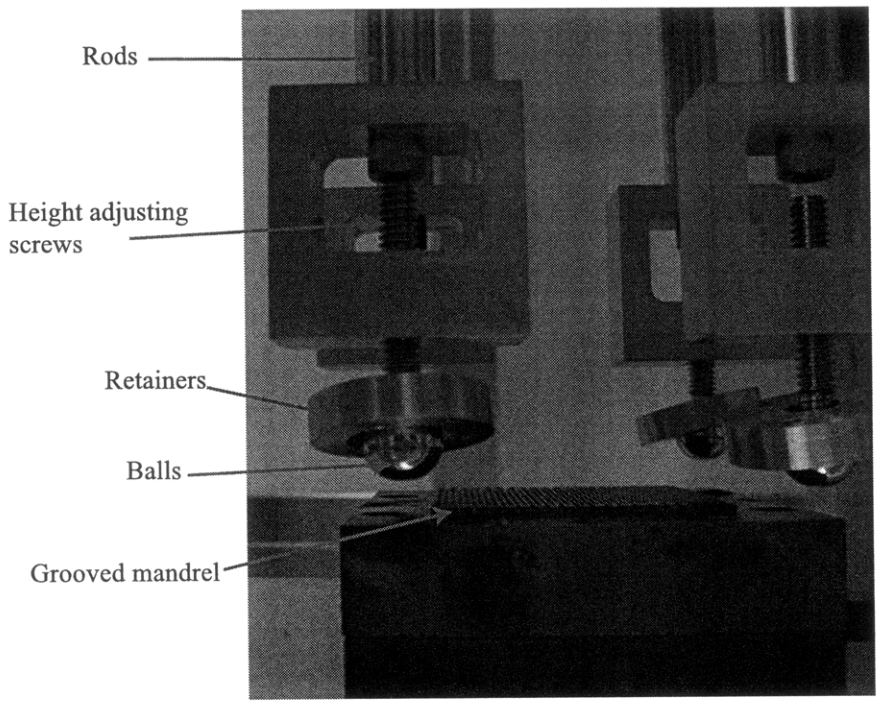

Figure 4-18: Balls and retainers used to connect rods to pressure sensor plate, which is not shown in the figure

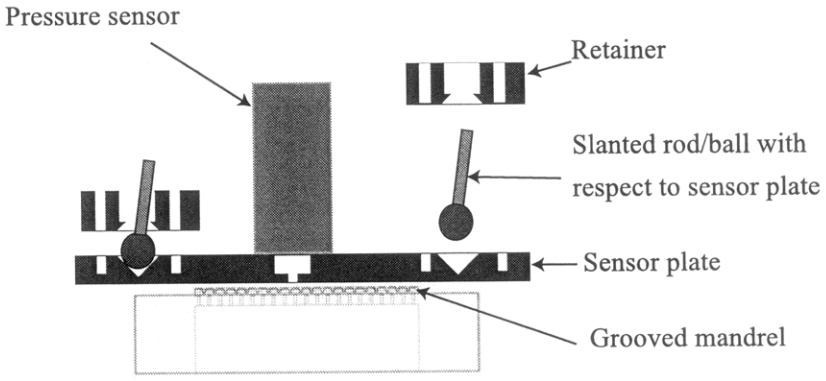

Figure 4-19: Sensor plate carrying rods slanted with respect to grooved mandrel. Angular error exaggerated for clarity

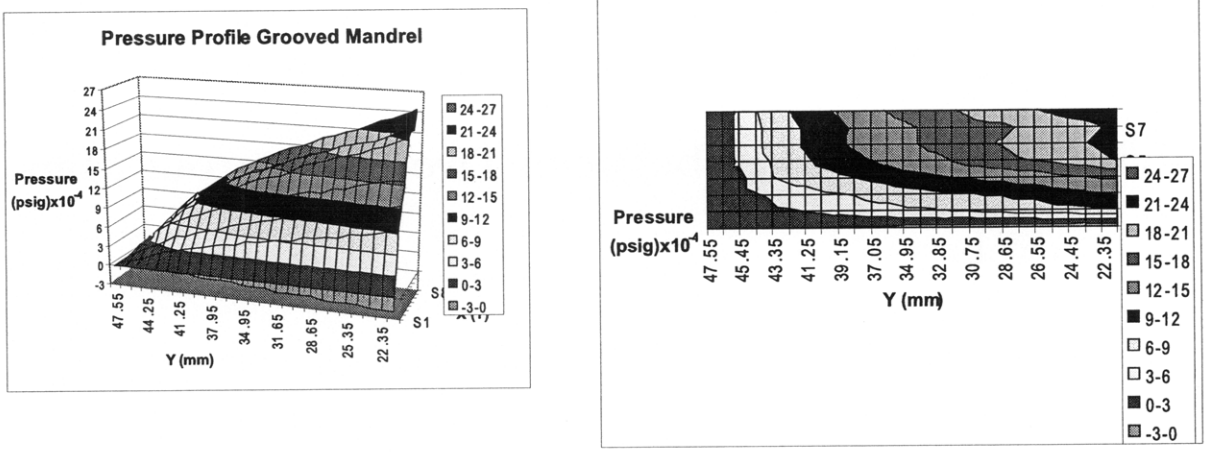

(a) *(b)*

Figure 4-20: *(a)* 3D profile of pressure in 10 μm air gap at a supply pressure of 0.3 psi. *(b)* Top view of pressure profile in the gap.

the permeability of a porous ceramic with millions of sub-micron sized holes blowing viscous air at 600°C. In other words, the resistance to flow through the stainless steel grooved mandrel is smaller, thus the pressure loss is smaller across its thickness.

Bow of Glass due to Falling Edges Since the pressure at the edges of the mandrel is atmospheric, there are no forces on the edges to carry the load of the optic. This is not a problem at room temperature, when the glass sheet is a rigid body, and the overall forces from the air pressure can carry its weight; however, as the glass softens, the unconstrained edges are free to fall and touch the mandrel. This automatically introduces a bow on the glass surface equal to the size of the air gap on which glass floats, which is on the order of 10-15 μm.

Given the errors from the difference in temperature across the glass thickness, the falling edges of the glass as its softens and the pressure gradient on one side of a glass sheet when the other side sees a constant atmospheric pressure, the glass bows. To avoid this pressure differential across the glass sheet, the concept described in Section 3.3.5 is considered and followed. An equal pressure from opposing mandrels, each

located on one side of a glass sheet, would force it to find an equilibrium position halfway between the two mandrels and flatten it.

4.3 Slumping Glass between Two Flat Porous Mandrels

Since gravity affects the final shape of glass as it softens and slumps, the vertical configuration of slumping is engineered next to improve the flatness of sheet glass. Section 3.3.1 shows the effect of gap size variation on the overall pressure of air in the gap. When approaching a glass sheet on its two faces, it is absolutely critical to control the forces applied on both faces to make sure the desired shape is obtained. Since a flat glass is what is needed as a start, the pressure force on both faces of the glass must be equal.

Sources of error that can alter the final result include variation in the thickness of the glass sheet itself, variation in the gap size separating the glass from the mandrels and variation in the pressure of air going through the porous mandrels and against the glass.

When the flatness of a glass sheet varies, it changes the gap size as well and thus results in higher pressure on one face of the glass than the other. When the glass is soft, this pressure difference between its two faces shapes the glass by pushing it so it is midway between the two flat mandrels. This improves its overall flatness. The thickness variation of glass results in a change in the air gap size, as shown in Figure 4-21. This results in different pressure forces on both sides of the glass sheet, which could become a limiting factor. When the thickness of the glass is different along its length, then the air gap, and thus forces, vary along the length of the glass. The difference between flatness and thickness variation is discussed in Section 2.1.1.

As for pressure variation on both sides of the glass sheet, the main reasons why pressure would be different are:

1. the supply pressure is different in both plenums,

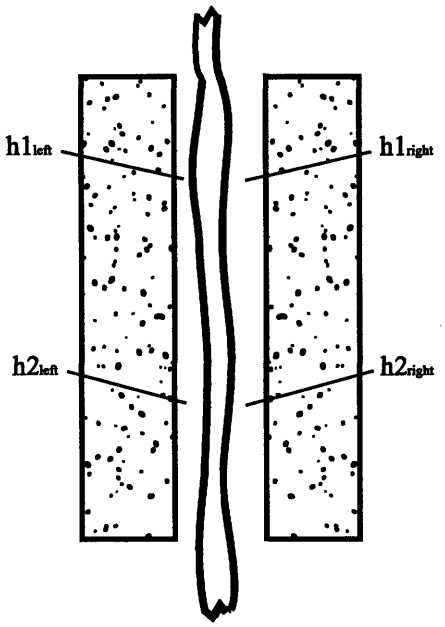

Figure 4-21: Gap variation on both sides of glass due to glass thickness variation. The overall gap size $h1_{left}$+$h1_{right}$ is smaller than the gap size $h2_{left}$+$h2_{right}$, where the glass is thinner

2. the permeability of the two mandrels is different resulting in a different flow configuration across the porous mandrel,

3. the gap size between the mandrel and the glass sheet is different on each side.

Perhaps the most difficult criterion to model and control is the effect of permeability of the porous material on flow. Usually manufacturers are not interested in this parameter and do not measure it. One way of ensuring that the two separate mandrels have the same permeability is by making them from the same batch.

Gap variation can result from glass thickness variation, mandrel non-flatness and mandrel non-paralellism to each other, as shown in Figure 4-22. These parameters become essential in the design process and are discussed later in this chapter.

4.3.1 Design Criteria for Mandrel and Housing

The starting point for this concept is finding the material needed to make two flat mandrels, since the porous ceramic from *NewWay Air Bearings* has been sealed after

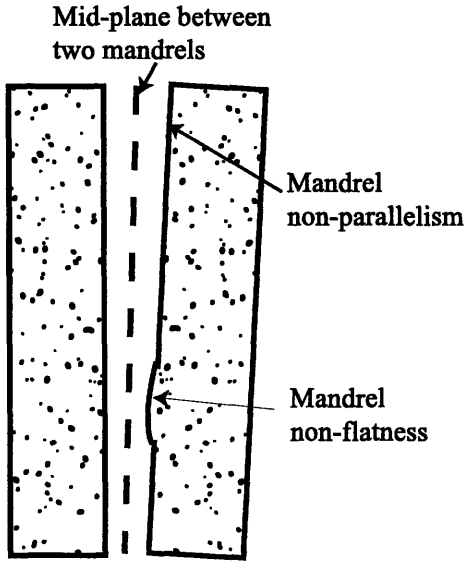

Figure 4-22: Mandrel non-flatness and non-parallelism result in air gap size variation.

the CVD coating process. Porous ceramics are typically inexpensive after a mold is manufactured; however, the mold itself has a high initial fixed cost. When looking for manufacturers, what is essential in determining which vendor to go with is whether the vendor is knowledgeable about the ceramic they are selling, and the vendor is willing to share basic ceramic properties, such as material compositions, Young's Modulus, thermal conductivity and CTE.

Refractron Technologies Corp is a company that manufactures advanced ceramics for chemical, petrochemical, dental, healthcare, filtration and many other applications. The two main materials they use for manufacturing porous ceramics are alumina and silicon carbide. A few samples are tested for porosity and air flow before purchasing two large silicon carbide plates with a porosity of $\sim$40% and dimensions of 12" $\times$ 12" $\times$ 0.5". It should be noted that these plates were originally manufactured as part of a larger order for another customer and thus were sold at less than $300 each.

With the mandrel material on hand, the next criteria to consider are summarized in Table 4.3 as a set of requirements and design parameters for assembling a mandrel and a housing in preparation for slumping. Each of the line items in Table 4.3 is

analyzed and discussed below.

Housing Material and Design

The housing, which constrains the mandrel and provides a plenum, is the second critical component that forms the assembly. A plenum is needed to evenly distribute the supply pressure on the back side of the mandrel. For typical porous material applications, such as air bearings, a housing made of plastic or metal is used; however, in this application, given that the temperature of the experiment changes with time to reach a maximum close to 600°C, the housing material becomes critical to the overall performance of the mandrel.

Depending on the design of the housing, its dimensional change with temperature must not impart stresses on the mandrel. The reason why this is important is because if a flat mandrel is constrained by a structure that heats up or cools down at a different rate, the housing structure would induce stresses on the mandrel causing it to bow and altering its nominal surface flatness. Since the parts go through many heat cycles, thermal fatigue can become an issue as well.

Metals typically have a CTE much higher than porous ceramics at elevated temperatures. Even Invar, which has a low CTE of 1.2×10^{-6}/°C at room temperature, has a CTE of 11.4×10^{-6}/°C at the elevated temperatures of this application [54]. Metals are also typically heavier than ceramics, and since a vertical configuration is considered, carrying the heavy load of a metal housing becomes a disadvantage.

Macor is a machineable glass-ceramic developed by *Corning Inc.* and is stable at temperatures up to 800°C. It has a density of 2.53 g/cm^3, which is very close to that of the porous silicon carbide mandrel and thus is comparable in weight. Macor can be machined to very tight tolerances using carbide tools, which is attractive since the machining can be done in-house. The thermal properties of Macor on the other hand are different from porous silicon carbide. Macor has a conductivity of 1.46 W/m-K compared to the 155 W/m-K of silicon carbide and a CTE of 9.3×10^{-6}/°C compared to the 4.5×10^{-6}/°C of silicon carbide. In other words, during the transient stages, it takes much longer for Macor to heat up than silicon carbide, and at steady state,

Requirements	Design Parameters
Housing material - thermal stability	Machineable ceramic such as Macor
	Metal
	Same material as mandrel either porous or pore-free
Housing and mandrel joint - thermal stability	Bolts
	High-temperature adhesive
	Compressive force
	Vacuum or magnetic force
	Flexure joint between mandrel and plenum to accommodate CTE mismatch
Leakage control	Glaze plates
	Flexible/spring seal around the edges
	Permanent bond between two plates
Controlled pressure	One air source for both sides
	One air source for each side
	Pressure-flow control open loop
	Pressure-flow control closed loop
Equal permeability for two mandrels	Make mandrels of same plate/batch
Assemble two mandrel/housing units - thermal stability	High-temperature extension springs to pull units together
	Rod, nuts and washers to pull units together
	Another clamping mechanism to pull units together
	Mandrel/plenum thermal isolation from rest of assembly

Table 4.3: Requirements and design parameters for slumping glass between two mandrels - structural components

Macor expands twice as much as silicon carbide.

A steady-state FEA model with a silicon carbide mandrel and a Macor housing was performed. First the thermal loads were calculated as the temperature of the parts is increased from 25°C to 600°C. Once these loads were calculated, structural analysis was done to determine the stresses imparted by the Macor housing onto the porous silicon carbide plate. A cross-sectional view of the stress distribution is shown in Figure 4-23. The model has the left edge fully constrained, and is such that the Macor housing carries the load of the mandrel along the x direction, the vertical direction, as shown in Figure 4-24. The resulting stress of the porous mandrel ranging between 340 and 510 MPa, as shown in Figure 4-23, is higher than the tensile strength of pore-free silicon carbide or any other engineering ceramic, which ranges between 35 and 140 MPa [55]. Although this may not be the exact final geometric configuration, it gives a clear idea about the levels of stress involved when using Macor and porous silicon carbide. Thus a housing made of Macor is not recommended for this application.

Making the housing out of the same material as the mandrel is considered next. A pore-free silicon carbide housing has relatively the same CTE of 4×10^{-6}/°C as the porous mandrel but a much higher thermal conductivity of 120 W/m-K and a larger density of 3.1 g/cm^3 than porous silicon carbide, which has 20-40 W/m-K and 1.9 g/cm^3, respectively. This means that the transient behavior of mandrel and housing is different for each part. A porous housing on the other hand has the exact same properties as the mandrel; however it leaks, which may or may not be an issue.

A glassy glaze Aremco-Seal 617 manufactured by *Aremco* was tested on the porous silicon carbide plate to see if it forms a hermetic seal on the surface of the porous housing if necessary. The glaze is applied on the porous material and heated to 800°C, at which it flows and seals the surface pores. The glaze works to temperatures close to 700°C after it has set. The glaze does in fact seal the surface without penetrating the material pores; thus it was decided to use a porous silicon carbide for the housing and glaze the outer surfaces if leakage becomes a limiting factor. This ensures thermal stability throughout the experiment, which is another requirement set for this

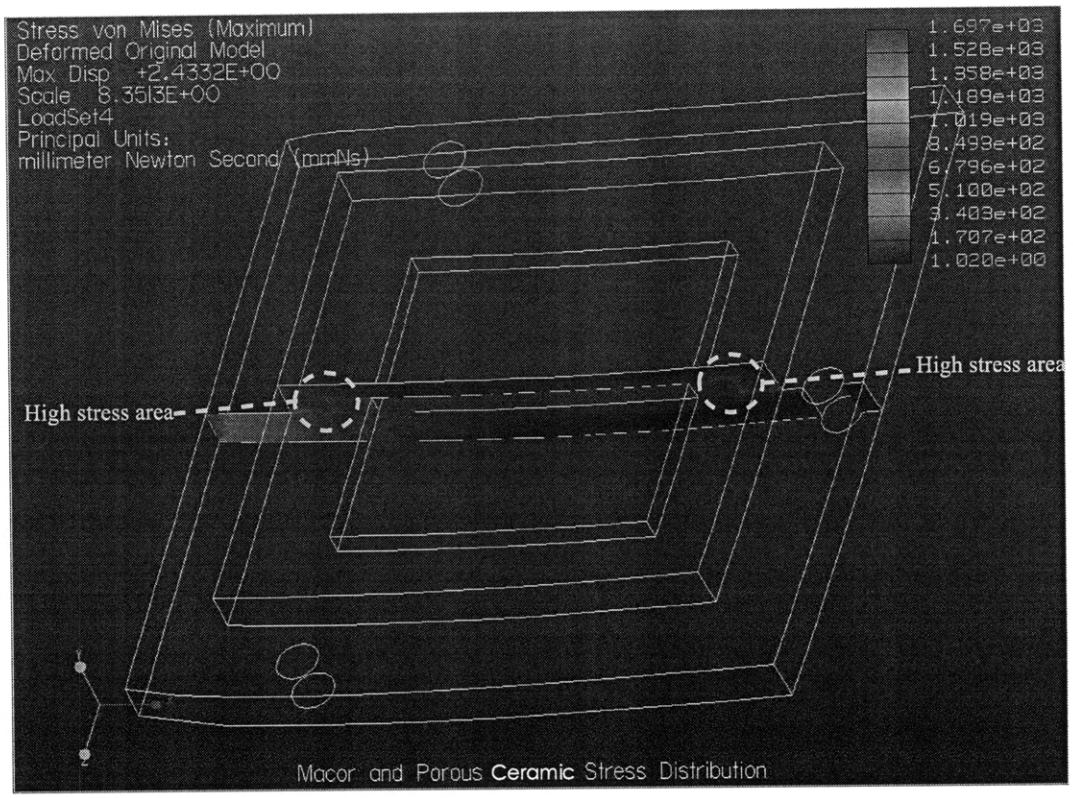

Figure 4-23: Cross-sectional view of stress distribution in a porous ceramic mandrel with Macor housing. Note that the gravity vector is along the x direction.

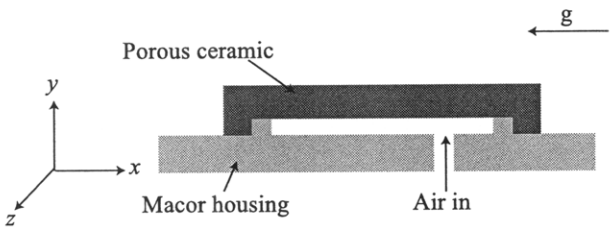

Figure 4-24: Model of porous ceramic and Macor housing. Note that the gravity vector is along the x direction.

experiment.

Housing and Mandrel Joint

The interface between the housing and the mandrel is critical in the overall performance of the assembly and the final shape of the mandrel.

If a permanent bond is used to join the mandrel and the housing, such as a high-temperature adhesive, then the mandrel's critical top surface must be ground after it has been bonded with the housing. Adhesives that withstand 600°C are not numerous. *Aremco*, a company dedicated to manufacturing adhesives, sealants and ceramics that withstand high temperatures, sells two adhesives that have good bonding capabilities to silicon carbide. These are Ceramabond 865 and 503, where the main component in the former mixture is aluminum nitride and the latter mixture is alumina. Both have been purchased and tested. The adhesives were applied on pairs of porous silicon carbide ceramic beams using a brush, clamped and placed in a furnace to heat-treat the samples to the temperatures specified by the manufacturer. Ceramabond 865 did not have the strength needed for the slumping experiment. In fact, the two beams bonded by Ceramabond 865 could easily be separated by hand. Ceramabond 503 seemed promising.

Adhesives are weakest in tension and strongest in compression. Air flowing through the mandrel pushes it away from the housing, thus imposing tensile forces on a layer of adhesive as shown in Figure 4-25*(a)*; however, since the vertical direction is along the x direction in this figure, the adhesive also sees a shear force when carrying the load of the porous mandrel. Placing a layer of adhesive as shown in Figure 4-25*(b)* applies shear forces on the adhesive as a result of the air pushing the mandrel away, which is better than the tensile forces in the first configuration. The weight of the porous mandrel applies compressive forces on the right adhesive in Figure 4-25*(b)* and tensile forces on the left adhesive.

By looking at Figures 4-25, the configuration shown in Figure *(a)* is easier to assemble than the configuration in Figure *(b)*. The adhesive can easily be applied on the ceramic in Figure 4-25*(a)*, whereas in Figure 4-25*(b)*, the adhesive must be

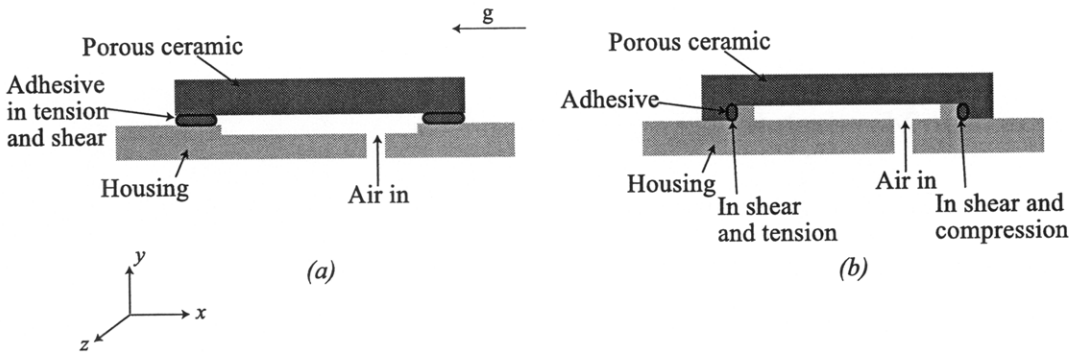

Figure 4-25: Different ways of bonding mandrel to housing. Note that the gravity vector is along the x direction.

squeezed between the two ceramic pieces. It is also easier to apply clamping forces against the parts once the adhesive is applied in Figure 4-25*(a)*.

A dual column material testing machine manufactured by *ADMET* was used to test the strength of the bond in shear. Figure 4-26 shows the test setup. Two silicon carbide beams, 0.5" $\times$ 0.5" $\times$ 1" in dimensions, were bonded using Ceramabond 503. One beam was constrained while the rod of the tensile gauge system pushes against the other beam in an effort to shear the bond. The load cell attached to the top of the rod of the tensile gauge measures the force applied with the rod displacement.

Three samples were prepared, and the bond strength measured. The resulting force-displacement diagrams are shown in Figure 4-27. As can be seen from these figures, the strength of the adhesive is not repeatable. The first sample had a minor fracture at a little over 400 N and then an ultimate fracture at about 1,800 N, after an overall rod travel of 2.4 mm. The second sample had minor fractures along the travel of the rod until final fracture happened close to 3,000 N after a total rod travel of about 2.4 mm. The third sample fractured at only 600 N and a total rod travel of 1 mm.

The bond thickness is a varying parameter when applying the adhesive on the ceramic. The adhesive material is extremely viscous and requires a high torque mixer to mix properly and make it uniform in consistency. This affects the adhesive performance. The thickness of Sample 1 had not been measured, but the thickness of

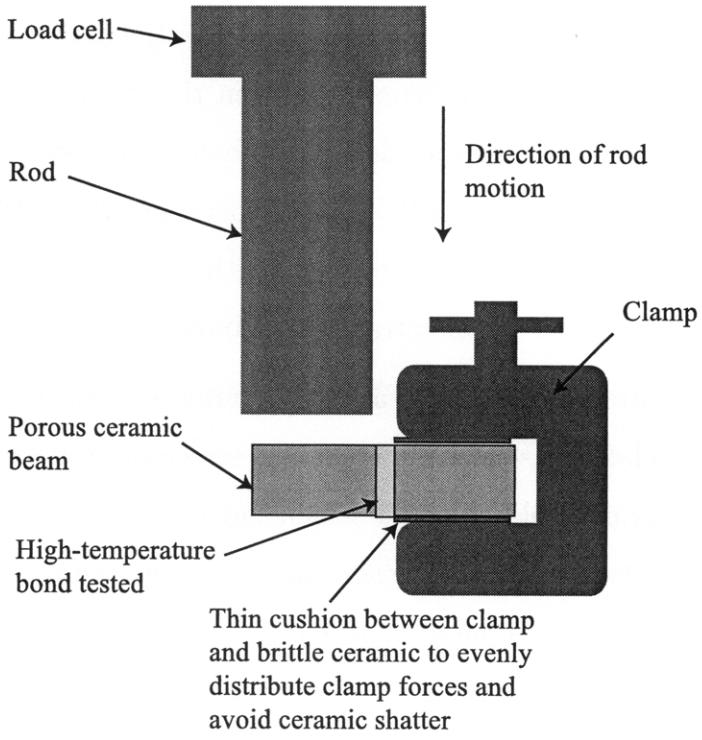

Figure 4-26: Shear test set-up of bonded beams. Rod attached to load cell moves downwards shearing the bond between the two ceramic pieces while the load cell measures the force with displacement until the bond fractures. Figure not to scale.

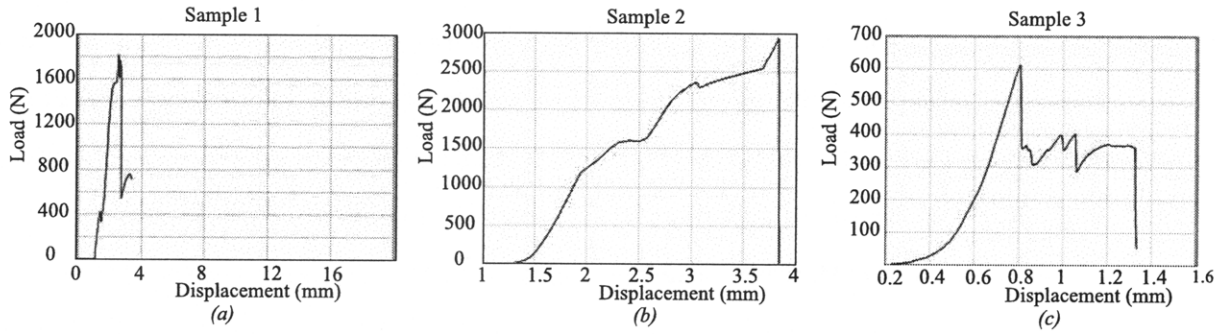

Figure 4-27: Load vs displacement diagrams for three samples of equal size bonded by Ceramabond 503

Samples 2 and 3 was measured to be 0.318 mm and 0.356 mm, respectively. The bond-free ceramic pieces are measured separately and after bonding, the thickness of the bonded stack is measured. The difference between the stack thickness and the sum of the individual ceramics is the thickness of the bond. Another parameter that affects the performance of the adhesive is the presence of air bubbles in the bond layer. Bubbles are weakness areas reducing the overall strength of the bond. Unfortunately, using a brush alone does not get rid of entrapped air bubbles in the adhesive layer.

Screen printing was attempted to apply a layer of uniform thickness of the ceramic adhesive on the porous plates. As normally practiced, screen printing utilizes a screen with a fine mesh, where paint is placed on the screen and a squeegee is used to push the paint through the screen holes. The thickness of the paint going through the screen is equal to the thickness of the screen mesh material. This is a process followed to color T-shirts for instance. For this experiment, a very coarse mesh was used to push the ceramic adhesive through; however, even when the adhesive goes through the holes of the screen, it would stick to the back of the screen instead of the porous ceramic plates and comes off as the screen is removed. It has been found that to make the adhesive stick to the porous material, a large clamping force must be applied on the bonded plates for an extended period of time with heat treatment.

Since the bond has different material properties from the silicon carbide mandrels, thermal gradients can cause cracks and result in bond failure. Applying a bond between two plates and varying the setup temperature generally results in an overall curvature of the plates and bond as a result of a difference in CTE, Young's modulii and geometry. If a bond is applied between two identical plates, and the temperature is varied, then the curvature is eliminated as a result of equal and opposing forces on both sides of the bond. However, the bond-plate interface is under a shear stress. In this particular experiment, the bond CTE is $7.2 \times 10^{-6}/°C$, whereas the CTE of the silicon carbide plates is $4 \times 10^{-6}/°C$. This means that the bond is in compression as the temperature of the setup is raised, which reduces the possibility of cracks forming in the bond; however, the interface between the bond and the porous plates sees a shear stress during every heating cycle, and it might fail as the temperature is varied.

Since the silicon carbide plates are thicker than the bond between them, it is assumed that the final length of the bonded plates is equal to the length of the plates at the elevated temperature. For a temperature increase of ~580°C and a plate length of 6" or 153 mm, the resulting difference between the final lengths of the bond and the plates is 0.283 mm. By looking at the strength of the bonded material measured at room temperature and shown in Figure 4-27, this displacement corresponds to a very small portion of the ultimate strength of the bond in shear.

The reason why the bonding layer is needed is to provide a force that acts against the plenum air pushing the mandrel away from the housing and to carry the load of the mandrel, which is about 5.5 N for a part that is 6" × 6" × 0.5" in dimension and 1.9 g/cm^3 in density. The force of the air pushing against the 4" × 4" surface of the mandrel is at most 70 N for a supply pressure of 1 psi (6,897 Pa), which is much larger than what is anticipated to be used in these experiments. Thus the total sum of forces the adhesive must withstand is not more than 80-90 N, which is much smaller than what the adhesive can withstand before rupture, based on the data in Figure 4-27.

Bolts and nuts can also be used to join the mandrel and housing; however, the surface of the mandrel must be ground after the bolts have been tightened at a known torque to ensure flatness. The advantage of using bolts and nuts is that the mandrel and housing can be separated whenever necessary, such as when the mandrel or the housing is damaged and needs to be replaced, thus only one part needs to be remachined. The disadvantage is the fact that most bolts and nuts have a CTE and thermal response different from ceramics and would expand at a different rate from the ceramic. This results in loss in the clamping force from the bolt and more importantly, a change in the surface flatness of the mandrel with heat. Another disadvantage is the addition of parts to the assembly. If many bolts are used to ensure proper sealing between the two surfaces, where every bolt must be tightened again before every test is run, this significantly adds to the time to assemble the parts.

A compressive force pushing the housing against the mandrel at critical positions can constrain the two surfaces. This is described in detail in further sections.

Finally, other methods of constraint using magnets and vacuum are more challenging to pursue in this application. Magnetic force is lost with temperature and the use of vacuum in a porous structure where pressurized air is flowing results in a high flow rate of air within the porous part. Using vacuum also requires a separate vacuum line to be introduced in the high temperature furnace environment, which is already crowded with pressure lines.

Having looked at the different options to join the mandrel to the housing, either the high-temperature adhesive or the simple compressive force method will be followed.

Leakage Control

The presence of an easy path for air to escape between the mandrel and the housing significantly alters the results of the experiment. This is because air escapes the plenum through this leak area instead of going through the mandrel and shaping the glass as it exits from the top of the mandrel. Thus, the joint area between the mandrel and the housing must be well sealed.

If an adhesive is used to join the housing and mandrel, then the adhesive inherently seals the interface between the mandrel and the housing. If a compressive force is used, then by grinding the back of the mandrel and the top of the housing flat and applying a compressive force, a tight contact is formed, and thus a seal between the two surfaces is established. A rather flexible seal composed of a thin mica sheet can also be squeezed between the mandrel and the housing to ensure a tighter sealing if necessary.

It is unclear this early in the design process, whether leakage from the porous parts themselves is problematic. Since the housing is also made of porous silicon carbide, air escapes through its walls just as air escapes through the top flat surface of the mandrel; however, this is a constant leakage controlled by the pore size of the ceramic for a given flow rate of air.

If it is found that the leakage through the side walls of the mandrel and housing is a problem, the glassy glaze *Aremco* 617 described in Section 4.3.1 can be used to seal the surfaces of the porous parts.

Controlled Pressure

A very critical parameter in the success of this concept is the pressure of air exiting the flat mandrel surface and shaping the glass. What matters is not the absolute value of this pressure in one plenum, but rather the difference in pressure on the opposite sides of the glass sheet, since a difference in pressure results in a difference in glass sheet curvature.

This pressure is controlled by various parameters including the flow rate of air, the number of bends in the tube carrying the air into the plenum, the heating of the tubes carrying the air into the plenum, the leakage of the housing and mandrel, the permeability of the mandrels and the size of the air gap between the glass sheet and the mandrel top surface. Some of these parameters are discussed in more detail below.

A single line can be used to transport air into the two plenums, with the line dividing right before reaching the two plenums, as shown in Figure 4-29*(a)*. This eliminates errors in the pressure of air reaching both mandrels caused by the bends and heating of the tubes. Although flow at the same pressure is entering the two plenums, equal pressure at the glass interface is not necessarily the case because of possible different permeabilities of the ceramics and different leakage rates if any. Figure 4-28 shows an analogous circuit using resistance to represent the change in pressure. In order for the glass to slump flat, P_1' must equal P_2'; however, this may not be the case even if the starting pressures are equal to P, since the permeability R_P and the air leakage R_L are not necessarily the same on both sides.

Since the temperature of the experiment is raised to 600°C, it is very difficult to introduce control valves and pressure sensors inside the furnace and adjust these valves during the experiment; thus, control and monitoring of flow is done outside the furnace. The disadvantage of having one line becomes the fact that the two different plenums can no longer be controlled separately from outside the furnace. This is also a disadvantage when a different pressure is desired on each side of a glass sheet to change its curvature.

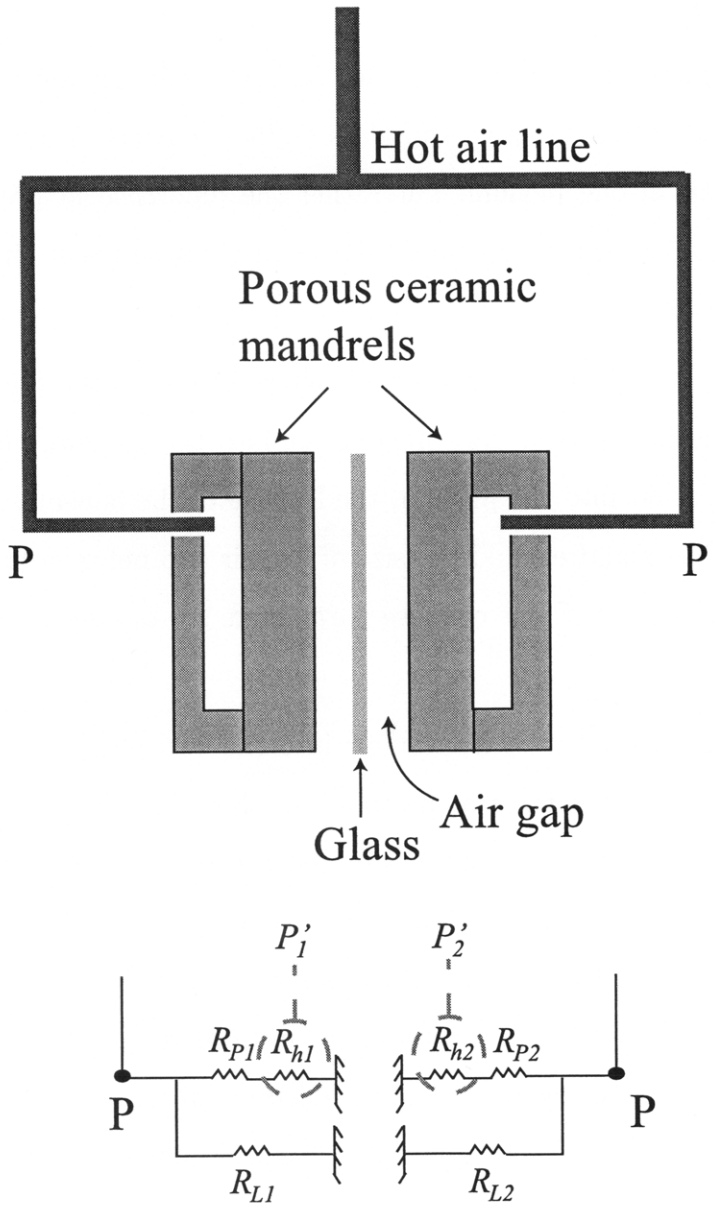

R_P: Resistances of porous mandrels (permeability)
R_L: Resistance due to leakage if any
R_h: Resistance due to air gap thickness
Required $P_1' = P_2'$

Figure 4-28: The pressure in the air gap P' depends on the loss of pressure as a result of porous ceramic permeability R_P and presence of leakages R_L.

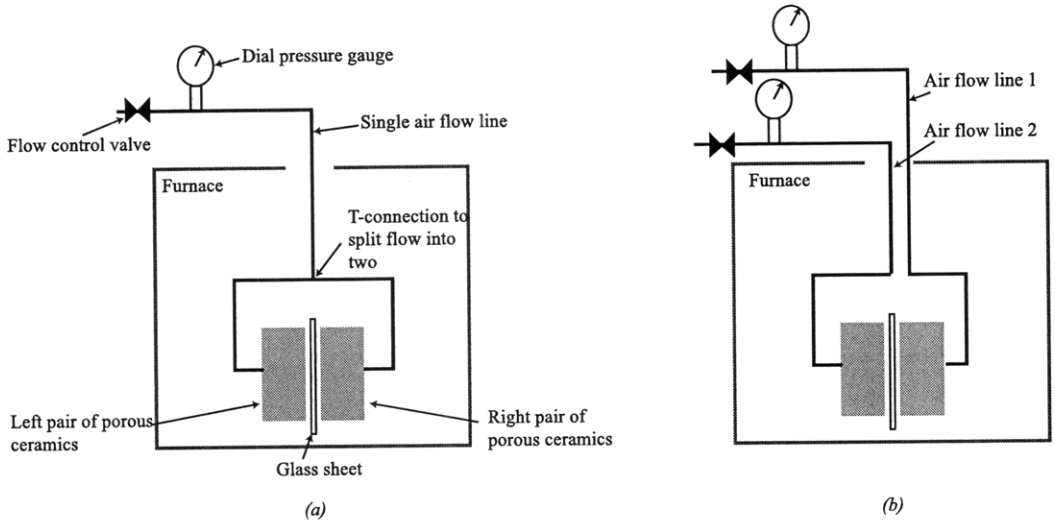

Figure 4-29: *(a)* A single tube carrying air into the furnace is divided into two separate lines and connected to the individual plenums. *(b)* Two separate tubes or lines, each controlled separately, carrying air into the furnace and connected to each plenum

Alternatively, two separate lines can be used to transport air into the two plenums, as shown in Figure 4-29*(b)*. This helps control the two lines independently, which is important when intentionally bowing glass sheets by applying more pressure on one side. It also helps fine tune the pressure in both plenums. The disadvantage though is the fact that two separate lines would have different bends and could heat up at different rates, which results in pressure differences between the two. This can be minimized by having the same length of tubing bent at the same locations for the two lines with the same radii of curvature and both placed at the same distance from the heating elements of the furnace. Stainless steel tubes are chosen, which withstand slumping temperatures. Two 4 ft long tubes are bent and placed inside the furnace near the heating elements to heat the air while transporting it from outside the furnace to inside the plenums. A flow control valve and a dial pressure gauge are used outside the furnace to control the flow rate and roughly measure the dynamic pressure, as shown in Figure 4-29.

As mentioned earlier, the critical pressure is in the air gap between the glass sheet and the flat mandrels. Since this gap is relatively small and in a very hot environment,

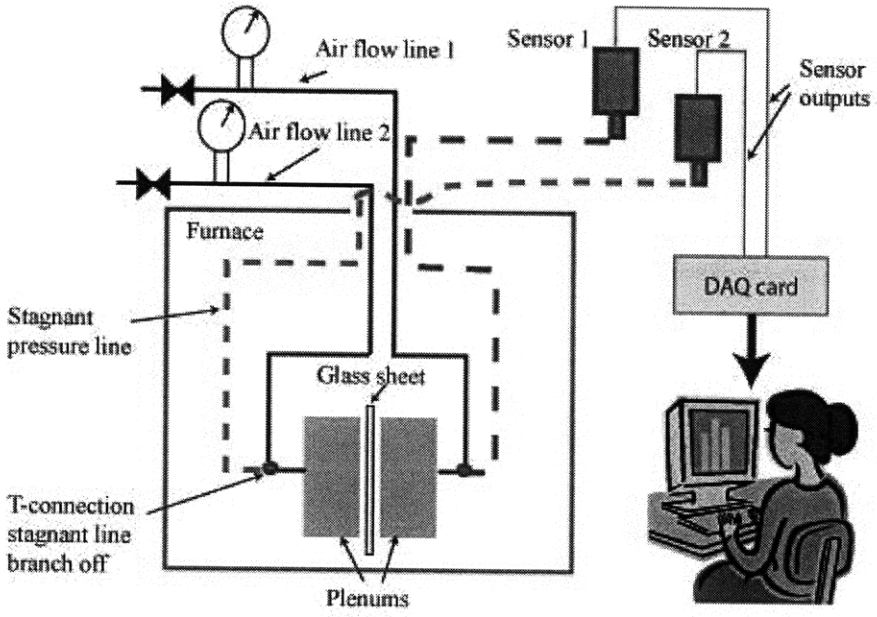

Figure 4-30: A T-connection used before the plenum to divide the incoming pressure line into a stagnant one connected to sensors outside the furnace environment and a dynamic one going into the plenum to shape glass. The sensor output is connected to a *National Instruments* Data Acquisition Card (DAQ Card), which in turn connects to a computer to plot the pressure variation with time as the experiment proceeds.

placing a pressure sensor in the gap is challenging. However, the pressure of air going into each plenum can be measured by having a stagnant line branch off from the two main lines right before connecting them to the ceramic plates, as shown in Figure 4-30. This stagnant line is taken outside the furnace and cooled before a high precision pressure transducer is connected to it. The tubes are made of stainless steel. To estimate the length of tubing needed outside the furnace for the air in the tube to cool before reaching the sensor, the following equation is used to describe the governing steady state condition:

$$\frac{d}{dx}\left(kA_c\frac{dT}{dx}\right) - hp(T - T_\infty) = 0, \tag{4.3}$$

where x is the direction of flow of air, k is thermal conductivity, A_c is the tube cross-section, T is the temperature at x, h is the heat transfer coefficient, p is the surface

area of the tube and T_∞ is the ambient room temperature. The boundary conditions are that the temperature at the exit of the furnace where $x = 0$ is at T_b, which is a maximum when the furnace is at 600°C, and the end of the tube where the pressure transducer is located is insulated, thus $\frac{dT}{dx} = 0$. The resulting solution is given by [56]

$$\frac{T(x) - T_\infty}{T_b - T_\infty} = \frac{\cosh a(L - x)}{\cosh aL}, \tag{4.4}$$

where $a^2 = \frac{hp}{kA_c}$ and L is the tube length.

The tubes used have an outer diameter of d_2=0.25" or 6.35 mm and an inner diameter of d_1=0.125" or 3.175 mm. Thus the surface area $p = \pi d_2 L = 0.0199L$ m^2. The equivalent KA_c takes the conductivity of air and stainless steel into consideration, such that

$$kA_c = k_{air}A_{air} + k_{SS}A_{SS}, \tag{4.5}$$

where k_{air} and k_{SS} are the thermal conductivities of air and stainless steel, respectively and A_{air} and A_{SS} are the cross-sectional areas of the air and stainless steel portions of the tube, respectively. For k_{air}=0.692 W/mK and k_{SS}=16.2 W/mK, the resulting kA_c=3.901×10^{-4} Wm/K.

By solving Equation 4.4 at $x = L$, where the temperature must be at most 25°C, the required length L is

$$L = \frac{0.843}{\sqrt[3]{h}}. \tag{4.6}$$

For a heat transfer coefficient of 60 W/m^{2}K, which is typical for a metal-air interface, the required tube length between the exit of the furnace and the sensor is 0.215 m or 8.5". As a worse case scenario, for a heat transfer coefficient of 5 W/m^{2}K, the required tube length is 0.49 m or 19.4". A length of 20" is selected for the experiment, and a small fan is placed against the tubes to enhance the cooling process and avoid damaging the sensors.

The pressure sensors selected are the Baratron 740B21TFE3GA manufactured by *MKS Instruments, Inc.*, with a pressure range of 20 Torr (0.3867 psi), an accuracy

of $\pm 1\%$ of reading, a repeatability of $\pm 0.1\%$ of reading and a resolution of 0.01% of full scale or 4×10^{-5} psi, as quoted by the manufacturer [57]. These sensors are custom built at an average price of $800 per sensor. Sensors with a better accuracy are also available from the same manufacturer at a much higher price. Based on the modeling done in Section 3.4, a pressure differential of 0.006 psi between the two plenums is tolerable, resulting in surface errors of 0.497 - 5.326 μm, depending on how the glass sheet is constrained during slumping. Thus the sensors purchased with an accuracy of $\pm 1\%$ of reading are sufficient for these tests. Before every experiment, these sensors are cross-referenced to ensure that the pressure in the two plenums is equal. It should be noted that even though the pressures are set equal to a specific value at the beginning of the experiment when the furnace is at room temperature, as the temperature of the experiment increases, the pressure increases as well at a constant flow rate. The reason for this is the fact that the viscosity of air increases with temperature, increasing resistance to flow and thus pressure in the system. Figure 4-31 plots this pressure variation in both sensors with time and temperature.

MKS Instruments, Inc. also sells high precision flow controllers that can both measure and control flow to an accuracy of $\pm 1\%$ of reading. Model number 1179A01353C51BB is recommended for this application; however, the price per unit is close to $1,200. To better control the process, a closed loop between the pressure sensors and the flow controllers can be established to constantly feed the output of the pressure sensor into the flow controller and adjust flow accordingly. An additional controller, such as the 247D at the price of $1,482, is needed in this case to connect the pressure sensor outputs to the flow controller input. Since two pressure sensors, two flow controllers and one interface controller would be needed, the total price of the flow control set-up would be close to $5,500, which is rather high. As a starting point, the pressure sensors are purchased, and regular flow control valves and flow meters are used in an open loop set up. Figure 4-32 shows the pressure readings as a function of time in a line after the flow control valve is set. No parameters are varied while the pressure readings are taken. As can be seen from the figure, it takes about an hour before the flow control valve settles and provides a controlled flow. This should be kept in mind

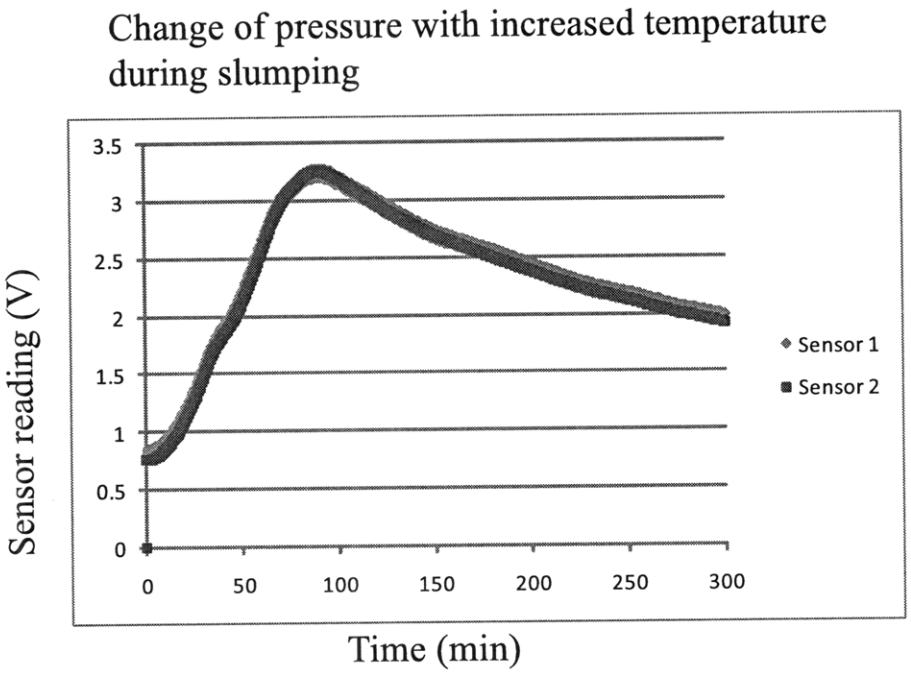

Figure 4-31: The variation of pressure with temperature during a slumping test. Data from two sensors measuring each plenum is plotted.

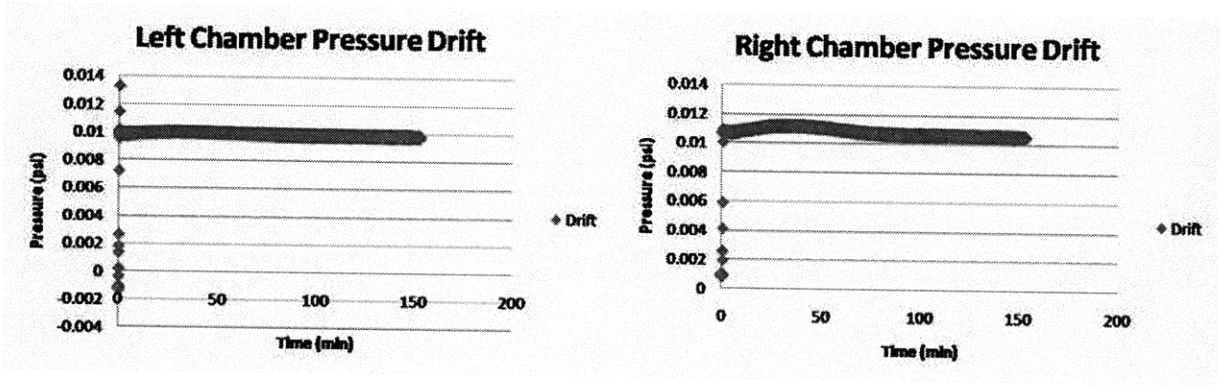

Figure 4-32: The variation of pressure with time for a given flow. This variation during the first hour is a result of the flow control valve error after it is set to a specific dial.

when running experiments. After the flow is regulated, the control valve should be left for a period of time for it to settle, and then the experiment can be started.

Equal Permeability of both Mandrels

The permeability of the mandrels is perhaps the parameter that is the most difficult to control once the original porous ceramic parts have been manufactured. As mentioned earlier, the permeability of porous ceramics is not commonly measured by manufacturers. If the permeabilities of the two mandrels are different, then even if the supply pressure in each plenum is the same, the resulting pressure drop across the mandrel thickness is different on each side, resulting in a different pressure profile in the air gap. This in turn compromises the flatness of the slumping glass.

To ensure that the two mandrels have similar permeabilities, a large plate, 12" $\times$ 12" $\times$ 0.5" was purchased and divided into four smaller plates, two forming the mandrels, and the other two forming the housings. Since this single plate was manufactured in one step at a uniform temperature and isostatic pressure, it is considered to be homogeneous with isotropic material properties, and thus the four smaller plates would have similar permeabilities.

With the design of the porous ceramic parts on hand, the next step is to under-

stand how the glass sheet is placed and shaped between the two mandrels.

4.3.2 Design Criteria for Glass Sheet Constraint and Shaping

A set of requirements were developed for setting the glass sheet between the two mandrels and controlling the thermal shaping or forming process. These requirements and their corresponding design parameters are summarized in Table 4.4 and are further discussed below.

Glass Constraint

Properly constraining the glass sheet between the two flat mandrels is very critical for the success of the experiment. The glass sheet must be constrained vertically, equidistant from both mandrels and such that the difference in the CTE of glass and silicon carbide does not cause thermal strains on the glass sheet as the overall assembly goes through the heat cycle.

Clamping the glass sheet from the top requires thin, temperature-resistant clamps that both fit in the narrow opening between the two mandrels and impart minimal thermal stresses on the glass. To make sure the glass is equidistant from both mandrels, the clamping mechanism can be connected to a journal bearing and a shaft, as shown in Figure 4-33. The advantage of using a journal bearing at the top is that it provides zero friction in the lateral direction; therefore, as the air flows through the two flat mandrels at equal pressure, the clamped glass sheet is free to move laterally until it reaches the equilibrium position half-way between the two mandrels, where the pressure forces are equal on both sides of the sheet. Since this set up is in a furnace, the need for a high precision shaft, a journal bearing and an additional pressure line going into the furnace to connect to the journal bearing all add to the cost and complexity of the design.

An easier, though potentially less accurate way of constraining the glass sheet is through the use of spacers between the glass and each of the mandrels with compressive forces, as shown in Figure 4-34. This method not only constrains the glass, but

Requirements	Design Parameters
Glass constraint in vertical plane	Constrain glass on one edge from top
	Constrain glass using spacers and compressive force
	Constrain glass at two points on its lower edge
Glass equidistant from two mandrels	Glass top constraint is on a horizontal journal bearing so glass finds the mid-plane between two mandrels when air flows through mandrels and pushes glass between the two
	Constrain glass using precision spacers
	Constrain glass at a predetermined distance from one mandrel
Controlled air gap size	Fine-pitch screws/micrometers separating two mandrels
	Precision spacers between two mandrels
	Self align porous mandrels to each other by using one as reference and placing the other on a gimbal with air flowing through second mandrel
Parallelism between two mandrels	Same parameters as controlled air gap size
Dust particle elimination	Large enough gap size to eliminate dust effect
	Thorough cleaning of assembly before testing
	Covering assembly with a box inside furnace to avoid funace insulation particles from settling on glass

Table 4.4: Requirements and design parameters for slumping glass between two mandrels - glass shape

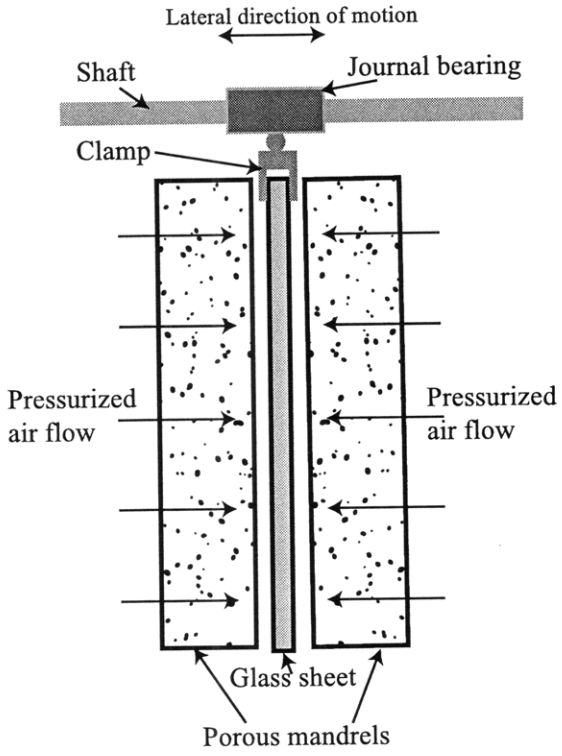

Figure 4-33: Clamped glass sheet connected to a journal bearing free to move in the lateral direction to place glass equidistant from both pressurized mandrels. Figure not to scale.

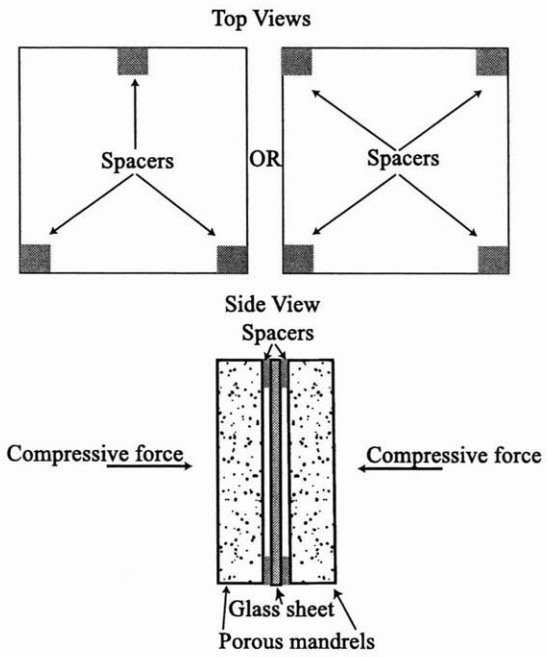

Figure 4-34: Three (left) or four (right) spacers used to constrain glass and determine air gap size. Figure not to scale.

also controls both the size of the air gap between the glass and the mandrel and the parallelism between the two mandrels. Three or four such spacers can be used, as shown in Figure 4-34.

The major risk involved in this design is the thermal stresses on the glass sheet due to its higher CTE than that of the silicon carbide mandrels. In other words, as the temperature of the experiment is raised, the thin glass expands more than the silicon carbide plates; however, the spacers constrain the top and bottom edges of the glass, introducing compressive forces on the glass and possibly causing it to buckle. A model calculating the buckling load of the glass sheet is described below. Another concern is the fracture of the glass sheet at the spacer interface due to the compressive forces. Modeling this possibility is more difficult, since it depends on the presence of surface microcracks at the glass-spacer interface. These microcracks can easily develop into larger cracks due to compressive forces on the glass surface.

If glass buckling is found to be a problem, then the spacers can be relocated to minimize the compressive forces on the glass. Figure 4-35 shows three different

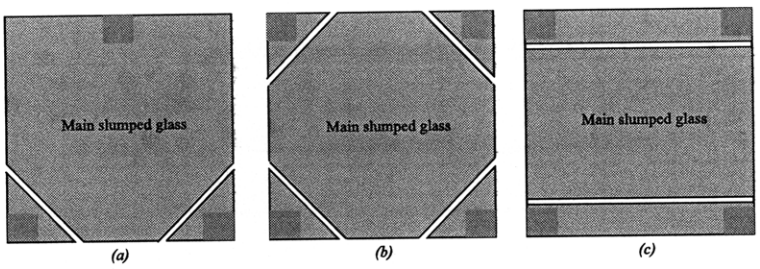

Figure 4-35: Different ways of controlling gap and constraining glass sheet. *(a)* Glass cut on lower two corners separated from the main glass sheet. *(b)* Glass cut at four corners separated from the main glass sheet. *(c)* Glass cut along its two edges. Figure not to scale.

configurations in which the glass can be constrained without buckling. Figure 4-35*(a)* has the risk of the glass shattering due to the concentrated compressive forces on the top spacer. Figure 4-35*(b)* has the risk of the glass jamming at the lower two edges when the assembly is in the vertical configuration. Figure 4-35*(c)* has the risk of the glass jamming at the lower edge in addition to sealing the exit path of air from that side. All of these constraint methods, however, reduce the buckling effect.

As for the thickness and materials of the precision spacers, the foils provided by *A.D. Mackay* and described in Chapter 5 were used. High temperature foils thinner than those provided by *A.D. Mackay* were not found commercially at this time. Chemical or physical vapor deposition, sputtering or evaporation methods are only cost effective for a maximum of a couple of microns of material thickness and thus were not considered as spacer replacement possibilities.

Glass Buckling Analysis It is difficult to perform an accurate modeling on the glass since at the slumping stage, it is a visco-elastic material with complex boundary conditions; however, to have an estimate of whether buckling is a possibility in this experiment, the glass is treated as an elastic plate with a very low Young's modulus.

Badger [58] and Stong [3] have run experiments to determine the effect of thermal history and temperature changes on the Young's modulus of glass. In his paper,

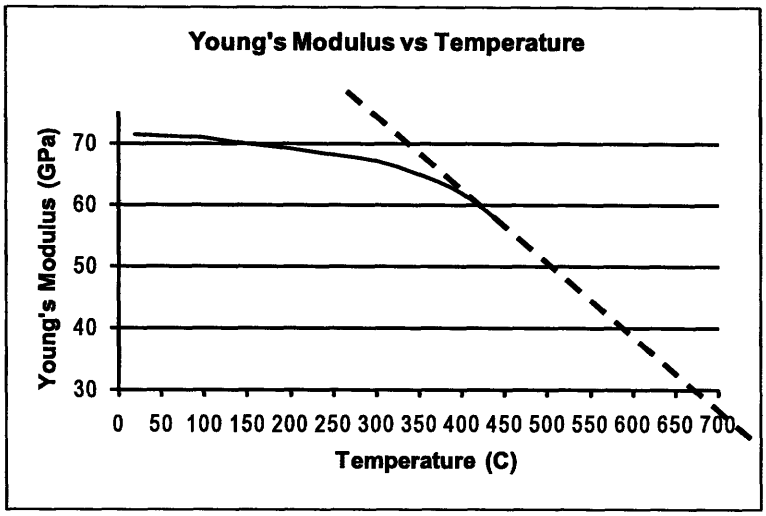

Figure 4-36: Data from Stong's [3] experiments of heating glass and measuring its Young's modulus. The dotted line is extrapolated for temperatures above 450°C.

Stong plots the drop in the Young's modulus as the temperature of the glass sample is increased, as shown in Figure 4-36. His experiments are only conducted to a temperature of 450°C, mostly because glass loses mechanical integrity at a much faster rate after this temperature as it softens. If a linear extrapolation is done on Stong's data between the temperature of 400°C and 450°C, the estimated Young's modulus is around 40 GPa at a temperature of 570°C. The actual modulus is most likely less than this value; however, this value is used to understand the order of magnitude of the forces involved, and whether buckling is a possibility.

The glass sheet is modeled as a plate, where the critical load for buckling P_{cr} is given by

$$P_{cr} = k_c \frac{\pi^2 D}{b}, \tag{4.7}$$

where b is the plate width and D is given by

$$D = \frac{Eh^3}{12(1-\nu^2)}, \tag{4.8}$$

where E is the Young's modulus, h is the plate thickness and ν is the Poisson's ratio of glass.

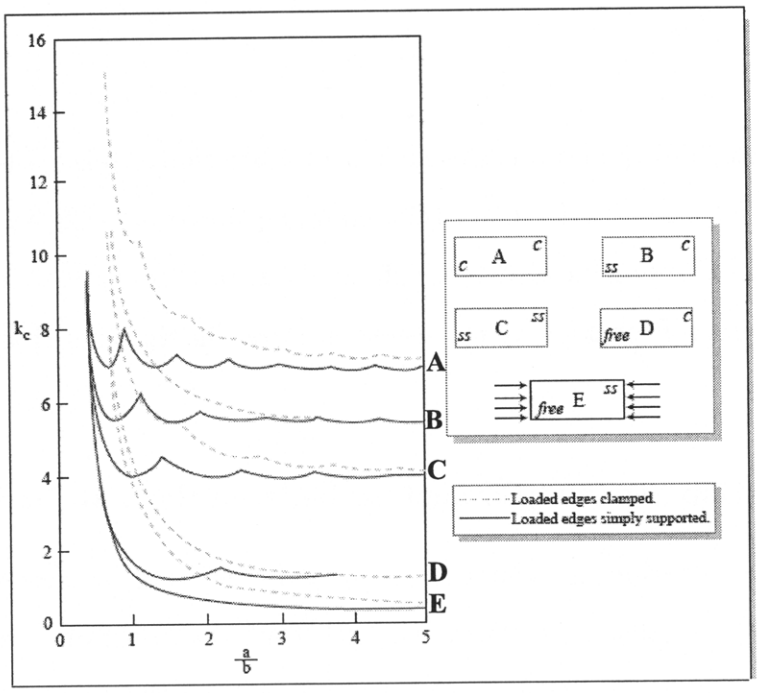

Figure 4-37: Buckling coefficient in the theory of buckling of plates. Different curves represent different boundary conditions under compressive forces.

The buckling coefficient, k_c, is shown in Figure 4-37. For a plate with edge ratio a/b of 1, different boundary conditions determine the value of k_c. In this case, the glass sheet is clamped at specific areas where the spacers make contact, whereas the remainder of its edges are free. This particular case is not represented in Figure 4-37; however, the values of k_c range between 1 and 8 for the basic boundary conditions.

For a glass plate with $E = 40$ GPa, $h = 0.4$ mm, $b = 100$ mm, $\nu = 0.208$, the critical buckling load P_{cr} is $22k_c$. Thus based on the boundary conditions of the glass sheet, the critical load varies between 22 N for $k_c = 1$ and 176 N for k_c=8. Since the unloaded edges of the glass sheet are free (which is not represented in Figure 4-37), and the largest portion of the loaded edges are free, k_c is closer to 1 if not smaller. This critical load represents the friction between the glass sheet and the spacer, since this is the force stopping the glass from expanding freely. Friction on the other hand is the result of the clamping force of the assembly. Thus, the critical clamping force F_{cr} is

$$F_{cr} = \frac{f}{\mu} = \frac{P_{cr}}{\mu}, \tag{4.9}$$

where f is the friction force and μ is the coefficient of friction and is 0.7 between glass and metal [55]. Thus for k_c=1, the critical clamping force is $\sim$ 32 N. This is very small for the clamping force needed, as is shown later in this chapter, and it is very likely that the glass will buckle, which results in errors in the final slumped surface of the glass.

Controlled Air Gap Size and Parallelism between the Two Mandrels

To avoid pressure variation associated with air gap variation, as described earlier, the two flat mandrels must be constrained such that their surfaces are parallel to each other while being separated by a distance larger than the nominal thickness of 0.4 mm of the glass sheets. In air bearing applications, the porous ceramic surface is usually aligned by having it rest on a gimble, turning the air pressure on and directing the flow against a flat guide or surface. This would align the bearing such that it is parallel to the flat surface at a gap of $\sim$10 μm. The same method can not be followed reliably for gaps of 0.4 mm and application temperature of 600°C.

Fine-thread precision screws can be used to separate the two mandrels from each other; however, this requires either drilling the ceramics to attach the screws to them or attaching the ceramic to another plate that has the screws. In addition, given that the temperature of the experiment is raised to about 600°C thermal matching is needed to ensure the ceramic is not over-stressed or the gap does not vary with time.

Thin precision spacers can be used to control the thickness of the gap. Three or four such spacers can be placed between the glass sheet and each of the mandrels, not only to control the size of the gap, but also to constrain the glass and maintain parallelism between the two mandrels, as shown in Figure 4-34.

The surface of the mandrels is very critical for the final shape of the glass, since surface irregularities are imprinted on the glass shape. The machining of the mandrel and housing to the required geometries was done by *Machined Ceramics* in Kentucky. Facilities equipped with proper metrology and machining tools for grinding the surface

of a porous silicon carbide to the sub-micron requirement are not numerous. In fact of the many companies contacted, only *Professional Instruments Company* was willing to try the grinding process on such a material with such tight tolerances for the price of $500 per plate.

The design was modified to have a slumping area of 4" × 4". The mandrel was designed such that this area is protruded from the remainder of the 6" × 6" plate, as shown in Figure 4-38. Dry grinding was done on both the 4" × 4" area and on the back of the plate in order to achieve the initial goal of 1 micron flatness P-V. The task was found to be more challenging than the machinists had anticipated, since the grinding wheel can easily clog the pores. Grinding was done on two axes, such as shown in Figure 4-39, where the workpiece is rotating about the z axis and the grinding tool is rotating about the x axis while moving along the x direction. Both axes utilize a high stiffness air bearing to better control the grinding process. Several grinding wheels were tried until one with a fine grit size achieved the requirement. Surface flatness was measured by scanning a line near the edges of the area avoiding the critical center part, since the measurement tool relies on contact that can damage the surface as it is being measured. This, in turn, only guarantees that the measured edges and not the entire surface meet the flatness requirement. A better metrology method must be pursued to measure the full surface of the plate during the grinding process.

To have an estimate of the surface flatness of the mandrel, a thin silicon wafer quoted to have a thickness variation of 1 μm was placed on the mandrel, and vacuum was applied to force the wafer to conform to the shape of the mandrel. The two surfaces were thoroughly cleaned to avoid having particulates trapped between the two. An optical flat was then carefully placed on top of the silicon wafer, and monochromatic green light was used to assess the fringes formed by the air gaps where the two surfaces are not in perfect contact, as shown in Figure 4-40. With green light of wavelength ~546 nm, every 4 fringes correspond to a ~1 μm deviation from flatness. Flatstones purchased from *Professional Instruments, Inc.* were used to remove any burrs and particles trapped in the pores of the mandrels. This was accomplished by

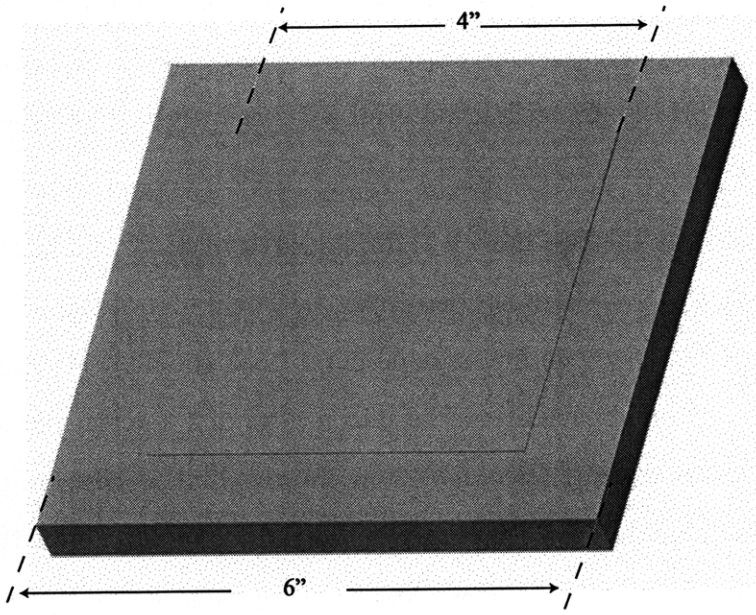

Figure 4-38: Porous silicon carbide 6" × 6" plate machined such that 4" × 4" is protruded as slumping area.

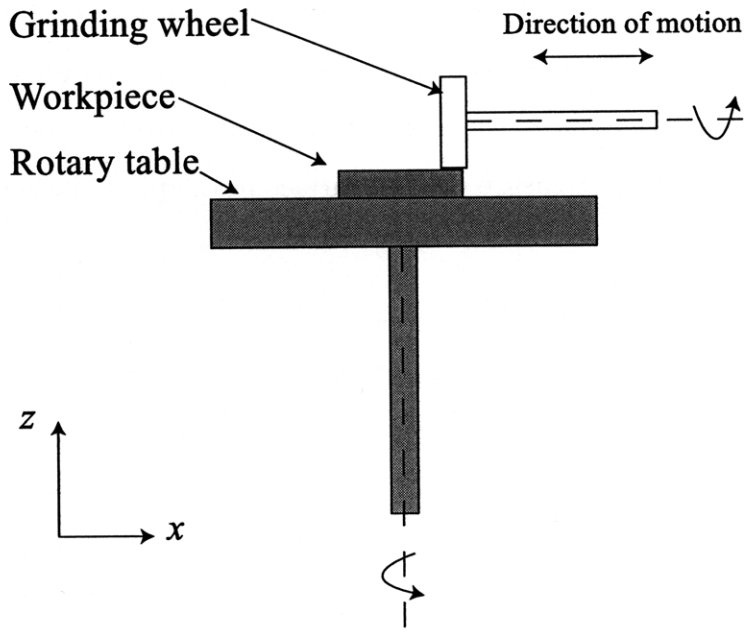

Figure 4-39: Grinding of mandrel (workpiece) using two rotary and one translational motions. Figure not to scale.

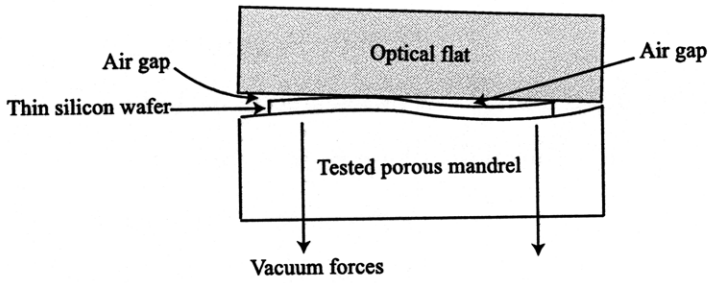

Figure 4-40: A silicon wafer is placed on the mandrel tested using a small force of vacuum. An optical flat is put on top of the silicon wafer to observe the fringes created by the air gap between the two surfaces when viewed under a monochromatic green light.

sliding the stones with slight pressure against the mandrels and cleaning the mandrel with air blast afterwards. The silicon wafer was then placed on the mandrel again, a small vacuum force applied, and the optical flat placed on top of the wafer for fringe assessment. This process was repeated until the fringe pattern would remain the same after taking the silicon wafer off, cleaning the two surfaces with the flatstone and air blast and measuring again. The number of fringes in the central region of the mandrels was about 5 between the peak and valley on one mandrel and 13 on the other. This corresponds to a surface figure of $\sim$1 μm P-V on the first mandrel and $\sim$3 μm P-V on the second in the central region. The edges, however, had a higher number of fringes indicating a worse surface figure. This is anticipated since the grinding wheel first impacts the edges when shaping the surface of these mandrels. This metrology technique does not provide an accurate surface map of the mandrel; however, it gives us an idea of the order of magnitude of the actual surface flatness.

Dust Particle Elimination

The limiting factor in most slumping techniques is the presence of particulates between the glass sheet and the mandrel. It is quite difficult to completely eliminate particulates in a high-temperature furnace environment, since the insulation material used inside the furnace releases such particles everytime the furnace door is closed

Requirements	Design Parameters
Housing material - thermal stability	Porous silicon carbide
Housing and mandrel joint - thermal	Compressive force
Leakage control	Glaze plates if necessary
Controlled pressure	One air source for each side
	Pressure-flow control open loop
Equal permeability for two mandrels	Make mandrels of same plate/batch
Glass constraint in vertical plane	Constrain glass using precision spacers
Glass equidistant from two mandrels	Constrain glass using precision spacers
Controlled air gap size	Precision spacers between two mandrels
Parallelism between two mandrels	Same parameters as controlled air gap size
Dust particle elimination	Large enough gap size to eliminate dust effect
	Thorough cleaning of assembly before testing

Table 4.5: Summary of design parameters selected to meet the requirements of slumping glass sheets between two porous mandrels

and re-opened. Dust also sticks to the surface of the mandrel and the glass sheet during experiment set-up.

The advantage of using air bearings, as has been described in earlier chapters, is the presence of the thin layer of air that absorbs these dust particles, which are typically on the order of 5-10 μm [31]. Thus by having an air gap larger than 10 μm, the dimples on the glass sheet seen as a result of contact with the dust particle is eliminated.

Better cleaning the mandrel and the glass sheet before starting the experiment also ensures better results. In fact, since there is a thin layer of air between the glass sheet and the mandrel, fusion between the two is no longer a problem, as is the case with slumping directly on a mandrel; thus, slumping on a layer of air also reduces the requirement for absolutely clean working surfaces.

With all the requirements addressed and analyzed, Table 4.5 summarizes the design parameters selected for testing.

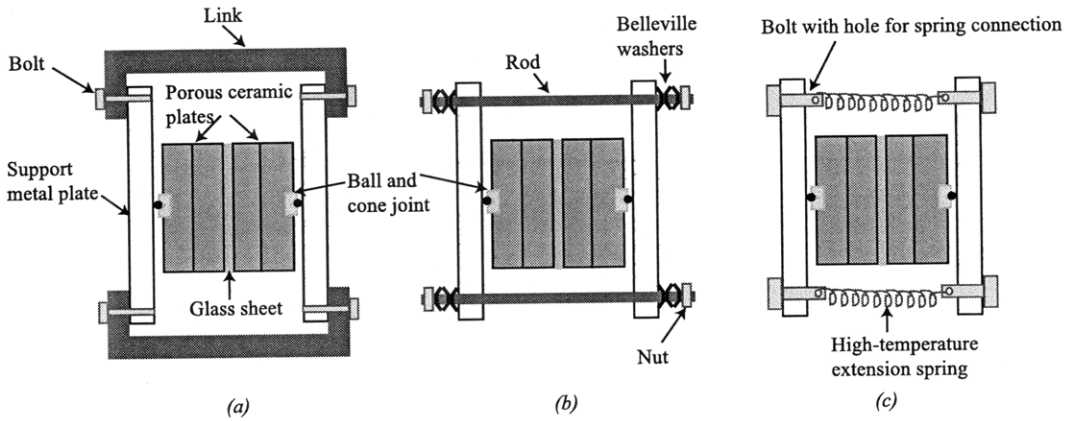

Figure 4-41: Assembly of porous ceramics using metal support plates and *(a)* links, *(b)* rods, nuts and belleville washers and *(c)* extension springs. Figure not to scale.

4.3.3 Design Criteria for Assembly of Two Mandrel/Housing Units

Having considered the design of the porous ceramic parts and the glass sheet constraint, the overall assembly is next. Since spacers have been selected previously, an assembly constraining the mandrel and housing pair and applying a compressive force is required to hold everything together during the experiment.

Assembly Technique

A straightforward way of clamping the two units together is through the use of plates and a connecting mechanism, such as a link, a rod and nuts or a spring, as shown in Figure 4-41. Since ceramic machining requires special tools not available at MIT, using metals for the non-critical parts is more practical to perform the machining at the MIT facilities; however, if metals are used, the design of the assembly takes CTE mismatches into consideration to avoid bowing the high-precision ceramic plates due to thermal stresses.

By constraining the ceramic plate at its center, it can expand at a different rate from the metal plates constraining it without distortion, since its edges are free. This is shown in Figure 4-42. A ball and cone mechanism is used to connect the metal

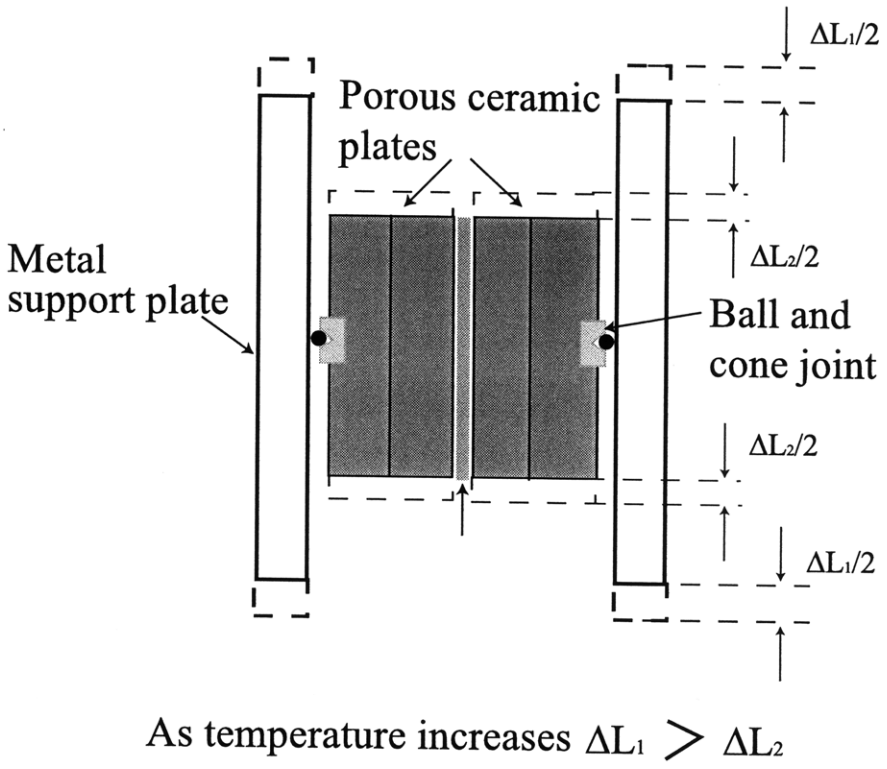

Figure 4-42: Porous ceramic plates constrained using a ball and cone joint and two metal support plates. Joint located at the center of the ceramic plates. As the temperature of the parts increases during slumping, the increase of the metal support plate length ΔL_1 is larger than the increase in the ceramic plate length ΔL_2 without affecting the shape of the ceramic plate. Figure not to scale.

plate to the ceramic housing. The center carries the load of the ceramic mandrel and housing unit and applies the compressive force on the housing. The resulting stresses must be calculated to ensure the housing stresses are below the ceramic's ultimate strength.

As for the clamping mechanism, the link shown in Figure 4-41*(a)* expands faster than the ceramic plates causing them to separate. Most metals, with the exception of molybdenum, tungsten and tantalum, which are all difficult to machine, have a CTE much higher than that of ceramics. Titanium's CTE is relatively low, about $8\times10^{-6}/°C$; however, it is one of the more expensive metals; thus, links are not the most efficient alternative. By using a rod and nuts as shown in Figure 4-41*(b)*, a series of belleville washers can be used to compensate for the differential increase in the length of the rod, which could be made of stainless steel. This is an economical and easy-to-make solution. Depending on the load needed and the spacing available, extension springs can be an option as well, as shown in Figure 4-41*(c)*.

To estimate how much compressive force is needed, the forces acting on the system are analyzed. The overall assembly requires compressive forces to:

1. carry the load of the glass sheet,
2. carry the load of the ceramic mandrel,
3. counterbalance the separating force of the pressurized air in the plenum.

Load of Glass Sheet The load of the glass sheet is involved only if the optic is carried by the friction force with the spacers, as shown in Figure 4-43. The force required to carry the load of the glass sheet is negligible when compared to the other forces involved; however, the calculation is performed for the sake of completeness. The weight of a 4" $\times$ 4" $\times$ 0.4 mm D-263 glass sheet is $\sim$ 0.1 N. What keeps the glass sheet from falling when held in the vertical is the friction force resulting from the clamping force. Thus for a coefficient of friction of 0.5 between metal (spacers) and glass, the required clamping force is 0.2 N.

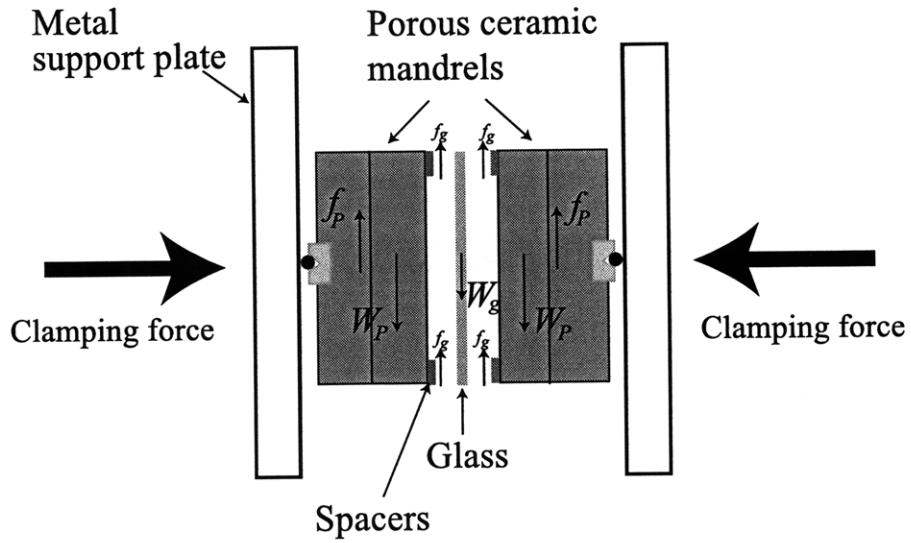

Figure 4-43: Forces acting on the assembly in the vertical direction. Friction forces f_P and f_g counteract the porous mandrel weight W_P and the glass weight W_g, respectively, to stop them from sliding. Figure not to scale.

Load of Ceramic Mandrel Since the ceramic mandrel will not be bonded to the housing, the only force keeping it from sliding is friction between the mandrel and the housing. The weight of each of the 6" $\times$ 6" $\times$ 0.5" porous silicon carbide plates is 5.5 N. The required clamping force to keep the two mandrels from sliding is 28 N for a coefficient of friction of 0.4 between two dry silicon carbide surfaces [59].

Separation Force from Pressurized Air in Plenum The pressurized air inside the plenum is typically an order of magnitude smaller than 1 psi during slumping; however, the separation force resulting from this pressure is calculated based on a pressure of up to 1 psi in case the flow control valve is accidentally opened while setting up the experiment. This pressure acts on an area of 4" $\times$ 4", the area of the plenum. The resulting force is 16 lb or 71 N per housing and mandrel or 142 N for both. If this force is larger than the clamping force, the air separates the mandrel from the housing, allowing air to leak through the joint area and causing the mandrel to slide down.

Therefore, the overal sum of forces required to maintain the assembly during the

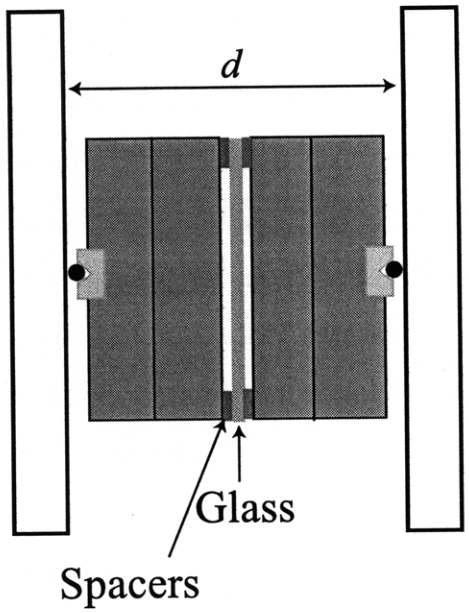

Figure 4-44: Distance between two metal support plates, d, represents required extended spring length. Figure not to scale.

experiment is $\sim$ 170 N. As a reminder to the reader, the estimated clamping force which results in glass buckling is 32 N, which is smaller than the 170 N force needed to hold all the parts together, reinforcing the possibility that the glass will buckle during the experiment.

The advantage of using springs for the needed clamping force is that they provide a predetermined linear force. If using two springs, a force of 85-90 N is needed per spring. The distance between the two metal support plates d is $\sim$ 2.8", as shown in Figure 4-44, which is the thickness of the ceramic plates combined, the glass sheet, the spacers and the thickness of the ball/cone joint. Thus if a spring is used with an initial length varying between 2" and 2.5", the resulting deformation is between 0.8" (0.02 m) and 0.3" (0.0076 m). To have the required force of 85-90 N, the spring stiffness at 600°C must be between 4,250 N/m (24 lb/in) and 11,840 N/m (67 lb/in).

Commercially available springs that withstand high temperatures are made of different grades of stainless steel, even though most rated temperatures are lower than the slumping temperature required. The most suitable spring found to meet the

length and stiffness requirements is from *McMaster-CARR*, with a spring length of 2.36" and a stiffness of 10.34 lb/in at room temperature. This is smaller than what is calculated above; however, it works if the pressure of the air in the plenum does not exceed 0.21 psi at room temperature. The anticipated design pressure for the experiment is not to exceed 0.1 psi at room temperature. Both the Young's modulus and the yield strength of stainless steel drop with temperature though, which means that the spring can yield even at lower pressures simply because it is overextended at high temperatures. Testing the springs at the slumping temperatures is an easy way of finding out whether they can be used or not. As an alternative, high-temperature springs made of Inconel X750 #1 temper, which resist relaxation with heat can be used; however, their price for 4 pieces is $240 per spring as quoted by *Draco Spring Manufacturing.*

Rods and nuts on the other hand are easy to manufacture and relatively inexpensive; however, they apply a rotary force in addition to the linear force, which can become a problem during alignment. For a force of 170 N, the nuts on each rod should be tightened to provide a preload of ~85 N. Torque on bolts and nuts is approximated by [60]

$$T = 0.2Fd, \tag{4.10}$$

where T is the torque calculated, F is the required force and d is the screw diameter. In this case, for a diameter of 3/8" or 9.525 mm, the required torque is 0.16 N-m or 1.4 lb-in. This is rather small. At room temperature a larger torque must be applied because as the temperature of the experiment is increased, the nut relaxes, the rod expands and the belleville washers lose stiffness. Tests were run with nuts tightened at different torques. It seems from experiment a torque of 20 lb-in is sufficient. The corresponding force on the ceramic housing by using Equation 4.10 is 266 lb or ~1,200 N per rod. Since there are two such rods, a total force of 2,400 N is imparted on the central region of the ceramic, distributed over a diameter of 1", the diameter of the cone part.

Finite element analysis was performed on the porous silicon carbide housing with

this force at the center. The boundary conditions are such that the surface mating with the mandrel is fully constrained. The resulting deformation and stresses are shown in Figure 4-45. As can be seen, the displacement is close to 16 μm, and the maximum stress is about 25 MPa. The tensile strength of pore-free silicon carbide at room temperature is 300 MPa. Assuming this strength decreases by the same order of magnitude as the Young's modulus does with porosity, which is by one third, then the tensile strength of the plate is 100 MPa. Thus at room temperature and during assembly, applying a torque of 20 lb-in is safe.

Once the assembled parts are placed in the furnace and the air connection established with the plenum, the pressurized air inside the plenum now pushes the housing in the opposite direction as the clamping force, reducing the stress on the housing as the temperature of the experiment is raised. Since the force is applied at an area where the ceramic housing makes no contact with the critical ceramic mandrel due to the presence of the plenum in between, these deformations with torque and pressure are not transmitted to the mandrel and thus to the glass sheet. It should be noted that the deformation of the mandrel caused by the pressure in the plenum is negligible and is counterbalanced by the force of the air in the air gap on the opposite side.

Assembly Steps

Figure 4-46 lists all the parts involved in the assembly process. Even though the experiment was conducted with the glass and ceramic plates held in the vertical direction, the actual assembly is done with the glass and ceramics placed in the horizontal direction. This removes the need to constrain the weight of the parts while precisely aligning and constraining them.

The furnace was first prepared by placing two sets of tubes, each over 4 m in length, for the air to enter the furnace, heat up and connect to the housing pairs. A second set of tubing was also placed in the furnace to read the pressure of the air in the plenum.

The next step involves the actual assembly. Two aluminum structures with 3 balls are placed at a determined distance from each other. The three ball tips form the

Displacement due to clamping force

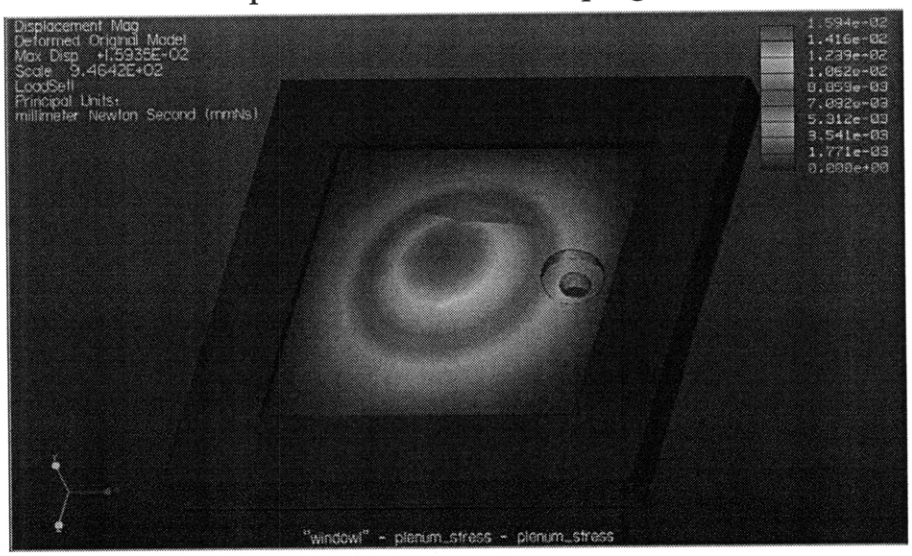

Stress due to clamping force

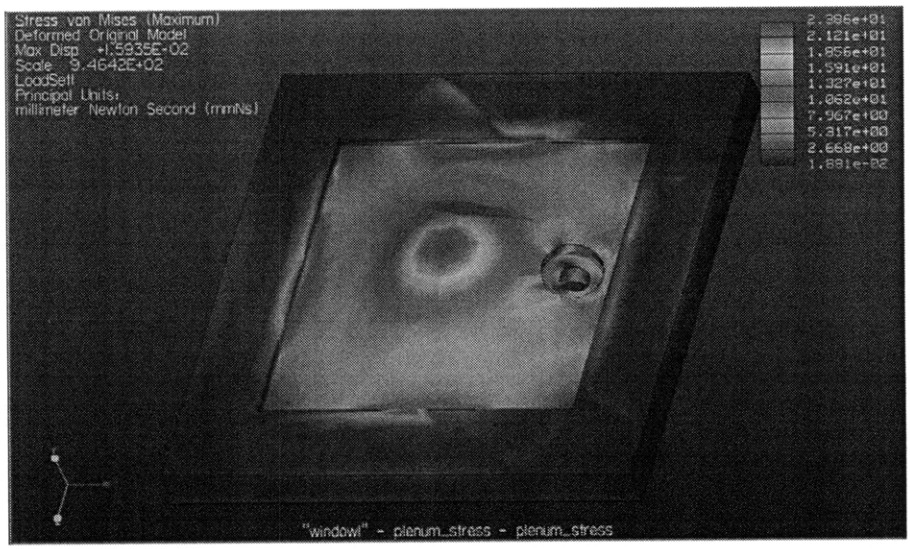

Figure 4-45: Displacement (maximum is 16 μm) and stress (maximum is 24 MPa) of housing ceramic plate as a result of a torque of 20 lb-in on each rod to clamp the plates together.

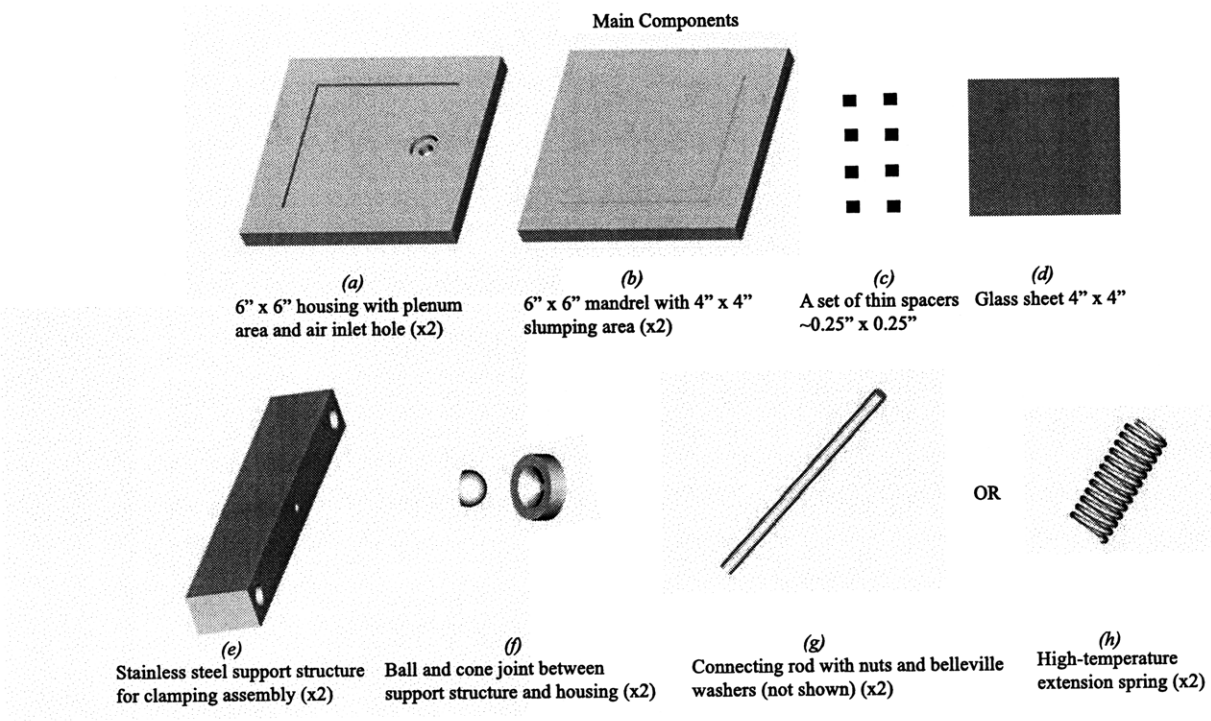

Figure 4-46: All parts involved in the assembly process.

reference plane in which assembly begins. Three alignment posts are located on one of the aluminum structures. These posts align the ceramic plates to one another. Figure 4-47 shows the step-by-step assembly process, both in a schematic drawing and in actual pictures.

The first step is to place the first stainless steel support structure shown in Figure 4-46*(e)* with the two springs or connecting rods between the aluminum structures, as shown in Figure 4-47*(b)*. The next step is to place the first housing on the three reference balls, as shown in Figure 4-47*(b)*. The housing is pushed against the alignment rods to constrain it in the x and y directions. Then the first mandrel is placed on top of the first housing while pushing it against the alignment posts, as shown in Figure 4-47*(c)*. The first set of spacers is then placed at the corners of the slumping area on the mandrel. The glass sheet is then placed on top of the spacers and the second set of spacers is placed on the glass sheet, as shown in Figures 4-47*(d)*, *(e)* and *(f)*. A different spacer configuration can be done at this step if necessary, as discussed in Section 4.3.2. With the glass and spacers in place, the second set of

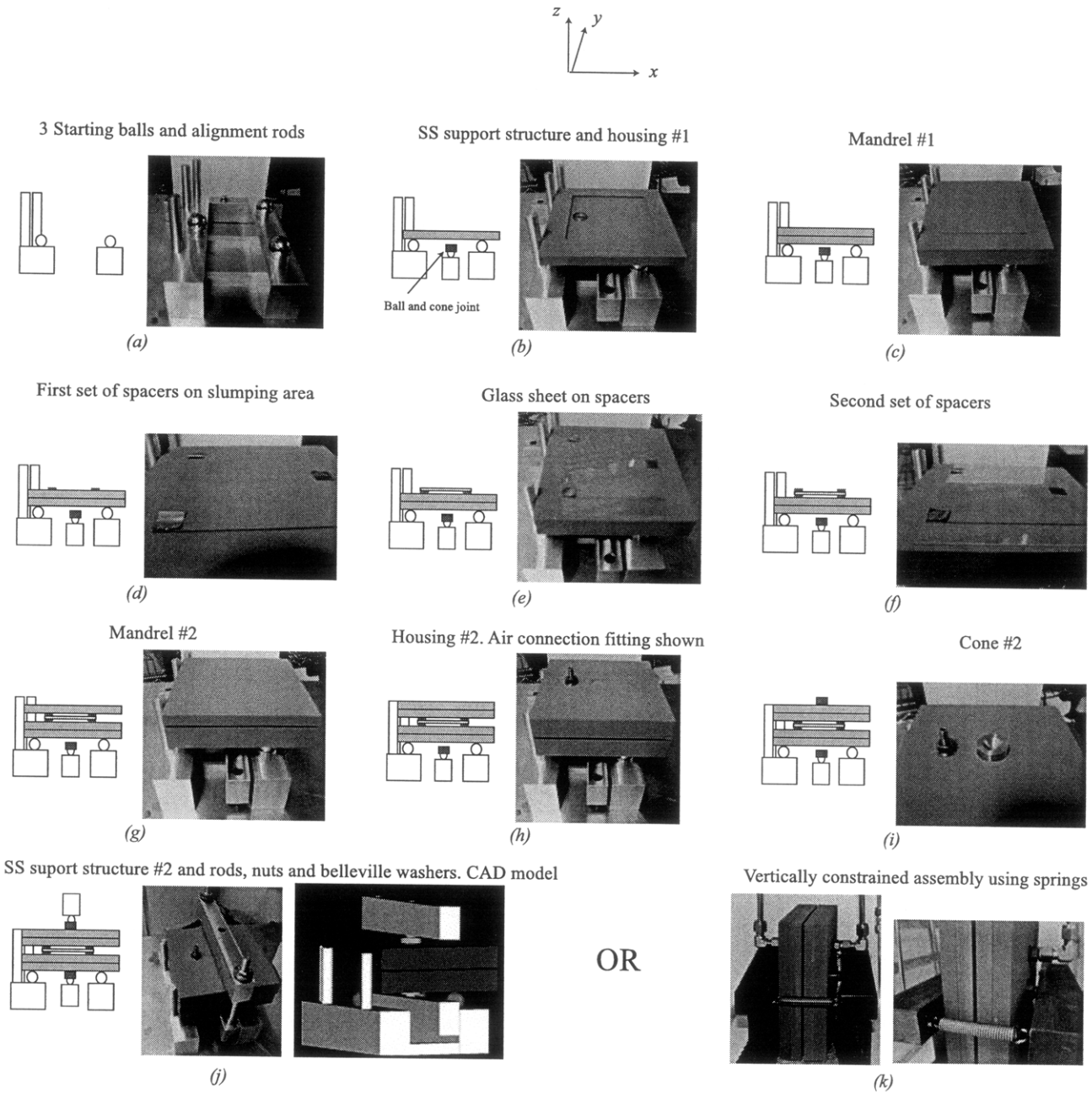

Figure 4-47: Assembly steps. Schematic figures showing side view not to scale. Steps explained in text.

mandrel/housing is ready to be assembled. The mandrel is carefully placed on top of the spacers while pushing it against the alignment rods to ensure it is aligned with the lower ceramic plates, and the second housing is placed next similarly, as shown in Figures 4-47*(g)* and *(h)*. The second cone part is placed on the back of the housing, as shown in Figure 4-47*(i)*. The housing has a recess that is 0.05" or 1.27 mm deep and of the same diameter (with a tolerance of +0.003") as the cone part (diameter tolerance -0.003") to facilitate placing the two cone parts against the two housings. The second stainless steel support structure is directly placed on the cone or slid along the connecting rods, such that the ball bolted on the support structure mates with the cone. If springs are used, the springs are then hooked to the top support, as shown in Figure 4-47*(k)*. If a rod is used, the second set of belleville washers are put around the rod, and the nuts are tightened using a torque wrench to a torque of 20 lb-in, as shown in Figure 4-47*(j)*.

Since springs do not have a rotational factor that might compromise alignment during assembly, they were tested first. The ceramic plates are pulled together by the force of the spring, as shown in Figure 4-48; however, after the temperature of the furnace was raised to 570°C, at which point glass sags due to its weight in a 10 minute interval, the springs began to plastically deform, and the mandrel slid along the housing. Silica seals in the form of thin, wide ropes were placed underneath the ceramic plates to minimize the impact, should they slip as a result of joint loosening; however, the mandrels do not fall far enough to make contact with the bottom of the furnace.

Instead of purchasing the expensive high temperature inconel springs, the rod and nut design was tested. By ensuring the rotational force from the wrench is not transmitted to the ceramic plates, the alignment of the plates is maintained while the nuts are tightened. At 20 lb-in torque per rod, the plates are properly sealed at the mandrel-housing joint. Higher torques can easily break the brittle ceramic housing, since the concentrated force is directed at the center of the housing.

The overall assembled parts are shown in Figure 4-49, connected to the tubes inside the furnace. With the assembly ready at hand, testing can be done. The next

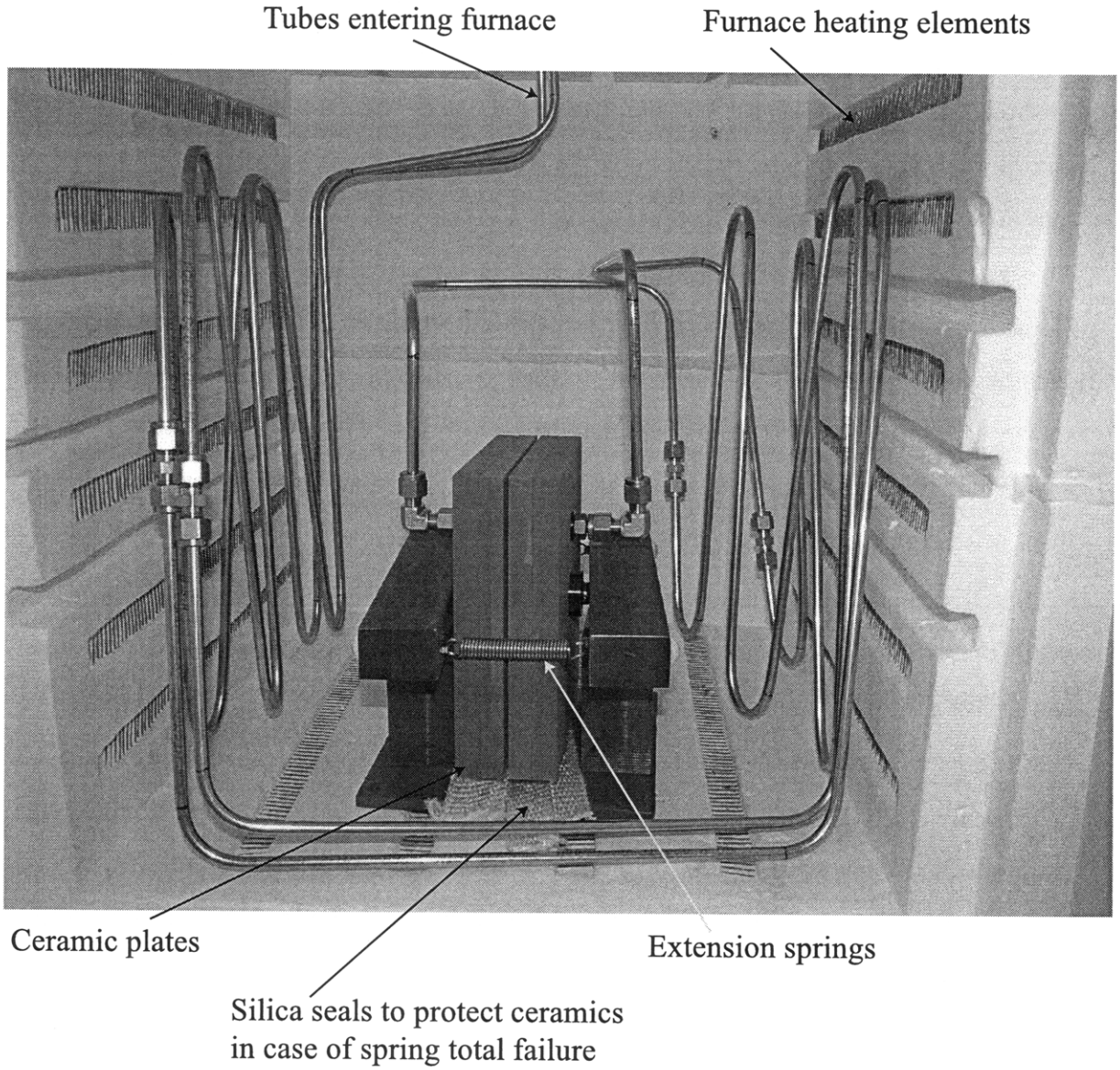

Figure 4-48: Ceramic plates assembled using stainless steel extension springs. Note this picture does not include the stagnant lines to be connected to the housings to measure the pressure at the plenum using high precision pressure transducers located outside the furnace.

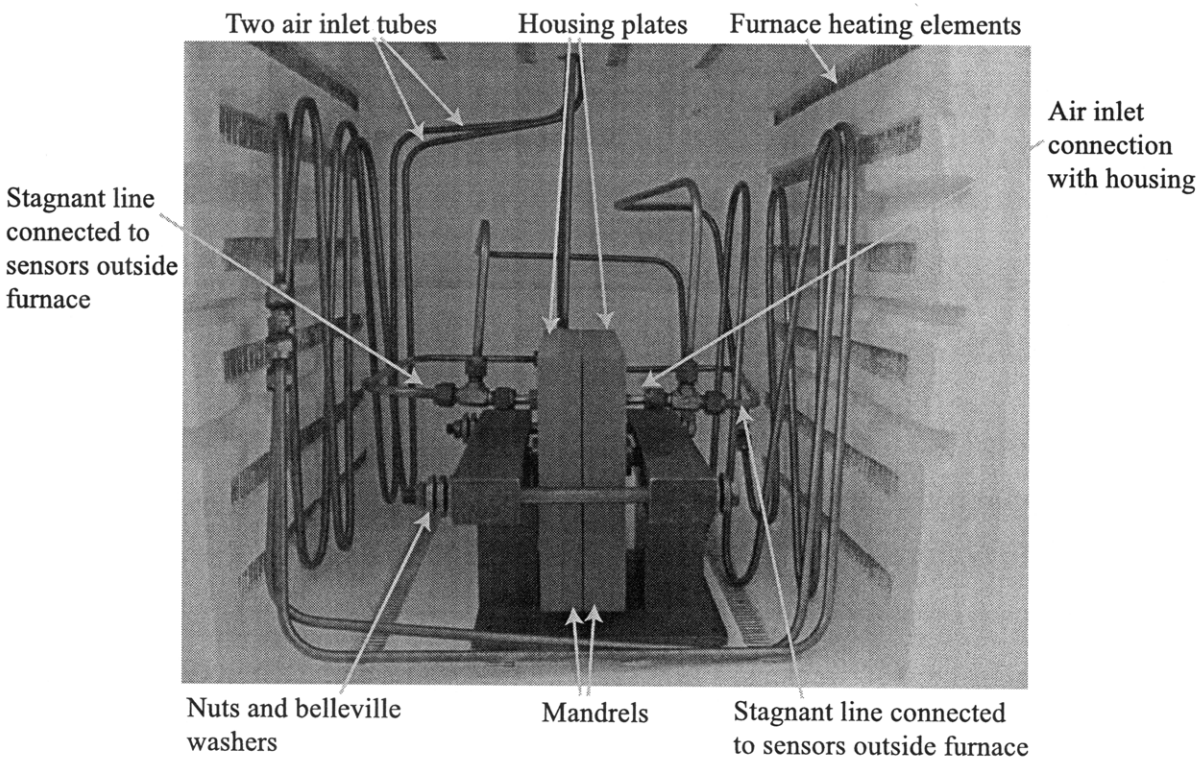

Figure 4-49: A sheet of glass between two flat mandrels ready for slumping inside a furnace.

chapter discusses the different experiments conducted and the results obtained with this configuration.

4.3.4 Error Budget

To estimate how much of an error is accumulated during assembly, an error budget was performed for an assembled scheme with coordinate systems shown in Figure 4-50. The coordinate systems translate but do not rotate, as can be seen in the figure. The errors are mostly the result of random errors in the form of machining tolerances of all parts involved and surface flatness irregularities in the ceramic pieces. Table 4.6 shows the sum and the root sum square (RSS) of errors in the x, y and z directions. The nominal value of x in the table represents the size of the gap between the two ceramic mandrels, where the glass sheet and spacers would be placed. As can be seen

Nominal Coordinates	Sum Random Errors	RSS Random Errors
$x = -0.0167$	$\delta x = 0.0012$	$\delta x = 0.0006$
$y = 0$	$\delta y = 0.003$	$\delta y = 0.0016$
$z = 0$	$\delta z = 0.001$	$\delta z = 0.0007$

Table 4.6: Error budget of assembly with coordinate systems shown in Figure 4-50. The assembly considers spacers that are 0.0005" (12.7 μm) thick. Units are in inches.

from this table, the gap can vary by 0.0006" or $\sim$ 15 μm. The systematic errors in the form of deformations resulting from the clamping force and hertzian stresses cancel out due to the symmetry of the design.

It should be noted that if a design air gap of 12.7 μm, which represents the thinnest titanium spacer available, is used between the glass sheet and each mandrel, then an error of up to 15 μm in the gap in addition to the glass sheet's original surface warp (up to 0.6 mm P-V) and thickness variation (up to $\pm$20 μm) can result in the glass making contact with the ceramic in some areas. This would in turn cause the glass sheet to stick to the mandrel. Experiments can show whether this is the case or not, but if this turns out to be a problem, the thickness of the spacers can be increased such that the variation in gap due to design errors, glass warp and glass thickness variation can be accommodated.

4.4 Conclusion

A method of slumping glass sheets on grooved surfaces is developed in an attempt to control the air-gap pressure profile shaping the sheet. The results show that when slumping on one side of the sheet only, the glass tends to maintain a bow.

As a next step, an apparatus using two porous ceramic mandrels is analyzed and developed. The different design parameters are studied and optimized to ensure the apparatus is capable of overcoming high-temperature related challenges. The experimental results are discussed in the following chapter.

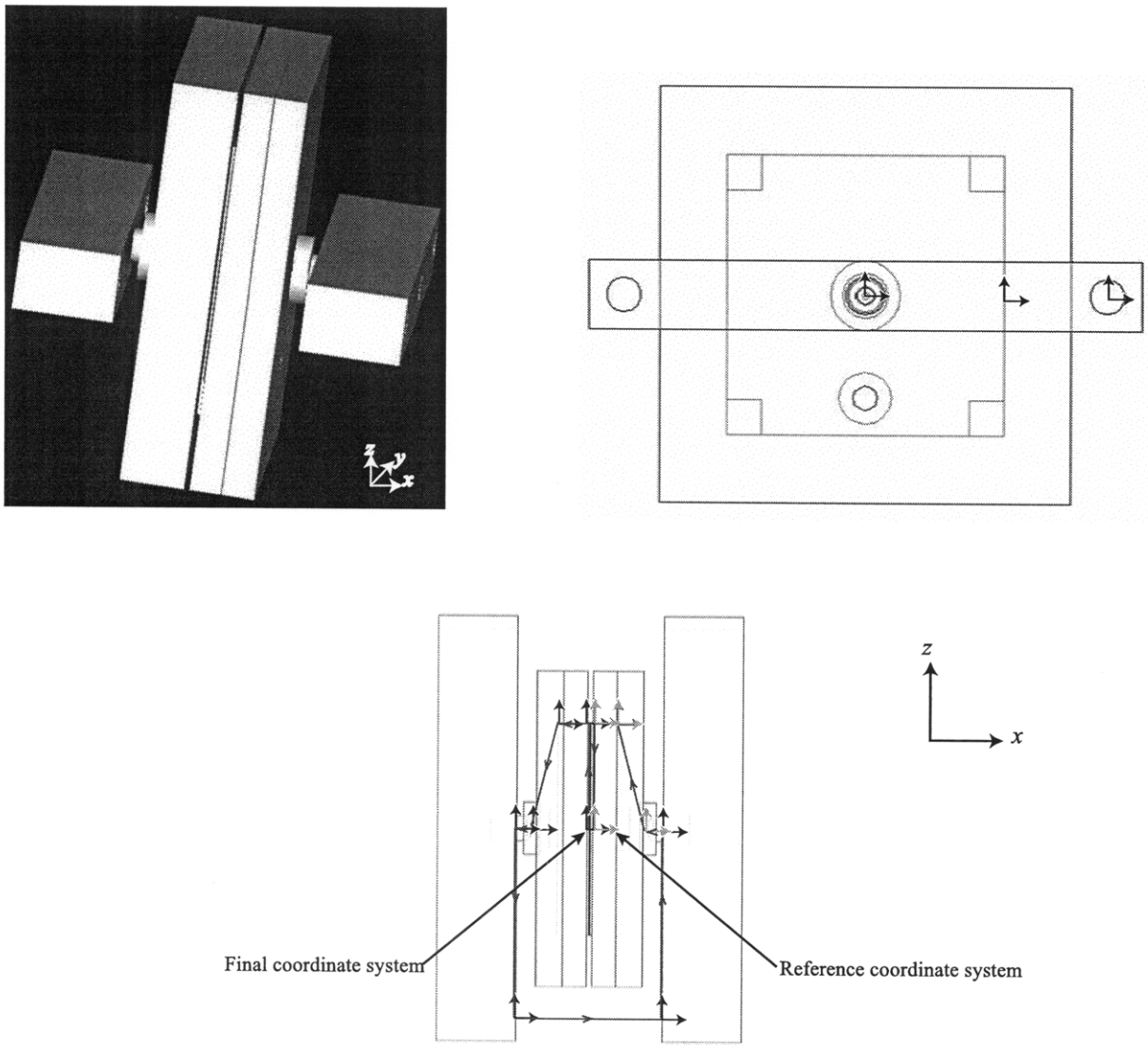

Figure 4-50: Coordinate systems connecting the flat face of one mandrel (left mandrel) to the flat surface of the second mandrel (right mandrel) acting as a reference.

Chapter 5

Slumping Results and Discussion

With the slumping apparatus ready, testing can be performed to see the results of shaping glass sheets with hot fluids, air being the fluid of choice for this particular application.

The metrology system used to measure the surface of glass is the in-house developed Shack-Hartmann system, which utilizes a deep-ultraviolet (UV) light from a mercury arc lamp to measure the whole surface of glass sheets [61]. The largest sheet this system is designed to measure is 100 mm $\times$ 140 mm in area. The UV light reflects off the test substrate and is directed into a camera by a series of optics. An array of microlenslets is placed at the system image plane, where each microlenslet focuses the part of the incident beam it sees onto a charge-coupled device detector to form a spot on the detector. A planar waveform reflecting from a flat optic produces a regular array of spots, whereas an aberrated waveform from a warped optic produces a distorted pattern of spots. The difference between the spot locations from a reference flat mirror and the test substrate determines the slopes of the wavefront hitting each microlenslet. Software then reconstructs the test wavefront utilizing Zernike polynomials. The overall repeatability of this system is 0.4 arcsec.

A challenge when measuring the surface flatness of optics with high accuracy is the limited dynamic range of the metrology tool. In other words, as the optic surface further deviates from nominal flatness, the metrology tool can no longer analyze the surface. In the case of the Shack-Hartmann system, each microlenslet has a specific

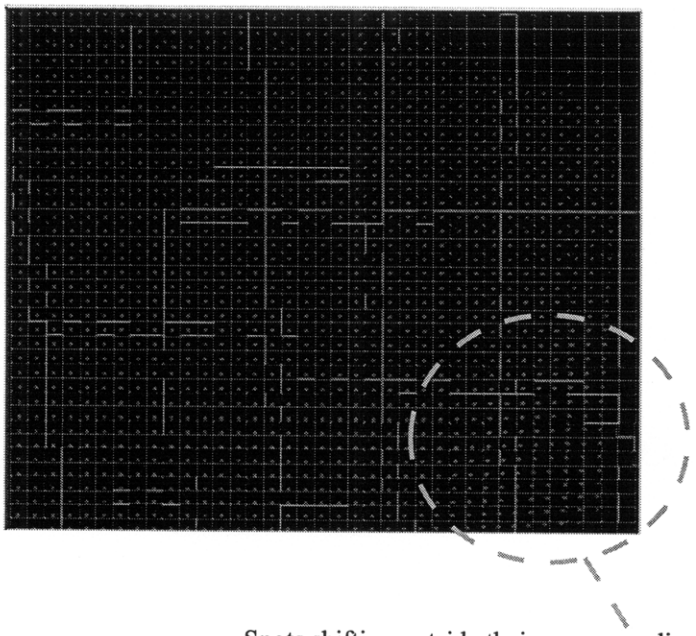

Figure 5-1: Microlenslets focus spots on the detector. The array of boxes represents the areas-of-interest (AOI). The central region of this optic is relatively flat, whereas on the right side and the lower right corner, the spots shift from their corresponding AOI to the neighboring ones indicating the optic is distorted near the edge.

area on the detector dedicated to this lenslet. Such an area is referred to as an area-of-interest (AOI). The Shack-Hartmann system becomes "out of range" when the focal spot of one microlenslet is in the AOI of another lenslet. This is the result of a large distortion in the wavefront hitting the lenslet. Figure 5-1 shows the spots on the detector from an optic with a relatively flat surface in the middle and a deformed surface near the lower right corner. This distortion causes the focal spots to shift into neighboring AOI's.

Andrew Lapsa [62] developed a code to track focal spots found on the detector and assign them to the appropriate lenslet for the software to reconstruct the wavefront correctly. This has increased the dynamic range of the Shack-Hartmann; however, limitation remains when the optic is warped enough that a number of microlenslets focus the wavefront in one region, making it difficult to identify the boundaries of a

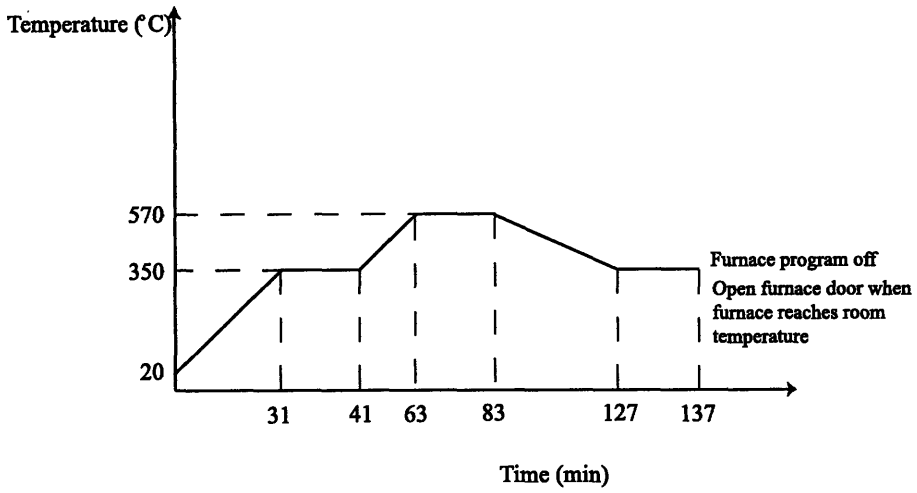

Figure 5-2: Temperature profile used after many iterative trials for slumping glass sheets

single spot and associate it with the correct lenslet.

5.1 Spacer Configuration and Thickness Selection

The first test is to see whether a glass sheet buckles or is stressed as it is subjected to the slumping time-temperature profile discussed in Chapter 4. This is the result of the glass sheet expanding more than the silicon carbide mandrels while being constrained by thin spacers between the mandrels. A sheet of glass is assembled and slumped, using the temperature profile shown in Figure 5-2. The glass sheet is then placed in the Shack-Hartmann field of view and constrained by a device specifically designed to hold thin optics without distorting them and with a repeatability of 1 arcsec [4].

Looking at the raw data of the spots on the detector, as shown in Figure 5-3, it can be seen that the edges where the spacers make contact with the glass are highly distorted, and the optic's surface quality is very poor in those areas.

This has been anticipated in the previous chapter, Section 4.3.2, and different spacer configurations have been proposed. The first configuration, shown in Figure 4-35*(a)* was tried first. A sheet of glass was cut diagonally at its lower edges. During assembly, one spacer 0.25" $\times$ 0.25" in area, was placed in the middle of the top edge

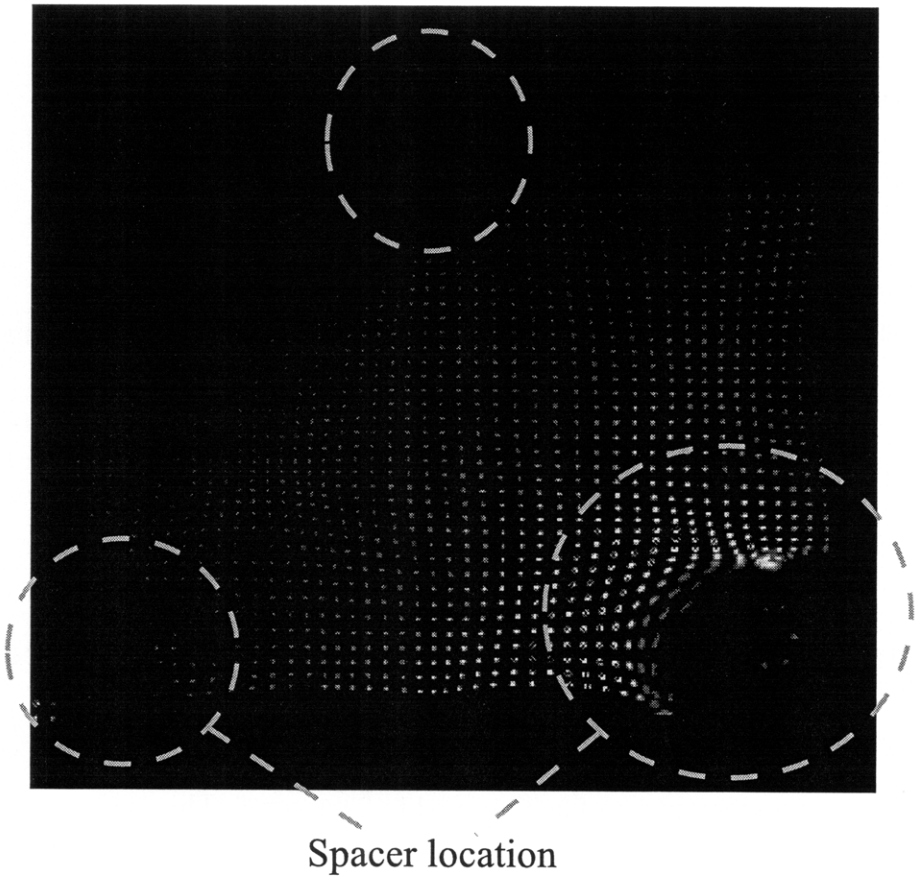

Figure 5-3: Spots from a glass sheet constrained by three pairs of spacers during slumping. The effect of the spacers can be seen in the dotted circles. The glass expands faster than the silicon carbide mandrels shaping it; thus, since the glass is rigidly clamped by the spacers, it distorts during the slumping process resulting in a badly warped surface with poor edge quality.

of the glass on each side, such that the glass would hang from this spacer when held vertically. The remaining two spacers of equal size were placed where the glass is cut. The small pieces of glass cut from the main sheet were squeezed between the two lower pairs of spacers to ensure the gap is equal at the three spacer locations. The assembly was completed and the glass slumped following the same profile as shown in Figure 5-2. After disasembly, the glass sheet was found to be cracked at the top around the spacer, and the crack had propagated through the length of the glass. Placing a spacer directly on the main glass sheet and applying clamping forces results in high stresses on the glass surface, which can lead to fracture, especially if the glass has initial surface imperfections.

The configuration shown in Figure 4-35*(b)* was tried next. During assembly in this lay-out, the glass sheet makes no contact with the adjacent small pieces that are placed between pairs of opposing spacers. This is only true when the glass is in the horizontal plane while it is being assembled; however, after the assembly is clamped and rotated such that the glass and mandrels are placed vertically inside the furnace, the glass sheet then slides downwards with gravity until it is stopped by the small pieces of glass between the spacers. This is shown in Figure 5-4. This means that the glass is no longer free at these contact edges, which might cause the glass to warp near the contact points during slumping. As the air is turned on to flow through the mandrels, the glass is pushed away from the left mandrel to become equidistant between the two mandrels; however, if jammed at the lower edges, then as the glass softens, its top free end finds an equilibrium position between the two mandrels, whereas the lower jammed ends remain in their original position.

As a reminder, the thickness of the spacers used is 12.7 μm. These are the thinnest spacers found at this time that can withstand slumping temperatures. It is noted that the glass sheet is not free to move when assembled, even though none of its edges is making contact with any obstacles. This is because the warp of these glass sheets is on the order of tens if not hundreds of microns, and when a sheet of glass is squeezed in a nominal gap of 12.7 μm, the surface of the glass sheet makes contact with the silicon carbide mandrels. The results after slumping were very discouraging. The

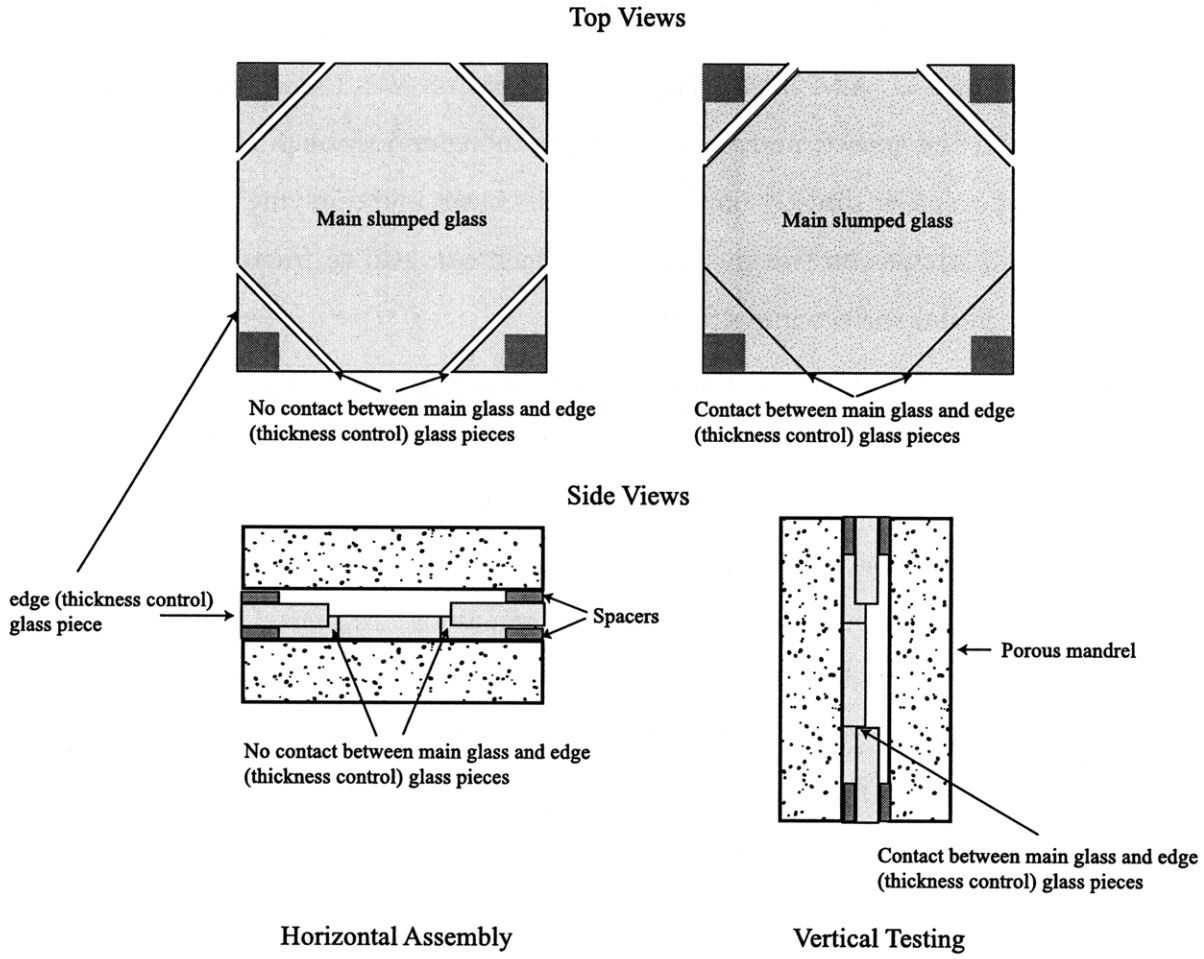

Figure 5-4: *(Left)* Glass edges free during assembly. *(Right)* Glass edges make contact once assembled and rotated into vertical direction for slumping. Edges where contact happens can jam and lead to errors in the slumped glass shape. Figure not to scale for clarity.

slumped glass sheet was seen to have many dimples and fractures on its surface as a result of being squeezed between and sticking to the mandrels at numerous spots, even though the mandrels have pressurized air flowing through them.

If glass D-263 or any other flat-panel display glass is to be used in its current state as it is sold by the manufacturer, then the size of the air gap must be increased to accommodate the initial large warp these glasses have. All glass manufacturing processes that allow glass to flow with gravity have surface flatness errors on the order of tens and hundreds of microns. This is because there is no precise lateral control on the glass as it is flowing vertically downwards in its viscous state to form sheets. An attempt was made to first slump the glass sheet against a flat mandrel horizontally, with no air flow; however, the dimples introduced on the surface of the slumped glass due to the presence of particulates represent high-spatial frequency errors that were more difficult to correct than was the case with the original low spatial-frequency error or warp of the glass sheet.

A.D. Mackay was contacted to see what other options are available for spacers. It is noted that the available foil thicknesses made of materials that withstand high temperatures are 12.7, 17.5, 25, 50 and 75 μm. The first two and the last options are made of titanium. The third thickness listed is made of tantalum, and the fourth thickness is made of tungsten. Since the first thickness does not seem to be effective for glasses with large initial warp, and the second option is not much thicker than the first, the choice is between the 25, 50 and 75 μm thick foils. The mean of 50 μm was selected for the next set of experiments as a starting point. A second advantage of using a thicker spacer, and thus a larger gap, is the resulting looser tolerance on surface cleanliness, since this gap is large enough to absorb the average size of particles varying between 5 and 10 μm. This is ideal in a glass manufacturing facility, where refractory materials are surrounding the sheet as it is being formed. It should be noted that even though this gap is much larger than what is typically recommended for air bearing applications, viscous flow is still achieved in the case of slumping at close to 600°C mainly because the viscosity of air increases by 122%, as shown in Section 3.2.1. It should also be noted that having the glass sheet constrained vertically between two

porous mandrels is an advantage in this case, since this minimizes the load carrying requirements from the mandrels at larger gaps.

5.2 Slumping Results

In order to evaluate the performance of this process, several tests were planned. At first, a single glass sheet was slumped, and both its front and back surfaces measured. A second test involved a second glass sheet slumped and both surfaces measured. A third test involved one of the already slumped sheets, which would be slumped again, and both surfaces measured. This would provide a picture of the repeatability of the process, and identify its limitations.

5.2.1 Results of Individual Sheets

The first sheet tested is referred to as Glass 1. The sheet's corners were cut such that it had the final shape shown in Figure 4-35*(b)*. Both the front and the back surfaces were measured, the sheet was then assembled, slumped, disassembled and measured again. The glass front and back surfaces are arbitrarily chosen and labeled before the experiment is conducted.

The back surface of Glass 1 before slumping is shown in Figure 5-5. It has a surface of 440 μm peak-to-valley (P-V). Unfortunately, the front surface results in inseparable spots on the Shack-Hartmann detector, and thus its 3-D surface map could not be generated. The spot distribution on the detector, however, indicates that the front surface is concave while the back surface is convex.

During assembly, the front or concave surface of Glass 1 was put face down, thus facing the left mandrel. After slumping, the surfaces were measured again, and the results are shown in Figure 5-6*(a)*. As can be seen, the front surface has a P-V of 14.72 μm, whereas the back surface has a P-V of 16.19 μm. Since this measurement is a peak-to-valley measurement, it should be noted that the peak in the figures is where the glass sheet makes contact with the lower spacer areas. As anticipated, this contact area is causing errors in the readings. If the lower spacer areas are removed

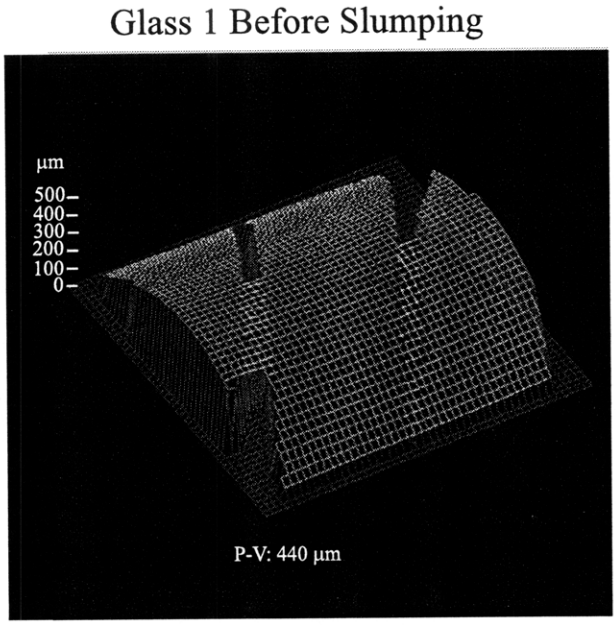

Figure 5-5: Front surface of Glass 1 with 440 μm P-V of initial warp as obtained from manufacturer

from the reading, the peak-to-valley value drops to ~ 8 μm.

A second glass sheet, named Glass 2, was also slumped. The sheet's front surface of 413.13 μm P-V before slumping is shown in Figure 5-7. This time, the convex part of the sheet was placed face down during assembly facing the left mandrel and the assembly completed. The slumping profile followed was the same as Glass 1. The measured surfaces after slumping are shown in Figure 5-8, where the front is shown in Figure *(a)* to have a surface of 14.19 μm P-V and the back shown in Figure *(b)* to have a surface of 15.04 μm P-V.

Glass 1 was slumped again and referred to as Glass 1a. In this case, the edge constraint was changed by having a point contact instead of a line contact at the edges, as shown in Figure 5-9. The glass sheet was placed in the exact same orientation and direction it was during the first run. After slumping, the front and back surfaces were measured, as shown in Figure 5-10, where the front surface is 11.19 μm P-V, and the back surface is 11.71 μm P-V. It was initially thought that by minimizing contact with the spacer constrained edge glass pieces, the main glass sheet slumps to a flatter

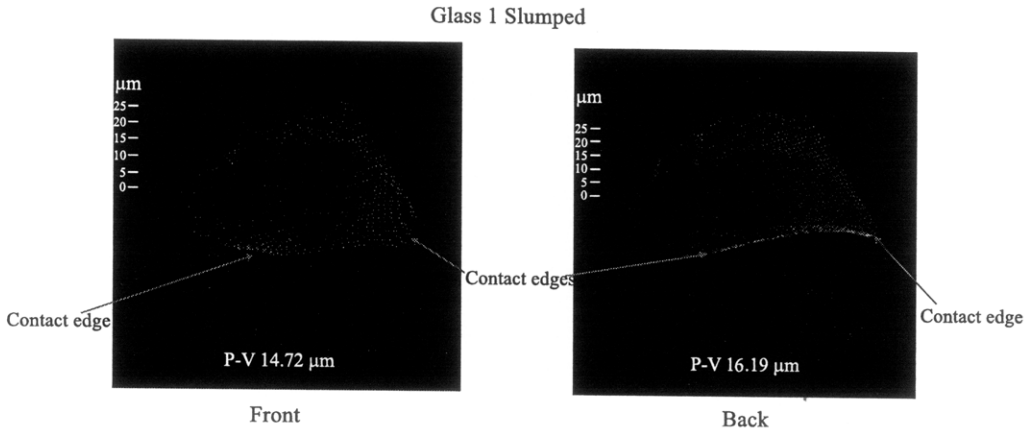

Figure 5-6: *(Left)* Front surface of slumped Glass 1. *(Right)* Back surface of slumped Glass 1. When flipping the glass sheet from front to back, the right edge in the front picture becomes the left edge in the back picture; however, the top and bottom edges of the glass remain unchanged.

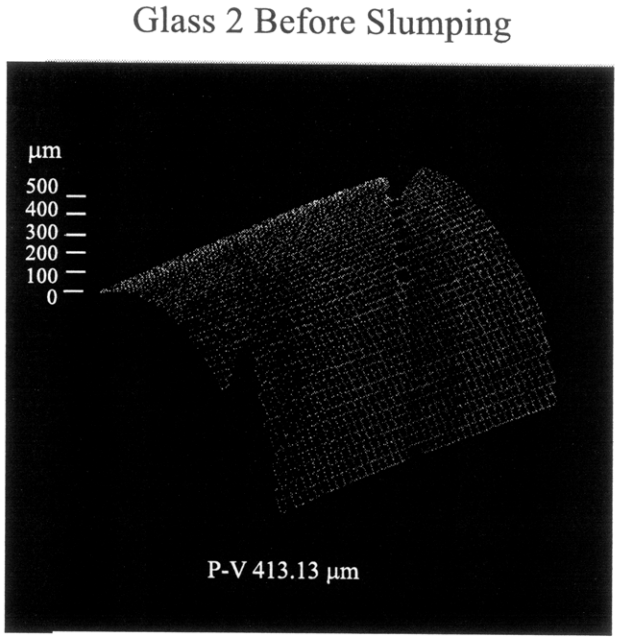

Figure 5-7: Front surface of Glass 2 with over 400 μm P-V of initial warp as obtained from manufacturer

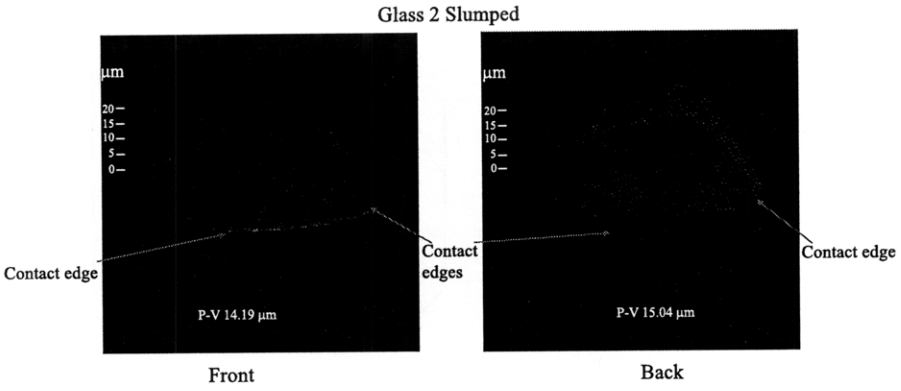

Figure 5-8: *(Left)* Front surface of slumped Glass 2. *(Right)* Back surface of slumped Glass 2. When flipping the glass sheet from front to back, the right edge in the front picture becomes the left edge in the back picture; however, the top and bottom edges of the glass remain unchanged.

final shape. This is tested with a third glass sheet Glass 3.

The original shape of Glass 3 is shown in Figure 5-11, with a surface of 84.72 μm P-V, which is much flatter than the first two sheets. All glass sheets are randomly selected from a batch. The glass sheet was assembled such that it makes a point contact on each of its lower edges, as shown in the right of Figure 5-9. After slumping, both the front and back surfaces are measured, as shown in Figure 5-12. The front has a surface flatness of 10.67 μm P-V, whereas the back has a surface flatness of 9.66 μm. This surface is initially believed to be of better flatness for two main reasons: The edges of the glass are constrained at a point rather than a line, and the starting warp of the glass sheet has less than half of the warp of the previous two glass sheets; thus, for the same slumping period, better surface flatness is achieved with this glass than with the previous two. A more detailed analysis below shows that in fact, the central region of Glass 3 is worse than the two sheets before.

It seems that the edges are introducing arbitrary warp on the surface of the sheet, depending on how it is constrained during slumping. Since the silicon carbide mandrels have a flatness of ~4-5 μm P-V in their central region, the goal is to reduce the glass surface peak-to-valley value to the same order as that of the mandrels in the

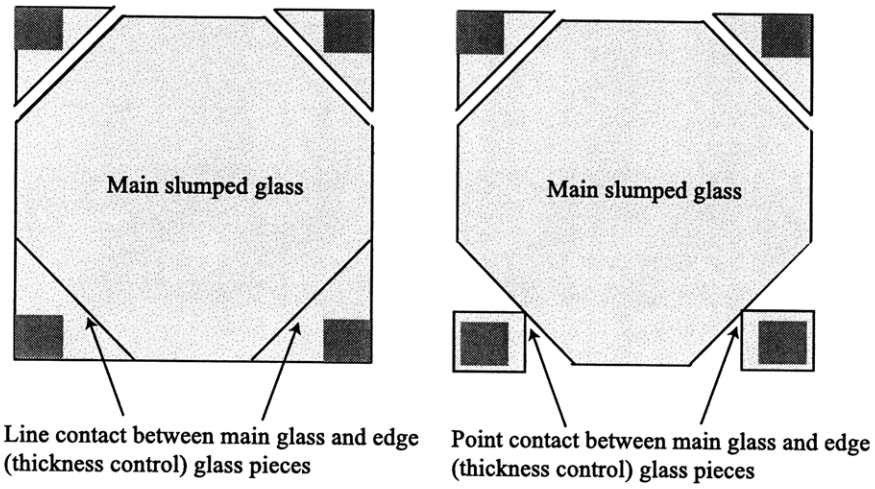

Figure 5-9: *(Left)* Main glass sheet making line contact with lower edge glass during slumping *(Right)* Main glass sheet making a point contact with the lower edge glass during slumping. The lower edge glass with spacers control the gap thickness. Figure not to scale.

central region and avoid the edge effects.

5.2.2 Comparison between Different Results Using Zernike Polynomials

Zernike polynomials are a set of orthogonal polynomials described within a unit circle and are typically used to describe wavefronts. The higher the order of the polynomial used, the more details can be described accurately on a given wavefront. Since the polynomials are orthogonal, the effect of each order can be studied independently from the remainder of orders used to depict a wavefront [63]. These polynomials are used to study the detailed variation in the surface of the glass sheets tested. Since the effect of the spacers seems to dominate the peak-to-valley value of the glass sheet surface, Zernike polynomials are extracted and compared for the central region of the glass sheet only, to avoid edge effects.

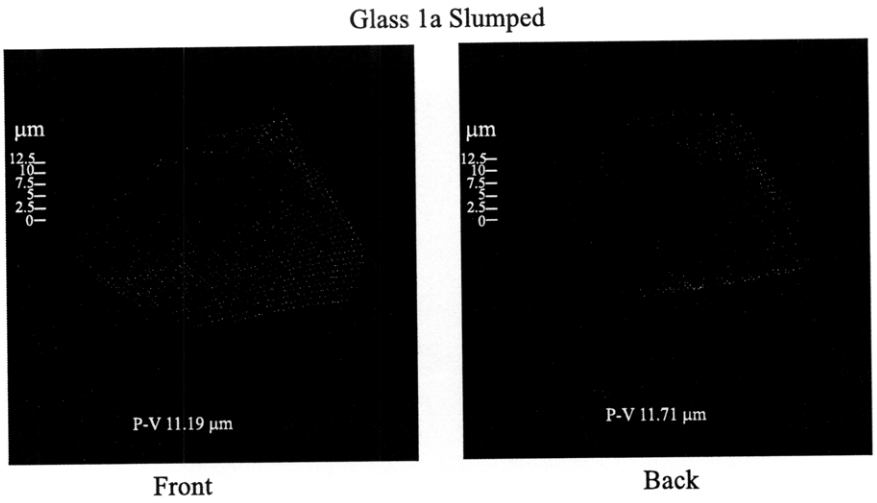

Figure 5-10: *(Left)* Front surface of slumped Glass 1a. *(Right)* Back surface of slumped Glass 1a. The glass is constrained at a point instead of a line at each of the lower edges. When flipping the glass sheet from front to back, the right edge in the front picture becomes the left edge in the back picture; however, the top and bottom edges of the glass remain unchanged.

Repeatability of a Single Glass Sheet

Table 5.1 shows the Zernike coefficients of the front surface of Glass 1 after it is slumped the first time and the second time. These polynomials are obtained in a circle of radius ~ 30 mm at the center of the sheet to reduce the effects of the edges. As can be seen, the difference between the two slumping steps is submicron in all the coefficients. By using this difference, a 3-D plot showing the change between the two runs can be reconstructred, as shown in Figure 5-13, where the peak-to-valley value of the surface is 1.3 μm. Figure 5-14 shows the angular repeatability with 6.23 arcsec RMS along the x direction and 5.68 arcsec RMS along the y direction. To have a better understanding of the distribution of the data, Figure 5-15 shows the histogram of the difference in topography and angles between the two slumping steps.

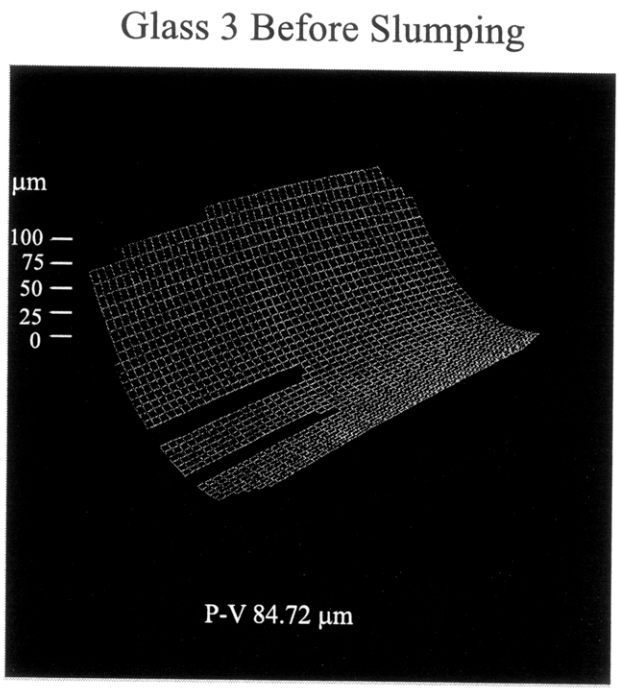

Figure 5-11: Front surface of Glass 3 with 84.72 μm P-V of initial warp as obtained from manufacturer

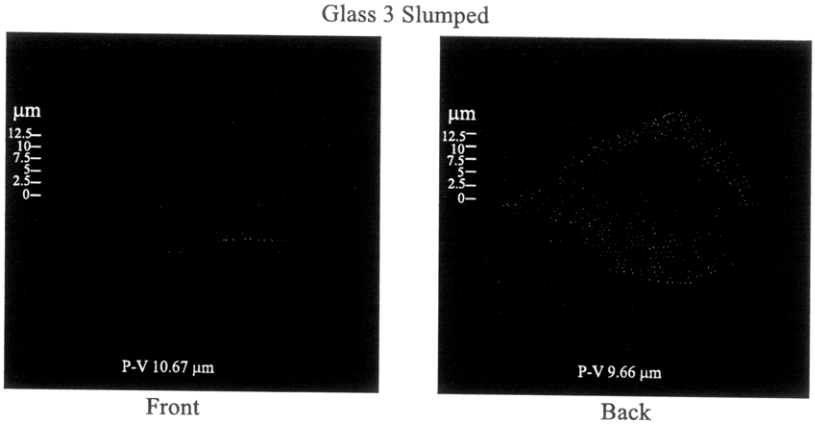

Figure 5-12: *(Left)* Front surface of slumped Glass 3. *(Right)* Back surface of slumped Glass 3. The glass is constrained at a point instead of a line at each of the lower edges. When flipping the glass sheet from front to back, the right edge in the front picture becomes the left edge in the back picture; however, the top and bottom edges of the glass remain unchanged.

Zernike Coefficient	**Glass 1 front surface (μm)**	**Glass 1 front surface 2^{nd} run (μm)**	**Difference (μm)**
Z20	-1.316	-1.81	-0.494
Z21	0.022	0.366	0.344
Z22	0.526	0.452	-0.074
Z30	0.1025	-0.129	-0.2315
Z31	0.0945	0.172	0.0775
Z32	0.43	0.2645	-0.1655
Z33	0.5165	0.442	-0.0745
Z40	-0.129	-0.098	0.031
Z41	-0.00049	0.0775	0.078
Z42	-0.0065	-0.077	-0.0705
Z43	-0.081	-0.1565	-0.0755
Z44	-0.0825	-0.119	-0.0365

Table 5.1: Zernike coefficients over a 60 mm diameter of the front surface of Glass 1 after it is slumped twice

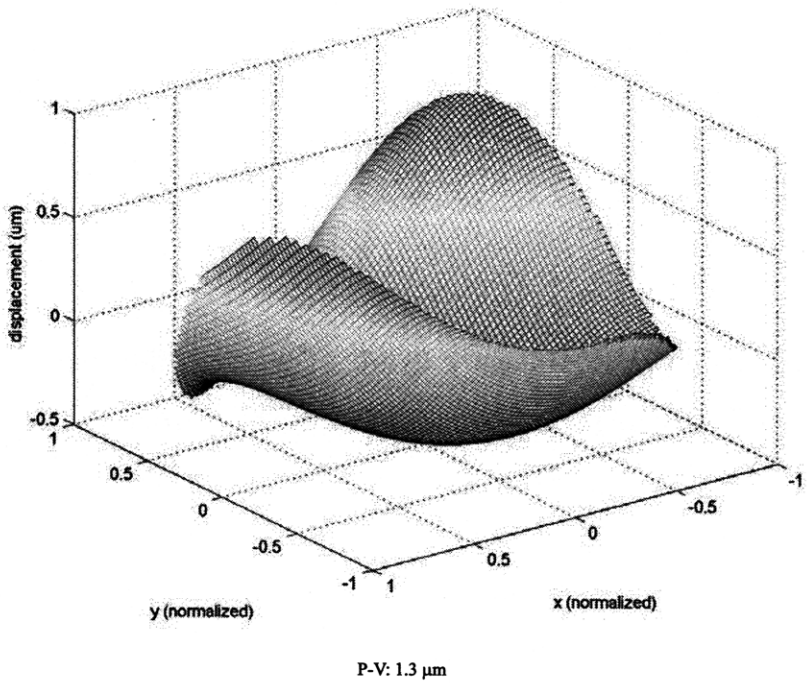

Figure 5-13: Difference in the surfaces of Glass 1 over a 60 mm diamater after it has been slumped twice

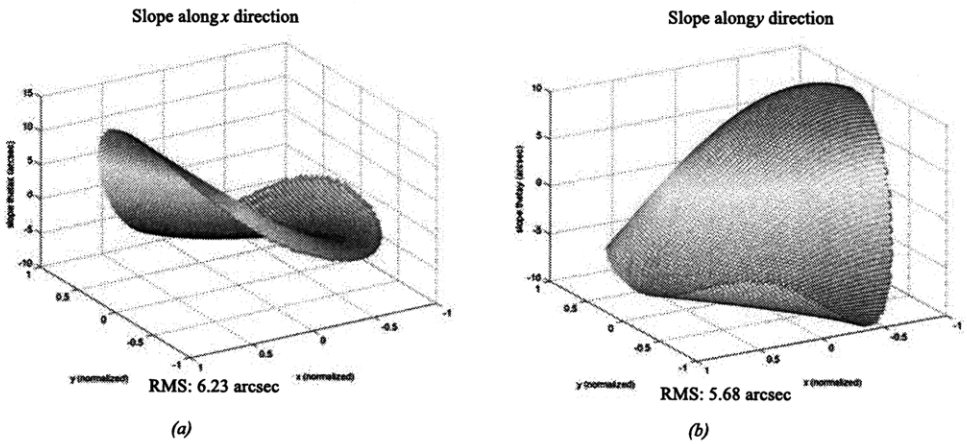

Figure 5-14: Difference in the angles of the surface of Glass 1 over a 60 mm diameter after it has been slumped twice. *(a)* Slope along the x axis. *(b)* Slope along the y axis.

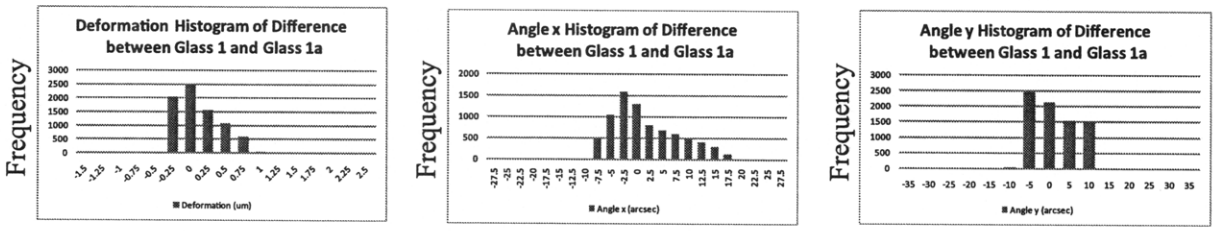

RMS 0.31 μm (a) RMS 6.23 arcsec (b) RMS 5.68 arcsec (c)

Figure 5-15: Histogram of the difference in the topography and angles of the surface of Glass 1 over a 60 mm diameter after it has been slumped twice.

Repeatability of Two Different Glass Sheets

Having seen how the same glass behaves after two slumping attempts, the difference between two different glass sheets after they are slumped is studied next. The Zernike coefficients of Glass 1, Glass 2 and their difference is shown in Table 5.2. The surface of the difference is reconstructed and shown in Figure 5-16. As can be seen from this figure, the peak-to-valley value of the difference in this case is 2.4 μm. Figure 5-17 shows the angular repeatability with 5.63 arcsec RMS along the x direction and 13.78 arcsec RMS along the y direction. To have a better understanding of the distribution of the data, Figure 5-18 shows the histogram of the difference in topography and angles between the two slumping steps.

Discussion

As can be seen from the above cases, the peak-to-valley value is relatively small, within a few microns; however, the angular repeatability is compromised. The y angle repeatability between Glass 1 and Glass 2 indicates a strong dependency on the alignment with the gravity vector, which is along the y axis in the figures. Some of the sources causing these differences in readings between slumping steps include:

1. inability to properly control the pressure on each side of the glass sheet with high precision, since the flow control valves have a course resolution and creep with

Zernike Coefficient	**Glass 1 front surface (μm)**	**Glass 2 front surface (μm)**	**Difference (μm)**
Z20	-1.316	-1.2675	-0.0485
Z21	0.022	0.052	-0.03
Z22	0.526	-0.245	0.771
Z30	0.1025	0.06	0.0425
Z31	0.0945	0.03	0.0645
Z32	0.43	-0.211	0.641
Z33	0.5165	0.1405	0.376
Z40	-0.129	-0.0965	-0.0325
Z41	-0.00049	-0.0745	0.074
Z42	-0.0065	-0.19	0.1835
Z43	-0.081	-0.0044	-0.0766
Z44	-0.0825	-0.0225	-0.06

Table 5.2: Zernike coefficients over a 60 mm diameter of the front surface of Glass 1, Glass 2 and the difference between the two

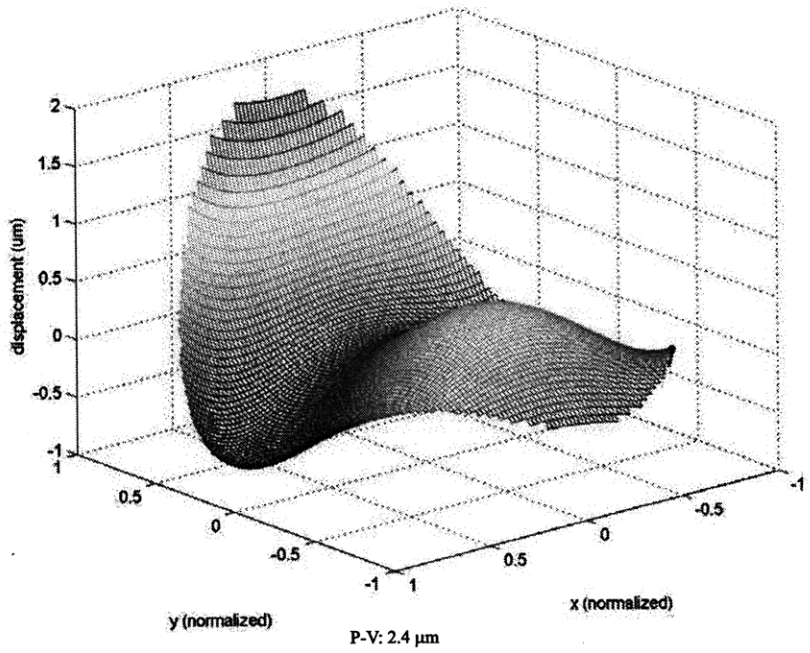

Figure 5-16: Difference in the surfaces of Glass 1 and Glass 2 over a 60 mm diameter after both have been slumped using the same temperature profile

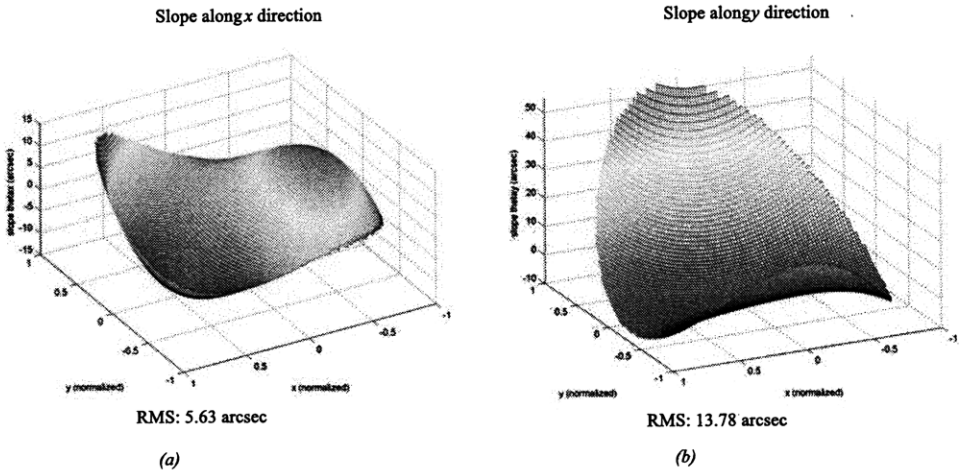

Figure 5-17: Difference in the angles of the surface of Glass 1 and Glass 2 over a 60 mm diameter after each has been slumped using the same temperature profile. *(a)* Slope along the x axis. *(b)* Slope along the y axis.

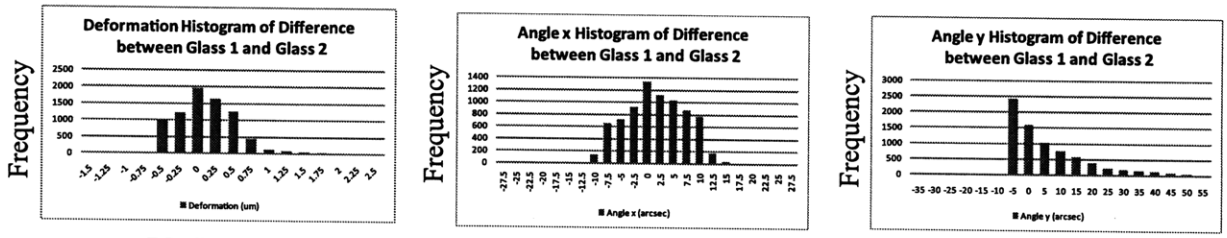

RMS 0.42 μm (a) RMS 5.63 arcsec (b) RMS 13.78 arcsec (c)

Figure 5-18: Histogram of the difference in the topography and angles of the surfaces of Glass 1 and Glass 2 over a 60 mm diameter.

time, as was discussed in Chapter 4,

2. difference in alignment with gravity during every run, which would mostly be seen in the y angle repeatability in the plots shown,

3. different edge constraint representing different boundary conditions during every run, Glass 1 was constrained along lines the first time and at points the second time

4. glass thickness variation when comparing two different sheets, which results in a different final shape of the sheet after slumping.

Figure 5-19 shows the topography and angular histograms of each of the three sheets. As can be seen, Glass 3 and Glass 1a, which is Glass 1 when slumped the second time, both have a worse angular distribution. Both these sheets were constrained at a point instead of a line.

The effect of pressure control is studied next, followed by the possibility of removing the effect of contact at the lower corners of the sheet.

5.2.3 Pressure Differential across Glass Sheet Thickness during Slumping

The next step of tests involves understanding how a pressure differential between the two plenums affects the shape of the slumped glass, and how well this effect can be

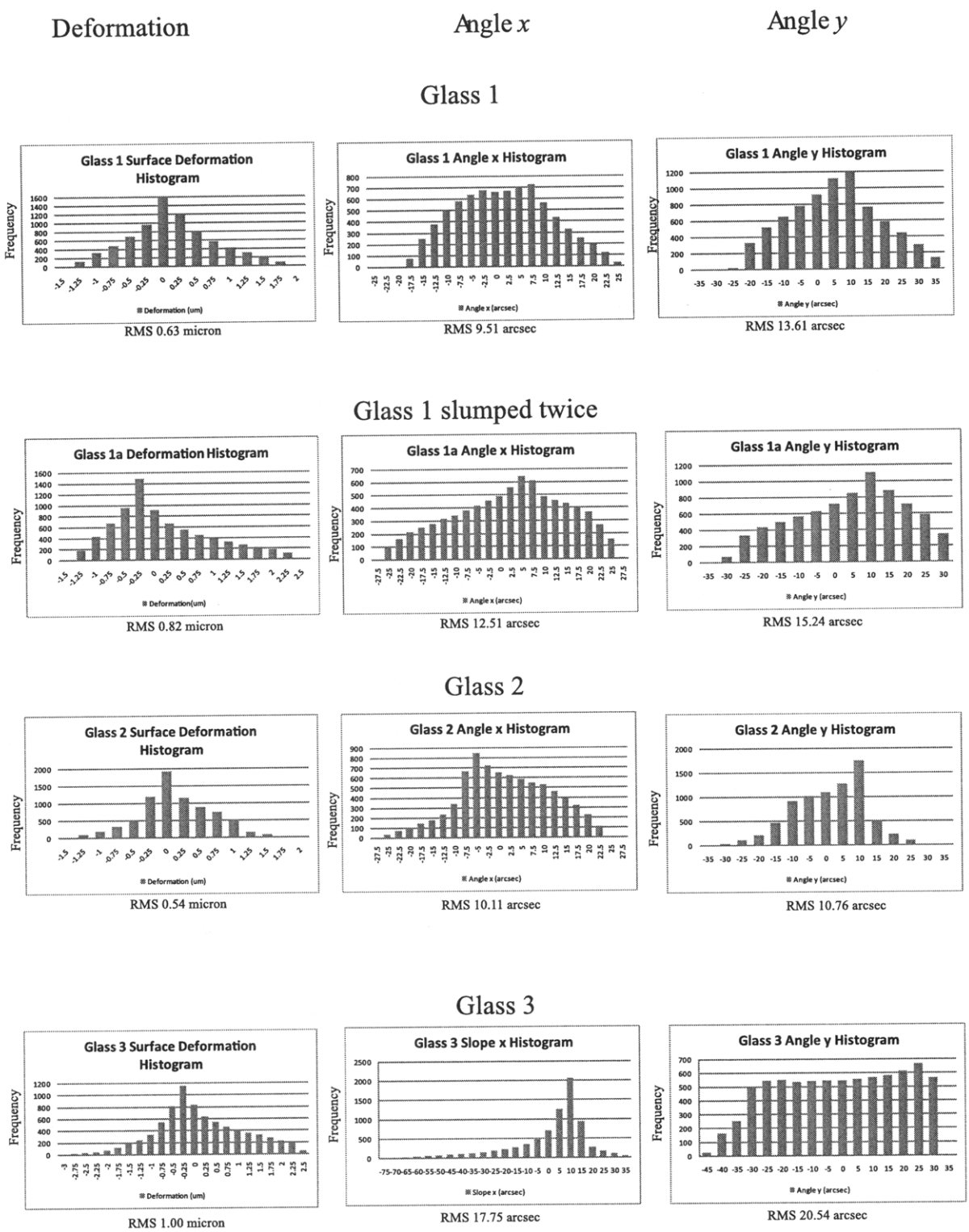

Figure 5-19: Histogram of the difference in the topography and angles of the surfaces of Glass 1, Glass 1a, Glass 2 and Glass 3 over a 60 mm diameter.

controlled.

Glass 3, which was slumped once before, was assembled again for a second slumping step. This time, a pressure differential of 0.004 psi was introduced between the two plenums at room temperature before the start of the experiment. This pressure differential increased to $\sim$ 0.03 psi at the slumping temperature of 570°C, based on the readings from the two sensors outside the furnace and connected to each of the plenums, as described in Section 4.3.1. In fact, the actual pressure variation at the slumping temperature was fluctuating with time due to the poor control of flow in the setup; however, the average value of the difference was $\sim$0.03 psi.

Figure 5-20*(a)* shows the front surface of Glass 3 with an aperture of 60 mm after it had been slumped once, and Figure 5-20*(b)* shows the same surface after it had been slumped with a pressure differential of 0.03 psi at 570°C. The value at the center point of the sheet is shown in both figures. Figure 5-20*(c)* shows the difference between the surfaces of Figure 5-20 *(b)* and *(a)*. As can be seen from these results, the center of the sheet deforms by $\sim$1.4 μm due to the pressure difference in both plenums. By looking back at Figure 3-20, where a model was developed to estimate the deformation of a sheet of glass due to a pressure differential in the two plenums, the anticipated bow at the center of the sheet is $\sim$ 2 μm. The model established in Section 3.4 assumes that the glass is fully compliant and responds to the forces imposed on its surfaces; however, in reality, the glass sheet is visco-elastic, and its final shape for a given force distribution along its surfaces is time-dependent. This experiment followed the temperature profile shown in Figure 5-21, where the slumping time at 570°C was increased by 10 minutes from what was used in previous experiments. It is possible that the glass did not reach its final equilibrium position during this period of slumping time.

5.2.4 Spacer-Effect Elimination

So far, the glass sheet has been constrained at its lower two corner edges during slumping. This constraint affects the final shape of slumped sheets, where higher distortions are seen near the contact areas. In order to reduce this dominant effect,

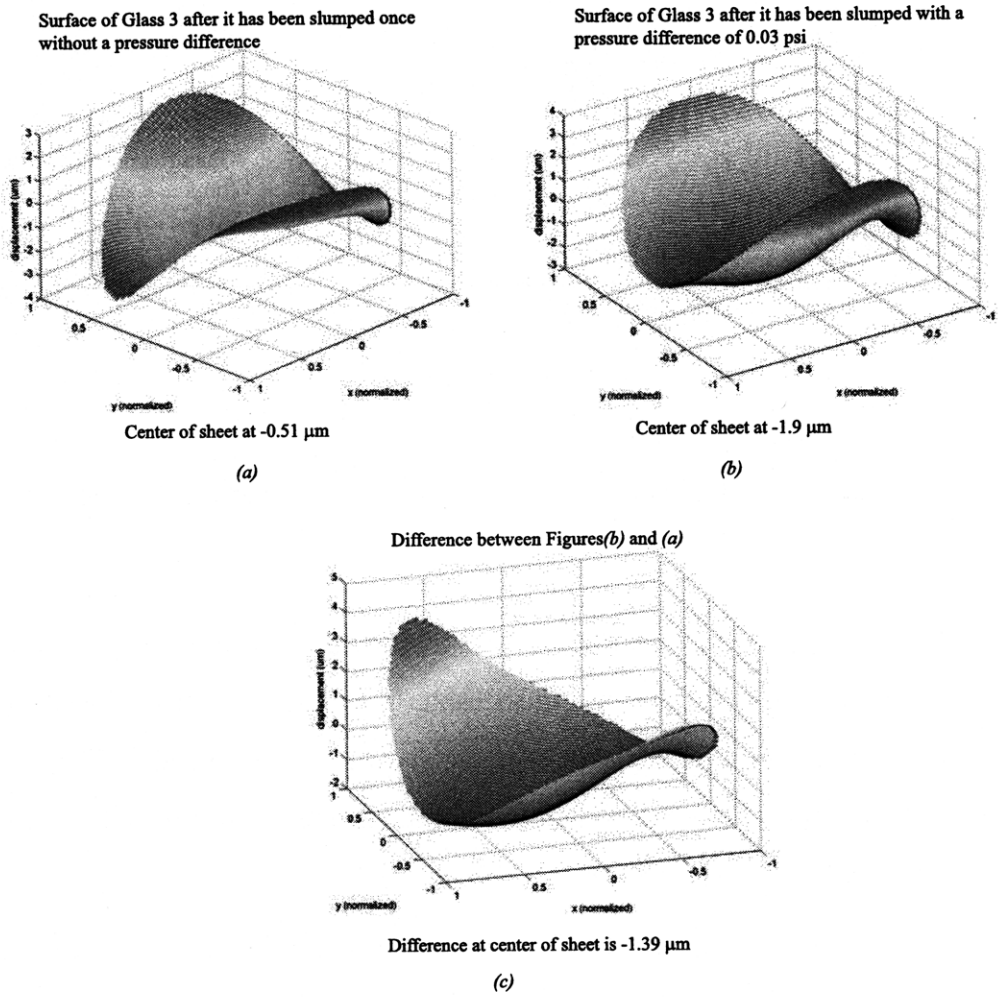

Figure 5-20: *(a)* Surface of Glass 3 after it had been slumped with equal pressures in both plenums. *(b)* Surface of Glass 3 after it had been slumped with a pressure difference of 0.03 psi at 570°C between the two plenums. *(c)* Difference between the two previous figures. Aperture = 60 mm.

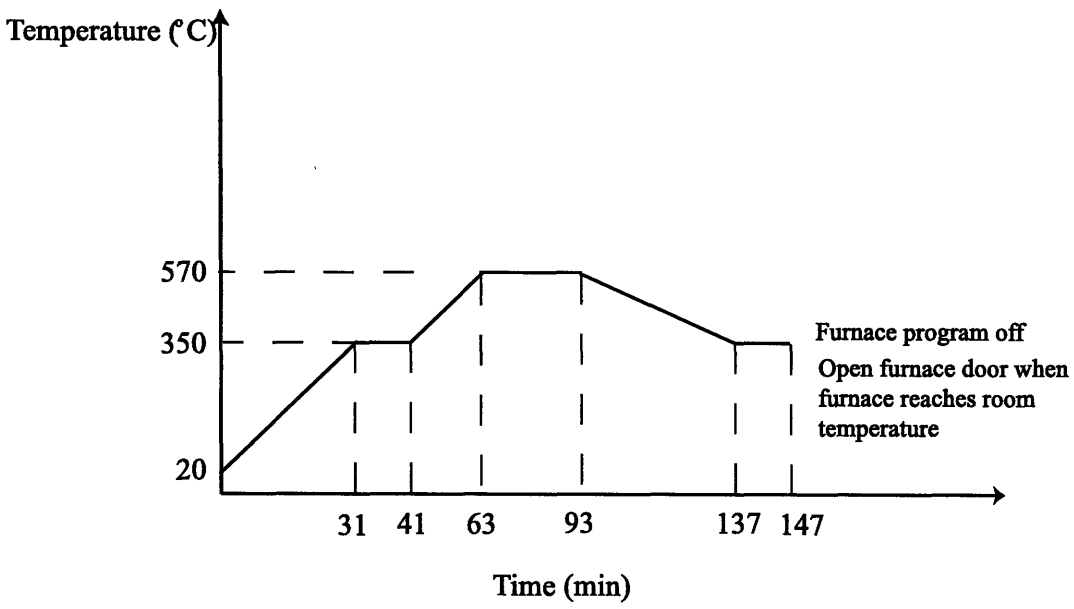

Figure 5-21: Modified temperature profile followed during slumping

contact at the edges of a sheet is eliminated by suspending the glass sheet from the top. Two holes, 1/16" in diameter, are machined using laser ablation (laser wavelength of 248 nm) near the top edge of a glass sheet, as shown in Figure 5-22. Thin copper wires are used to suspend the sheet from the holes, such that all glass edges are free. The slumping profile followed is similar to Figure 5-21.

The results are analyzed over the 60 mm aperture to minimize the errors introduced by the warped edges of the porous mandrels. Figure 5-23 shows the surface of one sheet, labeled GlassH 1, after slumping, and Figure 5-24 shows the histograms of the surface topography and the angles x and y of the same sheet. As can be seen from these figures, the sheet has a surface flatness of 2.26 μm P-V, 0.39 μm RMS and an angular distortion of 7.53 arcsec along the x direction and 12.22 arcsec along the y direction.

The same slumping process is performed on a second sheet, labeled GlassH 2, and the results are shown in Figures 5-25 and 5-26. As can be seen from these figures, the sheet has a surface flatness of 3.41 μm P-V, 0.67 μm RMS and an angular distortion of 8.05 arcsec along the x direction and 19.13 arcsec along the y direction.

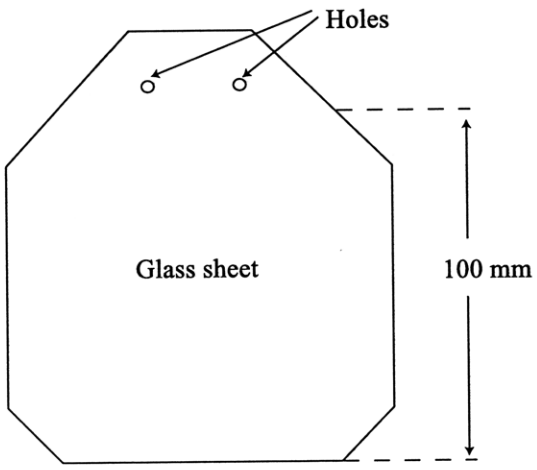

Figure 5-22: Holes machined into a glass sheet using laser ablation

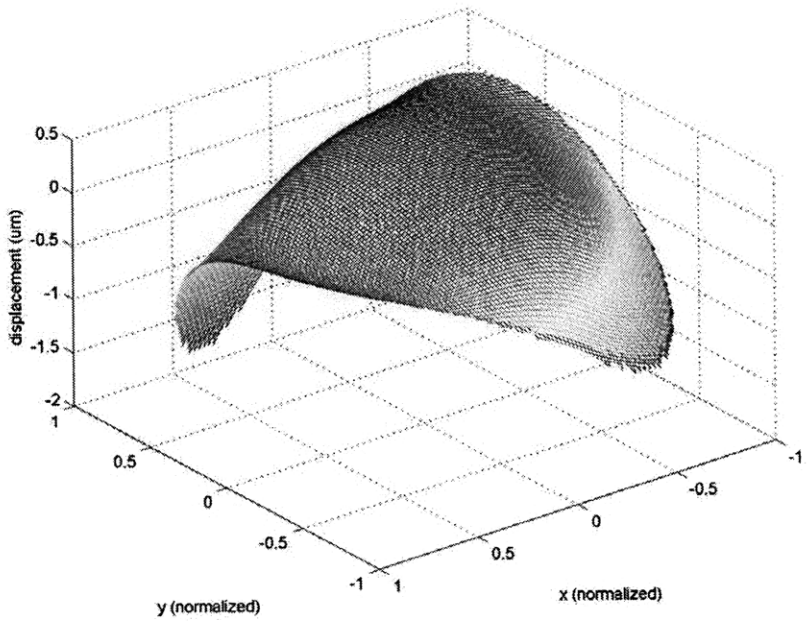

P-V: 2.26 μm

Figure 5-23: Surface of GlassH 1 with 2.26 μm P-V of warp after slumping

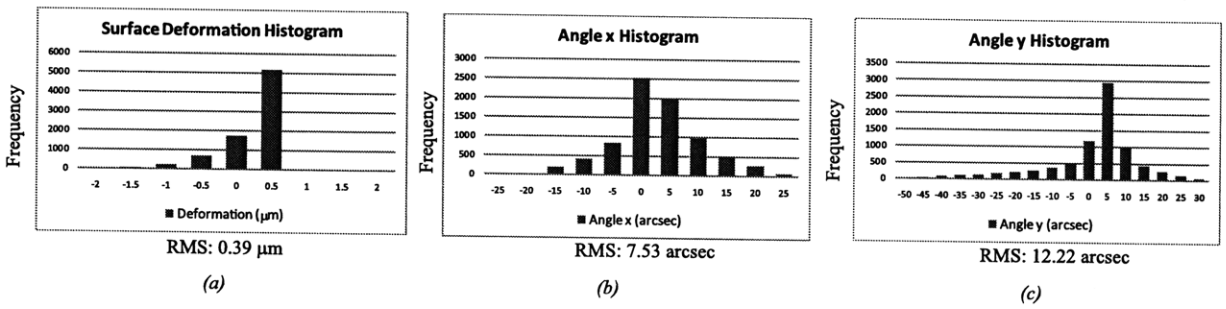

Figure 5-24: Histograms of surface of GlassH 1 after slumping

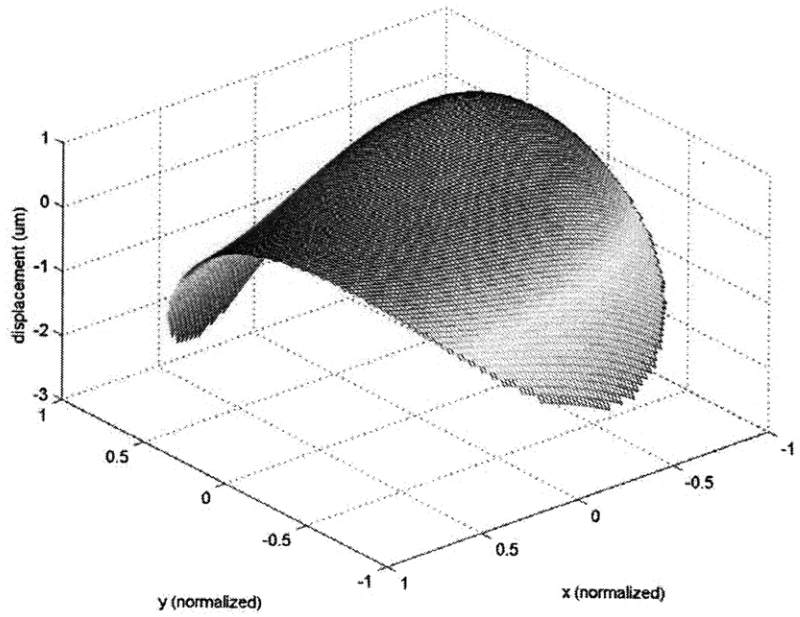

P-V: 3.41 μm

Figure 5-25: Surface of GlassH 2 with 3.41 μm P-V of warp after slumping

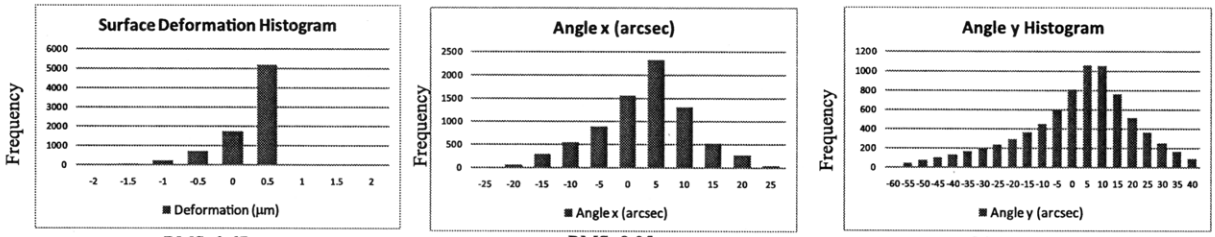

Figure 5-26: Histograms of surface of GlassH 2 after slumping

The difference between GlassH 1 and GlassH 2 is shown in Figures 5-27 and 5-28, where the resulting surface topography is 1.6 μm P-V, 0.35 μm RMS, and the angular distortions are 3.30 arcsec in the x direction and 8.13 arcsec in the y direction.

5.3 Summary of Results and Discussion

The original strategy of constraining a glass sheet between a set of spacers results in the glass sheet distorting with the clamping forces holding the overall assembly together. Thus the glass sheet being slumped has been removed from between the spacers and constrained at its lower corner edges, as was shown in Figure 5-4.

Table 5.3 shows a summary of how the different sheets of glass are constrained during slumping. Table 5.4 shows the shape and slopes of the same sheets over a diameter of 60 mm to minimize edge effects. Table 5.5 summarizes the repeatability of the setup with the different constraints.

Certain parameters summarized in Figure 5-29 affect the accuracy and repeatability of the setup developed and the final results. These are discussed in detail below.

5.3.1 Accuracy

When slumping sheets of glass with an initial surface warp of up to 450 μm P-V, the final result has a surface topography better than 16 μm P-V when the entire

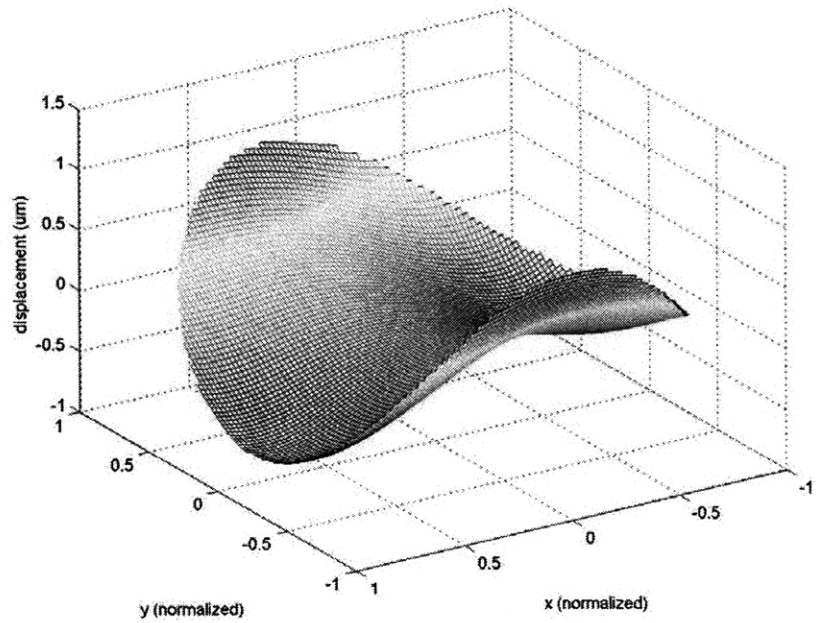

Figure 5-27: Surface of the difference between GlassH 1 and GlassH 2 with 1.61 μm P-V of warp after slumping each individually

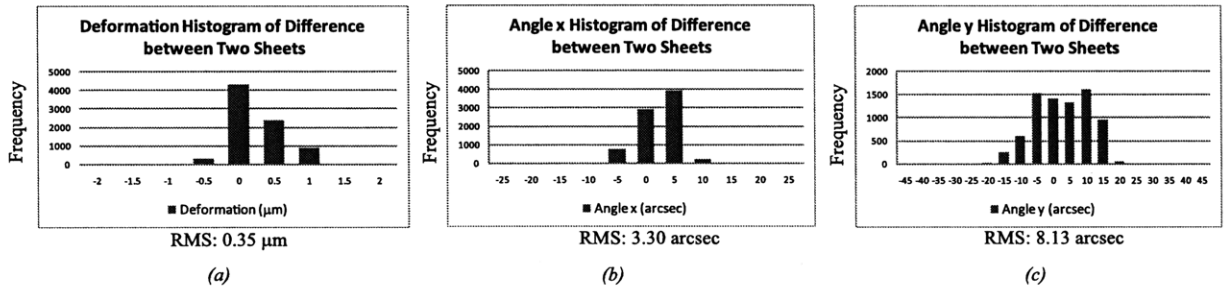

Figure 5-28: Histograms of the difference between GlassH 1 and GlassH 2 after slumping each individually

Sample	Original surface P-V (μm)	Edge conditions
Glass 1	440	Line contact at lower two corners. Other edges free
Glass 1a	14.72	Glass 1 reslumped with point contact at lower two corners. Other edges free
Glass 2	413.13	Line contact at lower two corners. Other edges free
Glass 3	84.72	Point contact at lower two corners. Other edges free
GlassH 1	64	Hung from wires through two holes in glass. All edges free
GlassH 2	95.6	Hung from wires through two holes in glass. All edges free

Table 5.3: Summary of slumping results seen on five separate sheets of glass. Measurements are taken on the entire glass sheet (100 mm $\times$ 100 mm)

Sample	Surface P-V (μm)	Surface RMS (μm)	Angle x RMS (arcsec)	Angle y RMS (arcsec)
Glass 1	3.33	0.63	9.51	13.61
Glass 1a	3.80	0.82	12.51	15.24
Glass 2	3.17	0.54	10.11	10.76
Glass 3	5.50	1.00	17.75	20.54
GlassH 1	2.26	0.39	7.53	12.22
GlassH 2	3.41	0.67	8.05	19.13

Table 5.4: Summary of slumping results seen on five separate sheets of glass. Measurements are taken on the central 60 mm diameter area.

Test/Repeatability	Surface P-V(μm)	Surface RMS (μm)	Angle x RMS (arcsec)	Angle y RMS (arcsec)
Glass 1 slumped twice	1.31	0.31	6.23	5.68
Glasses 1&2 slumped	2.42	0.42	5.63	13.78
GlassesH 1&2 slumped	1.61	0.35	3.30	8.13

Table 5.5: Repeatability of the slumping process on a 60 mm diameter aperture avoiding edge effects

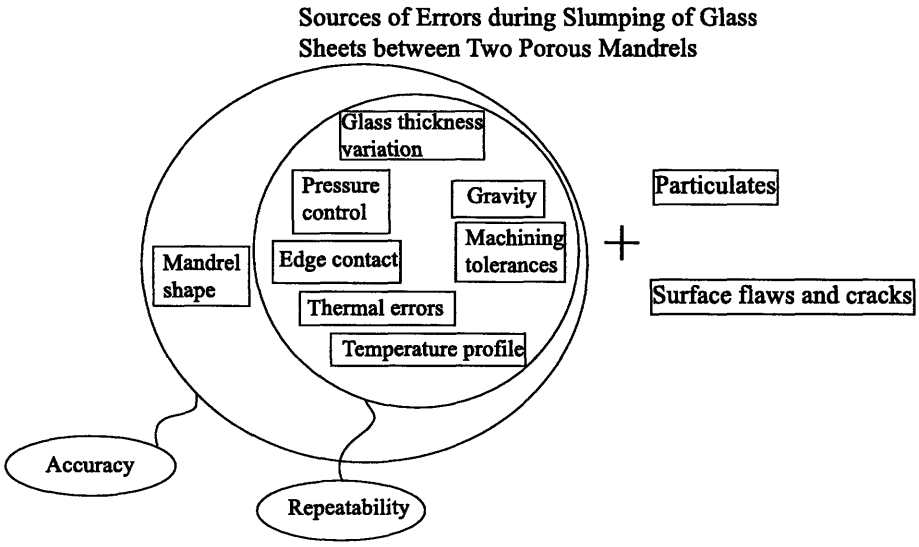

Figure 5-29: Sources of error affecting the final shape of a glass sheet slumped between two porous mandrels at elevated temperatures.

surface area is studied. When focusing on the 60 mm diameter central region of a sheet after it has been slumped to minimize errors from the edges, the resulting surface topograpy is better than 6 μm. The significantly better results in the central area indicate the importance of controlling the boundaries of the glass sheet during slumping. The initial results measuring only the peak-to-valley value of the surfaces is misleading, since a focus on the data distribution of the surface shows different results. For instance, when comparing Glasses 1 and 3, the overall peak-to-valley value indicates that Glass 3 is flatter than Glass 1, as shown in Figures 5-6 and 5-12; however, by eliminating the edges from the calculations and concentrating on the central regions, it is seen that Glass 1 is in fact flatter than Glass 3, as shown in Table 5.4.

Mandrel Shape

As was discussed in Section 4.3.2, the central region of the porous silicon carbide mandrels is flat to within 1 μ P-V for one mandrel and 3 μm P-V for the second. The edges on the other hand have a worse surface topography as a result of the grinding process. Thus the surface of the glass sheet slumped between these two mandrels can not be better than the surfaces of the mandrel if equal pressure is used in both. Section 3.5 describes the effect of the mandrel shape on the slumped sheet surface, where the ratio $\frac{B}{A}$ is found to be 0.5. If a mandrel total surface error of ~ 4 μm P-V is assumed, such that the surface error on both is concave, which represents the worst case of gap variation on each side of a glass sheet, then the glass sheet surface would have 2 μm P-V.

In order to minimize such errors induced by the grinding process, a larger mandrel can be used in the future, such that the edges where the grinding wheel first makes contact with the workpiece mandrel are outside the critical slumping area. As for the central area, better results can be obtained if the grinding facility utilizes a more reliable metrology system to evaluate the performance of their grinding steps. At this point, only a small area of the workpiece was measured using a contact probe during the grinding process. Since the probe can damage the surface it touches, the

machinist did not use it on the central region of the mandrels, and thus could not properly evaluate the final surface topography of that area.

Glass Thickness Variation

This is perhaps the limiting factor of this process. Since the slumping temperature is not high enough to cause an in-plane flow of glass, the original thickness variation of the sheet is maintained throughout the slumping process. If all other sources of error are eliminated and equal pressure is used in both plenums with the sheet being midway between the two mandrels, the final surface flatness of the sheet would be very close to its thickness variation, since this would be the equilibrium position where the pressure on both sides of the sheet is equal. This is not a major concern in the flat panel display industry; however, it might prove to be a limiting factor for x-ray telescopes, in which case double-side polished glass sheets with a uniform thickness can be used instead. The sheets utilized are quoted to have a thickness variation of ± 10 μm. some The thickness variation of some sheets was measured using a micrometer and found to vary between 1 and 5 μm P-V.

Pressure Control

The current setup utilizes two flow control valves that have a coarse resolution in an open-loop configuration. In other words, as the temperature of the experiment increases, the pressure in the system increases, and this change in pressure is not fed back to the control valves to regulate the flow. Each valve reacts differently to the increase in pressure, which results in a pressure difference in the two plenums as a function of time and temperature. This, in turn, leads to a pressure difference across the thickness of the glass sheet, and the sheet bows. Section 3.4 discusses this phenomenon in more detail, and Section 4.3.1 provides recommendations on better-resolution flow controllers. In most of these experiments, the pressure difference observed was between 0.01 and 0.02 psi, which corresponds to an error of 0.8-1.5 μm P-V from Figure 3-20.

Edge Contact and Sheet Constraint

Contact at the lower corner edges of the slumping glass sheets causes errors in the glass surface. As can be seen in Figure 3-8, the pressure at the edges of the glass sheet is atmospheric, thus there are no forces acting on the edges. If the corner edge is constrained at a specific position not midway between the two mandrels because of contact with the spacer area, this error is imprinted in the final shape of the slumped sheet. This was seen in Glasses 1, 2 and 3. To avoid such a problem, two holes were created on the surface of the glass sheet, outside the critical slumping area, such that the glass sheet could be hung from these holes using very fine copper wires. In this case, all the glass edges are free during slumping. The result shows a significant improvement in the surface topography, which had a deformation of ~ 2.3 μm P-V in the central sheet region.

Thermal Errors in the Case of Edge Contact

The presence of contact points on the lower edges of the glass can also cause additional bow seen near the lower edges because as the glass expands faster than the silicon carbide mandrels, its lower edges are not free to expand, causing stresses due to overconstraint. This phenomenon is eliminated when hanging the sheet from wires.

Slumping Temperature Profile

The temperature profile followed during slumping has been modified several times. The initial tests were run with the maximum slumping temperature held for 20 minutes. This was sufficient to decrease the surface topography peak-to-valley value by over 400 μm. This surface improvement is sufficient for the flat panel display industry but necessarily for the x-ray telescope industry. This time interval was later on increased to 30 minutes to give the glass additional time to change shape. As the glass surface topography becomes closer to that of the mandrels, it takes much longer periods of time to further change the sheet's surface at the same temperature. Increasing the slumping temperature can reduce the time interval needed to reach

equilibrium; however, other challenges arise at higher temperatures, such as the creep and loosening of the non-ceramic materials used in the assembly, and the additional pressure differences between the two plenums.

Alignment with Gravity

Aligning the glass sheet with gravity is critical both for the accuracy and repeatability of results. If the glass sheet is at an angle with respect to the gravity vector, it would sag due to its own weight, in addition to change its shape with the pressure forces. The current setup does not incorporate a method for aligning the sheet with gravity or ensuring that the sheet is repeatedly placed at the same angle with respect to the gravity vector. This is an important design parameter that must be kept in mind for future design and testing. A Model 900 inclinometer purchased from *Applied Geomechanics, Inc.* was used to align the assemblies of GlassH 1 and GlassH 2 to each other to within 0.8°; however, this alignment was not performed on the other slumped sheets.

Assembly Tolerances

The errors accumulated as a result of the assembly-part tolerances was described in Section 4.3.4, where an error of $\sim$15 μm was estimated in the spacing between the two flat porous mandrels. This error includes the error from the surface topography of the ground mandrels. Such an error results in gap variation, which in turn leads to different pressure forces acting on the surface of the glass sheets. The effects of gap variation were described in Sections 3.5 and 4.3.

5.3.2 Repeatability

When it comes to measuring how well the setup produces repeatable results, the same parameters described above are considered. All except for the shape of the mandrel, which is a constant in every experiment, determine the final shape of the glass sheet. When the same sheet of glass constrained at its lower edges is slumped twice following

an identical temperature profile each time, the resulting difference between the two surfaces is 1.3 μm P-V and 0.31 μm RMS, with an angular repeatability of 6.23 arcsec RMS in the x direction and 5.68 arcsec RMS in the y direction. When two separate sheets constrained at their lower edges are slumped and their surfaced compared, the difference between the two is 2.4 μm P-V and 0.42 μm RMS, with an angular repeatability of 5.63 arcsec RMS in the x direction and 13.78 arcsec RMS in the y direction. When two sheets of glass hung from wires through holes are slumped, the difference between the two is 1.6 μm P-V and 0.35 μm RMS, with an angular repeatability of 3.30 arcsec RMS in the x direction and 8.13 arcsec RMS in the y direction. These numbers are well within the 15 arcsec requirement for the *Constellation-X* mission. By addressing the different parameters described above, such as using better control flow valves, repeatably aligning the sheet with the gravity vector and eliminating contact at the glass corners, these numbers can be further reduced to have a tighter tolerance on the repeatability of the slumping process.

5.3.3 Effect of Particulates and Surface Flaws

Perhaps one of the biggest advantages of slumping a sheet of glass between to porous mandrels with a thin layer of air flowing between the two is the absence of the effects of particulates. Both the mandrel and glass sheet surfaces were cleaned by air blast; however, no additional extensive cleaning was done to the surfaces, and the assembly was not covered while in the furnace, and thus was exposed to the particulates from the insulation material inside the furnace. As can be seen from all the results shown, no high-spatial frequency errors typically associated with particulate entrapment between the glass sheet and the mandrel are seen on the surfaces of the slumped glass sheets. The glass sheet maintains its pristine optical qualities after slumping, which is highly desired for both the flat panel display and x-ray telescope industries.

The presence of micron sized surface cracks was a concern when slumping. Such microcracks were monitored using an optical microscope before and after slumping, and no major change in their dimensions was observed. When the glass sheet is resting on its lower two corners, the weight of the sheet applies compressive forces on

the surface cracks, thus stopping them from further propagating. When the sheet is hanging from copper wires going through the two holes in the sheet, the weight then applies a tensile force, which could open the cracks and lead to fracture; however, this was not observed. In fact, since the manufacturing of such sheets relies on the pulling of glass, as was described in Chapter 2, and since this phenomenon does not result in the propagation of surface fractures within the manufacturing facilities, it should not be a problem in this smaller setup.

Chapter 6

Further Implementations of Slumping Glass Sheets between Two Porous Mandrels

The analysis and technology development presented in this thesis is a proof-of-concept for the shaping of thin glass or any other thermoplastic sheets using forces from hot gases flowing through two porous mandrels and onto the surfaces of the sheets. The results shown in previous chapters are very promising when it comes to reducing the surface warp of individual sheets; however, different requirements are present for both the x-ray telescope and the flat panel display industries. Flat panels require sheets with less surface warp in order to be able to utilize thinner substrates that would reduce the weight of the large displays without compromising the performance of the display. The x-ray telescope mirrors require smooth sheets with specific curvatures to reflect and focus incoming x-rays.

6.1 Shaping Glass during its Manufacturing Process

In general, if the process of slumping is incorporated during the manufacturing of sheet glass, the final sheets would have much smaller surface warps than the current technology is capable of producing. As was described in Chapter 1, sheet glass is

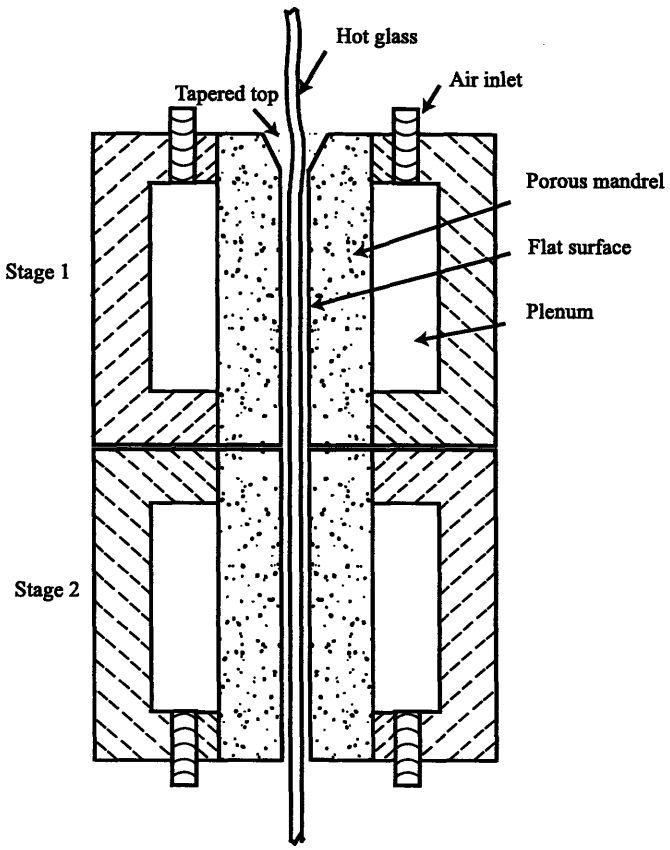

Figure 6-1: Glass sheet's surface warp reduced by using opposing porous mandrels with gas (such as air) flowing through the mandrels and against the surface of the glass sheet, as it flows downwards. The two stages represent slumping done at different temperatures with the temperature of stage 1 being higher than that of stage 2.

typically manufactured such that the sheet is flowing downwards with gravity. External factors, such as vibration and a temperature gradient across the sheet thickness result in the surface warp currently found in sheets.

By placing two flat porous mandrels on opposite sides of the flowing glass sheet in its hot stages, the resulting sheet can be produced with significantly less surface warps. Section 3.3.5 describes the flow of pressurized gas through porous mandrels and against the two sides of a moving sheet. Figure 6-1 shows a schematic of such a setup, where the molten glass sheet is introduced between two porous mandrels as it flows downwards while being manufactured.

If the starting warp of the sheet is much larger than the nominal gap between the sheet and each of the porous mandrels, then the top region of the porous mandrels, where the glass is introduced, can be tapered to accommodate initial large warps and direct the sheet between the two flat mandrel surfaces. The viscous forces of the hot gas flowing through the porous mandrel would shape the sheet and place it midway between the two mandrels, assuming that the gases are at an equal supply pressure. With equal supply pressures and flat mandrels, the surfaces of the sheet would have a significantly reduced warp.

It should be noted that this process would only work when the glass is in a fluid state; thus, slumping must be done above the glass transformation temperature, which is the point where the viscosity of the glass sheet changes such that it transforms from a solid to a fluid state. In fact, the higher the temperature of the sheet, the quicker its response to gas forces, since the relaxation time for glass described in Section 2.1.4 decreases as its temperature increases. Thus depending on the velocity of the sheet flowing downwards, the ideal temperature for slumping can be calculated such that the sheet has enough time to deform with the gas forces as it goes along the length of the mandrels.

Since the glass sheet is cooled as it flows further downward, the gas going through the mandrels must be at a controlled temperature along the length of the sheet. Although glass solidifies once its temperature goes below the transformation point, it is recommended to continue with the slumping between two mandrels at temperatures below the transformation point to ensure that the glass has completely solidified and any forces from vibration and temperature gradients would no longer imprint on the sheet. This can be done by having different sections, as shown in Figure 6-1, where the temperature in the sections decreases along the length of the sheet as it flows downwards.

Such a setup would improve the surface figure of sheet glass without contacting the surface, thus preserving its original surface qualities. By having glass sheets with less surface waviness, substrate yield for the flat panel display industry increases and mura caused by glass substrate waviness diminishes, as explained in Chapter 1,

resulting in less display manufacturing costs.

As an alternative, a different station can be set up to slump individual substrates in a continuous fashion, as shown in the last embodiment of the patent in Appendix B.

6.2 Shaping Glass for X-ray Telescope Applications

Chapter 1 describes the Wolter I and Kirkpatrick-Baez configurations used for the mirrors of x-ray telescopes. Both these configurations require specific curvatures in addition to surface smoothness. This was not addressed in this thesis, which focuses on obtaining flat substrates instead. Several modifications to the slumping approach mentioned before can be made to obtain the sheets with specific curvatures.

The shapes of the mandrels themselves can be changed, such that the glass sheet slumped between the mandrels responds to their surface curvature. This can be achieved by grinding the porous mandrels to the required shape. It can also be achieved by applying forces on the mandrel itself to elastically deform it and change its curvature. The effect of changing the surface curvature of the mandrels was discussed in Section 3.5, where the effects of mandrel surface variation were studied. Such a set-up is relatively easy to achieve given the currently developed equipment; however, sheets of different curvatures require individual mandrels machined to the specified shape, which in turn raises the need for numerous mandrels.

Another way of controlling the final shape of a slumped glass sheet is by controlling the pressure along the surface of the mandrels. Instead of having one plenum feeding the supply pressure for the mandrel, as was the case in the experiments conducted in this thesis, individual pressure sources can be introduced near the mandrel surface to control the pressure force on specific areas of the glass sheet as desired. This adaptive method requires further development of the current set-up to incorporate the pressure sources; however, one advantage is the fewer number of mandrels needed to produce

sheets with different curvatures, since each curvature can be controlled by varying the pressure of gases from the individual sources.

Before attempting these different approaches, flow control valves of higher resolution and repeatability must be utilized to eliminate the errors introduced by the varying pressure in both plenums throughout the experiments.

Chapter 7

Assembly of Thin Optics

This chapter is specific to applications where stacks of thin substrates are required. X-ray telescopes utilizing thin optics represent one such application, where thousands of sheet substrates must be assembled with tight tolerances to form the mirrors and gratings of the telescope that is typically launched into space.

After thin optics have been precisely shaped, measured and coated to reflect x-rays with the accuracy needed, care must be taken during assembly such that all the extensive work done on the optics to improve their surface flatness up until this point is not compromised by the final assembly step. The challenges that exist while shaping and measuring thin substrates are present in the assembly steps as well.

7.1 Previous Assembly Methods

There have been various approaches to assemble thin substrates in ready-to-fly modules for x-ray telescopes. Some approaches developed at the NASA *Goddard Space Flight Center*, the MIT *Space Nanotechnology Laboratory* and the *Columbia Astrophysics Laboratory* are described and compared to better understand some of the advantages and disadvantages of the different processes. By closely examining these processes, a new list of functional requirements is proposed for the assembly step to lay the foundation of the assembly scheme developed and described in this chapter.

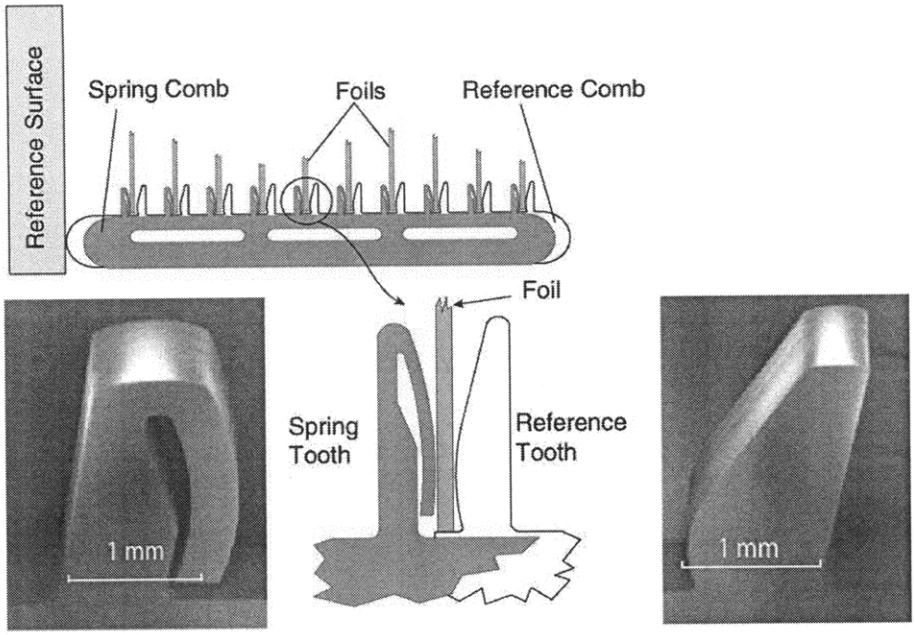

Figure 7-1: Silicon microcombs used to precisely align thin optics in a module. There are two sets of microcombs: the reference combs shown on the right against which thin optics are pushed and constrained, and the spring combs shown on the left which push the thin optics against the reference teeth.

7.1.1 Assembly of Thin Substrates Using Microcombs

A method pursued at the MIT *Space Nanotechnology Laboratory* some years ago utilized a set of high precision silicon microstructures called microcombs to perform the alignment of the substrates in a module, as shown in Figure 7-1. This scheme utilizes a flight module into which thin optics are loosely inserted. The module itself sits in a precision assembly truss, as shown in Figure 7-2, where the thin optics are manipulated by the silicon microcombs into their final positions and bonded in place. The flight module is then removed from the truss and assembled into the telescope structure. Meanwhile a new module can be reinserted into the assembly truss to align a new set of thin optics [64].

This truss has gone through two generations of design to improve its overall performance [64], [65]. The final design utilizes a reference surface used for alignment purposes and two sets of microcombs, whose accuracy is within 200 nm [66]: spring

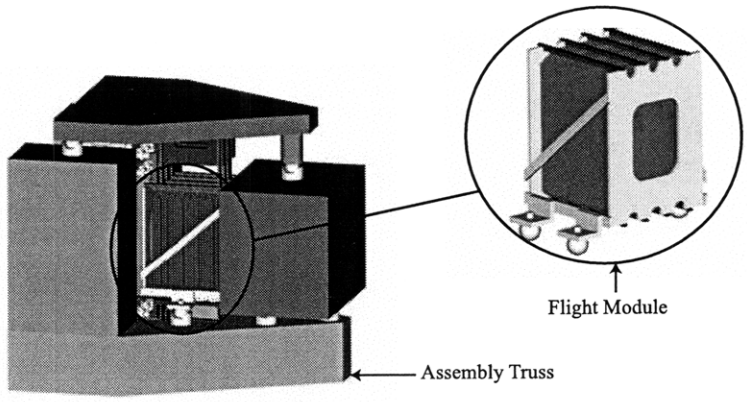

Figure 7-2: Flight module designed to loosely hold thin optics. The module is inserted in a precision assembly truss to accurately align the thin optics and glue them to the module.

teeth that actuate the edges of the glass sheets, and reference teeth against which the glass sheet rests when aligned. These combs are shown in Figure 7-1. Beads of epoxy are introduced afterwards to bond the optics to the module at eight distinct points [64].

The assembly truss utilizes kinematic couplings for assembly/disassembly to reduce random errors in the system. The overall repeatability of the second generation assembly truss is about 0.35 μm P-V, while its accuracy is about 2 μm P-V [64]. One of the major sources of error in the system is the friction force at the interface where the optic rests on the silicon reference microcomb while being pushed by the spring microcomb. Forest [64] estimates an error of 2 μm P-V due to friction during assembly. It was also found that the brittle silicon teeth used for aligning the sheets are prone to chipping and wear, which significantly reduces the accuracy and repeatability of the tool with time. Another drawback in this design is the relatively low natural frequencies of the assembled optics. Mongrard [65] has shown a finite element analysis of the natural frequencies of D-263 glass sheets with the dimensions of interest of 140 mm $\times$ 100 mm $\times$ 0.4 mm constrained at eight distinct points along the shorter edges. He has found that the first five modes range between 193 Hz

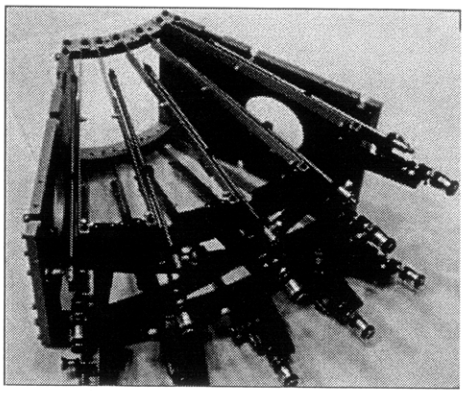

Figure 7-3: Housing used to align thin optics by means of five actuators placed at azimuthal locations at the top and bottom. *Taken from Petre et al.*

and 470 Hz. In order to avoid launch related frequencies that might cause resonance and shatter the glass sheets, the first mode of the sheet glass must be at frequencies higher than 200 Hz. Finally, since the optic is constrained at points along its edges, its final shape is sensitive to its alignment with gravity due to optic sag, which is critical when measuring the surface of the assembled optics and evaluating the process performance.

7.1.2 Assembly of Thin Substrates Using Independent Actuators

A method pursued at NASA's *Goddard Space Flight Center* utilizes a set of independent actuators, as shown in Figure 7-3, to manipulate the thin substrates and align them until the desired shape and angles are achieved. Glass sheets are placed loosely in the module referred to as the Optical Alignment Pathfinder 2 (OAP2). A total of ten micrometers placed equally along the length of the optic on both top and bottom edges are used to actuate the optic at ten points [29], [67].

In-situ metrology is performed during alignment using both an interferometer and the Centroid Detector Assembly method originally designed to align the mirrors on the Chandra X-ray Observatory [68]. Therefore, as the user turns the actuators to align the mirror, constant feedback is received from the metrology systems. All ten

actuators are manipulated until the desired optic shape and angle are achieved. At this point, epoxy is used to bond the optic to the OAP2 module. Once the epoxy has fully cured, the process is repeated for another module [67].

The second generation design of this concept replaces the manual micrometers with a series of flexures and piezo-actuators. This provides for better control during alignment. The thin substrate is actuated at five points on both its edges, similarly to the first generation concept, in order to obtain the final desired alignment and assembly [69].

Depending on the original shape of the assembled optic, this process can become time consuming and more challenging as thousands of optics are inserted in the housings to be assembled with appropriate surface shape and angular alignment. A similar concern to the previous method described is the natural frequency of such an assembly. In concept, the final result of this assembly scheme is very similar to the scheme utilizing microcombs, since both methods bond the thin substrate to a more robust housing using epoxy at distinct spots, resulting in a relatively low natural frequency and possible failure due to vibration. No data is found at this time regarding the natural frequency of the modules assembled using actuators and ten distinct points for bonding.

7.1.3 Assembly of Thin Substrates Using Graphite Rods

A third method followed at Columbia University performs both assembly and alignment in a single step, thus eliminating the need to iteratively align every substrate during assembly. The process is known as the *Error-Correcting Monolithic Assembly and Alignment* technique [70]. It utilizes a lightweight mandrel made of titanium that is mounted on a precision spindle. A series of graphite rods are bonded along the length of this mandrel and then machined such that their surface matches the shape of the glass sheet that will be glued to these rods, as shown in Figure 7-4*(a)*. At this point, the slumped glass reflective surface is bonded to the newly machined graphite rods, and a new set of rods are then bonded to the back surface of the glass. The process is continued until a stack of glass substrates has been assembled. Measure-

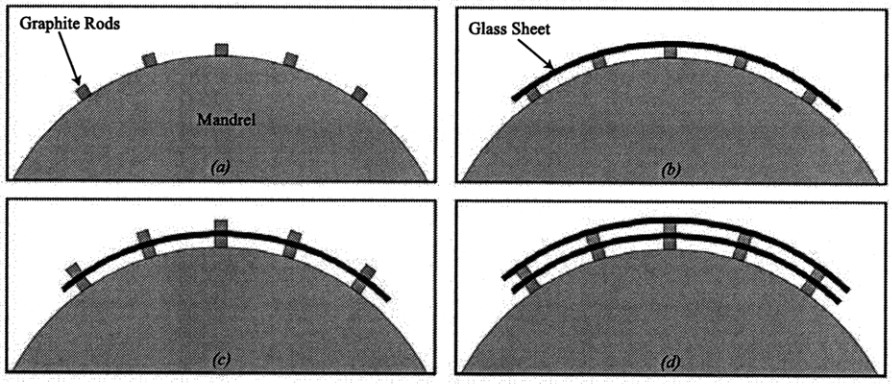

Figure 7-4: Assembly of sheet glass using the Error-Correcting Monolithic Assembly and Alignment scheme. *(a)* Graphite rods are bonded onto the mandrel and machined to the required shape. A thin layer of epoxy is placed on the rods (not shown). *(b)* A glass sheet is placed on the graphite rods such that the glass' critical, reflective surface is facing down towards the first set of rods. *(c)* A second set of graphite rods is bonded onto the back side of the sheet. *(d)* A second sheet is bonded to the rods and the stacking process is continued until the desired number of glass sheets is assembled. *Taken from Hailey et al.*

ments during the process are taken using a linear voltage displacement transducer (LVDT), which is used to scan the back surface of the assembled glass.

Some of the advantages of this process are: a) a low overall weight of the assembly, since the method utilizes thin rods of graphite and thin sheets of glass, b) elimination of stack-up errors, since every set of rods is machined with respect to the optical axis of the spindle, c) a more robust assembly, since the glass sheets are constrained along their lengths as opposed to distinct points, thus resulting in an assembly of higher natural frequency and lower gravity induced sag. Some of the disadvantages of this process are: a) the formation of a large quantity of particulates during the machining of the graphite rods, which can easily get trapped between the layers and lead to unnecessary glass surface errors, b) the measurement errors obtained from scanning the back surface of the assembled glass using the LVDT, since the glass sheets usually have a relatively poor thickness variation of up to ± 10 μm [16], and c) the difficulty

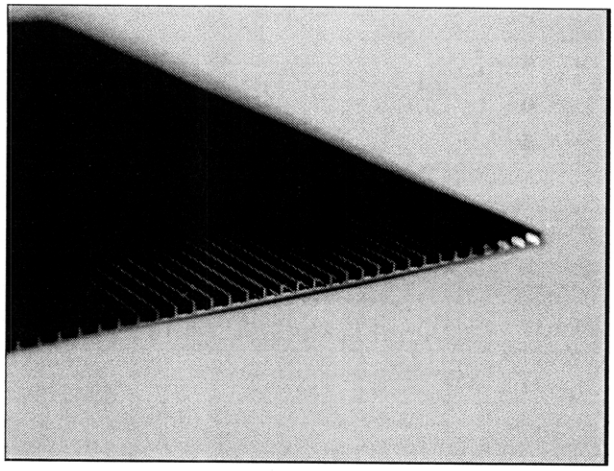

Figure 7-5: Grooves machined along silicon wafers using diamoned-sawing to result in ribs and channels. *Taken from Günther et al.*

in measuring the front surface of the substrate during assembly, since that surface is not easily accessible once bonded to the rods [70], [71].

7.1.4 Assembly of Thin Silicon Pore Optics

The European *X-ray Evolving Universe Spectrometer (XEUS)* mission requires a Wolter I arrangement of parabolic and hyperbolic mirrors as well. The European approach for shaping and assembling thin substrates is similar to the approach mentioned above, since spacers are used to attach thin optics to one another. The *XEUS* mission utilizes commercially available silicon wafers instead of glass. Silicon is slightly less dense than glass while having a higher Young's Modulus. Also, silicon's inherent properties are utilized to develop a robust, yet highly precise assembly scheme.

Double-side polished silicon wafers are grooved on one side by using a diamond saw and followed by KOH etching to remove any microcracks introduced by the sawing process. This grooving process leaves a thin membrane with many ribs, as shown in Figure 7-5. These ribs can be used to attach optics to one another by placing the ribs of one optic onto the flat front surface of another, as shown in Figure 7-6*(b)* [72].

This method, as pursued by Günther *et al.* provides a 64% useful collecting area

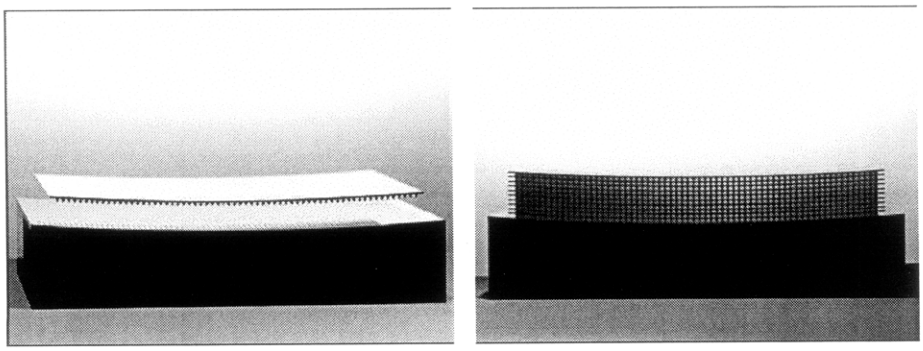

(a) *(b)*

Figure 7-6: *(a)* The first silicon wafer is placed against a thick silicon mandrel polished to the desired shape. *(b)* Silicon wafers assembled by placing ribs of one wafer onto the flat surface of another wafer. *Taken from Beijersbergen et al.*

per wafer. Once manufactured, the elastic properties of silicon are used to bend the wafers to cylindrical shapes. Since the wafers can only be bent in one direction, this assembly results in conical surfaces [73].

The assembly starts with a thick silicon mandrel polished to the required curvature. A thin grooved wafer is then pushed against this mandrel, as shown in Figure 7-6*(a)* [73]. Van der Waal forces between the two polished silicon surfaces keep the optic attached to the mandrel and resist the elastic forces trying to release the wafer; however, micron size particles trapped between the ribs and the flat silicon surface can result in millimeter sized, un-bonded areas that can weaken the bond strength and potentially change optic surface curvature [72]. Once the first wafer is optically bonded, a second wafer can be stacked on top. By following the same process, a series of wafers can be stacked on top of one another to result in an assembly as shown in Figure 7-6*(b)* [73] [74]. This concept is very sensitive to the presence of particulates between two sheets, since such particulates can cause surface errors on the mirrors assembled on top and can weaken the bond between two mirrors, which relies on direct contact between two silicon surfaces.

This configuration results in channels between optic-pairs for x-ray penetration and reflection. Since the only material used in this concept is silicon, the design

is thermally stable when exposed to a uniform temperature variation. Some of the disadvantages include a) stack-up errors, which once introduced, are very difficult to correct for, b) a significant loss in area ($\sim$ 36%) as a result of the many ribs covering each optic and c) the challenge in forcing flat sheets into curves, which typically results in some infidelity along the surface area of the sheets, as will be described in later sections, and in obtaining short telescope focal lengths, since that would require more curvature of the optics. The current design focal length for this concept is 50 m, compared to the 10 m focal length required for the *Constellation-X* mission.

7.2 Design Process

By understanding the strengths and weaknesses of the methods pursued previously, a set of requirements has been developed to come up with a new method of assembly.

7.2.1 Requirements

Some important factors that must be considered when designing for assembly are:

- the assembly process must not deteriorate the surface quality or flatness of the sheets assembled,

- parts involved in the assembly must be kept at minimal weight to avoid launch costs,

- the assembly natural frequency must not be close to launch frequencies to avoid resonance and optic shatter,

- assembly steps must be insensitive to particulate entrapment that could result in surface errors,

- the assembled optics must be stable with time to avoid surface degradation,

- the assembly must be rigid to facilitate moving it during metrology and mounting onto the telescope structure without breaking any of the assembled optics,

- the front, reflective surface of the glass sheet must be easily accessible for metrology and assembly evaluation,

- the assembly scheme must work for both flat gratings and conical mirrors.

By looking at the processes followed so far, it is noted that the assembly schemes utilizing ribs or rods and thus lines of constraint are more rigid and stable than those utilizing small beads of epoxy to constrain the optics. It is also noted that the pore-optic method, where the ribs are in direct contact with the silicon surfaces, is more susceptible to particulate-induced errors than the graphite-rod method utilizing a thin layer of epoxy between the rods and the optic surfaces, where particulates can be embedded in the epoxy. On the other hand, the graphite-rod method is more susceptible to epoxy creep and CTE mismatch errors than the single-material pore-optic method. The *in-situ* machining performed during the graphite-rod assembly method also introduces an additional intricate cleaning step necessary to remove the resulting graphite powder from the x-ray reflecting surfaces of the optics; thus, it is preferred to remove the machining-at-the-assembly-site step.

7.2.2 Concept Generation

From these observations, the line contact method was chosen to be pursued in the new assembly scheme. The use of ribs or rods is studied and developed.

The optics of interest are 140 mm long, 100 mm wide and 0.4 mm thick. Although a length of 200 mm is a possibility in the future, the current design focuses on a length of 140 mm. Both silicon and glass sheets are equal candidates, although glass wafers are in general less expensive than silicon with comparable surface roughness.

The ribs can either be an integral part of the optics, as is the case with silicon pore optics mentioned above, or they can be added during the assembly steps, as is the case with the error-correcting monolithic assembly and alignment method mentioned above as well. Machining channels into thin sheets of glass is not a trivial task, since glass is brittle and cracks can easily penetrate through the thickness of the sheet during machining and easily break the sheet. Also, as glass is manufactured, its outer surfaces are in compression because of the out-to-in cooling of the glass sheets; therefore, as surface layers are removed to machine channels and create ribs, the shape of the glass sheet changes due to variations in the stress levels across its thickness. Finally, sawing channels into the glass sheet results in sharp corners that act as stress

concentrators and weaken the assembled sheets. For these reasons, it is decided to pursue an assembly scheme that utilizes a separate set of ribs to be attached to the sheets.

In order to minimize the percentage of mirror or grating area covered by the ribs, both the number of ribs and their overall lateral dimensions must be kept at a minimum without sacrificing their mechanical integrity or that of the assembly. This also helps in keeping the overall weight of the assembly at a minimum.

The focus of this thesis is on assembling mirrors onto flat ribs and evaluating the final shape of the assembled optic. Analysis is also done on assembling mirrors in a hyperbolic configuration that can be used for Kirkpatrick-Baez x-ray reflecting mirrors, where a flat sheet is forced against hyperbolic ribs. A similar analysis can be done for Wolter-I optics.

Bending Theory of Plates

Modeling is performed on the sheets to better predict and understand how they would behave upon bending and forcing them to follow the shape of ribs. Modeling also helps determine how many ribs are needed to achieve the required final geometry for the sheet optics.

Bending of plates involves applying moments and/or transverse loads on the plates to deform them with a given set of boundary conditions. The bending equations presented in this section are valid for thin plates, where the plate thickness h is much smaller than the typical plate dimension L, $h \ll L$.

The bending rigidity of a plate D (N-m) is defined as

$$D = \frac{Eh^3}{12(1-\nu^2)}, \tag{7.1}$$

where E is the plate Young's modulus, h is the plate thickness and ν is the plate's Poisson ratio.

The plate bending equation in the x, y and z coordinate system is [75]

$$D\left(\frac{\delta^4 w}{\delta x^4} + 2\frac{\delta^4 w}{\delta x^2 \delta y^2} + \frac{\delta^4 w}{\delta y^4}\right) = q(x,y), \tag{7.2}$$

where D is the plate bending rigidity, w is the plate deflection and $q(x,y)$ is the transverse load applied on the plate and causing it to bend.

This equation can be re-written using the bi-Laplacian notation $\bigtriangledown^4 w$ to result in

$$D \bigtriangledown^4 w = q(x,y). \tag{7.3}$$

Finding an analytic solution to this equation is non-trivial. For simple boundary conditions, a solution with unknown constants is guessed and inserted into this equation to see if the solution satisfies the equation and boundary conditions, and to calculate the unknown constants of the solution suggested. As the plate boundary conditions become more complex, it becomes more difficult to find an analytical solution to Equation 7.3, and finite element analysis (FEA) becomes essential in finding the bending solution. Timoshenko provides different examples and solutions to cases of plates with both simply supported and clamped edges under different loads. His book covers solutions using the double trigonometric series, finite difference solutions, the strain energy method and other methods [75].

In the case of placing several rods or ribs along the surface of thin sheets and forcing the sheets against these rods, an analytical solution that depicts the final shape of the sheet is not easy to find. FEA is applied to predict the shape of the assembled sheet.

Finite Element Analysis of Sheet Optics

FEA was performed on mirrors that could be used in a telescope with a focal length of 10 m. The analysis applies to hyperbolic geometries.

The telescope configuration assumes that the first set of mirrors hit by the x-rays are parabolas (primary mirrors) followed by hyperbolas (secondary mirrors). The spacing between the two types of mirrors is 50 mm [76]. The focal length f of 10 m is measured from the primary-secondary intersection plane to the focal point of

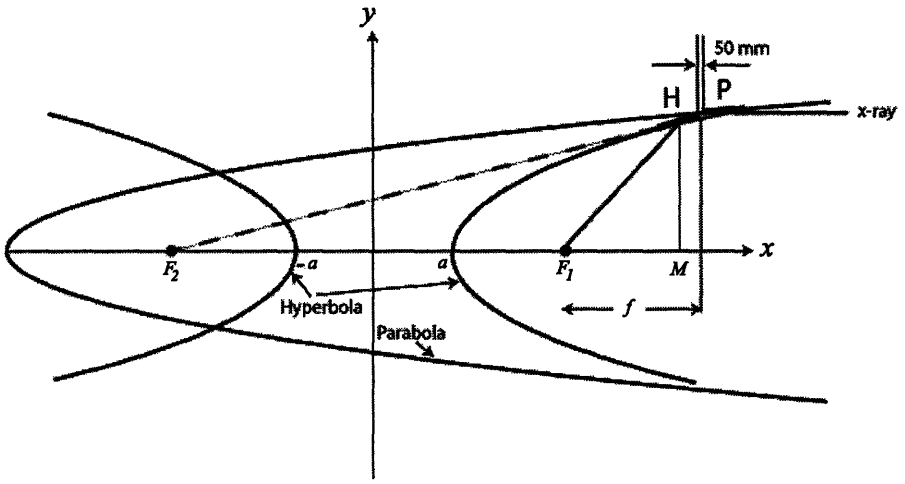

Figure 7-7: Telescope configuration showing the Parabolic mirror P and the hyperbolic mirror H, separated by a distance of 50 mm. The telescope focus f is 10 m. F_2 is the common focus point between the parabola and hyperbola. A ray hitting the parabolic mirror P reflects towards F_2 and then is intercepted by the hyperbolic mirror H to reflect towards F_1. M is at the midpoint of the hyperbolic mirror.

the telescope, where imaging technologies are located. The length of the mirrors is assumed to be 100 mm. Figure 7-7 shows this configuration.

The spacing between mirror layers is assumed to be 0.1 m, though this number can be changed as necessary. The first set of mirrors is 0.25 m away from the telescope axis. As a result, a total of 11 mirrors covers diameters of 0.5 m to 1.6 m.

For a hyperbola defined by

$$\frac{x^2}{a^2} - \frac{y^2}{b^2} = 1, \tag{7.4}$$

the equation of the tangent at any point with (x_0, y_0) coordinates is

$$y = \frac{b^2}{y_0}\left(\frac{x.x_0}{a^2} - 1\right), \tag{7.5}$$

where x and y are the points of interest, x_0 and y_0 are the coordinates of the point through which the tangent to the hyperbola is drawn, a is the major axis and b is the minor axis. The distance between the two focii of the hyperbola, c, is assumed

to be 20 m. This number can be modified as necessary. By knowing the distance between the first and second focii and the mirror along the x axis, F_1M and F_2M, respectively, the major axis a can be calculated as

$$a = \frac{1}{2}(F_2M - F_1M). \tag{7.6}$$

The minor axis b can be calculated using the hyperbola property

$$b = \sqrt{c^2 - a^2}. \tag{7.7}$$

If the mirror is originally flat and thus must be bent at certain points to resemble the required hyperbola, then the displacement needed at every point along the mirror in order for it to become hyperbolic can be calculated by taking the difference between the equation of the tangent to the mirror at point (x_o, y_o), Equation 7.5, and the equation of the mirror, Equation 7.4.

Figure 7-8 shows the shape of all eleven mirrors spanning a diameter of 0.5 m to 1.6 m. The center of the mirror has zero displacement, since this is where the tangent to the mirror is drawn. The displacements of every point along the length of the mirrors can be obtained from this data. In order to understand how an actual rectangular optic would behave if forced to comply to the shape of a hyperbolic mirror, FEA is done on a thin rectangular optic, 100 mm x 140 mm x 0.4 mm in dimensions.

FEA shows that the minimal number of ribs that can be used in order for the entire optic to replicate a hyperbolic shape is 3. Using one or two ribs results in a large deviation from a hyperbola in the areas away from the ribs. More ribs can potentially provide a better hyperbolic fidelity; however, this increases the weight of the assembly. Therefore, the analysis is performed on a rectangular optic with 3 ribs.

The initial design has one rib in the center of the optic with the other two on each end, as shown in Figure 7-9. This provides two large areas for x-ray reflection; however, due to the geometry of the optics available for experimentation, the two outer ribs have slightly been shifted from the edge of the optic.

This model assumes that the thin optic is flat to start with and is forced against preshaped ribs, where the ribs are either parabolic or hyperbolic, so the optic repli-

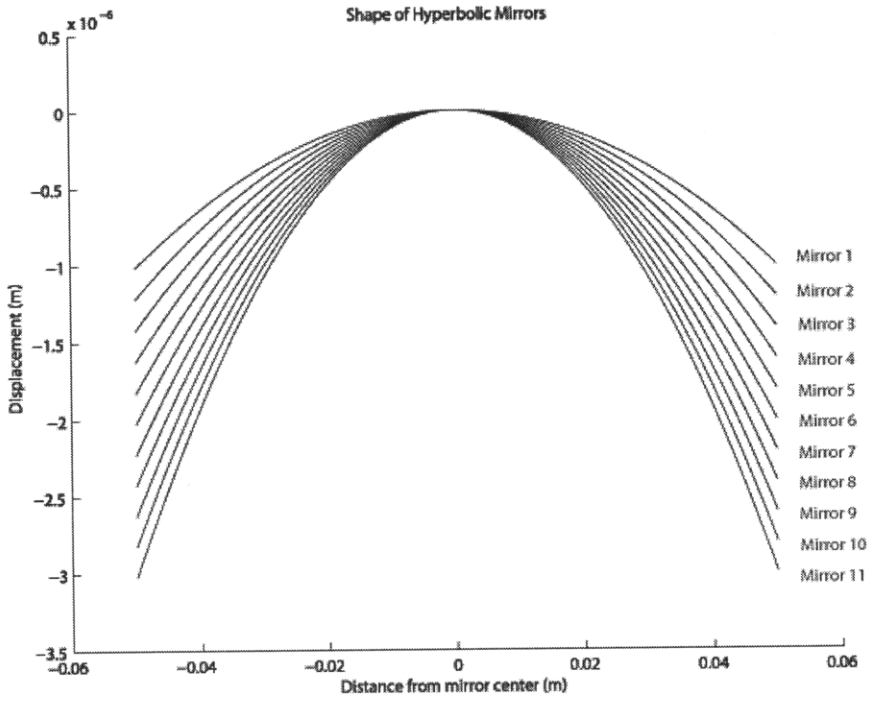

Figure 7-8: Shapes of hyperbolic mirrors, where mirror 1 has a diameter of 0.5 m and is the innermost shell, and mirror 11 has a diameter of 1.6 m and is the outermost shell of the telescope.

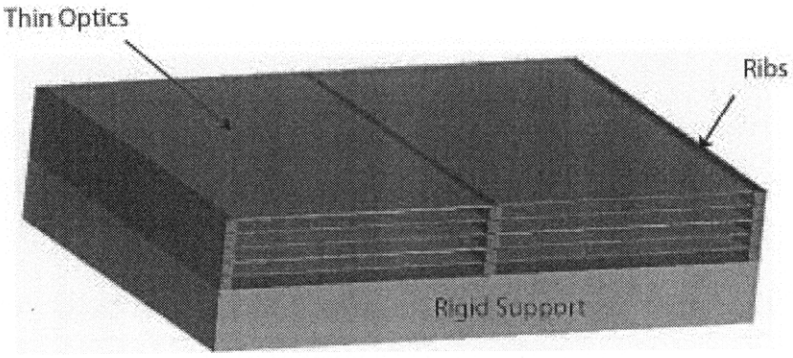

Figure 7-9: Assembled thin optics epoxied to one another and to a rigid support using precision spacers or ribs placed at the optic center and two edges

cates the shape of the ribs. For the case of the hyperbola, the 3-D solid model representing the thin optics has three lines of constraint, which are designated as the lines of contact with the hyperbolic ribs. As the optic is squeezed against the ribs at these 3 specific lines, the overall shape of the optic is analyzed. The FEA tool used is *Comsol Multiphysics.*

The curvature of every hyperbolic mirror is taken from the data in Figure 7-8. This data is placed as constraints along the three lines in contact with the ribs. The weight of the optic is not taken into consideration in the model, since these optics will be in space. Once material properties and constraints are entered in the 3-D model, FEA shows the final shape of the optic after it is forced against the ribs.

Figure 7-10 shows the shape of a mirror located at a distance of 0.25 m from the optical axis, after the optic has been forced against 3 hyperbolic ribs. This corresponds to Mirror 1 in Figure 7-8. The resulting deformation data indicates that the region of least fidelity is midway between the ribs.

To further analyze the difference between the required ideal hyperbolic shape and the resulting FEA model, the ideal and FEA data points from a line running along the length of the mirror parallel to the ribs and midway between two ribs were compared. Figure 7-11 *(a)* shows the ideal hyperbolic shape and the shape given by FEA at the midway between two ribs, and Figure 7-11 *(b)* shows the difference between the two.

It can be seen from Figure 7-11 *(b)* that the error is a maximum near the free edges of the optic and is close to 60 nm. The corresponding slope is calculated from the data to be 1.11 arcsec over a length of 15 mm. This means that the first and last 15 mm of the optic have a surface error of $\sim$1 arcsec, which is very promising for x-ray telescope mirror and grating applications.

A similar analysis is done for all 11 mirror sets. The results of Mirror 11 are shown in Figure 7-12. The resulting slope at the edges is calculated to be 3.33 arcsec over a length of 15 mm. This is the outermost mirror with a surface error that is still within the tolerance of the mission.

It can be seen that for hyperbolic mirrors, having 3 ribs is sufficient in changing the shape of a mirror from flat to hyperbolic. A similar analysis can be followed for

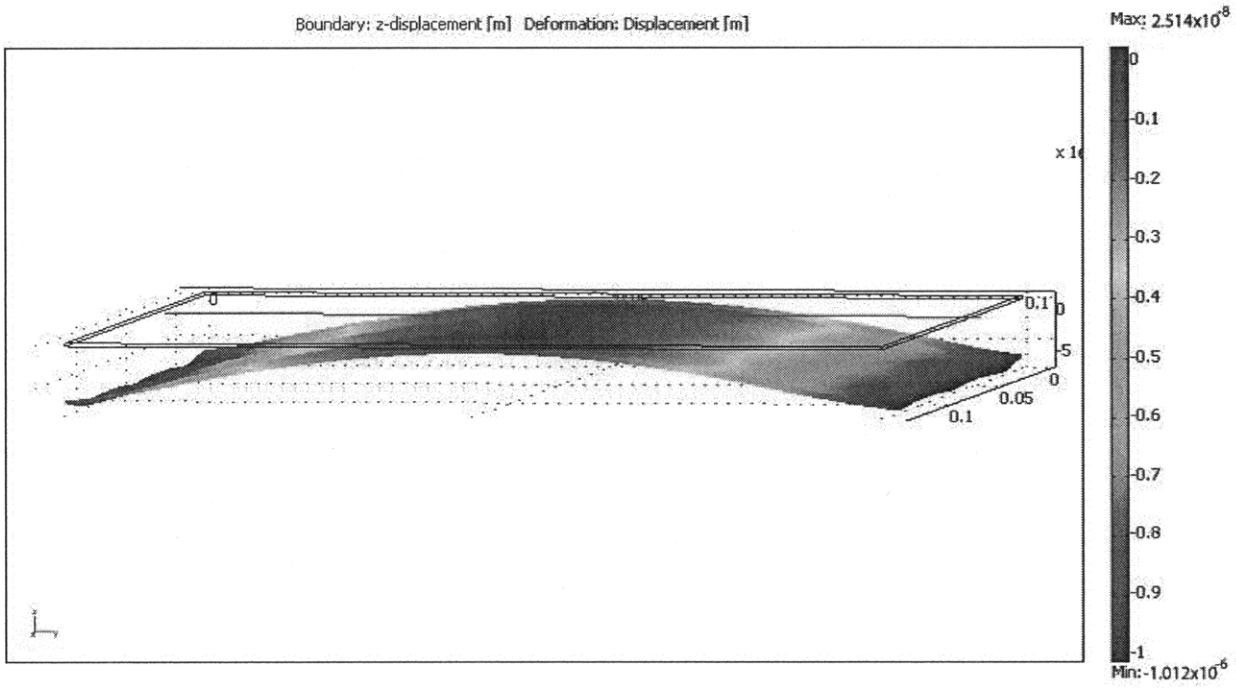

Figure 7-10: FEA results of shape of a mirror located at 0.25 m away from the telescope optical axis and forced against 3 hyperbolic ribs

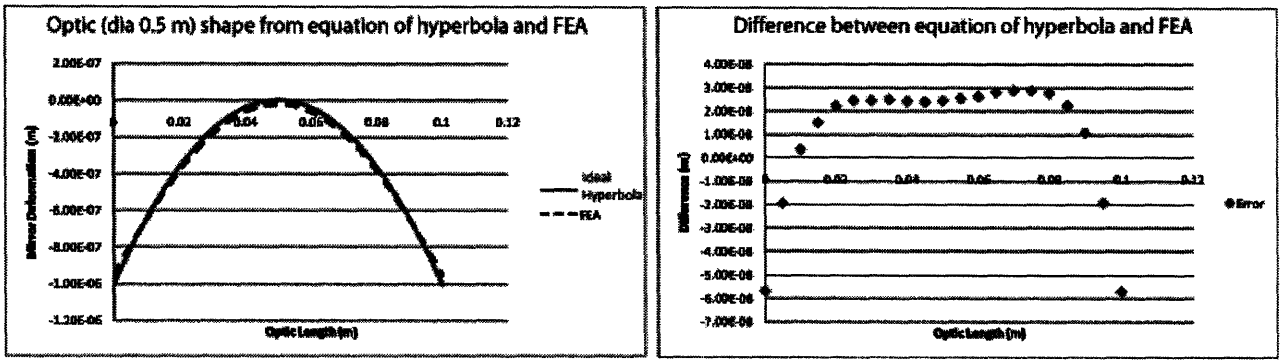

Figure 7-11: *(a)* Shape of a mirror at 0.25 m away from the telescope optical axis (Mirror 1) as calculated by the equation of a hyperbola and FEA. *(b)* Difference between the ideal shape and FEA result

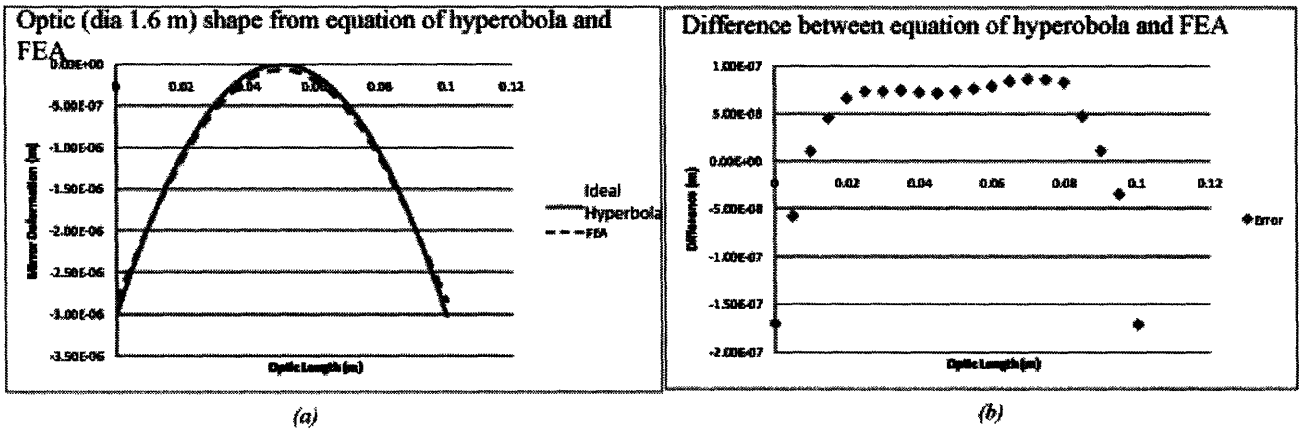

Figure 7-12: *(a)* Shape of a mirror at 0.8 m away from the telescope optical axis (Mirror 11) as calculated by the equation of a hyperbola and FEA. *(b)* Difference between the ideal shape and FEA result

parabolic geometries.

7.3 Design Parameters and Hardware Involved

Before trying to assemble hyperbolic mirrors, the first milestone is the assembly of flat sheets onto ribs without distorting their shape. At the time of these experiments, which were conducted before the slumping described in previous chapters was achieved, the flattest sheet found was a 6" diameter silicon wafer, with a peak-to-valley of ~ 10 μm. This is beyond the required tolerance for x-ray reflecting mirrors or gratings; thus, a new functional requirement of improving the surface flatness of sheets after assembly was added to the previous list. A set of components was designed to implement the assembly concept discussed. The effect of epoxy shrinkage and creep and the ability to improve the surface flatness of thin sheets during assembly were evaluated.

7.3.1 Metrology

Metrology is a key step during assembly. Metrology is performed using the Shack-Hartmann deep ultra-violet (UV) system described in Chapter 5 [64].

The metrology truss, shown in Figure 7-13, constrains the thin sheets during metrology while minimizing the effects of external forces, such as gravity, thermal expansion and friction. Such forces introduce errors in the surface measurements of thin substrates. This is achieved by using a series of monolithic flexures to hold the sheets. The metrology truss has a repeatability of 1 arcsec or $\sim$55 nm P-V [4].

7.3.2 Vacuum Chuck

In order to improve the surface flatness of thin optics and facilitate manipulating them during assembly, a special vacuum chuck was designed and used as part of the assembly steps. Thin optics are difficult to maneuver in general, since a user can easily distort them by implying manual forces and bowing them. It is also difficult to place

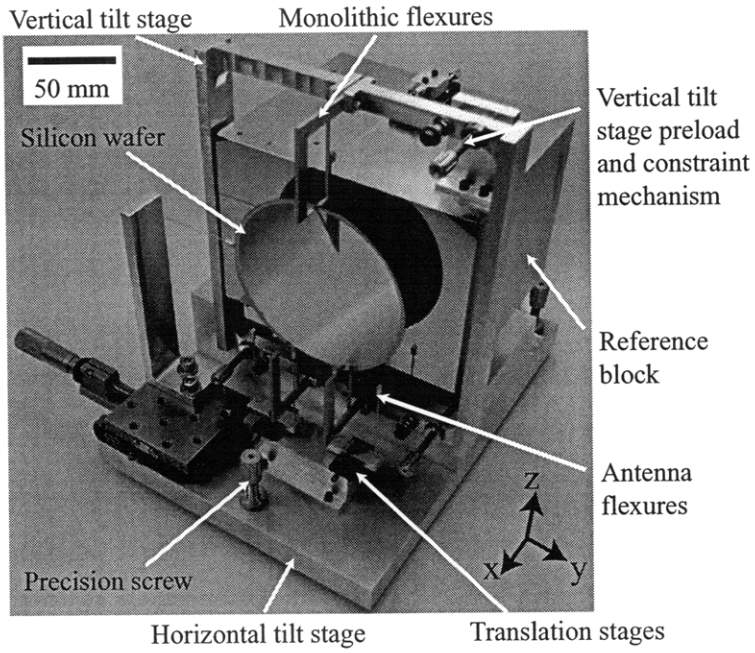

Figure 7-13: The Metrology Truss utilizes monolithic double-sided and antenna flexures to constrain a circular silicon optic during surface metrology [4]

a thin sheet precisely on a layer of epoxy without introducing additional distortions. If such temporary bows are not taken care of before the epoxy cures and solidifies, the final shape of the assembled optics will include errors. Thus the purpose of the vacuum chuck is to constrain the sheets during assembly in order to minimize such errors and better control the optics as they are placed against the layers of epoxy.

Thus the functional requirements of a vacuum chuck include constraining thin sheets without deteriorating their shape. Since vacuum forces the sheets to follow the surface of the chuck, the vacuum chuck itself must be flat to within the required tolerance of the sheets to avoid surface warp during assembly, as shown in Figure 7-14. A second concern is the entrapment of particulates between the sheet and the vacuum chuck. Such particulates result in dimples on the surface of the thin sheet as it is constrained by the vacuum chuck, as shown in Figure 7-15. This problem is prominent in the semi-conductor industry, where thin silicon wafers constrained against vacuum chucks have surface non-uniformities on the order of a few microns due to the particulates trapped between the chuck and the wafers. Another requirement is the ease of

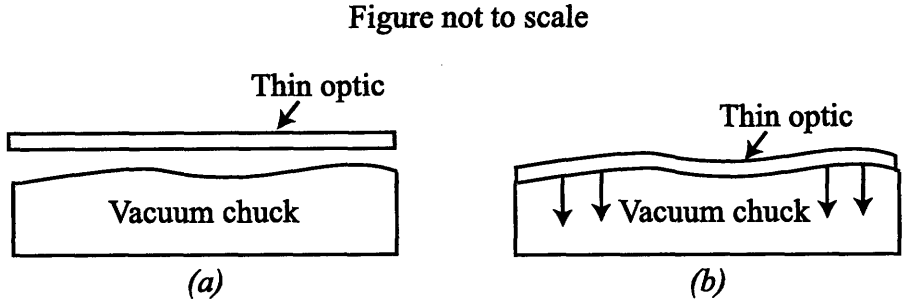

Figure 7-14: *(a)* A vacuum chuck with surface warp. *(b)* Once the thin sheet is held against the chuck by vacuum, the chuck warp is imposed on the sheet.

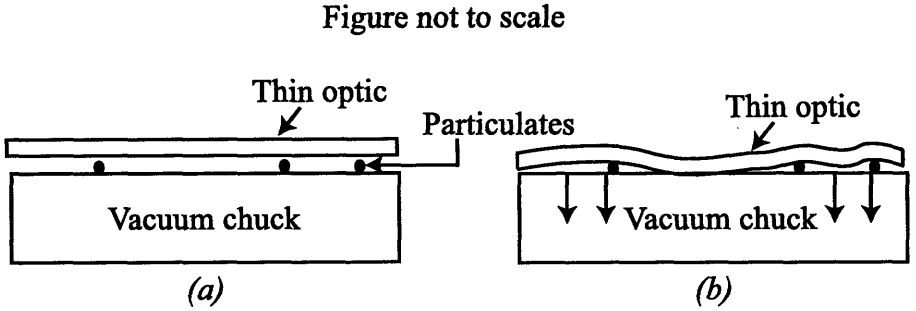

Figure 7-15: *(a)* A vacuum chuck with particulates on its surface. *(b)* Once the thin sheet is held against the chuck by vacuum, particulates are entrapped between the sheet and the chuck resulting in sheet surface warp.

the optic's front surface measurement while it is constrained. Placing the optic such that its back surface is against the vacuum chuck and its critical front surface is fully accessible for metrology, as shown in Figure 7-16, would incorporate errors associated with optic thickness variation. It should be noted that although silicon wafers are uniform in thickness, particularly the double-side polished ones, glass sheets used in display panels have a thickness variation on the order of tens of microns [16]. This is especially true for rectangular sheets, which are not usually polished. Thus placing the optics as shown in Figure 7-16 would include errors from vacuum chuck surface irregularities, particulate entrapments and sheet thickness variation.

Flattening the surface of the vacuum chuck can be accomplished using standard

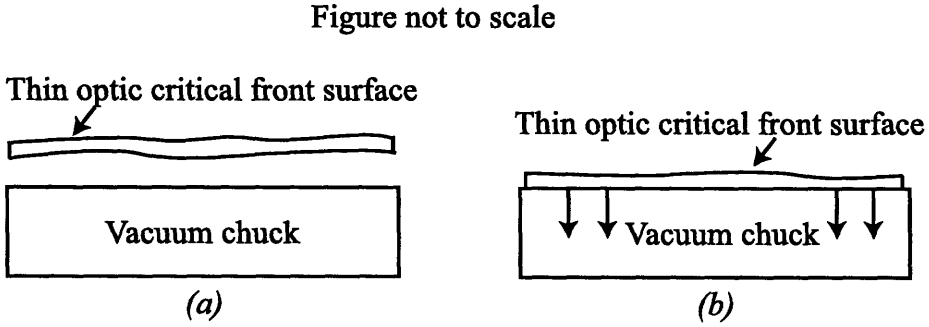

Figure 7-16: *(a)* A flat vacuum chuck and a sheet optic with non uniform thickness. *(b)* Once the thin sheet is held against the chuck by vacuum, the surface facing the chuck conforms to its flat surface but the thickness variation of the sheet can be seen on the opposite side of the sheet.

fly-cutting or optical polishing techniques. Eliminating the glass sheet thickness variation on the other hand is a more challenging task. Besides the fact that double-side polishing of commercially available sheet glass adds a machining step and an associated cost to the process, the rectangular geometry of sheet glass prevents the result of the rotary double-side polishing process from being as promising as is the case with circular geometries. It should also be noted that not many vendors have their polishing machines set up for rectangular geometries.

In order to avoid the sheet thickness variation and particulate entrapment challenges, the contact area with the designed chuck must be reduced, with the sheet placed such that its critical, x-ray reflecting surface is facing the flat vacuum chuck. This configuration requires the presence of metrology windows to access the front surface of the sheet.

Since the modeling shown in Section 7.2.2 reveals that forcing a sheet optic against three ribs is sufficient for the optic to conform to the shape of the ribs with acceptable errors, the design of a vacuum chuck that consists of three such ribs is considered, as shown in Figure 7-17. Such a design provides the metrology windows necessary to measure the critical surface of the constrained optics while minimizing contact with the optic surface.

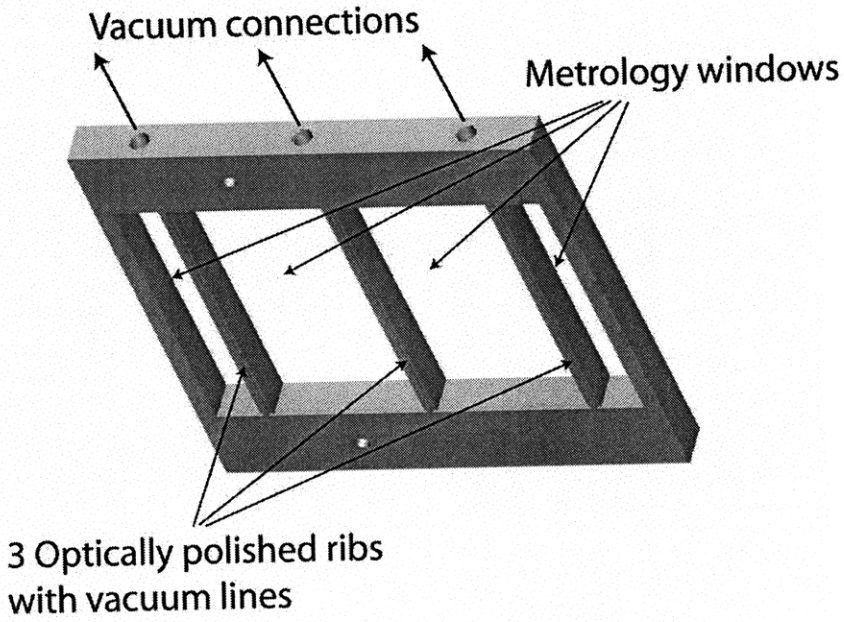

Figure 7-17: Optically polished vacuum chuck showing the three flat ribs, the vacuum lines running along the rib length, and the metrology windows

Optical polishing was chosen to improve the surface of the vacuum chuck, mainly because of the faster lead-time provided by *Surface Finishes*, the lower cost and the better accuracy control than the fly-cutting process. Because aluminum does not polish well unless it is nickel coated, stainless steel was chosen as a material for the vacuum chuck. Stainless steel has a higher Young's modulus than aluminum, thus it demonstrates a better rigidity while polishing. The plate is made of a 6" $\times$ 6" $\times$ 0.5" 440C stainless steel with metrology windows of the dimensions shown in Figure 7-18 machined within the plate to leave it with three ribs. Vacuum lines were drilled through the length of the ribs, as shown in the rib cross-section in Figure 7-18. At first, only one inlet hole was machined to connect the vacuum lines in the ribs to the vacuum connections to the chuck, as shown in Figure 7-18; however, it was noticed that this does not provide a strong enough vacuum along the length of the rib and the optic was not properly constrained on the edge further away from the inlet hole. Thus a second hole was drilled to strengthen the vacuum force and better constrain

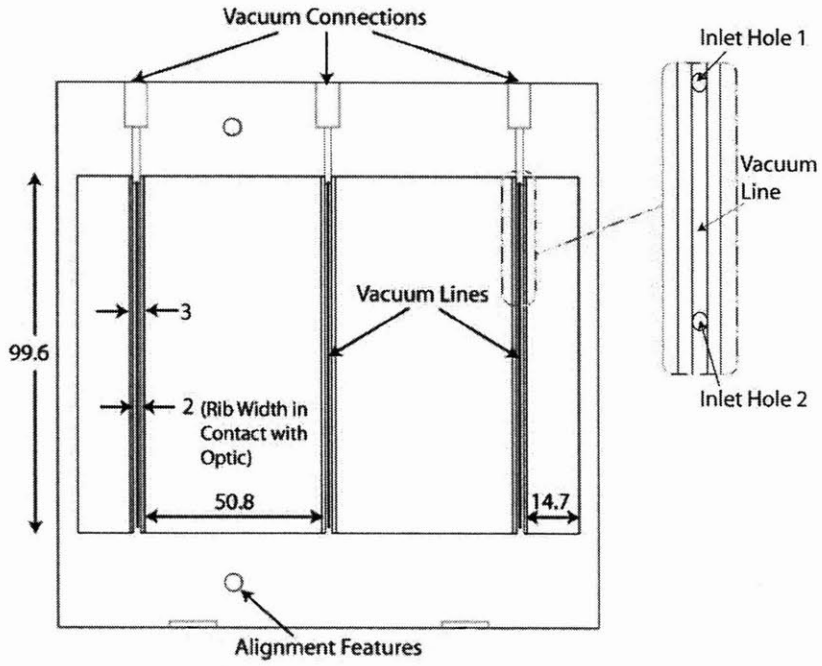

Figure 7-18: Critical dimensions in millimeters and features of the optically polished vacuum chuck

the optic. The plate was then heat treated to relieve internal stresses, hardened and ground to a flatness of ~25 μm. These three steps are necessary to obtain the flatness accuracy required during the optical polishing process. Afterwards, the plate was sent out to be polished to a quoted flatness of 50 nm. Once the ribs have been polished, the thin sheets should conform to the flatness of the ribs during assembly. The actual flatness of the vacuum chuck was measured to be ~200 nm P-V using the in-house Shack-Hartmann tool.

7.3.3 Rigid Support

The rigid support is what the optics would be assembled onto and is what would connect directly onto the telescope structure. For this experiment, a similar 440C stainless steel plate that is 6" × 6" × 0.5" in dimensions is used. The plate was stress-relieved, hardened and optically polished to a surface flatness of ~50 nm as

well, which was confirmed with the Shack-Hartmann tool.

7.3.4 Precision Ribs

Since the cross-section of the ribs is anticipated to be small, accurately machining long, thin ribs becomes more challenging as the length of the ribs increases. Thus, for the first set of experiments, it was decided to place the ribs along the 100 mm length instead of the 140 mm length to provide a better machining accuracy of shorter ribs. The first set of experiments was based on the assembly of flat gratings, where there is no significant bending of the optics required, thus bending challenges are not a concern.

Rib Material

When it comes to material selection, the lower the density of the ribs, the lighter the overall assembly would be. For the first set of experiments, metal is chosen; however, an alloy or ceramic with better thermal match with glass and possibly smaller density would be a more expensive but perhaps a better option. Aluminum is a good choice only if the machining of the narrow, long ribs is done utilizing a process that does not impart large machining forces on them, since such forces change their linearity. The relatively low Young's modulus of aluminum compared to stainless steel makes it inferior to the latter. Aluminum has a higher CTE of $27\times10^{-6}/°C$, compared to an average of $17\times10^{-6}/°C$ for stainless steel, $7\times10^{-6}/°C$ for glass and $2.6\times10^{-6}/°C$ for silicon. For tests conducted in the laboratory, stainless steel was chosen for the ribs machined using a milling machine. Wire electric-discharge-machining, however, is a process that can be utilized to manufacture different metals with higher accuracy.

Rib Cross-Section

The original cross-section considered was a T-section, as shown in Figure 7-19. The lower edge is 3 mm wide for increased stiffness during machining and easier manipulation during assembly, whereas the narrower 1 mm upper edge provides a smaller

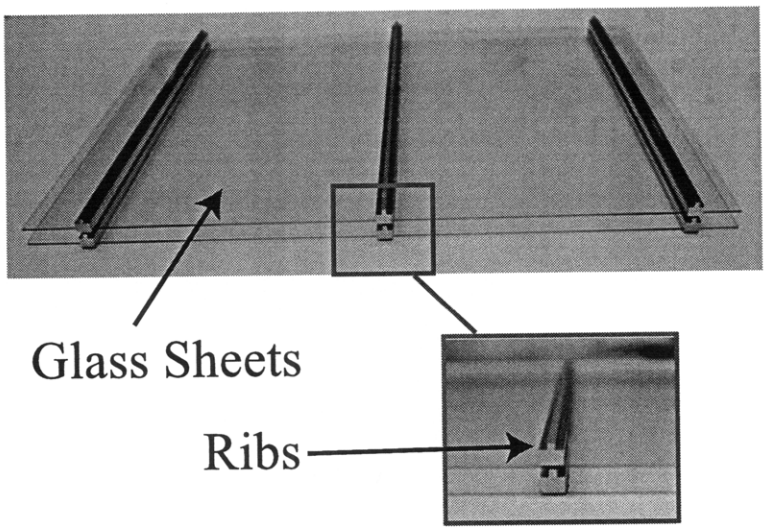

Figure 7-19: Glass sheets (140 mm x 100 mm x 0.4 mm) assembled utilizing 3 aluminum ribs with a T cross-section. The x-ray reflecting surface is in contact with the shorter edge of the T-rib.

contact area with the x-ray reflecting side of the sheets. Since the ribs are of a different material from glass or silicon, the possibility of a bi-layer effect, defined by Equation 7.8, is studied as the temperature of the assembled optics varies by the quoted 1°C for the telescope. The resulting curvature κ is given by

$$\kappa = \frac{(\alpha_2 - \alpha_1)(T - T_o)}{\frac{h}{2} + \frac{2}{h}(E_1 I_1 + E_2 I_2)\left(\frac{1}{t_1 b_1 E_1} + \frac{1}{t_2 b_2 E_2}\right)}, \tag{7.8}$$

where subscript 1 refers to glass and subscript 2 refers to the rib material, α is the CTE, $T - T_o$ is the temperature change, t is the individual thickness of the glass sheet or the spacer, h is the sum of t_1 and t_2, E is the Young's modulus, I is the bending moment of inertia and b is the width of the glass sheet or the ribs.

Figure 7-20 shows the two cross-sections considered for the ribs. Both ribs have a length of 100 mm, the length of the glass sheet. Table 7.1 shows the resulting curvature of the glass and ribs as a result of a temperature variation of 1°C in the laboratory or telescope environment.

As can be seen from Table 7.1, stainless steel induces the smallest curvature, and

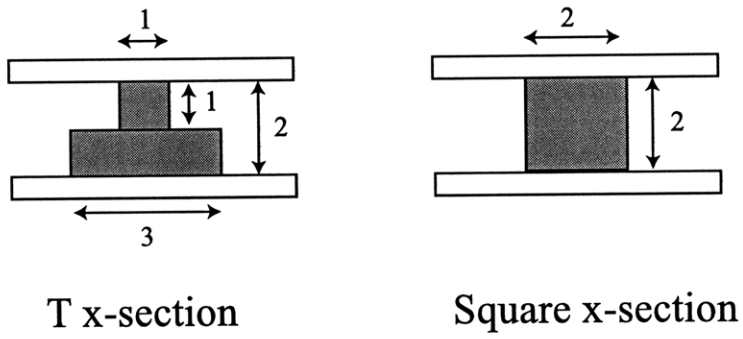

Figure 7-20: Two cross-sections considered for rib design. Dimensions are in mm.

		Aluminum	Stainless Steel	Brass
T x-section	1 mm top edge	0.01255	0.00633	0.00826
	3 mm lower edge	-0.01473	-0.00723	-0.00955
Square x-section	Top edge	0.01249	0.00598	0.00803
	Lower edge	-0.01249	-0.00598	-0.00803

Table 7.1: Curvature κ 1/m of glass-rib layers as a function of rib material and cross-section for a 1°C temperature variation

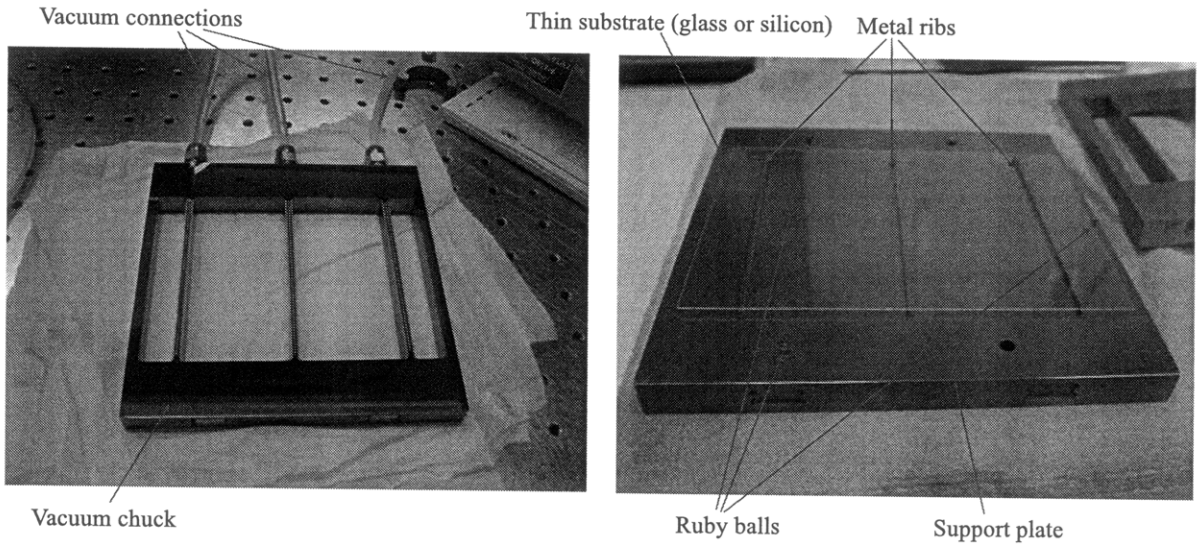

Figure 7-21: Parts involved in the assembly of thin sheets

thus the least amount of stress on the glass sheets. It can also be seen that for the T cross-section, the curvature induced on the narrower edge is positive and smaller than negative curvature on the wider edge, which is anticipated. The square cross-section, on the other hand, induces equally opposite curvatures on both edges in contact with the glass sheet. Thus, if a rib with square cross-section is attached between two glass sheets, as shown in Figure 7-20, the nominal resulting curvature is zero, minimizing the overall curvature of the stack of assembled glass sheets.

The overall covered area by the square ribs is less than 5% of the optic surface. The height of the ribs, which provides the gap through which x-rays can pass and hit the surfaces of the optics, is chosen to be equal to the width to avoid any orientational placement errors during assembly.

7.4 Assembly Steps

All the parts involved in the assembly process are summarized in Figure 7-21.

A 6" diameter silicon wafer was cut using a die-saw to be left with a rectangular sheet 140 mm $\times$ 100 mm in dimensions. This sheet was then placed in the metrology

truss and its front surface was measured, as shown in Figure 7-22*(a)*. Once this surface measurement data is available, assembly of the sheet can begin.

The next step in the assembly process is to assemble the precision spacer-ribs onto the rigid support. Three stainless steel ribs were machined to the required dimensions. For this experiment, the ribs were machined in the MIT *Central Machine Shop*; however, as mentioned earlier, better accuracy can be achieved if the ribs are machined using wire electric-discharge-machining. These spacer-ribs are then placed onto the vacuum chuck ribs, both having a width of 2 mm, as shown in Figure 7-22*(b)*. The vacuum connected to the chuck is then turned on and the ribs are fully constrained against the chuck. At this point, a thin layer of *Masterbond* EP 30-2 time-cure epoxy, which comes in two parts mixed in a ratio of 10:1 and has a linear shrinkage of only 0.03%, is applied onto the exposed surface of the spacer-ribs using a fluid dispenser purchased from *Norlico Corporation* in New Hampshire. The needle used in this epoxy application is *Techcon System's* TS30-1/4 model, which has an inner diameter of 0.152 mm. The vacuum chuck and ribs are then taken and placed against the support, as shown in Figure 7-22*(c)*, until the epoxy cures. Alignment rods are used to align the vacuum chuck and the support in the lateral direction. This ensures that the different sets of ribs are placed on top of one another within a tolerance of ± 2.5 μm. When the epoxy has cured, the vacuum is turned off and the chuck removed. The first set of ribs is now assembled onto the support.

The next step involves removing the silicon sheet from the metrology truss and placing it against the vacuum chuck. The initial warp of ~ 10 μm measured on the thin silicon sheet is significantly reduced as the vacuum is turned on, and the sheet is forced to conform to the optically-polished flatness of the vacuum-chuck ribs, as shown in Figure 7-22*(d)*. This is confirmed by measuring the front surface of the now constrained sheet through the vacuum chuck windows, as shown in Figure 7-22*(d)*.

A fresh layer of epoxy is applied on the spacer-ribs placed on the support. The vacuum chuck with the constrained sheet is brought closer to the spacer-ribs and placed at a precalculated distance from the support determined by the ruby balls shown in Figure 7-23, such that the silicon sheet is in contact with the epoxy on the

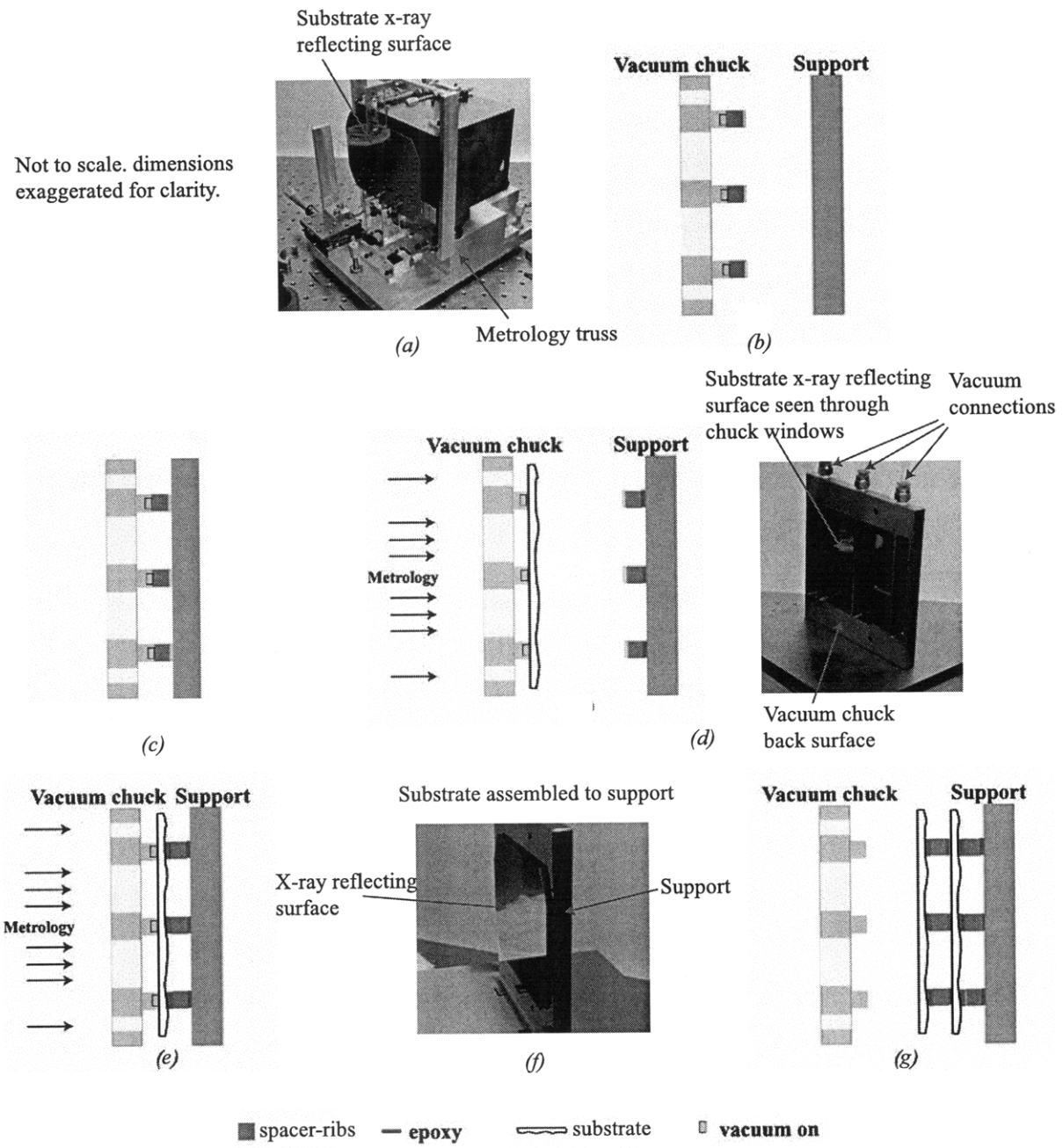

Figure 7-22: Thin sheet assembly steps. *(a)* A thin silicon substrate constrained by the Metrology truss to measure its front surface. *(b)* Spacer-ribs constrained by vacuum chuck, and a thin layer of epoxy applied on one face. *(c)* Vacuum chuck with spacer-ribs placed against support until epoxy cures. *(d)* Spacers mounted on rigid support with a fresh layer of epoxy on their exposed face, and silicon substrate constrained by vacuum chuck. *(e)* Thin substrate assembled on spacers and vacuum chuck retracted after curing of epoxy. *(f)* Thin substrate front surface measured for evaluation. *(g)* Second thin sheet assembled following previous steps

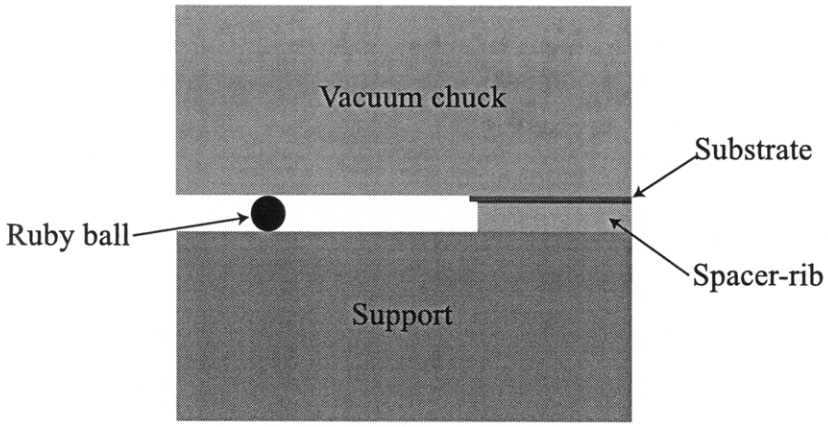

Figure 7-23: Cross-sectional view showing a ruby ball controlling the distance between the support and the vacuum chuck

spacer-ribs. The vacuum is left on as the epoxy cures to counteract the shrinkage forces the sheet sees during the curing process, as shown in Figure 7-22*(e)*. The front surface of the sheet can be continuously measured during this curing process through the vacuum chuck windows, as illustrated in Figure 7-22*(e)*. Once the epoxy has fully cured, the vacuum is turned off, and the vacuum chuck is removed from the assembly. The front surface of the newly-assembled sheet, referred to as *sheet 1* is measured for process evaluation, as shown in Figure 7-22*(f)*.

For this experiment, three high-precision ruby balls are used to control the distance between the vacuum chuck and the support as the epoxy attaching the sheet to the spacer-ribs cures. Figure 7-23 shows a schematic of this set-up, highlighting only one ball. In fact, by controlling the dimensions of all the parts involved and following an error budget to take tolerance and systematic errors into consideration, the overall thickness of the epoxy line can be determined to be $\sim$45 μm, with a thickness tolerance of $\pm$5 μm.

A second set of ribs is machined on the side, away from the assembly location, such that any errors seen on the assembled *sheet 1* can be accounted for in the machining of the next set of ribs. This minimizes stack-up errors. The new set of ribs can now be assembled along with a second sheet onto *sheet 1* by following the same steps

described above, as illustrated in Figure 7-22*(g)*. This process can be followed to stack substrates on top of one another to have a module with many gratings or optics.

7.5 Results and Discussion

The utilization of a flat, custom-designed vacuum chuck as discussed above helps the assembly scheme in two aspects: it improves the overall surface flatness of the optics during the assembly steps, and it facilitates manipulating the optics, since it rigidly yet precisely constrains them during assembly.

Figure 7-24 shows the shape of the silicon wafer as it goes through the assembly steps. The data shown covers the part of the optic seen through one window of the vacuum chuck. Figure 7-24*(a)* shows the surface map of a silicon optic with a surface topography of 9.4 μm P-V and 1.7 μm rms. This initial warp is much larger than the curvatures studied in the hyperbolic modeling described above. Once the optic is constrained by the vacuum chuck, its surface improves to 3.1 μm P-V and 0.6 μm rms, as shown in Figure 7-24*(b)*. This is a significant improvement in the overall flatness as a result of the optic's compliance to the flatness of the ribs on the vacuum chuck; however, the optic does not fully replicate the flatness of these ribs. Once the optic is assembled, and the epoxy has cured, the vacuum chuck is released and the optic's surface topography is measured to be 2.4 μm P-V and 0.5 μm rms. The natural frequency of the assembled optic is modeled and found to be 825 Hz for the first mode, as shown in Figure 7-25.

To better understand how this affects telescope performance, the angular histogram of the optic is studied throughout the assembly. Figure 7-26*(a)* shows the angular historgram of the free optic before it is assembled, with an rms of 52 arcsec. As the optic is placed against the vacuum chuck's flat ribs, and the vacuum is turned on, the surface rms drops to 30 arcsec, as shown in Figure 7-26*(b)*. Once the optic is assembled onto the rigid support, the angular histogram reveals an rms of 27 arcsec, as shown in Figure 7-26*(c)*. This is an improvement of $\sim$50%. The same optic surface is measured about a week later to evaluate the effect of the full curing of epoxy on the

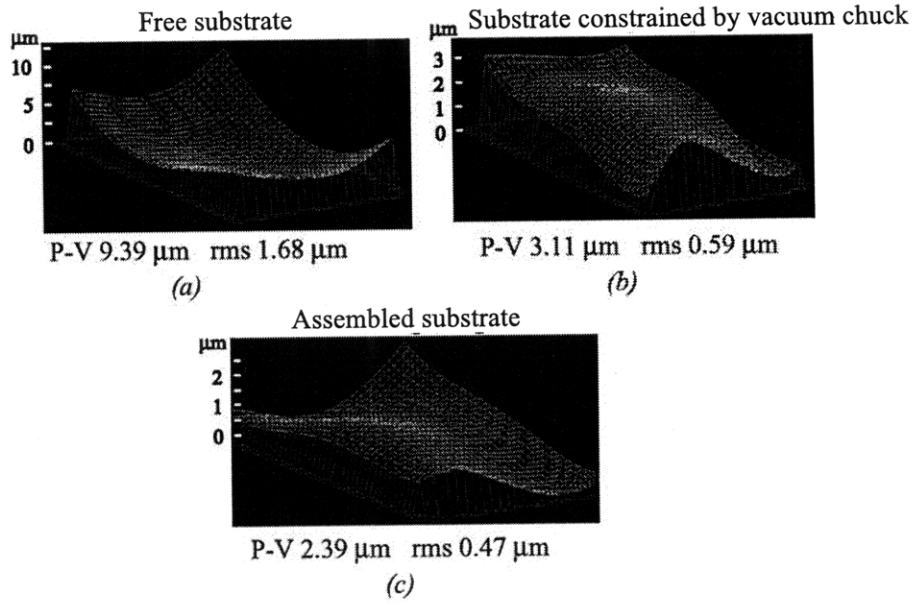

Figure 7-24: Surface topography of the thin substrate before and after assembly. This is the surface area seen through one of the windows of the vacuum chuck. *(a)* Free substrate when constrained by the thin optic metrology truss. *(b)* Substrate constrained by the vacuum chuck leads to a significant improvement in surface overall flatness. *(c)* Assembled substrate bonded to precision spacers

assembled sheet. A slight degradation is observed, where the angle histogram reveals an rms of 33 arcsec, as shown in Figure 7-26*(d)*. The optic's flatness changes to 3.33 P-V, which is a difference of $\sim$1 μm from the data collected a week earlier.

The epoxy used cures with time. During the assembly process, the epoxy curing step is done in a two-hour time frame, after which the epoxy is 80-90% cured. The epoxy continues to cure as the vacuum chuck is removed and the assembly is continued, altering the shape of the assembled sheet. One way to minimize this effect is to use epoxy that cures with ultra-violet light, such that full curing occurs during the assembly steps. This has not been pursued at this stage due to the inavailability of a portable ultra-violet source at the time of the test.

In order to understand why the optic does not faithfully replicate the flatness of the vacuum chuck ribs when the vacuum is turned on, another model is considered.

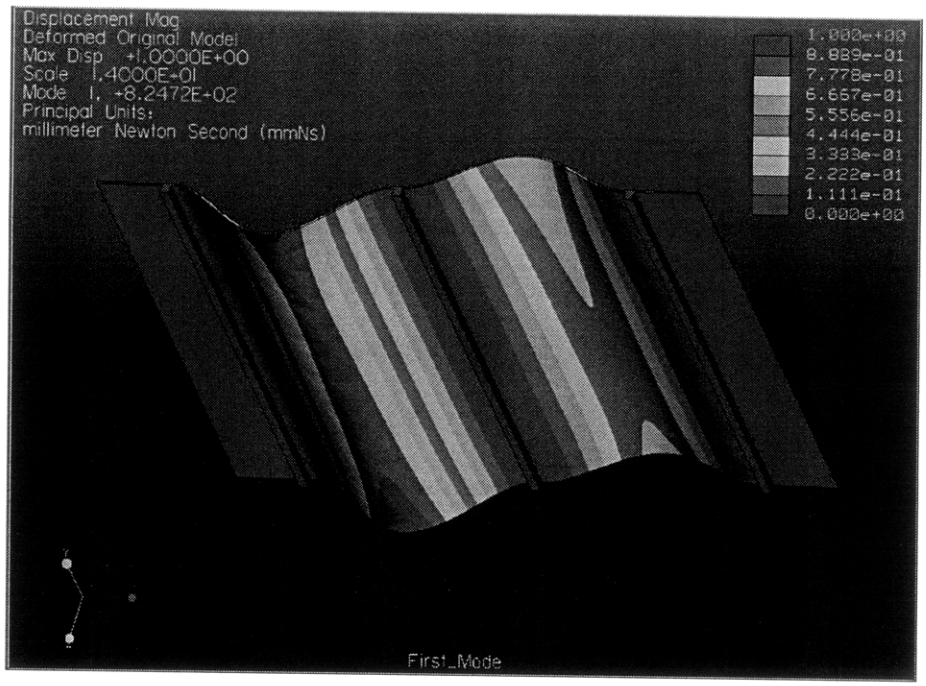

Figure 7-25: First mode of vibration indicating a natural frequency of 825 Hz for the first mode

This model forces a flat silicon substrate to conform to the shape of a hyperbola with a surface P-V of ~9.4 μm. This is the reverse of what the experiment is trying to achieve, which is to change the surface of an optic from a P-V of 9.4 μm to surface flatness of <200 nm, the quoted flatness of the ribs of the vacuum chuck. In the case of the experiment, however, the actual surface of the optic is much more complicated than the 2-D hyperbola the model considers.

The resulting solution, shown in Figure 7-27, indicates an error of 0.81 μm P-V and 0.24 μm rms. The rms is along the same order of magnitude as the experimental results; however the P-V in the experiment is three times as large as the theoretical estimation. Some of the factors that may have contributed to this include:

1. the original shape of the optic is not a simple 2-D hyperbola, but rather a more complicated 3-D shape, and thus the model is not an accurate representation but rather a back-of-the-envelope analysis,

2. the ribs on the vacuum chuck do not have a strong enough vacuum to force the entire length of the optic resting on them to conform to their shape, as the model

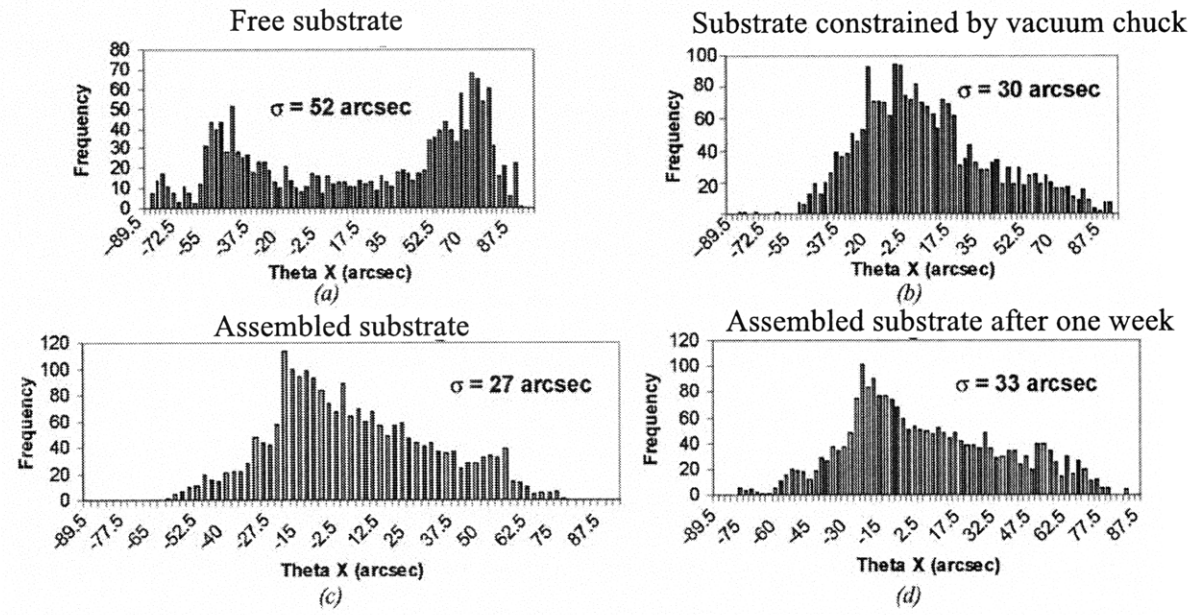

Figure 7-26: Angle histograms of one substrate before, during and after assembly. *(a)* Free substrate with 52 arcsec rms. *(b)* substrate constrained by the vacuum chuck with 30 arcsec rms. *(c)* Assembled substrate bonded to precision spacers with 27 arcsec rms. *(d)* Same bonded substrate measured a week later shows a slight variation of surface flatness with 33 arcsec rms.

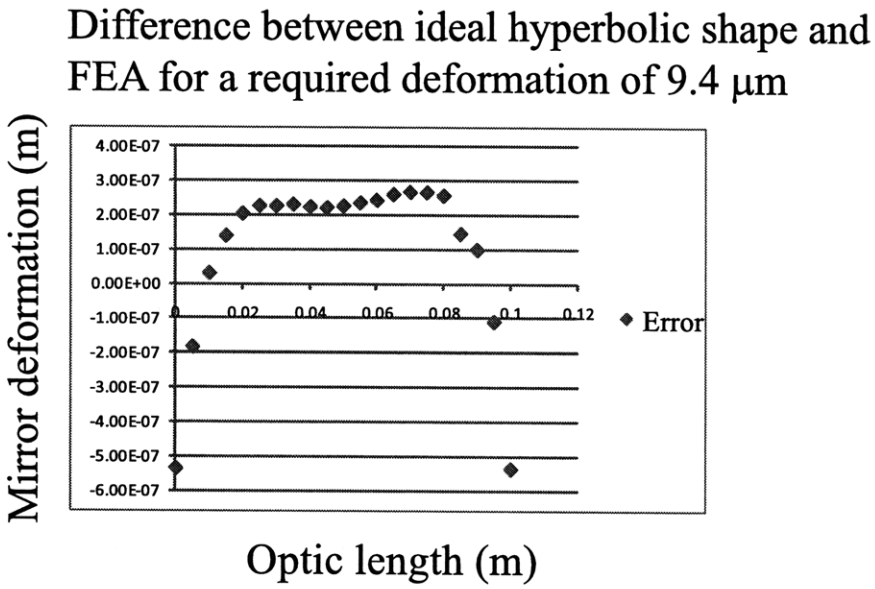

Figure 7-27: Difference between the ideal shape and FEA results for a hyperbolic mirror with 9.4 μm P-V forced against a flat vacuum chuck

requires. There are two vacuum holes along the length of the rib with a channel connecting the two holes and running down the length of the rib. As has been described earlier, the addition of a second hole has increased the strength of vacuum on the optic, and thus the addition of a third hole along the length of the rib would better constrain the lower end of the optic,

3. particulates trapped between the optic and the vacuum ribs can result in optic distortion at the rib interface and thus along the area of the optic.

As mentioned before, the required resolution for the *Constellation-X* mission is 15 arcsec. Though this assembly scheme is very promising, it does not yield the required results yet, mostly because the starting surface of the optic has errors much larger than the required tolerance. Utilizing optics that have a better surface flatness before the assembly will improve the outcome of the assembly scheme, since the shape of the optic is closer to the final shape needed. Another parameter that can be better controlled is the machining of the spacer-ribs, which are currently machined using a

mill. Wire EDM-ing these spacer-ribs instead would yield tighter tolerances on their geometry, and thus better control on the final shape of the assembled thin optics. Finally, utilizing an epoxy that has lower creep characteristics with time while having a low shrinkage during curing would also improve the final results of assembly.

7.6 Conclusion and Future Work

An assembly scheme is analyzed and developed to stack up thin optics while improving their surface flatness. The scheme relies on a custom-designed vacuum chuck that constrains thin, flimsy substrates and assembles them onto a rigid support.

The process has demonstrated a surface flatness improvement of 75%. A silicon sheet with an original surface bow of 9.4 μm P-V has a surface flatness of 2.39 μm P-V after it has been assembled. For x-ray telescope applications, the developed technology must still be pushed to obtain better results, which depend on the original shape of the thin substrates before they are assembled. At the time of this experiment, 6" diameter silicon wafers are found to have the best surface flatness commercially available. It is possible to use the Magneto-Rheological Finishing process described in Chapter 2 to improve their surface flatness before they are assembled. The same requirement is true for glass sheets, whose initial bow is on the order of hundreds of microns. A shaping process prior to assembly will produce better results.

The tests run have been for assembling and improving the surface flatness of a thin substrate without adding curvature to its surface; however, for the x-ray telescope optics, both parabolas and hyperbolas are needed to focus x-rays. This requires a modification of the vacuum chuck surface, such that it has the opposite of the curvature desired. A unique chuck would be required for the mirror segments of the same diameter. The remaining assembly steps are unchanged.

Appendix A

Matlab Code for Flow in Porous Media

A.1 Flow in Porous Media with Flat Surfaces

%Mireille Akilian

%Pressure distribution of air bearing for slumping with no grooves

%Last updated Tue 9 Feb 07

clc;

clear;

% number of nodes N x N x N

N=13;

%all dimensions in mm, but not a problem since this is a dimensionless

%solution, just make sure that the permeability is in the proper units of

%mm^2 rather than the regular m^2 (Darcy)

% permeability ratio Kx = kx/kz and Ky = ky/kz

Kx=1;

Ky=1;

kz=6*10^{-9}; %kx=ky=kz=10^{-14}m^2 at room temperature. note these are absolute permeabilities and not ratios. But this 6x10^{-9} is the value at 600C

% ceramic dimensions

X=100; %100mm

Y=100; %100mm

H=12.7; %12.7mm

% ceramic width to length ratio XY

XY=X/Y;

XH=X/H;

% air gap thickness h

h=50/1000; %50 um

% constant A used in first equation

A=2*(Kx+Ky*XY^2+XH^2);

% supply pressure to atm pressure ratio psa

psa=(14.5+0.3)/14.5; %this parameter is a ratio of absolute pressure used to absolute atm pressure;

pa=14.5; %absolute atm pressure

% feeding parameter lmda=12kzX$\hat{2}$/(h$\hat{3}$H)

lmda=12*kz*X^2/h^3/H;

% coefficients used in second equation

a=1./lmda+1/2*Kx*H*h/X^2;

b=1./lmda+1/2*Ky*H*h/X^2;

del=1/(N-3); % normalized del so that delx = dely = delz normalized, otherwise they are not equal

% pressure matrix NxNxN elements

P=zeros(N,N,N);

% BOUNDARY CONDITIONS

% bottom ceramic surface at plenum supply pressure

(:,:,1:2)=psa;

% ambient condition on ceramic top surface edges where p=patm

P(1:2,:,N-1:N)=1;

P(:,1:2,N-1:N)=1;

P(:,N-1:N,N-1:N)=1;

```
P(N-1:N,:,N-1:N)=1;
% FINITE DIFFERENCE ITERATION METHOD
for f=1:1:3000
for i=3:1:N-2
for j=3:1:N-2
for k=3:1:N-2
P(2,j,k)=(Kx*P(3,j,k)+Ky*XY^2*(P(2,j+1,k)+P(2,j-1,k))+XH^2*(P(2,j,k+1)+P(2,j,k-
1)))/(Kx+2*(Ky*XY^2+XH^2)); %these four lines are for the nodes on the sides of the
bearing along the y axis
P(1,j,k)=P(2,j,k);
P(N-1,j,k)=(Kx*P(N-2,j,k)+Ky*XY^2*(P(N-1,j+1,k)+P(N-1,j-1,k))+XH^2*(P(N-1,j,k+1)+P(i,j,k
1)))/(Kx+2*(Ky*XY^2+XH^2));
P(N,j,k)=P(N-1,j,k);
P(i,2,k)=(Kx*(P(i+1,2,k)+P(i-1,2,k))+Ky*XY^2*P(i,3,k)+XH^2*(P(i,2,k+1)+P(i,2,k-
1)))/(2*(Kx+XH^2)+Ky*XY^2); %these four lines are for the nodes on the sides of the
bearing along the x axis
P(i,1,k)=P(i,2,k);
P(i,N-1,k)=(Kx*(P(i+1,N-1,k)+P(i-1,N-1,k))+Ky*XY^2*P(i,N-2,k)+XH^2*(P(i,N-
1,k+1)+P(i,N-1,k-1)))/(2*(Kx+XH^2)+Ky*XY^2);
P(i,N,k)=P(i,N-1,k);
P(i,j,k)=(Kx*(P(i+1,j,k)+P(i-1,j,k))+Ky*XY^2*(P(i,j+1,k)+P(i,j-1,k))+XH^2*(P(i,j,k+1)+P(i,j,
1)))/A;
%corners
P(2,2,k)=(Kx*P(3,2,k)+Ky*XY^2*(P(2,3,k)+P(2,1,k))+XH^2*(P(2,2,k+1)+P(2,2,k-
1)))/(Kx+2*(Ky*XY^2+XH^2));
P(1,2,k)=P(2,2,k);
P(2,1,k)=P(2,2,k);
P(1,1,k)=P(2,2,k);
P(2,N-1,k)=(Kx*P(3,N-1,k)+Ky*XY^2*(P(2,N,k)+P(2,N-2,k))+XH^2*(P(2,N-1,k+1)+P(2,N-
1,k-1)))/(Kx+2*(Ky*XY^2+XH^2));
```

```
P(1,N-1,k)=P(2,N-1,k);
P(2,N,k)=P(2,N-1,k);
P(1,N,k)=P(2,N-1,k);
P(N-1,2,k)=(Kx*P(N,2,k)+Ky*XY^2*(P(N-1,3,k)+P(N-1,1,k))+XH^2*(P(N-1,2,k+1)+P(N-1,2,k-1)))/(Kx+2*(Ky*XY^2+XH^2));
P(N,2,k)=P(N-1,2,k);
P(N-1,1,k)=P(N-1,2,k);
P(N,1,k)=P(N-1,2,k);
P(N-1,N-1,k)=(Kx*P(N,N-1,k)+Ky*XY^2*(P(N-1,N,k)+P(N-1,N-2,k))+XH^2*(P(N-1,N-1,k+1)+P(N-1,N-1,k-1)))/(Kx+2*(Ky*XY^2+XH^2));
P(N,N-1,k)=P(N-1,N-1,k);
P(N-1,N,k)=P(N-1,N-1,k);
P(N,N,k)=P(N-1,N-1,k);
end
P(i,j,N-1)=(a*(P(i+1,j,N-1)+P(i-1,j,N-1))+b*XY^2*(P(i,j+1,N-1)+P(i,j-1,N-1))+del/2*P(i,j,N-2))/(2*a+2*b*XY^2+del/2); %note that in this equation there is no N for k only N-1
because we are assuming there is no pressure drop along the z axis in the air gap.
This is the Modified Reynold's equation boundary condition
P(i,j,N)=P(i,j,N-1);
end
end
end
for m=1:1:N-2
for s=1:1:N-2
S(m,s)=P(m+1,s+1,N-1);
Pbearing(m,s)=S(m,s)*pa-pa;
Load(m,s)=Pbearing(m,s)/0.145*10^3*X/1000/(N-3)*Y/1000/(N-3);
Q(m,s)=P(m+1,s+1,2);
R(m,s)=P(m+1,s+1,3);
end
```

```
end
%Plotting issues
figure;
x(1)=-X/2;
y(1)=-Y/2;
for i=2:1:N-2
x(i)=x(i-1)+X/(N-3);
y(i)=y(i-1)+Y/(N-3);
end
surf (x,y,Pbearing)
xlabel('x (mm)')
ylabel('y (mm)')
zlabel('Pressure distribution (psig) at Psupply=0.00347 psig')
%title('Pressure distribution along rectangular bearing area at supply pressure of
5 psig and a gap of 10 um')
%Load Capacity calculation
%W=double integral (p-pa)dxdy x and y from 0 to X,Y, this integral is the sum
of the
%pressures multiplied by the areas with the area limit going to zero or in other
words as small as possible, or in other words increase N so that deltaA is very small
deltaA=X/(N-2-1)*Y/(N-2-1)/1000000;
sum=0;
for i=1:1:N-2
for j=1:1:N-2
inc=(Pbearing(i,j)/0.145*1000)*deltaA;
sum=sum+inc;
end
end
W=sum;
```

fprintf('The load capacity of this bearing for a supply pressure of %g psig is %g N',psa*pa-pa,W)

A.2 Flow in Porous Media with Grooves on Surface

%Mireille Akilian

%This modeling uses the reynold's equation with proper modification to account for the grooves. There are grooves all over the bearing surface.

%Pressure distribution of grooved air bearing for slumping

%Last updated Wed 25 May 08

clc;

clear;

% number of nodes N x N x Nz

N=28;

Nz=10;

%all dimensions in mm, but not a problem since this is a dimensionless solution, just make sure that the permeability is in the proper units of mm^2 rather than the regular m^2 (Darcy)

% permeability ratio Kx = kx/kz and Ky = ky/kz

Kx=1;

Ky=1;

kz=10^{-6};

% ceramic width to length ratio XY

XY=100/100;

XH=100/14;

% air gap thickness h

h=10/1000; %10 um

% ceramic dimensions

X=100; %100mm

Y=100; %100mm

H=14; %14mm

% groove dimensions

gwx=305/1000; % groove width in y direction in mm affecting node properties in x direction

hgx=1000/1000; % groove height in y direction in mm

gwy=0/1000; % groove width in x direction in mm affecting node properties in y direction

hgy=0/1000; % groove height in x direction in mm

% supply pressure to atm pressure ratio psa

psa=(14.5+1.2)/14.5; % supply pressure is 0.8 psig. this parameter is a ratio;

pa=14.5; % absolute atm pressure

% feeding parameter lmda=12kzX^2/(h^{3}H)

lmda=12*kz*X^2/h^3/H;

% coefficients used in Reynold's equation

a=1./lmda+1/2*Kx*H*h/X^2;

b=1./lmda+1/2*Ky*H*h/X^2;

del=1/(N-3); % this is the normalized del which is equal to H/(N-3)/H. Before it was H/(N-3), not normalized, which gave a better looking result, but it should be dimensionless to fit in the equation. del has one value for all directions

delz=1/(Nz-3); % normalized del in the z direction

delx=3*gwx/del/X; % the ratio of the groove width to delta x

dely=gwy/del/Y; % the ratio of the groove width to delta y

deldelz=del/delz; %this is the ratio of the mesh size along x and y and the mesh size along z. mesh size along x and y is equal.

% coefficients used in the Reynold's equation to account for the grooves

t=H*((1-dely)*h^3+dely*(h+hgy)^3)/12/kz/X^2+H*Kx/2/X^2*((1-dely)*h+dely*(h+hgy));

o=H/12/kz/X^2*(X/Y)^2*((1-delx)*h^3+delx*(h+hgx)^3)+H/2/X^2*Ky*(X/Y)^2*((1-delx)*h+delx*(h+hgx));

% constant A used in mass continuity and Darcy combined equation

A=2*(Kx+Ky*XY^2+XH^2);

AA=2*(Kx+Ky*XY^2+XH^2/2*deldelz^2*(1+(1-delx)*(1-dely)));

% pressure matrix

P=zeros(N,N,Nz);

% BOUNDARY CONDITIONS % bottom ceramic surface at plenum supply pressure

P(:,:,1:2)=psa;

% ambient condition on ceramic top surface edges where p=patm

P(1:2,:,N-1:N)=1;

P(:,1:2,N-1:N)=1;

P(:,N-1:N,N-1:N)=1;

P(N-1:N,:,N-1:N)=1;

% FINITE DIFFERENCE ITERATION METHOD

for f=1:1:7000 % begin iteration for convergence

for i=3:1:N-2

for j=3:1:N-2

for k=3:1:N-2

P(2,j,k)=(Kx*P(3,j,k)+Ky*XY^2*(P(2,j+1,k)+P(2,j-1,k))+XH^2*(P(2,j,k+1)+P(2,j,k-1)))/(Kx+2*(Ky*XY^2+XH^2)); %these four lines are for the nodes on the sides of the bearing along the y axis

P(1,j,k)=P(2,j,k);

P(N-1,j,k)=(Kx*P(N-2,j,k)+Ky*XY^2*(P(N-1,j+1,k)+P(N-1,j-1,k))+XH^2*(P(N-1,j,k+1)+P(i,j,k-1)))/(Kx+2*(Ky*XY^2+XH^2));

P(N,j,k)=P(N-1,j,k);

P(i,2,k)=(Kx*(P(i+1,2,k)+P(i-1,2,k))+Ky*XY^2*P(i,3,k)+XH^2*(P(i,2,k+1)+P(i,2,k-1)))/(2*(Kx+XH^2)+Ky*XY^2); %these four lines are for the nodes on the sides of the bearing along the x axis

P(i,1,k)=P(i,2,k);

P(i,N-1,k)=(Kx*(P(i+1,N-1,k)+P(i-1,N-1,k))+Ky*XY^2*P(i,N-2,k)+XH^2*(P(i,N-1,k+1)+P(i,N-1,k-1)))/(2*(Kx+XH^2)+Ky*XY^2);

P(i,N,k)=P(i,N-1,k);

if k~=N-2 % the node before last on the top surface is different from the rest because the clogged groove does not allow for all the pressure to go through

P(i,j,k)=(Kx*(P(i+1,j,k)+P(i-1,j,k))+Ky*XY^2*(P(i,j+1,k)+P(i,j-1,k))+XH^2*(P(i,j,k+1)+P(i,j,1)))/A;

else

P(i,j,k)=(Kx*(P(i+1,j,k)+P(i-1,j,k))+Ky*XY^2*(P(i,j+1,k)+P(i,j-1,k))+XH^2*deldelz^2*((P(i,j,k+delx)*(1-dely))+P(i,j,k-1)))/AA;

end

P(2,2,k)=(Kx*P(3,2,k)+Ky*XY^2*(P(2,3,k)+P(2,1,k))+XH^2*(P(2,2,k+1)+P(2,2,k-1)))/(Kx+2*(Ky*XY^2+XH^2));

P(1,2,k)=P(2,2,k);

P(2,1,k)=P(2,2,k);

P(1,1,k)=P(2,2,k);

P(2,N-1,k)=(Kx*P(3,N-1,k)+Ky*XY^2*(P(2,N,k)+P(2,N-2,k))+XH^2*(P(2,N-1,k+1)+P(2,N-1,k-1)))/(Kx+2*(Ky*XY^2+XH^2));

P(1,N-1,k)=P(2,N-1,k);

P(2,N,k)=P(2,N-1,k);

P(1,N,k)=P(2,N-1,k);

P(N-1,2,k)=(Kx*P(N,2,k)+Ky*XY^2*(P(N-1,3,k)+P(N-1,1,k))+XH^2*(P(N-1,2,k+1)+P(N-1,2,k-1)))/(Kx+2*(Ky*XY^2+XH^2));

P(N,2,k)=P(N-1,2,k);

P(N-1,1,k)=P(N-1,2,k);

P(N,1,k)=P(N-1,2,k);

P(N-1,N-1,k)=(Kx*P(N,N-1,k)+Ky*XY^2*(P(N-1,N,k)+P(N-1,N-2,k))+XH^2*(P(N-1,N-1,k+1)+P(N-1,N-1,k-1)))/(Kx+2*(Ky*XY^2+XH^2));

P(N,N-1,k)=P(N-1,N-1,k);

P(N-1,N,k)=P(N-1,N-1,k);

```
P(N,N,k)=P(N-1,N-1,k);
end
P(i,j,N-1)=(t*(P(i+1,j,N-1)+P(i-1,j,N-1))+o*(P(i,j+1,N-1)+P(i,j-1,N-1))+del^2/2/delz*P(i,j,N-2))/(2*t+2*o+del^2/2/delz); %note that in this equation there is no N for k only N-1 because we are assuming there is no pressure drop along the z axis in the air gap. This is the Modified Reynold's equation boundary condition
P(i,j,N)=P(i,j,N-1);
end
end
end
for m=1:1:N-2
for s=1:1:N-2
S(m,s)=P(m+1,s+1,N-1);
Pbearing(m,s)=S(m,s)*pa-pa;
Load(m,s)=Pbearing(m,s)/0.145*10^3*X/1000/(N-3)*Y/1000/(N-3);
Q(m,s)=P(m+1,s+1,2);
R(m,s)=P(m+1,s+1,3);
end
end
%Plotting issues
figure;
x(1)=-X/2;
y(1)=-Y/2;
for i=2:1:N-2
x(i)=x(i-1)+X/(N-3);
y(i)=y(i-1)+Y/(N-3);
end
surf (x,y,Pbearing)
xlabel('x (mm)')
ylabel('y (mm)')
```

```
zlabel('Pressure distribution (psig) at Psupply=0.3 psig')
%title('Pressure distribution along rectangular bearing area with y-grooves at supply pressure of 8 psig and a gap of 10 um. Grooves are 20 um wide and 50 um deep')
%Load Capacity calculation
%W=double integral (p-pa)dxdy x and y from 0 to X,Y
deltaA=X/(N-2-1)*Y/(N-2-1)/1000000;
sum=0;
for i=1:1:N-2
for j=1:1:N-2
inc=(Pbearing(i,j)/0.145*1000)*deltaA;
sum=sum+inc;
end
end
W=sum;
fprintf('The load capacity of this bearing for a supply pressure of %g psig is %g N',psa*pa-pa,W)
```

Appendix B

Patent: Method for Shaping Sheet Thermoplastic and the Like

B.1 Background of the Invention

This invention pertains to the art of shaping sheet glass and sheet thermoplastic materials through the application of heat to soften the sheet and the use of a fluid or gas to form it. In this disclosure, the term thermoplastic refers to any material whose viscosity changes as a function of temperature, including silicate glasses such as borosilicate glass and fused silica, and polymeric materials such as polymethyl methacrylate (PMMA).

Glass sheets are used in a wide range of applications, such as flat panel displays, hard disk drives, car windshields, decorative ornaments, and optics used in x-ray telescopes. Different applications require different tolerances on the final shape of the sheets. The flat panel display and space telescope industries require thin sheets to minimize weight, yet substrates used in such applications require tight tolerances on their thickness uniformity and surface flatness in order to meet the required specifications for each field.

In the case of liquid crystal flat panel displays, two glass sheets are separated by a small gap of less than 10 μm in thickness, whereby this gap is filled by the liquid crystal. In order to prevent display mura such as color mura or contrast mura and to

impart good display performances such as uniform display, high contrast ratio, and wide viewing angle to the color liquid crystal display, one has to maintain the gap between the two glass sheets to be constant and uniform. This becomes a challenge when the glass sheets used have wavy surfaces which result in a variation in the gap size.

The shaping of glass and thermoplastic materials by applying heat and allowing the material to sag by gravity into a mold or mandrel is well known (U.S. Patents 4,349,374; 6,257,022; 3,560,182; 2,377,849; 3,414,395; 3,607,186). This process is also known as slumping. In this process the temperature of the workpiece is raised close to its softening point, and the heated sheet sags by gravity to conform to the shape of a mold, which can be of any general shape. Some methods use forces other than gravity, such as vacuum or a moveable plunger onto the surface of the thermoplastic sheet, in order to facilitate and accelerate the shaping process. In this process it is important that the mold be fabricated of a material which is able to withstand a temperature above the softening temperature of the sheet without damage or significant deformation. After the desired shape has been achieved, the sheet and mold are slowly cooled below the softening temperature of the sheet resulting in the solidification of the thermoplastic material into the desired shape.

Slumping onto mandrels of any shape and whose surface has been figured and polished to a desired tolerance can be used as a method to improve the surface flatness of thermoplastic sheets. Glass sheets manufactured using different processes, such as the float process, the fusion process and the slot-draw process, are commonly used as substrates for flat panel displays and space telescopes. The slot-draw and fusion processes have minimal or no contact between the glass sheet and any tools as the glass is formed. This is particularly important for the flat panel display industry because it eliminates the introduction of impurities or damage to the glass sheet, leaving its surface pristine and smooth and of a fire-polished quality.

Slumping such glass or thermoplastic sheets onto a mandrel in order to change the shape of the sheet or to improve its flatness can compromise the quality of the sheet's surface. Contact with the mandrel at the elevated temperatures required for the

process of slumping can mar the surface of the sheet. The presence of dust particles and other particulate impurities or thin contaminant materials sandwiched between the sheet and the mandrel can result in ripples in the final surface of the sheet after slumping. The removal of all dust particles and contaminants from the surface of the mandrel and the thermoplastic sheet can be difficult in a manufacturing environment.

In some cases, the complete removal of dust particles, for example by thorough cleaning and use of a clean room environment, can result in fusion of the mandrel with the workpiece. Fusion of the mandrel with the workpiece can also result from a slumping procedure which is excessively long or proceeds at too high of a temperature. This problem is well known to practitioners of the art of glass and thermoplastic molding. For example, glass artisans commonly apply a thin coating to the mold made of a slurry of fine refractory particles in order to prevent sticking during slumping. For another example, thin coatings of organic release agents are commonly applied to molds during the forming of thermoplastic polymers in order to prevent sticking. For another example, graphitic release agents are commonly applied to molds used during the forming of glass automobile windshields. In all these cases, however, the coating's roughness and the aforementioned effects of particulates and other surface contaminants can compromise the figure and surface quality of the final product.

The current invention eliminates the said deleterious effects of contact by the workpiece with the mandrel by introducing a thin film of moving fluid, such as air, between the sheet and the mandrel. The mandrel thus acts as an air bearing with the bearing fluid being a liquid or a gas. It is important to select a fluid that can withstand the high temperatures needed for the process, said temperature must exceed the softening temperature of the thermoplastic material. For example, for the case of polymeric materials the fluid may be water or oil. For the case of a borosilicate glass the fluid may be a gas such as air or nitrogen. The preferred gas for slumping glass is air.

It is also preferred that the gap between the mandrel and the sheet be controlled to a dimension that is larger than the typical maximum size of particulate impurities in the manufacturing environment. This condition allows the thin layer of fluid to

envelop or absorb the dust particles thus preventing said particles or surface contaminants from transmitting forces between the mandrel and workpiece. The fluid layer also provides the required force to shape the surface of the glass or thermoplastic material.

B.2 Summary of the Invention

A primary object of this invention is to overcome the aforementioned disadvantages of prior processes used for shaping sheet glass or sheet thermoplastic materials.

Another object of this invention is to shape sheet glass or sheet thermoplastic materials on an air bearing by using the force from a moving layer of fluid such as air sandwiched between the sheet and the reference mandrel. The air bearing can be made of porous material or of machined or fabricated materials.

This invention relates to the process and apparatus of shaping sheet glass or thermoplastic materials by utilizing the force from a layer of a fluid such as air sandwiched between the sheet and a mandrel. The shaping process is conducted at a temperature close to the softening point of the thermoplastic sheet when the system is in thermal equilibrium. The shape thus achieved by this process is preserved in the sheet by slow cooling through the material's softening point. The shape of the air bearing mandrel is critical in controlling the final shape of the thermoplastic material; however, it is not the only controlling factor. The pressure distribution of the fluid sandwiched between the sheet and the mandrel is another important factor in controlling the final shape of the sheet.

This process can be conducted on one surface of the sheet such that the force from the air layer is on one surface of the sheet. The process can also be conducted on multiple surfaces of the sheet such that the force from the air layer is on multiple surfaces of the sheet. The two configurations provide different results on the glass or thermoplastic sheet being formed. Using the process on both sides of a sheet is particularly useful in improving the flatness or figure of the sheet if applied while the sheet is being manufactured in a continuous process, such as the fusion and slot-draw

processes that are used to manufacture sheets for the flat panel display industry.

The size of the gap between the sheet and the mandrel is critical in determining the pressure profile of the fluid that fills the gap. The pressure profile of the fluid sandwiched between the sheet and mandrel is another factor that determines the final shape of the sheet being formed. In general, smaller gaps lead to larger viscous forces imparted by the fluid inside the gap onto the sheet glass or thermoplastic material. The pressure profile depends on the shape of the mandrel, the size of the air gap between the mandrel and the sheet and the supply pressure of the fluid squeezed between the mandrel and the sheet. These principles will become more apparent from the following description of the preferred embodiments taken in conjunction with the accompanying drawings.

B.3 Brief Description of the Drawings

FIG. 1 is a perspective view of a vertical configuration which represents the first embodiment of the invention. A thermoplastic sheet is squeezed between two mandrels while heated air blowing through the two mandrels shapes the surfaces of the sheet.

FIG. 2 is a sectional side view of the same embodiment of the invention in FIG. 1 shown without the mandrel sliding mechanisms.

FIG. 3 is a perspective view of a mandrel with machined grooves.

FIG.4 is a side view of a vertical configuration which represents a second embodiment of the invention. Two mandrels are placed on both sides of a wavy thermoplastic sheet such as glass while it is manufactured using a continuous process. Heated air blows through the mandrels and against the glass sheet to shape it.

FIG. 5 is a side view of a vertical configuration which represents a third embodiment of the invention. Two mandrels are placed on both sides of a glass or thermoplastic sheet. Heated air is introduced from the lower end of the glass sheet to flow parallel to the glass sheet, shape it and exit from the upper end.

FIG. 6 is a side view of a horizontal configuration which represents a fourth embodiment of the invention. A thermoplastic sheet such as glass is placed on top of one

flat mandrel with air blowing through the mandrel to carry the weight of the sheet and to shape it.

FIG. 7 is a side view of the same embodiment of the invention as in FIG. 6. The glass is shown to be shaped by the air blowing through the mandrel and against the glass sheet.

FIG. 8 is a side view of a horizontal configuration which represents a fifth embodiment of the invention. A thermoplastic sheet is placed on top of one curved mandrel shown to be convex in this diagram. Air blows through the mandrel to shape the thermoplastic sheet after it sags due to its own weight at elevated temperatures.

FIG. 9 is a side view of the same embodiment of the invention as in FIG. 8. The glass is shown to be shaped by the air blowing through the mandrel and against the glass sheet.

FIG. 10 is a side view of a sixth embodiment shaping discrete sheets in a continuous fashion.

B.4 Description of the Preferred Embodiments

The thermoplastic material shaping process according to the present invention involves shaping sheets of thermoplastic material by using a layer of fluid such as air sandwiched between the sheet and a pre-shaped air bearing mandrel. The thermoplastic material must be heated to a temperature close to its softening point. For the case of glass, this temperature could typically range between 400°C and 800°C. A furnace controls the temperature of the sheet, air bearing mandrel and forming air such that the process of shaping is conducted at close to thermal equilibrium.

FIG.1 shows a perspective view of a first embodiment which places one sheet between two air bearings oriented in the vertical plane. FIG. 2 is a sectional view of the same embodiment depicted without the sliding bearing structure. The desired result is to improve the surface flatness of the glass or thermoplastic sheet 6. A preferred sheet material is the borosilicate glass Schott D263T which is typically manufactured with a warp which is comparable to its thickness.

This first embodiment is implemented in an apparatus which can accommodate one sheet at a time. The air bearing mandrels **3** can be made of ceramic or refractory materials although metals can be used as well. A preferred material is porous alumina ceramic. The mandrels **3** are made of a porous material whose front surfaces **5** have been ground and lapped to the flatness desired to be achieved by the glass or thermoplastic sheet **6** being processed. The side walls **11** of the porous material are sealed using a high temperature glaze to avoid air leakage. One way to attach the ceramic mandrel **3** to the plenum structure **9** is through known methods of high temperature adhesive bonding, such as brazing or frit bonding. Use of a bolted joint or other types of mechanical fasteners is an option as well. It is preferable to complete the bonding of mandrel **3** to plenum **9** before conducting the said front surface lapping process in order to avoid distortion due to bonding stresses and thereby achieve superior flatness.

In this embodiment a controlled gap between sheet **6** and mandrels **3** is obtained by means of eight small precision spacers **12** of refractory material and equal thickness which are placed just inside the corners of sheet **6**. The spacers **12** are assembled in pairs as shown in FIGS. 1 and 2 oriented on opposite sides of sheet **6** and between the mandrels **3** in order to hold sheet **12** in place during slumping. For example, when slumping glass sheets of dimension 100 mm by 100 mm, preferred spacers are on the order of 10 mm by 10 mm and thus cover a small area of the sheet and do not impede the air squeezed between the sheet and mandrel from escaping to the atmosphere. The thickness of these spacers determines the size of the air gap between each mandrel **3** and the sheet **6**. For example, when slumping glass sheets, the preferred thickness of spacers **12** is between 10 and 50 microns.

In this embodiment, the thermoplastic sheet can alternatively be constrained in place using other methods such as suspending the sheet from the top. In this case the gap between the mandrels can be maintained by any precision mechanical assembly which is capable of holding a controlled and uniform gap between the surfaces of mandrels **3**. While this approach results in a more complicated slumping apparatus, the advantage is that a larger proportion of the substrate will be obtained with

improved flatness.

In the first embodiment of the invention the process of shaping a glass sheet proceeds as follows. The mandrels **3** with affixed spacers **12** and without glass sheet **6** are placed on sliding bearings **13** in a furnace (not shown) in an open position. The slumping assembly is initially held at a temperature lower than the softening temperature of sheet **6** to be shaped. The still-solid sheet **6** is introduced between the two open mandrels **3** using mechanical means not shown, and the mandrels **3** are moved closer to each other using sliding bearings **13** until the four spacers **12** on each mandrel **3** contact sheet **6** and squeeze it in place between mandrels **3**. Uniform contact force of spacers **12** onto mandrels **3** and glass sheet **6** can be achieved by means of precision mechanical design of and assembly of bearings **13**, or by compliant mechanisms (not shown) which allow small horizontal and vertical rotations of at least one of said mandrels. Following said assembly and compression of said sheet **6** between mandrels **3**, the temperature within the furnace is increased to the softening temperature of the sheet, at which point heated air is blown through the mandrels as described below. Alternatively, heated air can be blown through the mandrels before the aforementioned softening temperature is achieved.

Pressurized air is pre-heated and introduced into pressure plenums **1** through inlets **2**. Air must be introduced at the same temperature and pressure through both mandrels **3** placed to the left and to the right of the thermoplastic sheet **6** in order to avoid thermal gradients and force variations on both sides of the thermoplastic sheet **6**. For example, a difference in air temperature between the plenums **1** results in a temperature gradient across the thickness of the sheet **6** which in turn results in the bow of the sheet upon cooling. This thermal gradient can be implemented if the surface bow is a desired shape.

Air enters the porous air bearings at surfaces **4** and exits at surfaces **5**. Porous material is preferred for the air-bearing mandrels in this embodiment because porous materials provide a relatively uniform pressure distribution in the gap **7** separating the mandrels **3** and the sheet **6** as compared to compensated bearings, described below. Mandrels **3** on opposite sides of thermoplastic sheet **6** must be identical to

ensure force equality on both sides of the sheet. Lack of force equality can result in bowed sheets upon cooling.

Mandrels with different air diffusing mechanisms, also known as compensation methods, such as mandrels with holes machined into their surface or grooved mandrels with inlet holes and grooves, can be used as well. One configuration of such a mandrel is shown in FIG. 3. In this configuration, mandrel **100** has been fabricated with a plurality of holes **101** which provide a path for air to flow to sheet **6** from plenums **1**. The flow of air is spread by a plurality of channels **102** fabricated into the surface of mandrel **100**. Except for these details, the said fabricated mandrel **100** performs the same function as porous mandrel **9**.

Since this process is conducted when the thermoplastic sheet **6** is soft, the forces from air layers **7** can change the shape of sheet **6**. The forces in the air layer result from the viscous flow of air layers **7** as they exit the porous mandrels **3** at surfaces **5** with a pressure greater than atmospheric and flow towards the edges **8** of the mandrels **3**, where the pressure drops to atmospheric. Placing a second, identical mandrel on the opposite side of sheet **6** results in having an identical pressure supply on that side as well. This ensures the sheet is shaped in such a way that the forces on both sides of the sheet are balanced.

The forces from the air layers inversely depend on the gap thicknesses **7** between the mandrels **3** and the sheet **6** formed. As this gap decreases due to sheet initial waviness, the resulting forces from the air in the gap increase and vice versa. This property is critical in forming the sheet surface such that the surface flatness of the sheet **6** is improved. For an equal supply pressure in both plenums, a force equilibrium is reached when the gap size on both sides of the sheet **6** is equal at any given point along the length of the sheet. As a result, the glass thermoplastic sheet surface waviness is reduced and its surface flatness improved as shown in FIG. 2. The edges of the glass sheet that are not exposed to the thin layer of air remain warped.

Once the sheet is shaped, the temperature of the furnace is slowly reduced until the sheet solidifies at which point the mandrels are slid apart and the sheet is removed and placed in another thermally controlled chamber where it is allowed to further cool.

This process requires the thermal cycling of the mandrels with every sheet, which can be time consuming. A further embodiment, as described later, avoids the need for thermal cycling.

The wavy edges of the sheet which are outside the area of influence of the thin pressured air layer **7**, or are near the areas of contact with spacers **12**, can be cut away to be left with the large central part of the sheet that was shaped by the thin layer of air **7**. This shaping is achieved without compromising the quality of the sheet surface which does not come in contact with any other surface throughout the process.

A basic requirement for this process in this embodiment of the invention is the flatness of the air-bearing mandrels themselves. The sheet will only be shaped to be as flat as the mandrels. Well known techniques such as grinding, lapping or diamond turning can be used to fabricate mandrels to the required flatness.

Another requirement to improving the surface flatness of a sheet is the thickness uniformity of the said sheet. If a sheet is non-uniform in thickness, this invention will at best improve the flatness of the sheet such that it is equal to the thickness uniformity of the sheet. In most glass sheet manufacturing processes, the sheet thickness non-uniformity is at least one order of magnitude smaller than the waviness of the said sheet. Therefore, this embodiment improves the surface flatness or waviness of glass or thermoplastic sheets such that the surface waviness becomes comparable in order of magnitude to the thickness non-uniformity of the sheet.

Thickness uniformity can be improved by the well known process of double-sided polishing of thin sheets. Surface waviness, on the other hand, can not be improved by the double-sided polishing process because of the sheet's tendency to spring back to its former, wavy shape after it has been removed from the double-sided polishing tool.

A person of ordinary skill in the art could imagine alternative versions of the first embodiment of this invention wherein the desired form of sheet **6** is a non-flat shape such as a portion of a cylinder, sphere or paraboloid of revolution. In this case, opposing porous mandrels of matching convex and concave shapes conforming to the desired shape would be fabricated using well-known methods. Flat sheets

6 desired to be shaped into the said non-flat shapes by the procedure of the first embodiment could first be formed into an approximation of said desired shape, for example, by preliminary slumping onto a non-air-bearing mandrel using conventional methods. These pre-shaped sheets can then be assembled and slumped on the air bearing mandrel apparatus using the procedure of the first embodiment, as described previously.

A second embodiment of the invention is depicted in FIG. 4, wherein the desired result is to improve the surface flatness of a thermoplastic sheet as it is being manufactured using a continuous process, such as the slot-draw or the fusion processes for glass. This embodiment places sheet **10** and mandrels **16** in the vertical plane in which the glass sheet **10** is moving. In this embodiment, it is preferred that at the point of entry of sheet **10** into the slot between mandrels **16**, sheet **10** is close to or slightly above the softening temperature of the sheet material. As the wavy sheet **10** moves downwards due to gravity during manufacturing, it is introduced into the gap between two opposing air-bearing mandrels **16** that are placed in the path of the moving glass. The top part of the first set of mandrels is tapered at **21** to facilitate entry of glass sheet **10** between mandrels **16** where it will be shaped by the air in gap **20**. The shaping process is similar to that described in the first embodiment, wherein air enters plenums **14** through inlets **15**, and flows through mandrels **16**. The thin layers of air **20** squeezed between the moving sheet **10** and flat mandrels **16** shape the hot, soft glass to improve its flatness.

This shaping process can be conducted at different sections of the sheet as it moves downwards while it is manufactured, such that the sections that are the highest and thus the closest to where the sheet is introduced are conducted at higher temperatures, and the lower sections along the length of the moving sheet are conducted at lower temperatures until the thermoplastic sheet is cool enough to solidify and be transported outside of the air bearing to where, for example, it may be cut into segments. FIG. 4 shows only two such sections: the upper, hot one for shaping the sheet and the lower, cooler one where the sheet solidifies in its shaped form before exiting the mandrels. The number of thermally controlled sections can be varied to meet

different requirements. Heating elements **24** can be used to control the temperature of the different sections along the length of the moving sheet **10**.

Therefore, starting with a sheet that is uniform in thickness and following this embodiment of the invention produces better results in terms of reducing the said sheet's surface waviness.

The second embodiment as described above can also be used to change the curvature of a flat sheet as it moves between the two mandrels by using curved mandrels. Two mandrels, such as opposing concave and convex mandrels, can be used to squeeze a thin sheet between them and shape the sheet to conform to the mandrels' surface geometry. The effect of sheet gravity sag can be corrected in the design of the mandrels.

A third embodiment shown in FIG. 5 places the sheet and two mandrels also in the vertical plane. Non-porous mandrels 25 have their surfaces **26** ground and lapped to the desired flatness tolerance for forming thermoplastic sheet **30**. In this embodiment the forming air flows from the lower end **27** of the thermoplastic sheet **30** to the upper end **28** of the sheet. Air is introduced into the plenum **32** through the inlet **34** and enters between the sheet **30** and the mandrels **25** to shape the sheet. Heating elements **33** are used to control the temperature of the sheet. The sheet can be held in place using spacers **31** or other mechanisms as explained in the first embodiment. Once the solid sheet **30** is constrained between the two mandrels **25**, the temperature of the sheet **30** is increased to close to its softening point such that the viscous forces of the flowing air shape the two surfaces of the soft sheet **30**.

In this embodiment, the relationship between the air layer forces and gap thickness is similar to that in the first embodiment. This property is critical in shaping the sheet surface such that the surface flatness of the sheet **30** is improved. Both mandrel surface flatness **26** and sheet thickness uniformity are dominating requirements in this embodiment as well and must be well controlled to obtain better sheet flatness results.

All the embodiments described above can be conducted in a plane other than the vertical, for example when introducing curvature to the sheet surface; however, when rotated away from the vertical, the weight of the sheet becomes another critical

parameter that must be taken into consideration when designing the mandrels and controlling the pressure profiles in the air gaps. In general, higher pressures in the gap between mandrel and sheet tend to reduce the effects of gravity sag.

FIG. 6 shows a fourth embodiment, which places the sheet and mandrel in the horizontal plane. In this approach, only one pre-defined mandrel is placed underneath the thermoplastic sheet. The mandrel can be either porous or a solid with machined holes and grooves as necessary. The layer of air between the sheet **39** and the mandrel **38** carries the weight of the sheet. Heated air is introduced into the plenum **35** through the inlet **40**. Air enters the porous air-bearing mandrel **38** through surface **36** and exits the mandrel **38** through surface **37**. The forces on sheet **39** are a combination of the upward forces from the viscous air flow in the gap **41** and the downward load of the sheet **39**. The pressure at the edges of the mandrel is atmospheric. This configuration typically results in curved sheets as shown in FIG. 7. A finite element analysis incorporating the pressure forces from the viscous air on the sheet **39** and the load of the sheet **39** can be performed to predict the final shape of the sheet.

FIG. 8 shows a fifth embodiment, which places the sheet and a curved air-bearing mandrel in the horizontal plane. This configuration can be used when large sheet curvature is desired. The mandrel **47** is ground and lapped to the curvature required. The sheet **46** is placed on top of the mandrel. When cold, only a small area of the sheet **46** is in contact with the mandrel **47**. This area is not large enough for the viscous forces to lift the sheet when it is cold. As the temperature of the furnace is increased, the sheet **46** softens and starts slumping due to its own weight. As the sheet surface comes closer to the curved mandrel surface **45**, the forces from the viscous air flow become prominent and increase as the gap between the sheet **46** and the mandrel **47** decreases. As the air flow force increases, the sheet is lifted keeping the sheet from contacting the mandrel, as shown in FIG. 9.

FIG. 10 shows a sixth embodiment, which processes and flattens individual sheets forced between two mandrels for shaping in a continuous manufacturing process. Individual sheets of any geometry are shaped one after the other by air squeezed between the sheet and two mandrels on each side of the sheet in a continuous process.

A continuous ribbon **51** of refractory material, such as stainless steel, with slots **52** is used to move the sheets through the heated mandrels **49**, **50**. The thickness of the ribbon **51** is smaller than the thickness of the sheets **54**. The slots in the ribbon are designed to constrain the lateral motion of the sheets. A loading mechanism (not shown) places preheated solid sheets **54** in the slot of the ribbon at the position before entry between the mandrels **49**, **50**. The lower mandrel **50** acts as an air bearing carrying the load of the sheets. The ribbon moves this sheet which is now floating on the layer of air from the lower air bearing and introduces it into the area between the two mandrels **49**, **50** where heated air flows through the mandrels **49**, **50** and against the sheet to shape it. The tapered entrance **56** facilitates squeezing the sheet between the two air bearings. Heaters **53** are used to control the temperature of the mandrels and sheet as the sheet passes between the mandrels. The sheet temperature is raised to close to its softening point at the entry and cooled back to solid state at the exit. This guarantees that the shaped sheet does not lose its final shape, and that it solidifies before leaving the mandrels. After coming out of the mandrel area, the now shaped sheet is removed from the ribbon either by a mechanical arm (not shown) or by allowing it to drop to another conveyor belt **55** at a lower level to transport it away for further processing as necessary.

The forms of the invention shown and described herein represent illustrative preferred embodiments and certain modifications thereof. It is understood that various changes may be made without departing from the spirit of the invention as defined in the claimed subject matter that follows.

B.5 Claims

What is claimed is:

1. A method for shaping thermoplastic materials comprising:

Heating a workpiece of thermoplastic material to a temperature close to its softening point;

using a flow of gas to suspend the said softened workpiece away from at least one

surface;

waiting a period of time to allow said workpiece to take a desired shape;

cooling said workpiece below said softening point so that it substantially retains said desired shape.

2. The method according to claim 1, wherein said flow of gas is provided by means of an air bearing placed at one surface of said workpiece.

3. The method according to claim 1, wherein said flow of gas is provided by means of air bearings placed at multiple surfaces of said workpiece.

4. The method according to claim 1, wherein said workpiece comprises a plurality of discrete substrates fabricated of said thermoplastic material.

5. The method according to claim 1, wherein said workpiece comprises a substantially continuous flow of said thermoplastic material.

6. A system for shaping thermoplastic materials comprising:

means for heating a workpiece of thermoplastic material to a temperature close to its softening point;

means for directing a flow of gas to suspend the said softened workpiece away from at least one surface;

means for waiting a period of time to allow said workpiece to take a desired shape;

means for cooling said workpiece below said softening point so that it substantially retains said desired shape.

7. The system according to claim 6, wherein said means of directing said flow of gas comprises an air bearing placed at one surface of said workpiece.

8. The system according to claim 6, wherein said means of directing said flow of gas comprises air bearings placed at multiple surfaces of said workpiece.

9. The system according to claim 6, wherein said workpiece comprises a plurality of discrete substrates fabricated of said thermoplastic material.

10. The system according to claim 6, wherein said workpiece comprises a substantially continuous flow of said thermoplastic material.

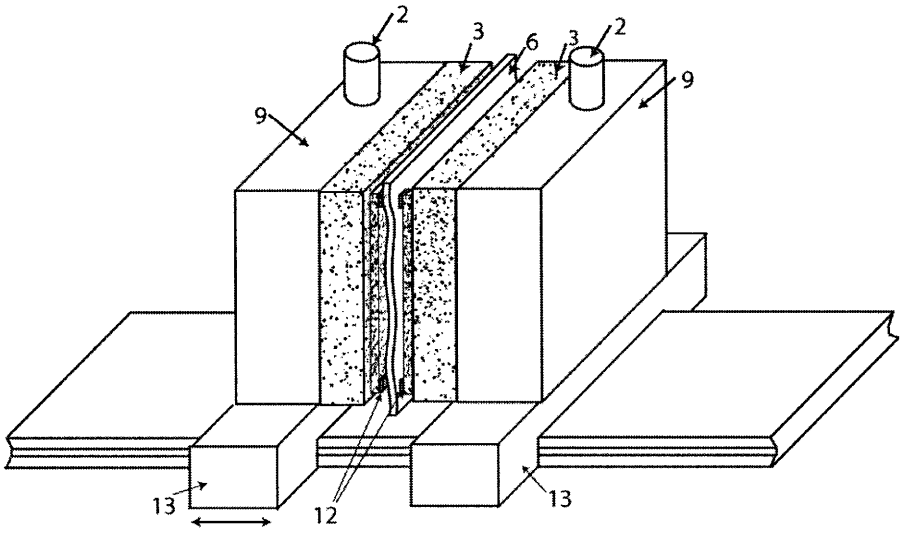

Figure B-1:

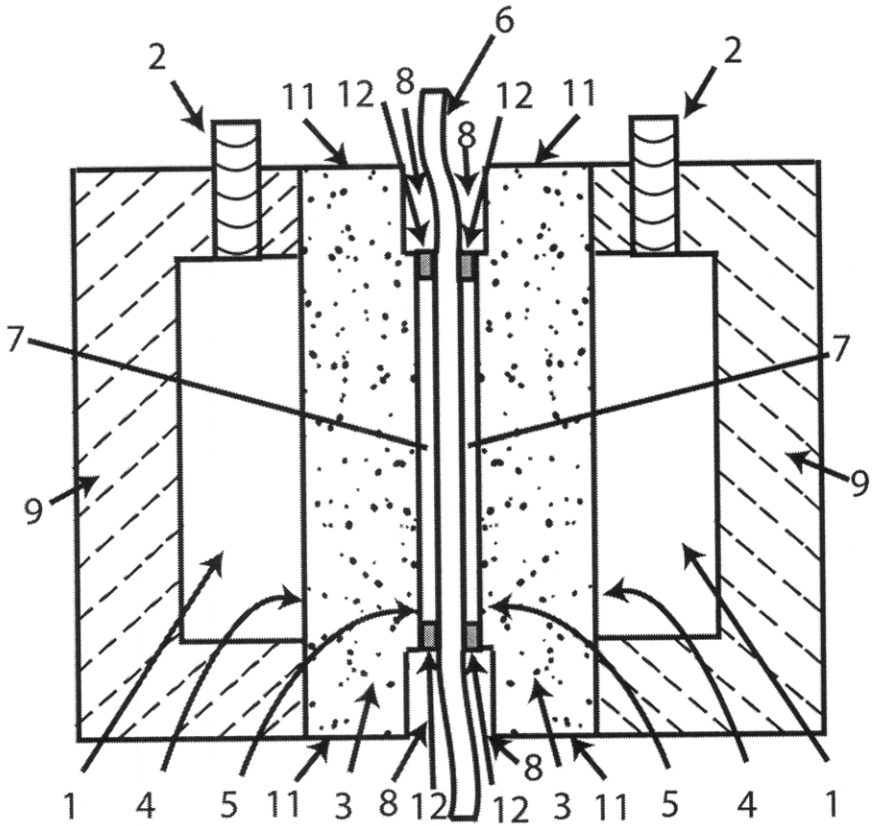

Figure B-2:

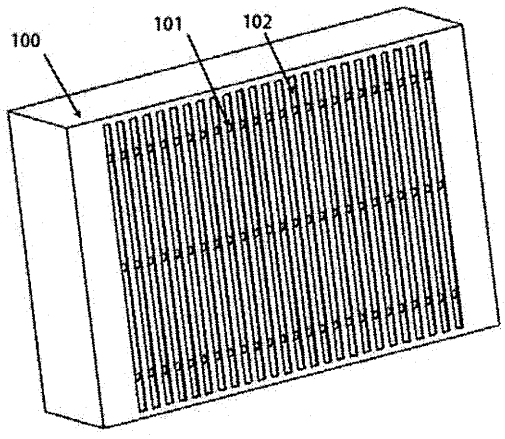

Figure B-3:

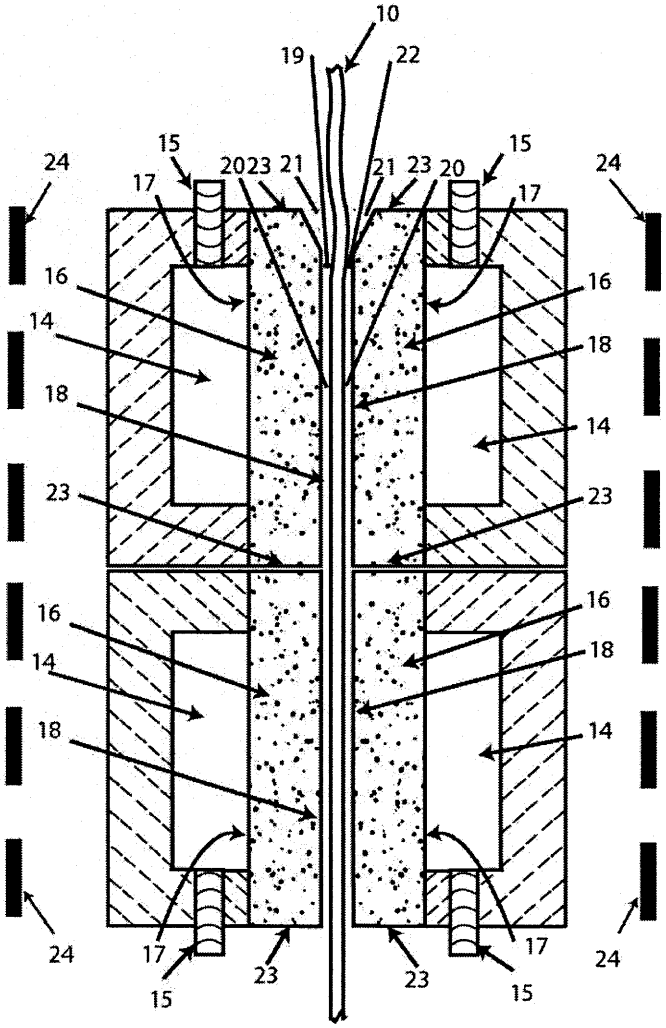
10
19
22
15
20
23
21
21
23
20
15
24
24
17
17
16
16
14
18
18
14
23
23
16
16
14
18
18
14
24
24
17
17
15
23
23
15

Figure B-4:

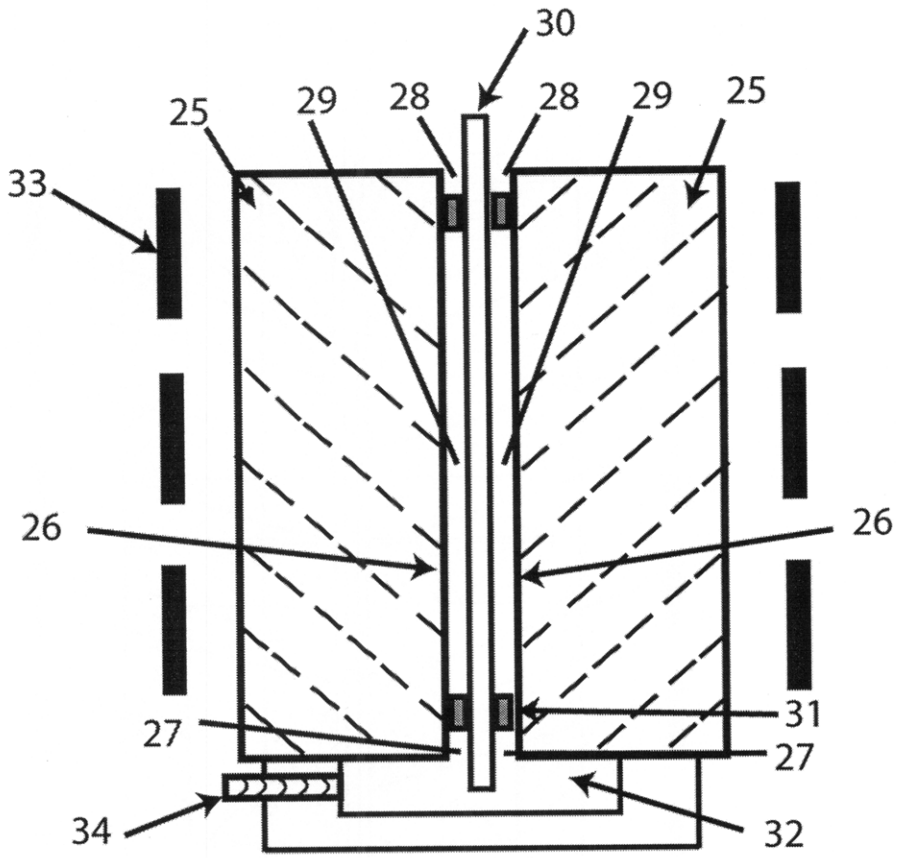

Figure B-5:

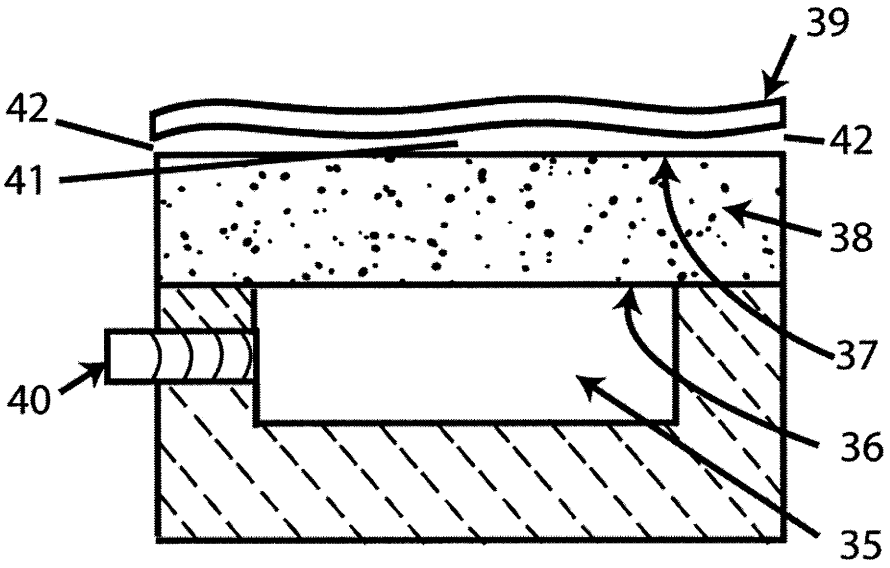

Figure B-6:

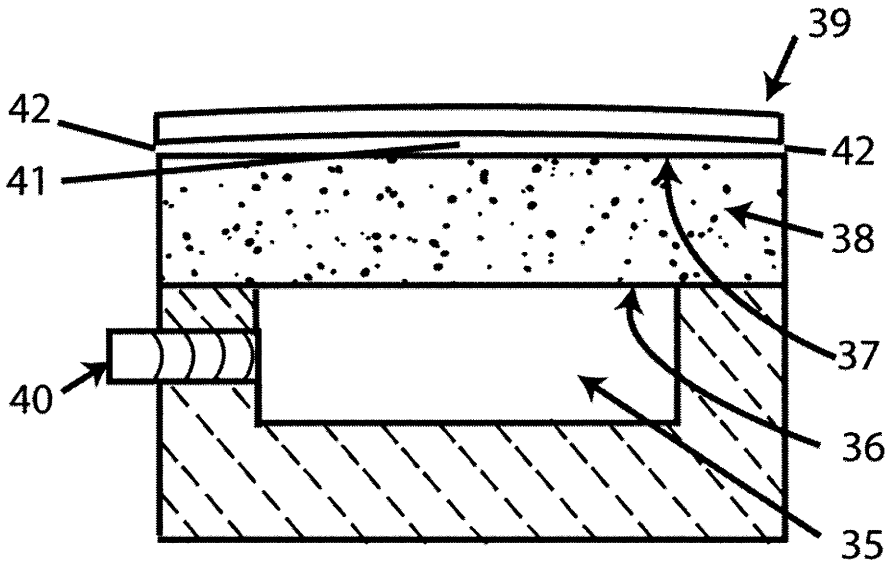

Figure B-7:

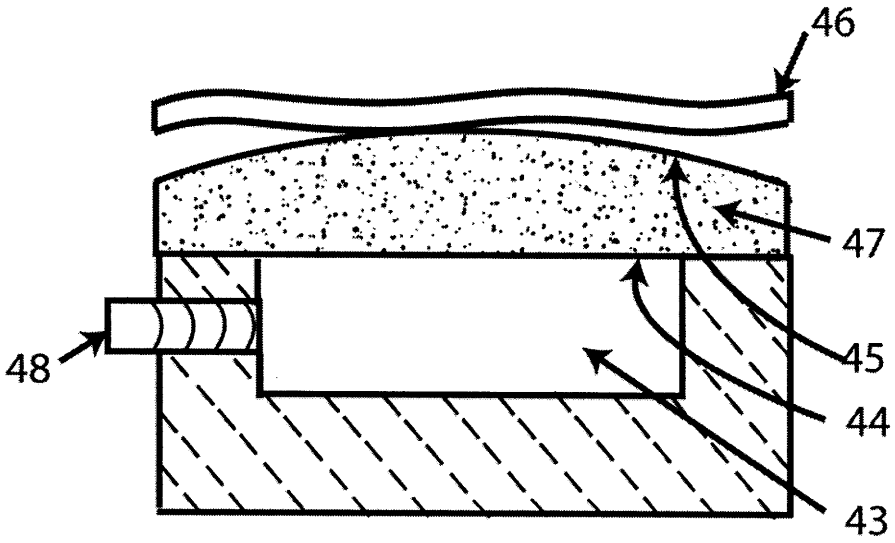

Figure B-8:

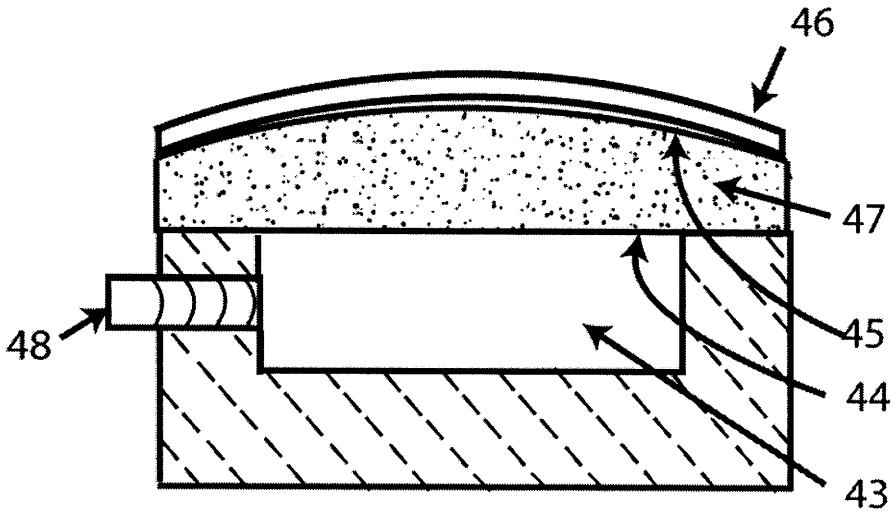

Figure B-9:

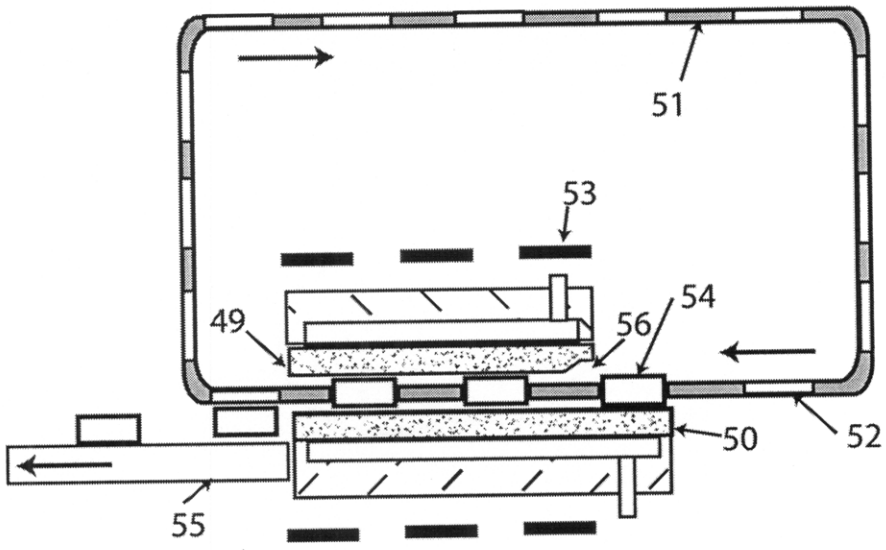

Figure B-10:

Bibliography

[1] Peter F. Gerhardinger and Richard D. Schave. Superior quality soda-lime float glass for large area flat panel applications. *Proc. of SPIE, Advanced Flat Panel Display Technologies*, 2174:147–154, 1993.

[2] Mary Tilton. Challenges of manufacturing lcds from active matrices. *Proc. of SPIE, Advanced Flat Panel Display Technologies*, 2174:181–189, 1994.

[3] Guy E. Stong. Modulus of elasticity of glass. *Journal of the American Ceramic Society*, 20:16–22, 1937.

[4] Mireille Akilian et al. Thin optic constraint. *Journal of Precision Engineering*, 31:130–138, 2007.

[5] L.A.B. Pilkington. The float glass process. *Proc. of the Royal Society of London A.*, 314:1–25, 1969.

[6] Y. Takahashi. Ultra-thin-glass production of low or non-alkali glass by float process. *The Ceramic Society of Japan and the International Commission on Glass, Tokyo*, 1989.

[7] Präzisions Glas & Optic. Available at: http://www.pgo-online.com/intlframes/catalogindexset.html.

[8] R.H. Mauch et al. Thin glass substrates for mobile applications. *Proc. of SPIE, Inorganic Optical Materials II*, 4102:162–168, 2000.

[9] M. Cable and J.M. Parker. *High-Performance Glasses.* Chapman and Hall, 1992.

[10] W.C. Hynd. Flat glass manufacturing processes. *Glass Science and Technology*, 2:83–100, 1984.

[11] S.M. Dockerty. *Sheet Forming Apparatus.* U.S. Patent 3,338,696, 1967.

[12] Business Wire. Strategy analytics projects 66 percent flat panel tv revenue increase in 2005; 17.5 million unit sales generates $25 billion, 2005. Available at: http://findarticles.com/p/articles/mi_m0EIN/is_2005_April_13/ai_n13606147.

[13] Klaus Freischlad. Large flat panel profiler. *Proc. of SPIE, Flatness, Roughness, and Discrete Defect Characterization for Computer Disks, Wafers, and Flat Panel Displays*, 2862:163–171, 1996.

[14] Josef C. Lapp et al. Advanced glass substrates for flat panel displays. *Proc. of SPIE, Advanced Flat Panel Display Technologies*, 2174:129–138, 1994.

[15] Henian Zhu, Qiang Lin, and Baizhe Zhang. Analysis of system error in the measurement of liquid crystal empty cell gap by means of interferometry. *Displays*, 21:121–126, 2000.

[16] Schott D-263 glass specifications. Available at: http://www.us.schott.com/special_applications/english/products/thin_glass/d263t.html.

[17] Josef C. Lapp. Glass substrates for amlcd applications: properties and implications. *Proc. of SPIE, Active Matrix Liquid Crystal Displays Technology and Applications*, 3014:2–9, 1997. Invited Paper.

[18] B.N. Shabestari and J.W.V. Miller. Automatic spacer evaluation system. *Proc. of SPIE, Advanced Flat Panel Display Technologies*, 2174:139–146, 1994.

[19] W.K. Pratt et al. Automatic blemish detection in liquid crystal flat panel displays. *Proc. of SPIE, Machine Vision Applications in Industrial Inspection VI*, 3306:2–13, 1998.

[20] Amir Peled and Ofer Saphier. Manufacturing large LCDs while maintaining yields. *Photonics Spectra*, pages 78–80, 2007.

[21] David Attwood. *Soft X-rays and Extreme Ultraviolet Radiation Principles and Applications.* Cambridge University Press, 1999.

[22] Eberhard Spiller. *Soft X-ray Optics.* SPIE Optical Engineering Press, 1994.

[23] P. Kirkpatrick and A. Baez. Formation of optical images by x-rays. *Journal of the Optical Society of America*, 38:766–774, 1948.

[24] R. Petre et al. The constellation-x spectroscopy x-ray telescope. *Proc. of SPIE, UV and Gamma-Ray Space Telescope Systems*, 5488:505–514, 2004.

[25] Chandra at a glance, 2004. http://cxc.harvard.edu/cdo/about_chandra/.

[26] R. Petre et al. The constellation-x spectroscopy x-ray telescope: recent technology development. *Proc. of SPIE, Space Telescopes and Instrumentation II: UV to Gamma Ray*, 6266:62661Q, 2006.

[27] George W. Morey. *Properties of Glass.* Reinhold Publishing Corporation, 1954.

[28] Mireille Akilian. Thin optic surface analysis for high resolution x-ray telescopes. Masters thesis, Massachusetts Institute of Technology, Department of Mechanical Engineering, 2004.

[29] Robert Petre et al. Recent progress on the constellation-x spectroscopy x-ray telescope (sxt). *Proc. of SPIE, Optics for EUV, X-Ray, and Gamma-Ray Astronomy*, 5168:196–206, 2004.

[30] Mario Jimenez-Garate. *The Development of Hard X-ray Telescope Optics and a Theoretical Model of X-ray Emission from Accretion Disks.* PhD thesis, Columbia University, Graduate School of Arts and Sciences, 2001.

[31] R. Heilmann et al. Novel methods for shaping thin-foil optics for x-ray astronomy. *Proc. of SPIE, X-ray Optics for Astronomy: Telescopes, Multilayers, Spectrometers, and Missions*, 4496:62–72, 2001.

[32] R. Heilmann et al. Shaping of thin grazing-incidence reflection grating substrates via magnetorheological finishing. *Proc. of SPIE, Optics for EUV, X-ray and Gamma-ray Astronomy II*, 5900:73–80, 2005.

[33] Alexander H. Slocum. *Precision Machine Design.* Society of Manufacturing Engineers, 1992.

[34] Frank M. White. *Fluid Mechanics.* McGraw-Hill, 1999.

[35] Ascher H. Shapiro. *The Dynamics and Thermodynamics of Compressible Fluid Flow.* Ronald Press Co., 1954.

[36] Michael F. Ashby and Harold J. Frost. *Deformation-Mechanism Maps: The Plasticity and Creep of Metals and Ceramics.* Pergamon Press, 1982.

[37] G. J. Weng. Some elastic properties of reinforced solids, with special reference to isotropic ones containing spherical inclusions. *International Journal of Engineering Science*, 22:845–856, 1984.

[38] P. A. Kakavas et al. Effective moduli of hyperelastic porous media at large deformation. *Acta Mechanica*, 160:127–147, 2003.

[39] J. Ju and T. Chen. Effective elastic moduli of two-phase composites containing randomly dispersed spherical inhomogeneities. *Acta Mechanica*, 103:123–144, 1994.

[40] A.R. Boccaccinin and Z. Fan. A new approach for the young's modulus-porosity correlation of ceramic materials. *Ceramics International*, 23:239–245, 1997.

[41] Z. Fan et al. Microstructural characterisation of two phase materials. *Material Science Technology*, 9:1094–1100, 1993.

[42] H. Mori, H. Yabe, and T. Shibayama. Theoretical solution as a boundary problem for externally pressurized porous gas-bearings. *Journal of Basic Engineering*, pages 622–630, 1965.

[43] B. C. Majumdar and J. Schmidt. Design of externally pressurized rectangular porous thrust bearings. *Wear*, 32:1–8, 1975.

[44] Steven C. Chapra and Raymond P. Canale. *Numerical Methods for Engineers.* McGraw-Hill, 1998.

[45] Murilo D. M. Innocentini et al. Permeability of refractory castables at high temperatures. *Journal of the American Ceramic Society*, 84:645–647, 2001.

[46] K. Kogure, R. Kaneko, and K. Ohtani. A study on characteristics of surface-restriction compensated gas bearing with t-shaped grooves. *Bulletin of the Japan Society of Mechanical Engineers*, 25:2039–2045, 1982.

[47] M. F. Chen and Y. T. Lin. Static behavior and dynamic stability analysis of grooved rectangular aerostatic thrust bearings by modified resistance network method. *Tribology International*, 35:329–338, 2002.

[48] T. Nakamura and S. Yoshimoto. Static tilt characteristics of aerostatic rectangular double-pad thrust bearings with compound restrictors. *Tribology International*, 29:145–152, 1996.

[49] Präzisions Glas & Optic. Available at: http://www.pgo-online.com/intl/katalog/D263.html.

[50] Wole Soboyejo. *Mechanical Properties of Engineered Materials.* Marcel Dekker, Inc., 2003.

[51] Raymond J. Roark. *Roark's Formulas for Stress and Strain.* McGraw-Hill, 1989.

[52] Marc Madou. *Fundamentals of Microfabrication.* CRC Press, 1997.

[53] Richter Precision Inc. Chemical vapor deposition coatings, technical data. Available at: http://www.richterprecision.com.

[54] National Electronic Alloys Inc. Invar 36 alloy. Available at: http://www.nealloys.com/invar.htm.

[55] James Schackelford and William Alexander. *Materials Science and Engineering Handbook.* CRC Press, 2000.

[56] Yunus A. Cengel. *Heat Transfer: A Practical Approach.* McGraw-Hill Science Engineering, 2002.

[57] Inc MKS Instruments. Types 740b, 750b baratron pressure transducers. Available at: http://www.mksinst.com/docs/UR/700seres.pdf.

[58] A.E. Badger and W.B. Silverman. Modulus of elasticity of glass in relation to temperature. *Journal of the American Ceramic Society*, 18:176–280, 1935.

[59] R.G. Munro. Material properties of a sintered alpha-sic. *Journal of Physical and Chemical Reference Data*, 26:1195–1203, 1997.

[60] Robert C. Junivall and Kurt M. Marshek. *Fundamentals of Machine Component Design.* Wiley, 1999.

[61] Craig R. Forest et al. Metrology of thin transparent optics using Shack-Hartmann wavefront sensing. *Optical Engineering*, 43:742–753, 2003.

[62] Andrew Lapsa. On improving the dynamic range of the class-2d Shack-Hartmann system. *MIT Kavli Institute for Astrophysics and Space Research*, 2003. Internal report.

[63] D. Malacara. *Optical Shop Testing.* Wiley, 1992.

[64] Craig R. Forest. X-ray telescope foil optics: Assembly, metrology, and constraint. Masters thesis, Massachusetts Institute of Technology, Department of Mechanical Engineering, 2003.

[65] Olivier Mongrard. High-accuracy foil optics for x-ray astronomy. Masters thesis, Massachusetts Institute of Technology, Department of Aeronautics and Astronautics, 2001.

[66] NASA Goddard Space Flight Center, 2001. Personal communication: Mark L. Schattenburg.

[67] Scott M. Owens et al. The constellation-x sxt optical alignment pathfinder 2 design, implementation and alignment. *Proc. of SPIE, Optics for EUV, X-Ray, and Gamma-Ray Astronomy*, 5168:239–247, 2004.

[68] Paul Glenn. Centroid detector assembly for the axaf-i alignment test system. *Proc. of SPIE, X-Ray and Extreme Ultraviolet Optics*, 2515:352–360, 1995.

[69] Scott M. Owens et al. Alignment and test of a constellation-x sxt mirror segment pair. *Proc. of SPIE, Space Telescopes and Instrumentation II: Ultraviolet to Gamma Ray*, 6266:62661W, 2006.

[70] Charles J. Hailey et al. Fabrication and performance of constellation-x hard x-ray telescope prototype optics using segmented glass. *Proc. of SPIE, X-Ray, and Gamma-Ray Astronomy*, 5168:90–99, 2004.

[71] Jason E. Kogley et al. Development of precision hard x-ray multilayer optics with sub-arcminute performance. *Proc. of SPIE, X-Ray and Gamma-Ray Telescopes and Instruments for Astronomy*, 4851:673–683, 2003.

[72] R. Günther et al. Production of silicon pore optics. *Proc. of SPIE, Space Telescopes and Instrumentation II: Ultraviolet to Gamma Ray*, 6266:626619–1 – 626619–8, 2006.

[73] Marco Beijersbergen et al. Silicon pore optics: novel lightweight high-resolution x-ray optics developed for xeus. *Proc. of SPIE, UV and Gamma-Ray Space Telescope Systems*, 5488:868–874, 2004.

[74] Marco Beijersbergen et al. Development of x-ray pore optics: novel high-resolution silicon millipore optics for xeus and ultra-low mass glass micropore optics for imaging and timing. *Proc. of SPIE, Design and Microfabrication of Novel X-Ray Optics II*, 5539:104–115, 2004.

[75] Stephen Timoshenko. *Theory of Plates and Shells.* McGraw-Hill, 1964.

[76] Timo Saha. NASA Goddard Space Flight Center. Design parameters and data for constellation-x engineering model telescope, 2001.